

**New insights into the structure and energetics of the  
Martian ionosphere**

by

**Christopher M. Fowler**

M.S., University of Colorado, Boulder, 2013

M.Phys., University of Southampton, 2011

A thesis submitted to the  
Faculty of the Graduate School of the  
University of Colorado in partial fulfillment  
of the requirements for the degree of  
Doctor of Philosophy  
Department of Astrophysics and Planetary Science

2016

This thesis entitled:  
New insights into the structure and energetics of the Martian ionosphere  
written by Christopher M. Fowler  
has been approved for the Department of Astrophysics and Planetary Science

---

Dr. Laila Andersson

---

Professor Robert E. Ergun

---

Assistant Professor David Brain

---

Assistant Professor Julie Comerford

---

Professor Jeffrey Thayer

Date \_\_\_\_\_

The final copy of this thesis has been examined by the signatories, and we find that both the content and the form meet acceptable presentation standards of scholarly work in the above mentioned discipline.

Fowler, Christopher M. (Ph.D., Astrophysics and Planetary Science)

New insights into the structure and energetics of the Martian ionosphere

Thesis directed by Dr. Laila Andersson

Understanding the formation and evolution of planetary bodies is of great interest and importance to humankind. Mars, being the closest analogue to Earth in our solar system, has been of particular importance. Having studied the red planet for many decades using landers and orbiting spacecraft, we are now laying the groundwork to venture there ourselves. The Mars Atmosphere and Volatile EvolutioN (MAVEN) mission recently went into Mars orbit to study the physical processes active within the Martian atmosphere, and to understand how the atmosphere itself has evolved throughout the planet's history. This thesis is based upon unraveling data from the MAVEN mission, with a focus on the structure and energetics of the Martian ionosphere. Data from many of the instruments carried by MAVEN have been analyzed in this work, in particular, analysis and fitting of current-voltage sweeps measured by the Langmuir Probe and Waves instrument. New insights have been gained about the operation of Langmuir probes in planetary ionospheres, and through first author papers, about the Martian ionosphere itself. The four papers presented in this thesis focus on the structure and energetics of the Martian ionosphere. The first in-situ observations of the Martian nightside electron density and temperature showed that an ionization source is needed to sustain the observed densities. Precipitating electrons were shown as a feasible source, agreeing with suggestions from previous modeling efforts. The transfer of energy from the solar wind to the atmosphere is an important energy source for the Martian atmosphere. An investigation of the electromagnetic environment at Mars shows how the distribution of wave power, and various plasma boundaries within the Martian magnetosphere, respond to upstream solar wind conditions, highlighting regions important for energy dissipation. The combination of magnetic field and ion data allows for the first time at Mars, ion conics to be observed. These show evidence of parallel acceleration and ion heating present at low altitudes in the ionosphere. Finally, an investigation

of sporadic disturbances observed below the Martian exobase showed that the Rayleigh-Taylor instability is present in the Martian ionosphere. Similar disturbances are present in the terrestrial ionosphere and are known as Equatorial Spread F (ESF). Such disturbances cause communication problems within the terrestrial ionosphere and similar problems may occur when humans reach the surface of the red planet.

## Acknowledgements

I have been incredibly lucky to have support and encouragement from a huge number of people throughout my graduate study. This support has helped me push through the hard times, enjoy the good times, and keep me somewhat sane after five years of work. There are too many people to list all here; for those that I can't mention, thank you for all your support and friendship over the years. Mum, dad, nans and grandads, you have supported, encouraged, and driven me to become what I am today; without that, none of what I have achieved would be possible - thank you. Andrew, you watched *a lot* of Star Trek, Star Wars, Stargate, and so on, with me, when we were both younger (who am I kidding, we still do). Thanks for being a fellow trekkie and setting me on this path. Katy - thank you for your unwavering support and confidence in me; you have always helped me to see the positive side even when things got tough, and never allowed me to give up. Laila, you have been awesome. Thank you for your support, patience, and genuine desire to help me succeed. You have taught me to not accept what is on the surface, but to dig deeper and to understand what is really there. You have also cracked the whip at times when it needed to be cracked, for which I'm very thankful (now). Bob, your excitement about everything science is contagious. Walking into your office to ask a 2 minute question, and leaving 60 minutes later after discussing something completely unrelated, keeps us (the grad students) going. My fellow LASP-ians, thank you for all of the thoughtful discussions, IDL-code-fixing-brainstorming-sessions, and cookie / cake sessions over the years - I would have gone crazy long ago if it were not for these. My fellow Mack-Shackers, your friendship and support during those first two years made adjusting to life in the US a great, and survivable, experience. You will be life-long friends. My fellow APS-ers,

you have supported me in and outside of my academic studies; from group homework sessions in the first year, to skiing on the slopes, thank you for everything, you are truly great friends. The Boulder and CU rugby clubs, thank you for all the bumps and bruises, and giving me a way to vent my frustrations. Thank you to my MAVEN colleagues who have asked tough questions and at times picked apart my work. You have pushed me to become a better scientist. You're also pretty fun to hang out with. Thank you to my thesis committee for taking the time and effort to read this thesis and for providing feedback to further improve my work.

## Contents

<b>Chapter</b>		
<b>1</b>	<b>Introduction</b>	<b>1</b>
1.1	Mars in our night sky . . . . .	1
1.2	The four Martian geological epochs . . . . .	3
1.3	Geological evidence for water on past Mars . . . . .	5
1.4	Mars' (lack of) global magnetic field . . . . .	7
1.5	Mars' early atmosphere . . . . .	8
1.6	Summary . . . . .	9
<b>2</b>	<b>The Martian atmosphere, ionosphere and beyond</b>	<b>10</b>
2.1	The onion layers of Mars' atmosphere . . . . .	10
2.2	The neutral atmosphere and corona . . . . .	11
2.3	The ionosphere . . . . .	14
2.4	Martian Plasma Boundaries . . . . .	18
2.5	Loss processes in the Martian atmosphere and ionosphere . . . . .	21
2.5.1	Jeans escape . . . . .	23
2.5.2	Photochemical escape . . . . .	23
2.5.3	Ion loss . . . . .	24
2.6	Estimates of current day escape rates at Mars . . . . .	27
2.7	Summary . . . . .	29

<b>3</b>	Density and temperature measurements of planetary ionospheres	30
3.1	How does a Langmuir probe work? . . . . .	33
3.2	Cylindrical vs Spherical Langmuir probes . . . . .	34
3.3	Cylindrical Langmuir probe theory . . . . .	35
3.4	Langmuir probe measurements in ionospheres . . . . .	38
3.4.1	LPW specific electron and ion populations . . . . .	41
3.4.2	Example of an LPW I-V curve . . . . .	50
3.4.3	Additional complexities for space-borne Langmuir probes . . . . .	52
3.5	The MAVEN LP fit algorithm . . . . .	59
3.5.1	Derivation of the numerically integrated electron current . . . . .	63
3.5.2	Derivation of the numerically integrated ion current . . . . .	72
3.5.3	Total numerically integrated current . . . . .	76
3.5.4	Probe end effects . . . . .	77
3.5.5	Implementation of the LPW fit algorithm . . . . .	77
3.5.6	A summary of the complexities, sources of error, and implemented solutions, in the analysis of LPW I-V curves . . . . .	106
3.5.7	Implementation on LPW data - a final fit example . . . . .	117
3.6	LPW wave sounding . . . . .	117
3.7	Summary . . . . .	120
<b>4</b>	Summary of my publication work	121
4.1	Paper 1: The first in-situ electron temperature and density measurements of the Martian nightside ionosphere . . . . .	121
4.2	Paper 2: Magnetic and electric variations in the near Mars environment . . . . .	121
4.3	Paper 3: Ion heating within a gradient magnetic field at low altitudes in the Martian ionosphere . . . . .	122
4.4	Paper 4: Observations of the Rayleigh Taylor instability in Mars' ionosphere . . . . .	122

<b>5</b>	<b>The First In-Situ Electron Temperature and Density Measurements of the Martian Nightside Ionosphere</b>	<b>123</b>
	Ionosphere	123
5.1	Abstract . . . . .	124
5.2	Introduction . . . . .	124
5.3	Data And Instrument Overview . . . . .	126
5.4	Electron Density And Temperature Observations . . . . .	128
	5.4.1 Individual Orbit Profiles . . . . .	128
	5.4.2 Statistical Profiles . . . . .	129
5.5	Discussion And Modeling Effort . . . . .	130
	5.5.1 Downward Flowing Ions . . . . .	131
	5.5.2 Precipitating Electrons . . . . .	132
	5.5.3 Electron Temperature . . . . .	133
5.6	Conclusions . . . . .	133
<b>6</b>	<b>Electric and magnetic variations in the near Mars environment</b>	<b>139</b>
6.1	Abstract . . . . .	140
6.2	Introduction . . . . .	140
6.3	Data . . . . .	143
	6.3.1 Description and caveats of the LPW wave spectra dataset . . . . .	144
	6.3.2 Combining the $LF_{lpw}$ , $MF_{lpw}$ and $HF_{lpw}$ spectral ranges . . . . .	146
	6.3.3 Flagging low quality spectra . . . . .	146
	6.3.4 Wave sounding . . . . .	148
	6.3.5 Effects of the spacecraft wake . . . . .	149
	6.3.6 Low frequency noise . . . . .	150
6.4	Analysis method . . . . .	151
	6.4.1 Example spectra . . . . .	153
6.5	Statistical Maps . . . . .	156

6.5.1	Electric and magnetic wave power . . . . .	156
6.6	Wave power as a function of upstream solar wind drivers . . . . .	158
6.6.1	Electric field: $N_{sw}$ , $B_{sw}$ and $V_{sw}$ . . . . .	158
6.6.2	Magnetic field: $M_a$ , $M_{ms}$ , $M_s$ and Beta . . . . .	160
6.6.3	IMF cone angle . . . . .	160
6.7	Interpretation and discussion . . . . .	161
6.8	Conclusions . . . . .	165
<b>7</b>	<b>Ion heating within a gradient magnetic field at low altitudes in the Martian ionosphere</b>	<b>181</b>
7.1	abstract . . . . .	182
7.2	Introduction . . . . .	182
7.3	Data . . . . .	184
7.4	Event . . . . .	185
7.5	Ion velocity distributions . . . . .	187
7.6	Interpretation and discussion of ion data . . . . .	188
7.7	Statistics of similar events . . . . .	191
7.8	Interpretation and discussion of statistical data . . . . .	192
7.9	Conclusions . . . . .	193
<b>8</b>	<b>Observations of the Rayleigh-Taylor instability in Mars' ionosphere</b>	<b>202</b>
8.1	Abstract . . . . .	204
8.2	Introduction . . . . .	204
8.3	Data . . . . .	205
8.4	Event . . . . .	206
8.5	Statistical Study . . . . .	210
8.6	Discussion . . . . .	211
8.7	Conclusions . . . . .	214

<b>9</b>	Future Work	219
	<b>Bibliography</b>	<b>222</b>
	<b>Appendix</b>	
<b>A</b>	Overview of the MAVEN spacecraft	240
	A.1 Overarching science goals . . . . .	241
	A.2 MAVEN scientific instruments . . . . .	242
	A.3 MAVEN ‘deep dip’ campaigns . . . . .	245
<b>B</b>	The LPW instrument	246
	B.1 General overview . . . . .	246
	B.2 LPW science goals . . . . .	246
<b>C</b>	Derivation of $\beta$	248
<b>D</b>	Summary of variables used in Chapter 3	<b>251</b>

## Tables

### Table

3.1	Definition of parameters and assumptions used in Equation 3.4, and reference in Figure 3.5. . . . .	47
3.2	The final fit parameters derived by the LPW fit software for the I-V curve shown in Figure 3.7. . . . .	119
D.1	Summary of the parameters used throughout Chapter 3. The first column is the variable, the second column is a brief description, the third column is the value if constant throughout the fitting algorithm, the fourth column references the section (S) or equation (E) within the main text where the variable is discussed. . . . .	252

## Figures

### Figure

- 3.1 Cartoon representations of spherical, cylindrical and planar Langmuir probes. The conducting material is exposed to the ambient plasma, allowing a measurement of the collected current to the probe to be made. . . . . 36
- 3.2 Panel A: Theoretical I-V curves for cylindrical (black) and spherical (blue) probes subject to identical plasma conditions. Panel B: Derivative,  $\frac{dI}{dV}$ , of panel A. . . . . 36
- 3.3 Cartoon representation of the MAVEN spacecraft traversing the Martian ionosphere. The spacecraft flies right to left at velocity  $V_{sc}$ . The ambient plasma surrounds the spacecraft except in the wake region, where the plasma density is roughly half that of the ambient plasma. Ions collide with the LPW probes at angles  $\theta_{sc,1}$  and  $\theta_{sc,2}$ ; sunlight strikes the LPW probes at angles  $\theta_{sun,1}$  and  $\theta_{sun,2}$ . . . . . 40
- 3.4 Panel A: Theoretical I-V curves for a cylindrical probe, under different spacecraft potential conditions. Panel B: Derivatives of panel A, where the vertical dashed lines mark the respective spacecraft potentials. . . . . 42
- 3.5 Cartoon depicting the method used to calculate the EUV intensity at the spacecraft as a function of position. EUV light is assumed to be absorbed between the inner dark blue and outer light blue circles (representing 100 km and 400 km altitudes respectively). The lower case letters a and b represent the lower and upper limits of integration in Equation 3.4 along the column depth in the Sunward direction. . . . . 48

3.6	Modeled EUV intensity at the spacecraft, as a function of altitude at the subsolar point. . . . .	49
3.7	Example I-V sweep measured by the LPW instrument. The electron and ion collection regions are where electrons and ions respectively are the primary charges collected by the probe. These regions allow derivations of electron and ion density respectively. The $T_e$ region is the region critical in determining the electron temperature. Positive current collection is defined as the collection of electrons. The derived $N_e$ , $T_e$ and $V_{scp}$ values were $2.35 \times 10^5 \text{ cm}^{-3}$ , 0.05 eV (550 K) and 0.58 V respectively. . . . .	51
3.8	Engineering schematic of the LPW instrument, showing the boom deployment mechanisms and the attached probe. Figure taken from <i>Andersson et al. (2014)</i> . . . . .	60
3.9	<b>Flow Chart 1 (FC1):</b> Flow chart summarizing how the numerically integrated electron and ion currents are calculated, using expressions derived in Sections 3.5.1 and 3.5.2. Detailed discussion is given of each stage within the main text and is referenced using the numbers to the left in each box. . . . .	62
3.10	Cartoon representation of electron current collection by the LPW probes. The red circle marks the physical cross section of the probe; the blue and green dashed circles represent the sheath surface for the sheath limited and orbit motion limited cases respectively. The yellow dashed line marks the most extreme attraction an electron can undergo upon entering the sheath at point $X_1$ , and still be collected by the probe, at point $X_2$ . The parameter $\theta_j$ shows the corresponding solid angle within which electrons are collected by the probe. Electron collection occurs from the entire sheath surface and so the contribution from point $X_1$ must be integrated across the entire sheath surface area. More discussion is given in the main text. . . . .	68

3.11 Cartoon representation of ion current collection by the LPW probes. The red circle marks the physical cross section of the probe; the dashed green line marks the sheath surface. The spacecraft velocity is much greater than the ion thermal speed at periapsis and so ions are collected purely from the RAM direction, denoted by the blue arrow. In the probe frame of reference, ions travel at the spacecraft velocity as marked by the black arrows. The yellow dashed line marks the most extreme deflection an ion can undergo upon entering the sheath at point  $X_1$ , and still be collected by the probe, at point  $X_2$ . Due to the large spacecraft velocity, ion collection occurs only between the two points labeled  $X_1$ , corresponding to the impact parameter  $2a_j$ . More discussion is given in the main text. . . . . 75

3.12 **Flow chart 2 (FC2):** Flow chart summarizing the LPW fit algorithm. Detailed discussion is given of each stage within the main text and is referenced using the numbers to the left in each box. . . . . 79

3.13 The weighting table corresponding to the I-V curve shown in Figure 3.7, used by the LPW fit software during the derivation of various parameters for this I-V curve. The horizontal axis is probe potential with respect to the spacecraft ground. The weighting table takes into account the fact that electron currents can be several orders of magnitude than collected ion currents, and prevents the electron side of the I-V curve from dominating the fit algorithm. The vertical lines mark  $V_{\text{ramp}}$ ,  $V_{\text{scp}}$ ; and the lower and upper bounds on  $V_{\text{scp}}$ , as described in Sections 3.5.5.3(1) and 3.5.5.3(3) . . . . . 81

3.14 Zoom in of the  $V_{\text{ramp}}$  region. The blue line is a straight line fit to the blue ion side data (note the horizontal axis does not cover the entire ion current range); the green vertical line marks  $V_{\text{ramp}}$ , the transition into the  $T_e$  fit region. The first six data points within the  $T_e$  fit region (marked in green) are used to determine the initial estimate of  $T_e$ . The red dashed vertical line marks the lower limit to spacecraft potential, as calculated in bullet 3. . . . . 84

- 3.15 The six green data points from Figure 3.14 are plotted here and used to obtain an initial estimate of  $T_e$ . The natural log of measured current (shown on the vertical axis) is linearly proportional to probe potential within the  $T_e$  fit region; the green line shows a linear absolute difference fit to these data. The inverse of the gradient of this line is equal to  $T_e$ . Several estimates of  $T_e$  are obtained from these data; the values noted in the figure are described in the main text. The red and blue lines show how the green fit varies when  $T_e$  is increased or decreased by 20%, respectively. 86
- 3.16 Derivative of the measure I-V curve shown in Figure 3.7 (black data points). The blue data points are used to determine  $V_{\text{ramp}}$  which is marked by the green vertical line. The six green data points are used to determine an initial estimate of  $T_e$ . The red data points mark the points used to determine the parameter  $\beta$  which is described in the main text. The purple line shows a theoretical derivative of electron current for this I-V sweep, divided by a factor of 2 so that it fits on the same plot. For ideal Langmuir probe behavior there is only one major peak in the derivative of measured current as seen in the purple line and this marks the location of  $V_{\text{scp}}$ . Atomic oxygen contamination of the probe surfaces, as discussed in *Ergun et al. (2015a)*, causes in some cases multiple peaks to be observed, complicating the derivation of  $V_{\text{scp}}$ . The solid red line marks an initial estimate of  $V_{\text{scp}}$ ; the two dashed red vertical lines mark the initial lower and upper bounds to  $V_{\text{scp}}$ . . . . . 88
- 3.17 The example I-V curve shown in Figure 3.7. Blue colors mark data points used to determine  $V_{\text{ramp}}$ , which is marked by the green vertical line. The six green data points were used to obtain the initial estimate of  $T_e$ . The red data points were used to determine  $\beta$ . The solid red vertical line shows in the initial estimate of  $V_{\text{scp}}$ ; the two red dashed lines show the initial lower and upper bounds on  $V_{\text{scp}}$ . . . . . 91

- 3.18 Individual I-V curves measured at different altitudes (marked by color) from the same periapsis pass as the I-V curve shown in Figure 3.7. The I-V curves have been multiplied by the noted factors so that they can be plotted on the same figure. The figure focusses on the electron collection region - the shape of the measured I-V curve here depends upon whether the probe sheath behaves as a sphere or cylinder. At high altitudes (low densities) the measured I-V curves show spherical behavior (the I-V curves are linear above about 2 V); at low altitudes (high densities) cylindrical behavior is observed (the I-V curves are no longer linear above 2 V). . . . . 92
- 3.19 The parameter  $\beta$  derived from the LPW fit algorithm for a weeks worth of data, as a function of Debye length,  $\lambda_D$ .  $\lambda_D$  is calculated from the corresponding derived values of  $N_e$  and  $T_e$  from the LPW fit algorithm. Color shows the altitude at which each I-V curve was measured at. Cylindrical sheath behavior corresponds to  $\beta = 0.5$ ; spherical sheath behavior corresponds to  $\beta = 1$ . . . . . 93
- 3.20 Zoom in of the ion saturation and  $T_e$  fit regions for the example I-V curve shown in Figure 3.7. The data are the numerically integrated ion currents as derived by the LPW fit algorithm for different average mass  $M_i$  values. The decimal precision mass value is the final value converged upon by the LPW fit algorithm and the black data points (and matching brown line) show these final numerically derived data points. . . . . 96
- 3.21 Statistical distribution of the LPW derived average ion mass as a function of altitude for the same data set used to produce Figure 3.19. The colorbar shows the time of measurement as a function of time elapsed (in days) from the first data point in the data set, 2015-04-17/01:13:24 UTC. . . . . 97
- 3.22 **Flow Chart 3 (FC3):** Flow chart outlining the refinement procedure to optimize individual I-V curve parameters. This procedure is called upon by boxes 15-18 and 20-24 in FC2. . . . . 100

- 3.23 Panel A: LP derived and waves derived electron densities from the LPW instrument. The outer dashed red lines show plus/minus 25% from the 1:1 value (middle red dashed line). The middle purple line shows the median fit to the data; the outer purple lines show plus/minus one standard deviation from this. Panel B: as for panel A, but for the empirically corrected LP densities. . . . . 107
- 3.24 Cartoon depictions of large (case A), medium (case B) and small (case C) spacecraft potentials. As spacecraft potential gets smaller, the (constant) probe potentials are able to ‘break out’ of the spacecraft potential well, as seen in case C. . . . . 108
- 3.25 Cartoon depiction demonstrating why spherical sheath behavior is observed at large  $\lambda D$ . The red rectangles represent the LPW probes of physical radius  $r_p$  and physical length  $L_p$ . The dashed green lines represent the sheath surface. Case A is for a high densities when the Debye length is small, leading to a small sheath radius  $r_s$ . Case B is for a low densities when the Debye length is large and correspondingly  $r_s$  is large. 111
- 3.26 Cartoon representation of the sheath collapse effect. Panel A shows the probe biased at a large negative potential; ions are attracted to the probe and the sheath is large. Panel B shows the probe biased to a small positive potential; ions are deflected from the probe, but the potential is not yet large enough to attract a significant number of electrons and so the sheath is small. Panel C shows two possible behaviors for the transition between large and small sheath sizes: the red line represents a smooth transition; the blue a sharp one. Sheath collapse occurs under the sharp transition; there is a corresponding spike in current collected by the probe, leading to larger uncertainties in the derived value of  $T_e$ . . . . . 114

3.27 The final numerically integrated fit derived by the LPW fit software. The measured I-V curve is shown by the black data points. The colored curves show various numerically integrated currents: black the total current collected by the probe; red; blue the ion current; brown and purple the photoelectron currents from the probe and spacecraft respectively; orange the hot electron current. The green data points mark the points used to determine the initial bounds for  $T_e$ . Panel A shows the entire I-V curve; panel B shows a zoom in on the  $T_e$  fit region. . . . . 118

5.1 MAVEN orbit coverage for November 2014 through February 2015 in the MSO coordinate frame for altitudes below 600 km. Color represents altitude in km. Curved dashed lines represent the labeled local times as projected onto the Y-Z plane. Solid curved lines represent SZA as projected onto the Y-Z plane. The direction of travel for any individual orbit is in the +Z direction. The thick black line represents the orbit track corresponding to the electron density and temperature profiles shown in Figure 5.2. . . . . 135

5.2 Altitude profiles of electron density (left) and electron temperature (right) for one periapsis pass between 2014-12-02T22:09 and 2014-12-02T22:32 UTC. The dawn terminator was approximately at periapsis. The inbound portion of the orbit is colored blue and is on the nightside. The outbound portion is colored red and is on the dayside. Representative error bars are shown as black horizontal lines. Altitude is calculated in the Mars IAU frame, which is referenced to the IAU 2000 Mars Areodetic ellipsoid. Reduced signal-to-noise ratios below densities of  $\sim 200 \text{ cm}^{-3}$  result in LP temperature measurement errors increasing to 100% or more and therefore such temperature measurements are omitted here. . . . . 136

5.3 Statistical median altitude profiles of electron density (A, left) and electron temperature (B, right). Both binned as described in the text. A local time of 18 corresponds to dusk; 24 to midnight and 6 to dawn. . . . . 137

- 5.4 (a) Densities for  $O_2^+$  and  $CO_2^+$  ions based on recombination as a function of time. (b) Input spectrum for downward traveling precipitating electrons, as measured by SWEA at  $\sim 500$  km on 2014-12-05T05:11:59 UTC. (c) Median statistical electron densities as in Figure 5.3 with simulation results over plotted as dashed lines. Dashed green shows the input ion density profile; dashed purple shows the resulting equilibrium ion density profile that was obtained after  $\sim 25$  minutes of run time. Precipitating electrons were included as calculated from the SWEA spectrum shown in the middle panel. . . . . 138
- 6.1 Highlighted caveats of the LPW wave spectra that are discussed in the text. Panels A and B show the ACT and PAS wave spectra; panel C shows the local electron density derived from the LPW wave sounding measurements in black and the Langmuir Probe in red. Panel D shows the percentage difference between these quantities. Panel E shows the spacecraft altitude. The lines L1 and L2 mark densities of  $1 \times 10^3 \text{ cm}^{-3}$  and  $2 \times 10^4 \text{ cm}^{-3}$  respectively. The four vertical black lines mark where the Langmuir Probe derived densities in Panel C cross these values. . . . . 168
- 6.2 Cartoon diagram of the binning method used to produce statistical maps in this study. Panel A shows the Y-Z plane cut into four regions - north (N), south (S), dawn and dusk. Data from these regions are used to produce the maps shown in panels B and C, looking at different planes. This system is used for both the MSO and MSE frames at Mars. Only data between  $-1R_M < 1.5 R_N$  is used when creating the statistical map shown in panel A. . . . . 169

6.3	Example electric and magnetic field wave power spectra for one orbit about Mars. Panels A and C show the ACT and PAS electric field power spectra respectively. Panels B and D show the time series electric field data from which these spectra were derived from. Panels E and F show the magnetic field power spectrum, and the corresponding time series magnetic field data, respectively. Panel G shows the spacecraft altitude in the IAU frame. E power has units of $V^2m^{-2}Hz^{-1}$ . B power has units of $T^2Hz^{-1}$ . . . . .	170
6.4	Statistical maps of LF (1 -5 Hz) electric field wave power in the MSE frame. Panels A, B and C show the X-Z, X-Y and Y-Z planes respectively. . . . .	171
6.5	Statistical maps of MF (5 Hz) electric field wave power in the MSE frame. Panels A, B and C show the X-Z, X-Y and Y-Z planes respectively. . . . .	171
6.6	Statistical maps of HF (1k - 5k Hz) electric field wave power in the MSE frame. Panels A, B and C show the X-Z, X-Y and Y-Z planes respectively. Note that due to the sporadic nature of electric field wave power in the HF range the statistical mean has been used to produce this map rather than the statistical median. . . . .	172
6.7	Statistical maps of ULF (0.01 - 0.1 Hz) magnetic field wave power in the MSE frame. Panels A, B and C show the X-Z, X-Y and Y-Z planes respectively. . . . .	172
6.8	Statistical maps of LF (1 - 5 Hz) magnetic field wave power in the MSE frame. Panels A, B and C show the X-Z, X-Y and Y-Z planes respectively. . . . .	173
6.9	Statistical maps of MF (5 Hz) magnetic field wave power in the MSE frame. Panels A, B and C show the X-Z, X-Y and Y-Z planes respectively. . . . .	173
6.10	Ratio of electric field wave power in the LF (1 - 5 Hz) range for upper to lower quartiles of solar wind upstream drivers. Panels a, b and c show ratios for upstream solar wind proton density, magnetic field and proton velocity. . . . .	174
6.11	Ratio of electric field wave power in the MF (5 Hz) range for upper to lower quartiles of solar wind upstream drivers. Panels a, b and c show ratios for upstream solar wind proton density, magnetic field and proton velocity. . . . .	174

6.12	Ratio of electric field wave power in the HF (1k - 5k Hz) range for upper to lower quartiles of solar wind upstream drivers. Panels a, b and c show ratios for upstream solar wind proton density, magnetic field and proton velocity. . . . .	175
6.13	Ratio of magnetic field wave power in the ULF (0.01 - 0.1 Hz) range for upper to lower quartiles of solar wind upstream drivers. Panels a, b, c and show ratios for upstream Alfvén mach number ( $M_a$ ), magnetosonic mach number ( $M_{ms}$ ), sonic mach number ( $M_s$ ) and proton beta (beta), respectively. . . . .	176
6.14	Ratio of magnetic field wave power in the LF (1 - 5 Hz) range for upper to lower quartiles of solar wind upstream drivers. Panels show the same upstream drivers as in Figure 6.13. . . . .	177
6.15	Ratio of magnetic field wave power in the MF (5 Hz) range for upper to lower quartiles of solar wind upstream drivers. Panels show the same upstream drivers as in Figure 6.13. . . . .	178
6.16	Ratio of electric field wave power in the HF (1k - 5k Hz) range for upper to lower quartiles of solar wind upstream drivers. Panels show the same upstream drivers as in Figure 6.13. . . . .	179
6.17	Panels a and c show the ratio of electric field wave power in the MF (5 Hz) range, for parallel ( $-B_x$ ) and anti-parallel ( $+B_x$ ) IMF directions. Panels b and d show the ratio of magnetic field wave power in the LF range for $-B_x$ and $+B_x$ IMF directions.	180

- 7.1 The MAVEN orbit trajectory in the Mars Solar Orbital (MSO) frame for May 4<sup>th</sup> 2015 between approximately 10:00 to 15:00 UTC. (A) is in cylindrical coordinates, (B) and (C) show the orbit from different perspectives in the MSO frame. All axes have units of Mars radii. The grey conics in (A) represent the empirical Bow Shock (BS) and Magnetic Pileup (MPB) plasma boundaries as derived by *Vignes et al.* (2000). The grey semi-circle represents an altitude of 400 km, the approximate extend of the Martian ionosphere. The heating event is marked by the thick purple line. . . . . 195
- 7.2 Panel A: ion energy spectrogram for all mass species, corrected for spacecraft potential. Panel B: ion mass distribution. Panels C and D: electron density and temperature respectively. Panel E: total magnetic field strength. Panel F: cone angle between the spacecraft velocity vector and magnetic field vector. Panel G: cone angle between the spacecraft radial position vector and the magnetic field vector. Panel H: magnetic field power spectrum. Panel I: electric field power spectrum. Panel J: altitude profile as referenced to the International Astronomical Union (IAU) 2000 Mars Areodetic ellipsoid. Energy flux has units of  $[\text{eV} (\text{eV cm}^2 \text{s sr}^{-1})]$ . . . . . 196
- 7.3 Spectrogram data showing energetic ions for all mass species. The analyzed ion distributions are averaged over the five segments shown in the figure, labeled with the numbering at the top of the panel. . . . . 197
- 7.4 Panels A and B: distribution functions of  $\text{O}^+$  and  $\text{O}_2^+$  ions when energetic ions were observed. Data is averaged between 12:21:45 and 12:22:44 UTC from segment 4 in Figure 7.3 and is presented in the Mars frame. Positive parallel velocity is in the magnetic field direction. Only positive perpendicular velocities are shown due to spacecraft contamination at negative velocities. . . . . 197
- 7.5 More typical non energetic ions observed at periapsis. The figure format is the same as Figure 7.4. Data is averaged from two periapses later between 21:21:00 and 21:22:00 UTC. . . . . 198

- 7.6 Observed ion pitch angles for different ion velocities compared to what a simple magnetic mirror would produce. Panels A and B show data for  $O^+$  and  $O_2^+$  respectively. The black lines show the measured pitch angle distributions obtained from analysis of Figure 7.4. Red lines show modeled pitch angle distributions resulting from the magnetic mirror force at various magnetic field strength ratios,  $B_r$ . . . . . 199
- 7.7 Electron fluxes demonstrating photoelectrons are leaving the planet parallel to the magnetic field (panel A) during the time that energetic ions are observed. No photoelectrons are observed moving towards the planet anti-parallel to the magnetic field (panel B) during the same time period. This suggests that one end of the magnetic flux tube is well connected to the deep Martian ionosphere; the other end is not. . . 200
- 7.8 The distribution of the 31 observed energetic ion events as a function of altitude. Events full filled three criteria: 1. They occur below 600 km altitude. 2: Ionospheric ions are observed between energies 10 - 50 eV with average energy fluxes greater than  $1 \times 10^7$  eV  $(\text{eV cm}^2 \text{ s sr})^{-1}$ . 3: A minimum in magnetic field strength is present when energetic ions are observed. All events are confirmed by eye. . . . . 201
- 8.1 Time series plasma data for the studied event. Panels are: A: LPW I-V characteristics. B: SWEA suprathermal electron energy flux. C: 3D magnetic field in the MSO frame. D: total magnetic field strength (black) and modeled magnetic crustal fields (red, *Morschhauser et al. (2014)*). E: high frequency variation in magnetic field. F: angle between magnetic field and vertical direction. G:  $N_e$  from LPW. H:  $T_e$  from LPW. I: Altitude in the IAU-Mars frame. The fluctuations in magnetic field and electron density mark the region of interest, between 21:03:00 and 21:05:30 UTC . . 216

- 8.2 Various parameters for the inbound segment of the orbit shown in Figure 8.1. Panels are: A: Collision and gyrofrequencies for the species labeled in the plot. B: Neutral CO<sub>2</sub> density (black), ion and electron density (blue and red respectively, both scaled by  $5 \times 10^5$ ). C: The percentage variation of the species shown in panel B. D: The high frequency variation in magnetic field. E:  $N_e$  for this event (red);  $N_e$  for neighboring orbits where fluctuations in magnetic field and plasma density were not present (lighter colors). . . . . 217
- 8.3 Statistical analysis of events similar to those shown in Figure 8.1. Panel A: the normalized distribution of events (black) and the total number of orbit samples (red) as functions of SZA. Panel B: the distribution of magnetic field angles for the events shown by the black line in panel A; 90° is horizontal, 0° and 180° are vertical field. Panel C:  $N_e$  profiles for the three events that comprise the spike in occurrence at -10° to 0° in the black line in panel A (colored lines). The gray dots show density profiles for  $\sim 25$  orbits either side of these events. . . . . 218

## Chapter 1

### Introduction

#### 1.1 Mars in our night sky

Mars has played an important role throughout human history, influencing religious, astronomical and scientific communities. The first recorded observations of Mars were made by the Egyptians in the 2<sup>nd</sup> Millennium BC. Astronomical alignments were used to determine important events (both religious and non religious) and were used to define the Egyptian 365 day calendar. The motion of Mars throughout the sky has been observed and recorded throughout history; observations made by various Chinese dynasties exist dating from around 1000 BC; the Babylonians and ancient Greeks are perhaps more recognizable cultures that were influenced by the motions of celestial objects. Indeed, the ancient Greeks developed the geocentric model of the solar system, believing that the motions of the planets were circular and that the Earth lay at the center of the solar system, with the other bodies orbiting around it. The first telescopic observations of Mars were made by Galileo Galilei in 1610 and the rapid development of telescopes meant that within a century astronomers of the time were able to distinguish distinct surface features on Mars such as the polar caps and large regions of similar geologic origin. Increasingly accurate measurements of the orbits of the planets in the 17<sup>th</sup> century revealed that their trajectories were in fact elliptical and this led to the proposition and mainstream acceptance of the heliocentric solar system model developed by Copernicus, Galileo and Kepler. In the late 1800s the Italian astronomer Giovanni Schiaparelli described what he believed were canals on the surface of Mars; the beliefs that these canals were artificial constructs made by Martians to transport water from the polar caps was

widely popularized by the astronomer Percival Lowell in the early 1900s. Further advancement of ground based telescopes in the early 1900s, however, led to skepticism of the existence of these canals; their existence was thoroughly disproved in the 1960s by the first NASA probes to explore the red planet up close. The earlier ‘observations’ of canals are now regarded as optical illusions.

Since the early 60’s, over 30 spacecraft have been sent to Mars and although not all were successful, a huge wealth of information and knowledge has been attained from these missions. The first successful mission to Mars was the Mariner 4 spacecraft that flew by the planet on July 14<sup>th</sup> 1965, sending 21 photos back to Earth (*Howell*, 2015). There were several more successful flybys of the Red planet shortly after, but the first successful extended study of Mars came from the Viking 1 and 2 missions. These both consisted of an orbiter and lander; the landers returned in-situ measurements of the Martian atmosphere, many of which have, up until the recent Mars Atmosphere and Volatile and Evolution (MAVEN) mission, remained at the core of most theoretical modeling efforts of the Martian atmosphere. These early successes and glimpses of a planet that in many ways looks very similar to Earth, and yet so different in many others, pathed the way for a multitude of future orbiters and landers to explore the Red planet.

Landers provide in-situ measurements from the ground and are able to classify the local geology. As with the Viking landers, in-situ altitude profiles can be measured on the descent to the surface providing information about the Martian atmosphere at the lowest altitudes (below about 100 km) that are unattainable by orbiting satellites. With current day technology these profiles are however one off measurements - once the lander is on the ground, it is there for good! Orbiting spacecraft provide a more global view of the planet; orbit parameters can be designed so that spacecraft gradually precess about the planet, enabling observations to be made across a wide range of local times, longitudes and latitudes.

There are however difficulties associated with interpreting single spacecraft and lander measurements at a planet; the most common is known as the ‘single point measurement’ problem. Each data point exists only at a single point in space and time, making it very difficult to infer what is happening across the rest of the planet at that time. An analogy is sending a lander to

Earth, with no prior knowledge of the global, or local, climatic conditions. If the lander were to land in the Atacama desert in South America (one of the driest deserts on the planet), or in the Amazon rainforest in Brazil, you would conclude two very different climates for the Earth from each location. The same is true for the Martian surface rovers and spacecraft orbiting Mars. Surface landers are typically able to travel across the surface although most landers are designed to travel a few tens of kilometers at most, and as such they will typically only explore one geologic region of the planet. One solution to this problem is to send multiple landers to different surface locations on the planet and this technique is currently employed at Mars. Orbiting spacecraft can utilize the precession of their orbits to mitigate the single measurement problem so that different parts of the near-Mars space environment are sampled over the course of a mission. The primary science goals of each individual mission affect how fast, or whether at all, this precession of the spacecraft orbit occurs.

## 1.2 The four Martian geological epochs

The question of whether liquid water once existed on the surface of Mars holds great importance not only for our understanding of the evolution of our Solar system, but also for the possibility that the Red planet once harbored conditions favorable for supporting life. Extensive studies by Earth-borne scientific observatories, Mars orbiting satellites and Martian surface rovers have compiled substantial evidence that liquid water was once present on the surface of the planet; estimates of the depth of past oceans that once existed range from a few meters to a few kilometers deep, for example. The question has since evolved: how much liquid water was once present on the surface of Mars and where did it go? Present day observations show a lack of liquid water on the surface of Mars; put simply, liquid water from the past had to go either into the ground or escape to space. Current day investigations are determining the relative contributions of these two paths by providing insight into the physical processes that are active for each at present day Mars, and throughout its history.

There have been many reviews discussing the presence of liquid water, its past abundance,

and the resulting closely linked climate evolution of Mars, for example, *Mutch and Head* (1975); *Pollack* (1979); *Pollack and Toon* (1982); *Hartmann and Neukum* (2001); *Jakosky and Phillips* (2001); *Carr and Head* (2003); *Borg and Drake* (2005); *Chevrier and Mathé* (2007); *Carr and Head* (2010); *Martínez and Renno* (2013); *Lasue et al.* (2013). The majority of Mars' geologic history is defined by three main periods: the Noachian (4.1 - 3.7 Gyr ago), the Hesperian (3.7 - 3 Gyr ago) and the Amazonian (3 Gyr ago till present). The pre-Noachian, the fourth epoch, is defined as from the time of formation of the planet, about 4.5 Gyr ago, to the start of the Noachian period. Little is known about the pre-Noachian due to extensive volcanic and geologic activity during this epoch and the substantial evolution of geologic features since then. Numerous large basin forming impacts occurred and the planet most likely held a global magnetic field. The nature of the atmosphere and the inventory of volatiles are unknown during the pre-Noachian; this information has been erased by the extensive geologic activity in this age and the early Noachian (*Carr and Head*, 2010).

The Noachian period is thought to be when the majority of surface weathering occurred on Mars: cratering, erosion and valley formation occurred at high rates. During the Hesperian epoch the majority of aqueous processes on the surface of Mars dwindled and the rates of cratering, erosion and valley formation all dropped significantly. Large, episodic floods were however still present, and may have left large bodies of water on the surface, particularly in the northern lowlands. Volcanism continued at a relatively high rate for the first half of the Hesperian, resurfacing at least 30% of the Martian surface. Geological activity slowed at the end of the Hesperian and the average rate of volcanism was about a factor of 10 lower in the Amazonian compared to the Hesperian. During the Amazonian, the erosion and weathering of surface features occurred at low rates and the epoch is characterized by the formation of features driven by the presence, accumulation, and movement, of ice. *Carr and Head* (2010), for example, provide a substantial review of these epochs and a useful visualization of the processes active within each in their Figure 1.

### 1.3 Geological evidence for water on past Mars

Given the active nature of the Noachian and early Hesperian periods in relation to surface weathering and erosion, and the formation of many geological features thought to be driven by aqueous processes, I briefly summarize here some of the key observations from these epochs that support the presence of liquid on the planet surface. Generally speaking, there are two scenarios that have been proposed to explain the observed features that are discussed in this chapter: the first is a ‘warm and wet Mars’, where the past climate was much warmer and wetter than present day conditions. A thicker atmosphere would have been present to support such conditions. The second scenario is a ‘cold and dry Mars’, where the planet has remained frozen for the majority of its history. Episodic and/or seasonal melting of snow and ice deposits is invoked to provide the liquid water necessary to produce the observed surface erosion features. The relative contributions from these two scenarios to Mars’ climate history is still under debate, e.g. *Pollack et al.* (1987); *Craddock and Howard* (2002); *Squyres and Kasting* (1994); *Toon et al.* (2010); *Wordsworth et al.* (2013, 2015).

Valleys and networks on the Martian surface are typically a few hundred km long with several reaching a few thousand km long (*Howard et al.*, 2005b). High resolution satellite imaging shows that these features are most densely populated within Noachian terrain and consist mostly of ‘U shaped’ valleys that typically form gradually rather than abruptly (*Carr*, 1996; *Carr and Head*, 2010). The formation of such features requires at least sporadic precipitation, surface run off, infiltration and ground seepage of liquid water (*Craddock and Howard*, 2002; *Irwin and Howard*, 2002; *Hynek and Phillips*, 2003; *Stepinski and O’Hara IV*, 2003; *Howard et al.*, 2005a; *Carr*, 2006; *Carr and Head*, 2010). The characteristic sizes of these valleys, and of the deltas and fans observed where these valleys enter lowlands, suggest that a similar volume of water was present during their formation as is seen with similar sized terrestrial drainage systems (*Malin and Edgett*, 2003; *Fassett and Head*, 2005; *Moore et al.*, 2003).

Drainage basins are present and are thought to have formed from the erosion of surface

material by the constant flow of liquid water, a process known as ground water sapping. In order to sustain the constant (or even episodic) flow of ground water it is acknowledged that a precipitation and hydrothermal circulation cycle would be required (*Pieri, 1980; Carr and Clow, 1981; Baker et al., 1990; Gulick, 1998*). Large flood features appear to have been rare in the Noachian period (due to the scarcity of flood-like features observed in Noachian terrain) and are thought to have been caused by the overflowing of upstream lakes (*Parker et al., 2000; Irwin et al., 2002, 2004*).

Evidence of surface erosion is also observed in ancient impact craters found on Noachian terrain. The largest craters and basins are severely eroded: impact ejecta, crater rims and central peaks are all typically removed. The smallest craters, less than  $\sim 15$  km in diameter, are scarce, suggesting that these have been completely eroded. Erosion rates during the Noachian period are thought to have been comparable to rates in dry regions at present day Earth, and were at least 1000 times greater than in the Hesperian and Amazonian epochs (*Chapman and Jones, 1977; Craddock and Maxwell, 1993; Carr, 1996; Golombek and Bridges, 2000*).

Geologic features found on Hesperian terrain are thought to have been carved out by sporadic flooding and it has been postulated that the northern plains were once an ocean, acting as the source of this flood water. Work by *Parker et al. (1989)* and *Parker et al. (1993)* mapped geological features that were interpreted as possible shorelines around the edges of the northern plains. Later work by *Carr and Head (2003)* analyzed data from the more recent Mars Global Surveyor (MGS) satellite to test this ocean hypothesis. They found little evidence for an ocean spanning the entire northern plain - many of the features previously interpreted as shorelines were shown to be volcanic in nature, and to show substantial variation in elevation. Rather, the authors found evidence for smaller, but still significantly large, bodies of water in the northern plains, in particular the Vastitas Borealis Formation. Estimates of the past water content of these various large surface reservoirs have been made and are typically presented as the global equivalent layer (GEL). This is the equivalent depth were these volumes of water to be spread over the surface of Mars. Estimates of GEL from multiple basins made by different authors are presented in Table 1 from *Carr and Head (2003)*; estimates range from a few meters GEL up to nearly 2.5 km GEL. The large range of GEL estimates arise

in part because the analyzed basins are inherently different in size and subsequently volume, but also due to the difficulty in identifying the volume of each basin that is thought to have once held water. For comparison, Earth has a surface GEL of roughly 3 km; some of the estimates shown in *Carr and Head* (2003) come close to this, but they are typically a factor of 10 to 100 less.

Plenty of evidence points to at least sporadically wet, warm surface conditions in the Noachian epoch with precipitation present. There is great uncertainty as to how sustained these conditions were, and plenty of questions still exist regarding, for example, a quasi-steady hydrologic system whereby precipitation and ground water were balanced by evaporation and the sublimation of water and ice (*Carr and Head*, 2010). I direct the reader to the aforementioned review articles for more detailed information on the geologic history of Mars.

#### 1.4 Mars' (lack of) global magnetic field

Current day Mars does not possess a global magnetic field and the planet is said to be unmagnetized. Historic Mars is, however, thought to have possessed a global magnetic field driven by an internal dynamo. Evidence of this past global field exists in the form of crustal magnetic fields: localized regions of crust that are magnetized and produce localized magnetic anomalies. These crustal fields were originally observed by the MGS spacecraft and are located mostly in the southern highlands (e.g. *Acuna et al.* (1999); *Connerney et al.* (1999)). They are typically absent in and around younger impact basins suggesting that the anomalies were created during the pre Noachian, Noachian and early Hesperian periods, when volcanic and geologic activity was prevalent (*Carr and Head*, 2010). As geologic activity subsided through the late Hesperian, it is likely that the internal dynamo and subsequent global magnetic field also perished. Subsequent impacts at later times would remove the afore mentioned crustal anomalies, explaining their lack of presence at these large, more recent impact basins. These crustal fields are typically a few tens of nT in strength at 400 km altitude (*Connerney et al.*, 1999) and in a few cases can reach strengths of a few hundred nT. Due to the lack of a dipole field at current day Mars, typical magnetic field strengths in non-crustal regions at similar altitudes are a few tens of nT, and subsequently, the

crustal anomalies can frequently be the dominant source of magnetic field at Mars. The lack of a global magnetic field at Mars leads to a different interaction with the impinging solar wind compared to magnetized planets such as the Earth. More detailed information is given in Chapter 2, but typically this interaction region is on a much smaller scale, where the stand off distances of various plasma boundaries at Mars are much closer to the planet than their counterparts at magnetized planets such as Earth, for example.

As an interesting side note, crustal magnetic fields are also present in the Earth's crust. They are produced by the Earth's global dipole field, although this field has been shown to reverse direction and change intensity throughout time (e.g. *Guyodo and Valet (1999)*). Under current day conditions, the global dipole field swamps these much smaller anomalies and they typically go unnoticed. Present day terrestrial volcanism and tectonic activity is constantly reshaping these anomalies.

## 1.5 Mars' early atmosphere

The extensive volcanism and geologic activity present in Mars' early history are thought to have provided a thicker atmosphere than is observed at present day Mars; one that was rich in CO<sub>2</sub> and possibly water. Geochemical analysis of Martian meteorites has been used to estimate the water content of the early Martian crust; up to 1.8% of this, by weight, may have been water, which is ~ 5 - 10 times lower than the current day terrestrial value (*McSween et al., 2001*). Impacts of large asteroids and comets were sources and sinks of the early Martian atmosphere (the pre Noachian and Noachian periods coincide with the heavy bombardment era within the solar system). Large impacts are thought to have removed between 50% and 90% of the early Martian atmosphere (e.g. *Melosh and Vickery (1989)*; *Brain and Jakosky (1998)*); volatile rich comets can however also contribute to Mars' atmosphere (*Chyba et al., 1994*), although the relative importance of loss versus supply is unknown. *Owen and Bar-Nun (1995)* have shown through analysis of heavy noble gas isotopes that the majority of volatiles in both Earth and Mars' atmospheres may have been supplied from cometary impacts. Current day Martian atmospheric conditions are discussed in

## Chapter 2.

### 1.6 Summary

Geologic observations suggest that ancient Mars was once a much wetter planet than it is today. Substantial surface water was required, at least over sporadic time intervals, to produce the erosion features observed on the surface. The prevalent volcanic and geologic activity present during the planets early history would likely have produced a much thicker atmosphere than is observed today and this would have helped support liquid water on the surface. Determining the fate of this early water and atmosphere poses many interesting and challenging questions that impact our understanding of planet formation and the evolution of planetary atmospheres. Advances in these fields will improve our understanding of our solar system neighbors along with that of the Earth, and will advance our search for likely habitable worlds further afar than our solar system.

## Chapter 2

### The Martian atmosphere, ionosphere and beyond

#### 2.1 The onion layers of Mars' atmosphere

The solid body of a planet, and the atmosphere it retains (if any), can be split up into different layers, much like the layers of an onion. Layers are typically defined by the physical processes that dominate in each and there are characteristic properties that broadly define each layer. Usually, these layers are not definitive in extent and they will typically overlap. Here, we briefly describe the layers above the Martian surface; the planet itself can also be split up in a similar fashion but that is not the topic of this thesis. The bulk of the neutral atmosphere is gravitationally bound to the planet and at Mars it extends from the planet surface up to about 400 - 500 km altitude. The atmospheric density profiles of each neutral species follow exponential profiles that depend upon the scale height of each species. Below the homopause, which is located at about 80-130 km at Mars (*Mahaffy et al.*, 2015b), the neutral atmosphere is well mixed: the compositional ratio of each species to every other is constant with altitude. Above the homopause, molecular diffusion dominates over eddy diffusion and atoms and molecules are separated by gravity due to their differing masses.

Solar photons with enough energy are able to photoionize the neutral atmosphere to produce ions and electrons that are free to move around in the atmosphere; these free ions and electrons constitute the ionosphere. The Martian ionosphere extends from  $\sim 100$ -500 km altitude, although it has been observed to be highly variable under certain conditions and the upper range can vary dramatically (e.g. *Lundin et al.* (2004, 2011); *Dubinin et al.* (2012); *Benna et al.* (2015); *Ergun et al.*

(2015a)). These bounds are determined by the rate of ionization (or ionospheric production) and ionospheric recombination, which in turn depend on several factors including the intensity of light as a function of wavelength, the neutral atmospheric and ionospheric densities, and various cross sections and coefficients that are typically species dependent. At Mars, solar Extreme Ultraviolet (EUV) light is the most efficient wavelength range for photoionization of the neutral atmosphere. The peak ionospheric density occurs at about 130 km altitude in the dayside Martian ionosphere (*Gurnett et al.*, 2005; *Němec et al.*, 2011; *Ergun et al.*, 2015a). Because solar EUV light is absorbed as it ionizes the neutral atmosphere, its intensity decreases with decreasing altitude; below the altitude of peak ionization, solar EUV intensity falls off rapidly and the rate of photoionization is small. The highly collisional nature of the atmosphere at such low altitudes below the ionization peak leads to the rapid recombination of charged particles.

The Martian magnetosphere encompasses the planet, neutral atmosphere and ionosphere. Cold, low energy particles are no longer present here, however, high energy particles exist at densities less than  $\sim 10 \text{ cm}^{-3}$ . Ion and electron energies are typically greater than  $\sim 50 \text{ eV}$ , and in many cases can be several KeV or more. Neutral particles found at such high altitudes constitute the Martian corona, as discussed next. To first order, any charged particles found at such high altitudes likely possess high energies and are escaping from the planet. Various plasma boundaries exist (described in detail in Section 2.4); the most well known being the planetary bow shock. This is the shock front at the interaction point between the solar wind and planetary obstacle. The various plasma boundaries facilitate energy transfer from the solar wind down to the ionosphere and neutral atmosphere, and are observed to respond in location and thickness to upstream solar wind conditions.

## 2.2 The neutral atmosphere and corona

The first in-situ measurements of Mars' neutral atmosphere were made by the Viking landers in 1976 (*Nier and McElroy*, 1977). Useful measurements were made between about 100 and 200 km altitude and the Martian neutral atmosphere was found to consist primarily of  $\text{CO}_2$  below 180 km.

$\text{N}_2$  and  $\text{CO}$  were the next most abundant species, at about an order of magnitude less dense than  $\text{CO}_2$ . The primary energy source of the neutral atmosphere is EUV light from the Sun. On the dayside of the planet, the neutral atmosphere is heated due to absorption of EUV light; dissociation and ionization of neutral particles also occurs and these processes depend on various cross sections, energy thresholds and the intensity of the incident EUV light as a function of wavelength (*Schunk and Nagy, 2009*). The EUV range is typically defined as wavelengths spanning 10-120 nm; the photoionization cutoffs for neutral  $\text{CO}$  and  $\text{O}$  are around 93 nm. The photodissociation of neutral molecules becomes important for light at wavelengths in the 120-200 nm range. As the planet (and atmosphere) rotate into darkness, this primary energy source is lost; the atmosphere typically cools, leading to a reduction in atmospheric scale heights and the neutral atmosphere ‘sinks’ in altitude (e.g. *Hantsch and Bauer (1990); Modolo et al. (2005); Bougher et al. (2015a)*). Thus, the dawn, sub solar and dusk neutral density and temperature profiles are different: the dawn neutral atmosphere is cold and low density; the sub solar point is hot with high density, and the dusk neutral atmosphere lies in between these two cases. Typical neutral densities at Mars reach  $10^{11}$ - $10^{12} \text{ cm}^{-3}$  at the lowest altitudes sampled by MAVEN,  $\sim 130$  km, although significant asymmetries likely exist in the neutral atmospheric density between the dawn and dusk terminators (*Andersson et al., 2016a*).

An important region within any atmosphere is the exobase. For any given neutral species this region is defined as the altitude range at which the mean free path becomes equal to the scale height. The exobase is not an exact boundary but rather spans a finite altitude range whose width and altitude depend upon the neutral species under consideration. Generally speaking, the exobase at Mars spans about 180-200 km. Below the exobase the atmosphere is dominated by collisions and the mean free path of any one particle is small. At Mars, photochemistry dominates in this collisional regime and chemical reactions that arise due to collisions between various species (charged and neutral) are prevalent at these low altitudes. Above the exobase, collisions are rare (due to low densities) and plasma processes start to dominate the motion of particles here. Because the peak ionization altitude of the ionosphere lies at around 130 km, a substantial part of the ionosphere lies

below the Martian exobase. The implications of this are discussed later.

Neutral winds exist in the Martian atmosphere and these drive large scale circulation patterns across the planet. These patterns have been modeled using global circulation models (e.g. *Bougher et al. (2015a)*) and are now thought to be measured for the first time by the Neutral Gas and Ion Mass Spectrometer (NGIMS, *Mahaffy et al. (2015b)*) instrument on board MAVEN. At the time of writing, analysis is still ongoing and no publication is yet available for citation.

To first order, the entire neutral atmosphere (bar H) is gravitationally bound to the planet: gravity is able to overcome the usual thermal motions of the neutral atmosphere and prevent it from escaping to space. The escape energy is the energy required by a single atom or molecule for it to overcome the gravitational potential of the planet from its current position and escape to space (technically to an infinite distance from the planet, but space is close enough!). It depends on particle mass and so lighter atoms find it easier to escape from a planet than heavier ones. At Earth, the escape energy of oxygen from the surface of the planet is 10.5 eV, or  $\sim 1.2 \times 10^5$  K. The smaller size and slightly lower mean density of Mars mean that the escape energy of oxygen from the Martian surface is only 2.1 eV, or  $\sim 2.3 \times 10^4$  K. Hence, far less energy is required to achieve the necessary escape velocity at Mars than it is at Earth. Despite this, a significant amount of energy is still required to enable escape even at Mars - the Martian neutral atmosphere is typically cold, around 200-300 K (*McElroy et al., 1977; Fox and Dalgarno, 1979; Mahaffy et al., 2015a*). The highly collisional nature of the neutral atmosphere below the exobase further inhibits loss to space from this region - when an atom or molecule gains a significant amount of energy (be it from the tail end of the thermal distribution or some process that provides energy) this energy is quickly lost through collisions with the neutral atmosphere and the particle thermalizes long before it escapes above the exobase.

The Martian corona can be thought of as an incredibly tenuous extension to the neutral atmosphere. It is comprised mostly of hydrogen and atomic oxygen (e.g. *Chaufray et al. (2007, 2008)*), and extends indefinitely in altitude. It has been detected at distances of 13 Mars radii from the planet by comparison against the interplanetary background. Hydrogen atoms in the hot

tail of the bulk neutral atmosphere below have large enough energy to reach such high altitudes; the dissociative recombination of  $\text{O}_2^+$  ions can provide enough energy for O to reach such high altitudes (e.g. *McElroy (1972)*; *Chaffin et al. (2015)*; *Deighan et al. (2015)*). The bulk of the corona is gravitationally bound to the planet, even at distances of  $\sim 10$  Mars radii. The corona acts as a source of mass loading for the solar wind, which is described in Section 2.4.

### 2.3 The ionosphere

The word plasma describes a gas that has been ionized such that it contains ions and free electrons. The net charge of this gas is zero; in other words, to first order, the number of ions is equal to the number of electrons. Plasma processes can only directly affect charged particles (ions and electrons) and this characteristic is important in relation to atmospheric loss as is discussed in Section 2.5.3.

The majority of the ionosphere is also gravitationally bound to the planet; this arises because the source of the ionosphere is the cold neutral atmosphere. When a neutral atom absorbs a solar EUV photon and an electron is ejected from the atom, the resulting ion possesses about the same energy as the neutral atom did just prior to the process taking place. The conservation of momentum means that the ion will recoil slightly, depending upon the energy and direction at which the liberated electron is ejected. For electrons that are liberated with 25 eV of kinetic energy, the recoiling ion gains about 0.01 eV (or  $\sim 100$  K) of energy. As such, all ions are created at temperatures slightly warmer, but still close to, the cold temperature of the bulk neutral atmosphere. Photoelectrons are created at high energies, typically between 10 and 30 eV, but quickly cool due to collisions with the neutral atmosphere and ionosphere. They feel a much smaller gravitational force due to their low mass and should be able to reach much higher altitudes than the heavier ions. As the electrons separate from the ions, an electric field (known as the ambi-polar electric field) forms which acts to conserve charge neutrality (e.g. *Collinson et al. (2015)*; *Ergun et al. (2016)*). This electric field means that the separation between electrons and ions is actually small, millimeters at most. The ambi-polar electric field accelerates electrons back toward the planet, and

accelerates ions upwards. Whether the energy gained by the accelerated ions is enough to enable them to escape the gravitational potential of the planet depends somewhat on the local conditions at the time of acceleration (*Ergun et al.*, 2016). The initial location of these accelerated ions significantly impacts whether they will ultimately escape from the planet: ions accelerated well below the exobase collide many times with the neutral atmosphere and thermalize long before they move upward through this region. Ions accelerated well above the exobase do not collide frequently and retain most of the energy gained from the ambi-polar electric field and are subsequently more likely to escape. The ambi-polar electric field is a significant source of ion loss at Earth’s polar regions (e.g. *Banks and Holzer (1968)*) and may have been a significant source of ion loss at Mars in the past under different solar conditions (*Ergun et al.*, 2016).

Ionospheric densities at and below the exobase are typically  $\sim 10^3$  to  $10^6$  times lower than the neutral density, meaning that there exists many neutral particles for a single ion and electron. Thus, at low altitudes, the neutral density and resulting collisions dominate the photochemical processes that occur. The ionospheric composition and structure below the exobase is determined by these photochemical reactions. Although many chemical reactions take place in the Martian atmosphere (e.g. Table 2 in *Krasnopolsky (2002)* cites 86 reactions), many of these relate to minor species and do not determine the overall basic structure of the atmosphere. Table 1 in *Andersson et al. (2010)* for example, outlines 19 photochemical reaction rates required to reproduce the typical ionospheric density profiles in the Martian atmosphere. The ionospheric structure above the exobase is strongly determined by plasma processes as collisions are rare here. The ionospheric composition above the exobase depends upon the local atmospheric and plasma conditions. The dominant source of ionospheric plasma can be from the photoionization of neutral particles, plasma that has been transported through the exobase, or plasma that has been transported from some other region of the atmosphere via magnetic flux tubes, for example. Ions and electrons in the ionosphere not only feel the force of gravity but also those from plasma processes. The most common forces associated with plasma processes arise from the interaction of charged particles with magnetic and electric fields: magnetic fields can change the direction of motion of a charged particle, whilst electric

fields can accelerate or decelerate charged particles, providing or sapping energy from them. These magnetic and electric forces are highly variable in space and time and thus the upper ionosphere does not typically follow an exponential profile but rather depends on the local plasma processes acting in the ionosphere at any one given time. Physical processes that provide energy to solely charged particles can be very efficient at energizing them. Assuming energy is spread equally to all charged particles, there are far fewer charged particles than neutrals, meaning that each charged particle can receive a significant amount of energy. When energizing processes provide energy to the neutral particle populations, there are so many neutral particles that any one individual neutral particle typically receives a negligible amount of energy.

The theoretical ionospheric density profile known as the Chapman profile (e.g. *Schunk and Nagy* (2009)) predicts the dayside electron density profile with respect to altitude. The derivation of this profile assumes a horizontally stratified atmosphere where photochemical collisions, photoionization, and gravity, are the only processes acting. Observations of the Martian dayside ionosphere fit this theoretical profile well below altitudes of  $\sim 180$  km, but above this, the profile does not describe the ionospheric density profile well due to the action of plasma processes here (*Gurnett et al.*, 2005; *Morgan et al.*, 2008; *Ergun et al.*, 2015a). The action of these plasma processes tends to provide ions and electrons with energy; subsequently, significant numbers of ions and electrons can be found well above the exobase, contrary to the theoretical Chapman predictions and despite the fact that the neutral atmospheric density falls off rapidly at these altitudes.

EUV light (10-120 nm) is the primary ionization source of the dayside ionosphere. The ionization efficiency depends on many factors such as neutral species density, EUV intensity (as a function of wavelength) and various ionization cross sections (*Schunk and Nagy*, 2009). EUV light is absorbed by the neutral atmosphere as a function of altitude, meaning that at the very lowest altitudes (typically below  $\sim 90$ -100 km at Mars), little to no EUV light is present here and subsequently photoionization is all but absent at these low altitudes. The peak in Martian electron and ion density varies with solar zenith angle: typically the peak is lowest in altitude for the lowest SZA (i.e. at the subsolar point of the planet). The dayside subsolar peak has been observed to lie

at around 125-130 km altitude based on a Chapman fit to in-situ electron density profiles, by, for example, *Gurnett et al. (2005)*; *Němec et al. (2011)*; *Ergun et al. (2015a)*; *Benna et al. (2015)*).

The first in-situ measurements of the Martian ionosphere were made by the Viking landers between altitudes of about 100 and 300 km (*Hanson et al., 1977*). The landers observed  $O_2^+$  to be the dominant ion species throughout this altitude range, particularly below 200-250 km. At the upper range of their measurements (250-300 km),  $O^+$  approached the  $O_2^+$  density. Subsequent instruments to observe the Martian ionosphere in-situ include the Analyzer of Space Plasmas and Energetic Atoms instrument (ASPERA-3) onboard the Mars EXpress spacecraft (MEX) (*Lundin et al., 2004*), the Neutral Gas and Ion Mass Spectrometer (NGIMS, Appendix A) instrument on board MAVEN, and the SupraThermal and Thermal Ion Composition instrument (STATIC, Appendix A), also onboard MAVEN. Inspection of ionospheric density profiles from, for example, *Benna et al. (2015)*, shows that  $O^+$  does indeed become the dominant ion species above about 300 km altitude at the dayside subsolar point. Comprehensive reviews of the dayside Martian ionosphere can be found in, for example, *Nagy et al. (2004)*; *Witasse et al. (2008a)*; *Withers (2009)*.

The nightside Martian ionosphere by contrast is less well understood. Without EUV light driving photoionization, the ionosphere recombines resulting in nightside ionospheric densities several orders of magnitude smaller than those observed on the dayside of Mars. Electrons that precipitate into the ionosphere are thought to be a dominant source of the Martian nightside ionosphere via electron impact ionization and can lead to localized regions of enhanced, ‘patchy’, ionospheric density (*Zhang et al., 1990*; *Haider et al., 1992*; *Fox, 1993a*; *Lillis et al., 2009*; *Němec et al., 2010*; *Lillis et al., 2011*). Plasma transport across the terminators can also be important for sustaining the ionosphere at solar zenith angles less than  $115^\circ$  (e.g. *Withers et al. (2012)*). The sporadic nature of nightside ionization makes the nightside ionosphere highly variable in both absolute density and composition. Remote sensing of the nightside ionosphere by various Mars missions has revealed highly variable density profiles (e.g. *Fjeldbo et al. (1970)*; *Kliore et al. (1970)*; *Savich and Samovol (1976)*; *Lindal et al. (1979)*; *Němec et al. (2010)*) and to our knowledge there has not yet been published a ‘typical nightside ionospheric composition profile’, due to the large

variabilities observed. *Fowler et al. (2015)* (this thesis) presented the first in-situ statistical density and temperature profiles of the nightside ionosphere, as observed by the MAVEN spacecraft, and showed that a nightside ionization source is required to reproduce the observed density profiles. Precipitating electrons were confirmed to be a viable ionization source, as has been postulated by previous authors.

The lack of a strong dipole magnetic field at Mars, coupled with the presence of localized crustal magnetic fields, adds an interesting complication when dealing with charged particle motion in the Martian ionosphere. These localized crustal magnetic fields are strong enough to significantly alter the motion of charged particles and they can return charged particles back to the lower atmosphere, greatly reducing their chance of escape (e.g. *Brain et al. (2007)*; *Nilsson et al. (2011)*). These anomalies have also been observed to ‘puff out’ the Martian ionosphere - the additional magnetic pressure, and charged particle motion along the magnetic field, results in greater ionospheric densities at a given altitude compared to regions where no magnetic anomaly is present (e.g. *Dubinin et al. (2012)*).

## 2.4 Martian Plasma Boundaries

The lack of a dipole magnetic field at current day Mars results in a different solar wind - planet interaction from that of magnetized bodies such as the Earth. With no large scale magnetic field to hold off the solar wind, the atmosphere and corona are subject to direct influence from the impinging solar wind. Ionization of the Martian neutral corona produces charged particles that are to first order stationary with respect to the impinging solar wind. The motion of these newly born charged particles (known as pickup ions) is governed by the solar wind magnetic field and they are swept along with it. When this happens, the conservation of momentum means that the solar wind velocity drops slightly; this process is known as mass loading. The density of charged particles that can be picked up by the solar wind like this increases as the solar wind approaches the planet. The lack of any obvious, large scale dipole magnetic field at Mars means that the solar wind interacts directly with the Martian atmosphere. Currents driven within the Martian atmosphere prevent

the solar wind magnetic field from penetrating deeper, and solar wind magnetic field drapes upon the topside of the Martian atmosphere, producing a stagnation point in the solar wind flow. The planetary bow shock forms upstream of the stagnation region, so that the solar wind flow is directed around the planetary obstacle. This type of planet - solar wind interaction produces what is known as an induced magnetosphere; the various plasma boundaries are located much closer to the planet due to the lack of a global dipole magnetic field (e.g. *Bertucci et al.* (2011)). The Martian bow shock is usually located at a planetocentric distance of  $\sim 1.6$  Martian radii (*Slavin et al.*, 1991; *Vignes et al.*, 2000); the terrestrial Bow Shock is typically located at around  $\sim 14.6$  Earth radii (e.g. *Fairfield* (1971)), for example.

The plasma boundaries that exist in planetary magnetospheres (induced or otherwise) mark dramatic changes in various plasma parameters and typically identify regions where different physical processes become dominant. The bow shock marks the location where the solar wind first encounters the planetary obstacle. The solar wind flow is supersonic upstream of the bow shock, and subsonic downstream of it. Typically, some fraction of incident solar wind charged particles are reflected upstream at the shock; they gyrate about the immediate upstream magnetic field, gaining energy from the solar wind motional electric field,  $E_{\text{sw}}^{\vec{}} = -V_{\text{sw}}^{\vec{}} \times B_{\text{sw}}^{\vec{}}$ , where  $V_{\text{sw}}^{\vec{}}$  is the solar wind velocity vector and  $B_{\text{sw}}^{\vec{}}$  is the solar wind magnetic field vector. This gain in energy is typically enough such that the particles can penetrate the shock potential when re-encountering it as a result of their gyro motion. These particles are subsequently convected downstream. Ion and electron thermalization occurs immediately downstream of the bow shock, in a region known as the magnetosheath, or sheath. This thermalization occurs so that the shock jump conditions are satisfied; these conditions are known as the Rankine-Hugoniot conditions and represent the conservation of energy and momentum across the shock interface (e.g. *Schunk and Nagy* (2009)). More detailed information on shock structure and the physical processes present can also be found in, for example, *Bale et al.* (2005) and *Burgess et al.* (2005a). The location of the Martian bow shock is observed to respond to upstream solar wind conditions (*Brain et al.*, 2005; *Edberg et al.*, 2009a,b; *Halekas et al.*, 2016); electric and magnetic field wave power also responds to upstream

solar wind conditions, highlighting changes in physical processes acting at the shock (*Fowler et al.* (2016), this thesis).

The magnetic pileup boundary (MPB) is a boundary specific to unmagnetized bodies subject to the solar wind; the Martian MPB is similar to MPBs detected at, for example, comets Halley and Grigg-Skjellerup (*Reme et al.*, 1993; *Mazelle et al.*, 1995; *Vignes et al.*, 2000). The MPB is typically a thin boundary denoted by a sharp increase in magnetic field strength, marking the location at which solar wind magnetic field lines drape upon the planetary obstacle (e.g. *Bertucci et al.* (2003)). The MPB can be identified at Mars using several methods and the identification of various quantities. The Induced Magnetosphere Boundary (IMB), for example, is identified by the transition from solar wind to planetary dominated plasma (*Nagy et al.*, 2004). It has not yet been proven that the various boundaries reported in the literature are always the same phenomenon. The MPB stand off distance is typically  $\sim 1.3$  Martian radii (*Vignes et al.*, 2000).

The transition from the near Mars space environment into the ionosphere is most commonly known as the ionopause, although the existence of such a persistent, definitive boundary is yet to be confirmed. The two most familiar methods of identifying the ionopause involve the analysis of electron density profiles: *Mitchell et al.* (2001) identify the ionopause as the point at which shocked, high energy solar wind electrons transition to colder planetary photoelectrons. Shocked solar wind electrons have typical energies of a hundred eV; planetary photoelectrons are produced by the photoionization of the planetary neutral atmosphere and have typical energies of 10-30 eV. The photoionization of CO<sub>2</sub>, for example, produces photoelectrons at energies of about 23 eV and 27 eV (*Frahm et al.*, 2006). The second method marks the ionopause as the point at which the high energy electron density, energies greater than a few hundred eV, substantially decreases (*Duru et al.*, 2009; *Vogt et al.*, 2015). It has yet to be proven that these two methods identify the same boundary.

Because the neutral atmosphere is the source of the ionosphere, these two regions overlap in physical space by a considerable amount. The altitude of transition from ionosphere to purely neutral atmosphere thus varies, depending upon the local neutral atmospheric conditions and the

intensity of EUV light reaching the local atmosphere. Meteoric layers (that consist of ionized metallic ions) have been observed at around 90 km altitude at Mars, with densities of  $\sim 10^3 \text{ cm}^{-3}$  (e.g. *Withers et al.* (2008); *Schneider et al.* (2015)). The permanent existence of such layers has yet to be confirmed at Mars, but significant densities (at least a few  $\text{cm}^{-3}$ ) of charged particles do not exist below these altitudes.

## 2.5 Loss processes in the Martian atmosphere and ionosphere

Atmospheric gases can be removed from an atmosphere through loss to the surface of a planet or escape to space. The formation of carbonate minerals removes atmospheric gas to the planet surface; in particular,  $\text{CO}_2$  can dissolve in large bodies of water (for example, at Earth, in the oceans) and carbonates have been found in Martian meteorites suggesting this process was (and most likely still is) active at Mars (*Jakosky and Phillips*, 2001). The amount of Martian atmosphere removed through this process is currently unknown but the small army of surface probes and rovers that have landed on the planet surface over the past decade or so are tasked in part with constraining this value. Atmospheric loss to space on the other hand requires orbiting satellites to be measured and constrained. The Sun is ultimately the main driver of atmospheric loss to space from all planetary bodies (and non planetary, such as comets) and in the simplest case, sunlight is absorbed by the neutral atmosphere, providing energy and increasing the atmospheric temperature. At Mars, the bulk of the neutral atmosphere is however still far too cold to escape the gravitational potential of the planet. A small fraction of the neutral population in the hot tail of the population will possess temperatures that are hot enough to escape the planet. This example is known as Jeans escape and further information on this process, and others, is given below.

Measurements of various isotopes in the Martian atmosphere show that loss to space has been significant; lighter isotopes from a particular atomic species are preferentially lost to space (due to their lower mass) and so the atmosphere becomes enriched with the heavier isotope (*McElroy and Yung*, 1976). Analysis of  $^{38}\text{Ar}/^{36}\text{Ar}$  at Mars, for example, shows that this ratio is about 30% greater than the terrestrial value, suggesting that between 50% and 90% of Ar has been lost to

space at Mars (*Jakosky et al.*, 1994; *Hutchins and Jakosky*, 1996). Table 1 in *Jakosky and Phillips* (2001) shows enrichment values for D/H, Ar, C, N and O. It should be noted that removal of atmosphere via impacts does not change these isotopic ratios - impacts remove gas from an entire column of atmosphere and all isotopes are removed equally. Impact removal most likely dominated during the early to mid Noachian period during the heavy bombardment phase of the solar system. The solar wind can also remove atmosphere from a planet and Mars is particularly susceptible to this loss due to its lack of a significant (if any) protective dipole magnetic field (*Acuna et al.*, 1998). Several escape processes exist that are at least in part driven by the solar wind and these are described below. Atmospheric loss from Mars via the solar wind has been most important from the late Noachian onwards, once Mars lost its dipole magnetic field.

Neutral and charged particles are able to gain energy after their creation, meaning that even if they are cold when created, they may still escape at a later time when subject to one or more of the escape processes described below. The highly collisional nature of the atmosphere below the exobase makes it very difficult to lose particles to space from this region; particles that gain greater than escape energy at such low altitudes collide many times with the neutral atmosphere and thermalize long before they escape. Within about 100 km above the exobase, collisions are rare, but the atmospheric density is small such that the number of atoms and ions that can be removed from the Martian atmosphere at these higher altitudes is small. Hence, the altitude region spanning the exobase is the most important for determining the rate of atmospheric loss to space as a whole. Particles who gain significant energy at the exobase stand a chance of passing through this region and retaining enough energy to still escape the gravitational potential of the planet once at higher altitudes. Several processes contribute to atmospheric escape; substantial reviews can be found in, for example, *Chassefière and Leblanc* (2004) and *Jakosky et al.* (2015a), and these processes are summarized next.

### 2.5.1 Jeans escape

Jeans escape is a thermal loss mechanism whereby a fraction of atoms in the energetic wing of the Maxwellian distribution have enough energy to escape the gravitational potential of the planet and can be lost to space. This process is most efficient for lighter atoms and subsequently affects H the most. Deuterium (D) and He are also lost via Jeans escape from the atmosphere but at much lower rates than H; heavier atoms, such as C, N and O, do not significantly escape via this process (*Chassefière and Leblanc, 2004; Jakosky et al., 2015a*).

### 2.5.2 Photochemical escape

Photochemical escape is a process through which neutral atoms can be lost to space as a result of exothermic chemical reactions. Typically, photoionized molecules recombine with electrons and excess energy is acquired by the resultant neutral atoms in the form of kinetic energy. This is known as dissociative recombination, and depending on the exact atomic states taking part in the reaction, this kinetic energy can be greater than the escape energy for that particular atomic species. Equations 2.1 to 2.3, taken from *Chassefière and Leblanc (2004)*, show three examples of dissociative recombination reactions that exist at Mars.



$$(\Delta E = 0.84 - 6.99eV)$$



$$(\Delta E = 1.06 - 3.44eV)$$



$$(\Delta E = -0.33 - 2.9eV)$$

The  $\Delta E$  value accompanying each equation shows the range of excess energy available (to be shared) between the resultant neutral atoms. For comparison, the escape energies of O, N and C at

the Martian exobase are approximately 1.9, 1.72 and 1.48 eV respectively: for all three cases above, the upper limit of  $\Delta E$  is close to or greater than the escape energy for each respective species. At Mars, the dissociative recombination of  $\text{O}_2^+$  is the current dominant loss mechanism for hot O (*McElroy and Donahue, 1972; Nagy et al., 1990; Lammer and Bauer, 1991; Luhmann et al., 1992; Zhang et al., 1993a,b; Lammer et al., 1996; Luhmann, 1997; Kim et al., 1998; Hodges, 2000; Fox, 1993b; Fox and Hać, 1999; Fox and Bakalian, 2001; Nagy et al., 2001*). The total loss rate of hot neutral atoms that are produced from dissociative recombination is ultimately limited by the rate at which charged molecules can be supplied to the exobase region (*Fox, 1997*). Photochemical escape can be a far less efficient loss mechanism at more massive planets. The escape energy of O at Earth, for example, is about 10 eV, and thus the dissociative recombination of  $\text{O}_2^+$  in the terrestrial ionosphere can only provide about  $\frac{1}{3}$  of the required escape energy. The lower gravitational potential of Mars is thus a significant factor influencing atmospheric escape there.

### 2.5.3 Ion loss

Jeans and photochemical escape typically influence neutral escape the most. There are several processes that influence charged particles only via the interaction of ions with magnetic and electric fields and these processes can result in ion loss from the planet. As discussed earlier, the energization of charged particles can be much more efficient than the energization of neutral particles.

#### 2.5.3.1 Pickup ions

Neutral atoms in the Martian corona can be photoionized by solar EUV light; the motion of these newly born ions is dominated by the solar wind magnetic field and they are swept along with it. These pickup ions are accelerated by the solar wind motional electric field, again defined as  $\vec{E}_{\text{sw}} = -\vec{V}_{\text{sw}} \times \vec{B}_{\text{sw}}$ . Pickup ions typically consist of  $\text{O}^+$ ,  $\text{H}^+$  and  $\text{C}^+$  due to the photoionization of the Martian corona.  $\text{O}_2^+$  from the upper ionosphere can also contribute to the pickup ion population (*Lundin et al., 1989; Leblanc and Johnson, 2001; Chassefière and Leblanc, 2004; Jakosky et al., 2015a*). 3D MHD and hybrid models have shown that  $\text{O}_2^+$  comprises the majority of total pickup

ion escape and that  $O^+$  from the corona constitutes about 10 - 25% of this total loss (*Liu et al.*, 2001; *Ma et al.*, 2002; *Kallio and Janhunen*, 2002; *Brecht et al.*, 2003). At high altitudes (greater than  $\sim 500$ -1000 km), these pickup ions tend to have large helical trajectories due to their motion about the solar wind magnetic field. Gyro radii up to  $\sim 30,000$  km are common and pickup ion energies can be greater than 10 keV. The orientation of the solar wind motional electric field (MSE) is controlled by the clock angle of the solar wind magnetic field, also known as the interplanetary magnetic field (IMF). The direction of positive electric field for typical solar wind IMF conditions is towards the Martian north pole and so pickup ions are usually accelerated over this pole; this phenomena is subsequently known as the polar plume. Mars orbiters prior to MAVEN did not possess both an ion instrument and magnetometer, and so the polar plume has only recently been confirmed by observations made by MAVEN (*Curry et al.*, 2015; *Dong et al.*, 2015). Prior missions observed what were thought to be pickup ions but the lack of magnetic field measurements prevented conclusive verification of this, for example *Lundin et al.* (2006a,b).

### 2.5.3.2 Sputtering loss

Although sputtering loss tends to involve the loss of neutral atmosphere, it is driven by ions. To keep in line with previous reviews of loss processes at Mars, I include sputtering loss under ion loss, despite this. Lower energy pickup ions have gyro radii less than the radius of Mars and so their gyro motion about the solar wind magnetic field can lead them to reimpact the Martian atmosphere. Collisions with the neutral and charged atmosphere can impart substantial energy to these particles that may result in loss to space, and usually heating of the neutral atmosphere. This process is known as sputtering (*Luhmann et al.*, 1992; *Johnson*, 1994; *Leblanc and Johnson*, 2001). Although not thought to be a major contributor to atmospheric loss at present day Mars, modeling has shown that it may have been significant in the past (*Luhmann et al.*, 1992; *Kass and Yung*, 1995; *Kass et al.*, 1996; *Luhmann*, 1997; *Johnson et al.*, 2000; *Leblanc and Johnson*, 2001, 2002). The lack of a global magnetic field at Mars allows this process to happen there; at Earth, for example, the global dipole field prevents pickup ions from reimpacting the atmosphere.

Solar energetic particles (SEPs) are also a source of atmospheric sputtering at Mars. SEPs are accelerated from the Sun during solar flares and coronal mass ejections (CMEs) and can possess energies up to 100s of MeV. They can produce similar effects to pickup ion sputtering, but at much lower altitudes in the atmosphere due to their significantly greater energies (*Leblanc et al.*, 2002). These somewhat impulsive events are thought to enhance atmospheric loss at Mars but a lack of critical measurements in the past, such as magnetic field, has prevented a complete understanding of the influences of these SEP events on escape to space (*Crider et al.*, 2005; *Espley et al.*, 2005; *Fu-taana et al.*, 2008; *Edberg et al.*, 2010). MAVEN observations will enable a complete understanding of how these SEP events influence atmospheric escape; indeed, changes in the Martian bow shock and magnetosheath, formation of wide spread diffuse aurora and an enhancement of pickup ions were observed during a CME passage in March 2015 (*Jakosky et al.*, 2015b). Although SEP events occur somewhat infrequently at present day Mars, the early Sun is thought to have been much more active, possessing a radiation environment several hundred times stronger than at present. The cumulative effects of such an intense bombardment on the Martian system may have been significant for atmospheric loss (*Lammer et al.*, 2003).

### 2.5.3.3 Bulk ion escape

Bulk ion escape is a sporadic process in which large ‘clouds’ of ionospheric plasma intermittently become detached from the Martian ionosphere and are swept downstream by the solar wind. The process is analogous to the detaching tail of a comet; magnetic reconnection and plasmoid type structures are possible at Mars due to the presence of the localized crustal magnetic fields that can produce these phenomena (*Eastwood et al.*, 2008; *Brain et al.*, 2010). Sporadic ion energization events, such as that described in Section 7 of this thesis, can also be categorized as bulk ion escape. The mechanism for bulk ion escape depends upon the situation under scrutiny; the escape of magnetic structures containing ionospheric plasma analyzed by *Brain et al.* (2010) is thought to be driven by magnetic reconnection at the top of crustal magnetic field loops. The energization processes discussed in Section 7 in this thesis, on the other hand, require the acceleration of ions

parallel to the magnetic field and an ion heating process that acts perpendicular to the magnetic field.

#### 2.5.3.4 Ion outflow

Ion outflow is a more continuous process whereby ions and electrons from the Martian ionosphere can flow along magnetic field lines into the solar wind. This continuous outflow is a result of the electron pressure gradient within the ionosphere: the subsequent formation of ambi-polar electric fields along open magnetic field lines (magnetic field lines where one end is attached to the ionosphere, and the other in the solar wind) allow ions to be accelerated upward, increasing their chances of escape (e.g. *André and Yau (1997); Ganguli (1996)*). The total number of charged particles lost to space can be influenced by additional factors. The relatively weak magnetic fields present at Mars, for example, are typically tens of nT in magnitude within the ionosphere, resulting in large ion gyro radii (several 10s of km or greater). If the gyration of ions is such that they gyrate back through the exobase, it is likely that these ions will in fact not escape the planet. Such considerations must be taken into account when attempting to identify ion outflows. The dipole nature of Earth's magnetic field means that intense ion outflows are driven in the terrestrial auroral regions, and this process is subsequently known as the polar wind. In contrast, the Martian crustal magnetic fields provide similar cusp like topologies over large areas of the surface, and not just at the polar regions. Polar wind like outflow in such crustal regions may be active at Mars (*Collinson et al., 2015*).

## 2.6 Estimates of current day escape rates at Mars

A review of estimated current day ion escape rates at Mars are given in Figure 32 of *Dubinin et al. (2011)*. Six estimates are presented and they span from  $\sim 5 \times 10^{22} \text{ s}^{-1}$  to about  $2 \times 10^{25} \text{ s}^{-1}$ . The large variation in estimated ion escape rates at Mars arises from the range of assumptions required by each study, some of which were lacking crucial measurements that thus required assumed values. The most recent ion instrument flown to Mars prior to those carried by MAVEN was the ASPERA-

3 Ion Mass Analyzer (IMA, *Barabash et al. (2004)*) on board MEX. This instrument was adept at measuring high energy ions but could not measure ions below 10 eV in energy. Given the relatively low velocities required by Martian ionospheric ions to escape the planet ( $\sim 2$  eV), cold ion outflow may contribute significantly to ion loss at Mars and subsequently escape rates derived using the ASPERA-3 dataset most likely represent lower limits. Spacecraft measurements provide single point measurements in space and time and so statistical averages (in both space and time) must be used to obtain global escape rates. Escape rates at Mars are known to vary with both of these; the polar plume for example produces strong ion escape over a certain spatial region, whereas large CMEs are thought to enhance escape over the bulk of the planet for a short period of time. The averaging of these effects causes uncertainties in global escape rates.

An initial lower bound estimate for the ion escape rate derived from MAVEN data has been calculated at  $\sim 3 \times 10^{24} \text{ s}^{-1}$  by *Brain et al. (2015)*. This was based on four months of data only and subsequently spatial coverage throughout the Martian magnetosphere was somewhat limited; instrument calibration was also not yet available for low energy ions. Improved spatial coverage and instrument calibration will lead to further refinement of this estimated global ion escape rate at current day Mars.

Estimates of neutral escape rates are much harder to calculate as escaping neutrals cannot be directly measured, typically because the densities of such escaping neutrals are far below those measurable by space borne instrumentation. As such, neutral escape must be inferred using a combination of other measurable parameters and numerical modeling. *Lillis et al. (2015)* describe the data, models and various influences that must be understood in preparation for undertaking this challenge with MAVEN data.

Although there is an ever increasing wealth of observational data of atmospheric loss to space at Mars, modeling efforts are still required to fill in the missing gaps, particularly when dealing with atmospheric loss in the past. The synthesis of current day measurements with knowledge of the many physical processes that affect escape, and the influence of temporal variability on these, will allow estimates of the total amount of atmosphere (and subsequently water) lost to space

throughout Mars' history to be made.

## 2.7 Summary

The Martian atmosphere and near space environment can be broken down into several regions defined by the physical processes that dominate within each. The low altitude atmosphere is a highly collisional environment; particles collide often and photochemistry determines the composition of the atmosphere here. Solar photons ionize neutral atoms to produce ions and free electrons - the ionosphere. This region overlaps widely with the neutral atmosphere but is generally located at higher altitudes where collisions start to become rare; magnetic and electric forces influence the motion of charged particles in the ionosphere and can be very efficient at energizing them, particularly at and just above the exobase. Plasma boundaries at higher altitudes define the Martian magnetosphere; some of those present, such as the MPB, are specific to non magnetized bodies, whilst others are typical of those found at all solar system bodies subject to the solar wind, such as the bow shock. Understanding the interactions between these various boundaries and how energy is transferred between them is crucial to determining atmospheric escape rates from the planet, and how these have been driven by solar conditions throughout Mars' history.

## Chapter 3

### Density and temperature measurements of planetary ionospheres

Planetary atmospheres can be observed using a variety of methods and instrumentation, each with their own strengths and weaknesses. Important characteristics of planetary atmospheres include the electron temperature and density. These parameters determine the rates of many chemical reactions present within planetary atmospheres, which in turn determine the overall structure and composition of the atmosphere. Further, assuming charge quasi-neutrality, the electron density can be used to aid in calibration of additional plasma measurements made by other instruments. As I am a member of the Langmuir probe and waves (LPW) instrument (an instrument that measures electron density and temperature) team, I briefly summarize several methods made by orbiting spacecraft that can be used to obtain the electron density and temperature. I then focus on Langmuir probes, the instrument with which I have been heavily involved with in developing and deriving science quality measurements for.

Remote observations made by orbiting spacecraft typically derive electron density by observing electromagnetic radiation that has passed through, been emitted, or reflected by, the ionosphere. Such techniques include radio sounders and radio occultation measurements. Radio sounders typically broadcast an electromagnetic pulse at frequency  $f$  vertically downward toward the planet surface. Electromagnetic radiation cannot propagate through the ionosphere at frequencies below the local plasma frequency, and assuming a horizontally stratified ionosphere, this results in an almost perfect reflection of the radio pulse at the point where the emitted frequency  $f$  is equal to the local plasma frequency. Analysis of the time it takes to observe the reflected echo provides the

height at the point of reflection; as the local plasma frequency is proportional to the local electron density, analysis of the reflected frequencies allows a derivation of the local electron density to be made at the reflection height. By stepping the emitted radio pulses through a range of frequencies, an electron density profile of the ionosphere can be constructed (e.g. *Gurnett et al. (2005)*, and references therein). Due to the measurement technique, radio sounders are unable to measure density depletions within ionospheres.

Radio occultation methods measure electron density via the analysis of radio signals transmitted through a planetary ionosphere by the spacecraft that are most commonly received at Earth. Occultations are able to measure depletions and enhancements in electron density, including measurements below the ionospheric density peak, but have two major limitations: the first is the required line of sight geometry between spacecraft and receiver means that, at some bodies, certain regions of the planetary environment cannot be measured. At Mars, for example, occultation methods cannot sample the nightside and subsolar ionosphere because of the geometrical constraints resulting from the orbits of Earth and Mars about the Sun. The second limitation is that a model atmosphere is required to extract the electron density profiles; the accuracy of this model thus determines the accuracy of the extracted density profiles. Many radio occultation measurements exist of Mars' ionosphere, for example *Fjeldbo et al. (1970)*, *Savich and Samovol (1976a)*, *Lindal et al. (1979)*, *Zhang et al. (1990)*.

In-situ measurements can also be used to determine the local electron density. The large range of electron energies present within a planetary environment leads to several in-situ measurement techniques. The cold, bulk electron population of a planetary atmosphere consists of electrons at energies below 1 eV. At such low energies, measurement of individual electrons is difficult and so bulk properties are typically measured that allow a derivation of the electron density and temperature to be made. A Langmuir probe performs such observations: the measured current-voltage (I-V) curve (this measurement technique is discussed in detail in Section 3.1) is representative of the bulk cold electron population and not individual cold electrons. The electron density and temperature can be derived from analysis of such I-V curves, as described in Section 3.3. At higher

electron energies, between a few eV and a few KeV, individual electrons can be counted as a function of energy by electrostatic analyzers (ESAs). The detectors in such instruments are typically micro channel plates (MCPs) that amplify the signal from a single electron, producing a current spike large enough to be measured by electronics. ESAs contain electro-magnetic optics that are placed at the instrument aperture so that only electrons within a certain energy range can reach the detectors. Additional optics can be employed to enhance the field of view (FOV) of ESAs. Electric fields are applied at the instrument aperture such that electrons whose trajectory would not have taken them into the aperture are now deflected into it. Once deflected into the instrument aperture, electrons are filtered by the ESA based on energy. Finally, high energy electrons, at energies greater than  $\sim 100$  keV, must be measured using solid state detectors. At such high energies, these electrons cannot be measured by MCPs. Solid state instruments typically consist of a baffle system, or heavily shielded telescope, mounted in front of the detectors. The baffle system defines the instrument field of view - the walls are designed to absorb electrons that pass through it, meaning that only electrons that travel down the telescope can reach the detectors at the end. Under typical atmospheric conditions, such high energy electrons do not exist in large quantities within the Martian atmosphere; they are deposited there by cosmic rays and solar events such as solar flares and coronal mass ejections.

One of the difficulties with measuring charged particles using spacecraft mounted instrumentation, is the effect of spacecraft potential (which is discussed in Section 3.4.3.1), which acts to accelerate or decelerate charged particles close to the spacecraft. On the MAVEN spacecraft, it can range from a few eV in magnitude up to 20 or 30 eV, depending upon the local plasma environment, spacecraft design, and spacecraft orientation. It can thus heavily influence the apparent energies of low energy electrons. ESA data can be corrected post measurement for spacecraft potential effects, assuming that the value of the spacecraft potential is known at the time of measurement, and that the energy resolution of the ESA is adequate. High energy particles (many keV) have large enough energies that they are not significantly affected by spacecraft potentials.

### 3.1 How does a Langmuir probe work?

A Langmuir probe is an instrument that measures electrical current. In its simplest form, a Langmuir probe is a wire placed in an ambient plasma that measures the net electrical current to it. In an ideal case (such as in the lab), the plasma consists of a single electron and single ion species and the net current collected depends on the respective densities and temperatures of these two charge populations. In more realistic cases, such as measurements within planetary ionospheres, there are additional electron populations and ion species that lead to additional sources of current; these are discussed in Section 3.4.1. When a potential is applied to the surface of the probe, the net current collected by the probe also changes, again depending on the density and temperature of the electron and ion populations present and the resulting net flow of positive and negative charges. A current-voltage (I-V) curve is thus generated by applying a series of potentials to the surface of a Langmuir probe, and recording the current collected at each potential. Example theoretical I-V curves are shown in Figure 3.2 for cylindrical and spherical probes; this figure is discussed in detail in Section 3.2.

The ambient plasma environment, probe sheath size, and shape, also affect the current collected by a Langmuir probe. The probe sheath is equivalent to the Debye surface of the probe - it is an imaginary boundary placed around the probe outside of which the ambient plasma is unaffected by potentials applied to the probe surface. Inside of the sheath, charged particles are influenced by these potentials and are attracted to, or deflected from, the probe, depending on the particle charge and the applied probe potential. There are two theoretical limits of probe sheath size; that where the sheath radius (or Debye length) is much smaller than the physical probe radius (known as the sheath limited case), and that where the sheath radius (or Debye length) is much greater than the physical probe radius (known as the orbit motion limited, or OML, case). The sheath limited case is typically the simplest case to deal with; under such conditions, the sheath surface can be approximated to simply be the effective surface area of the probe itself: any charged particles that enter the sheath are assumed to be collected by the probe. Conversely, for the OML case, the

orbits of individual charged particles within the sheath must now be considered. Knowledge of the sheath size is important to determine under which regime the probe is in. The sheath size must be known to high accuracy in particular for the sheath limited regime, because it is assumed that all charged particles entering the sheath under such conditions are collected by the probe.

The Debye length,  $\lambda_D$ , of a plasma that consists of electrons at density  $N_e$  and temperature  $T_e$  is defined later in this chapter by Equation 3.7. Most importantly,  $\lambda_D$  is proportional to  $\sqrt{\frac{T_e}{N_e}}$ . Thus, sheath limited cases occur under high density, low temperature conditions that are typically found at low altitudes in planetary atmospheres, where  $\lambda_D$  is comparable to the probe radius,  $\sim 0.3$  mm in the case of LPW. OML conditions typically occur at high altitudes in planetary atmospheres, where the electron density is low and temperatures are high; the resulting Debye length is large compared to the probe radius under such conditions.

### 3.2 Cylindrical vs Spherical Langmuir probes

The shape of a Langmuir probe influences the shape of the sheath and thus the analytical equations describing the current collected. The most common Langmuir probe shapes are cylinders and spheres, although planar probes are also used. Cartoon representations of spherical, cylindrical and planar Langmuir probes are shown in Figure 3.1. Cylindrical Langmuir probes tend to be easier to build than spherical probes. Densities derived from planar probes are typically subject to larger uncertainties due to the mounting geometry, which severely reduces the instrument field of view and current collection area.

Theoretical I-V curves for cylindrical (black) and spherical (blue) Langmuir probes, in identical plasma conditions, are shown in Figure 3.2. Panel A shows the theoretical I-V curve; panel B shows the corresponding derivative,  $\frac{\partial I}{\partial V}$ . The major difference between the two probe shapes is the behavior at large positive potentials: for cylindrical probes  $I \propto V^{\frac{1}{2}}$  and for spherical probes  $I \propto V^1$ . Langmuir probes flown on spacecraft can be used to determine an important parameter known as the spacecraft potential,  $V_{scp}$ . Spacecraft potential is discussed in Section 3.4, but I note here that it is often determined from the derivative curves shown in Figure 3.2. The clear peak in the black

derivative at 0 V marks the spacecraft potential for cylindrical probes, which corresponds to the start of the plateau for spherical probes. Typically, it is easier to identify the peak for cylindrical probes and this is one of the reasons cylindrical probes were flown for the LPW instrument.

A further advantage of cylindrical probes over their spherical counterparts is that the analytical equations for cylindrical Langmuir probes do not require knowledge of electron temperature when deriving electron density. This means that a full I-V sweep is not required to derive electron density; if the electron temperature and spacecraft potential are assumed constant then high cadence electron density measurements can be made by repeatedly measuring the current collected by the probe at a single voltage, as apposed to sweeping through the full range of voltages. A full I-V sweep is still required to determine electron temperature and spacecraft potential and so if two Langmuir probes are flown on the same spacecraft, one can operate in full I-V sweep mode to obtain measurements of electron temperature and spacecraft potential, whilst the second probe operates at a single potential, obtaining high cadence electron density measurements.

Langmuir probes can obtain accurate relative density measurements, but their absolute derived values tend to be less accurate. Absolute calibration of cylindrical Langmuir probe density measurements can be achieved if two or more probes are carried by the same spacecraft and wave sounding is undertaken. This method is described in Section 3.6 and is implemented by the LPW instrument.

### 3.3 Cylindrical Langmuir probe theory

The LPW instrument is a cylindrical Langmuir probe and I therefore present theoretical expressions derived and presented by previous authors in the analysis of cylindrical Langmuir probe data in this section. Theoretical expressions describing the current collected by Langmuir probes have been derived by several authors, for example *Mott-Smith and Langmuir* (1926); *Laframboise and Rubinstein* (1976); *Rubinstein and Laframboise* (1982); *Brace et al.* (1973); *Brace* (1998). These derivations typically deal with ideal case lab scenarios where only a single electron population and ion species exist. The analytical equations presented in *Brace* (1998) for determining the electron

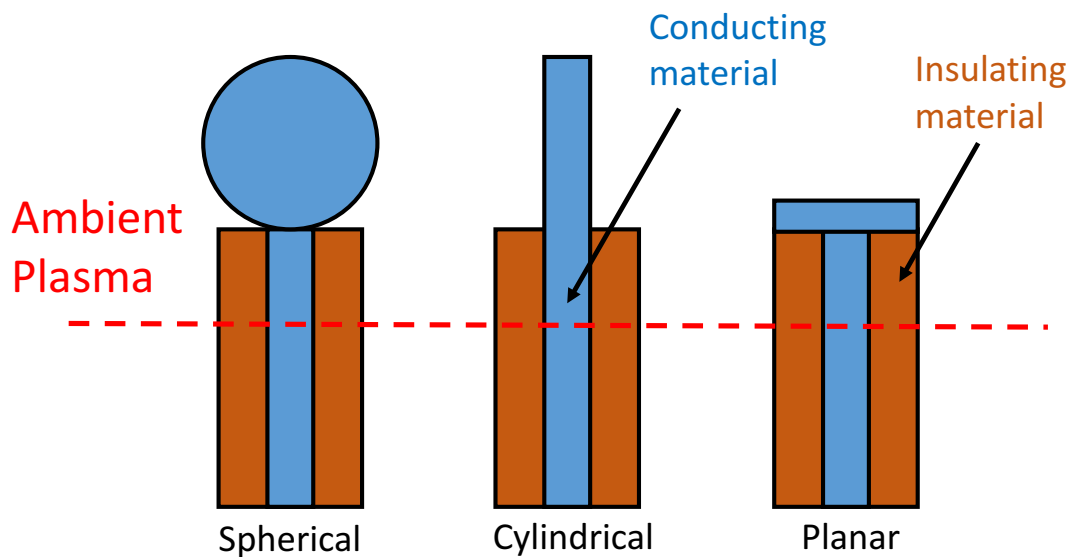


Figure 3.1: Cartoon representations of spherical, cylindrical and planar Langmuir probes. The conducting material is exposed to the ambient plasma, allowing a measurement of the collected current to the probe to be made.

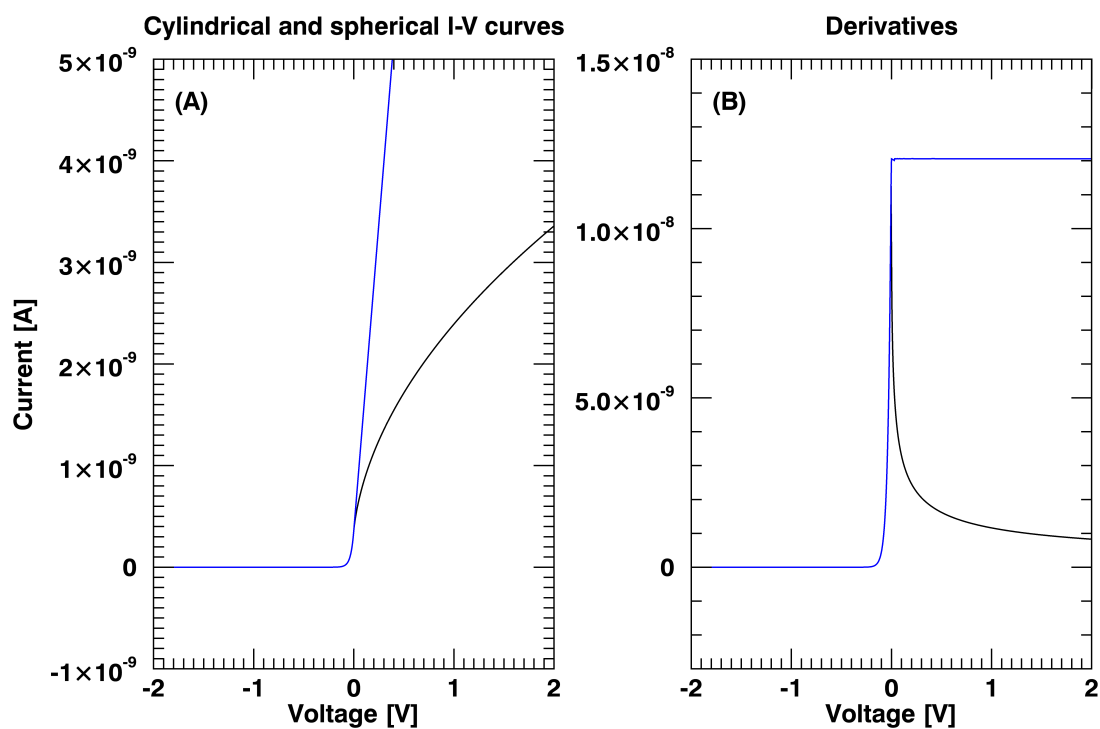


Figure 3.2: Panel A: Theoretical I-V curves for cylindrical (black) and spherical (blue) probes subject to identical plasma conditions. Panel B: Derivative,  $\frac{dI}{dV}$ , of panel A.

and ion densities ( $N_e$  and  $N_i$  respectively) from a single Langmuir probe I-V sweep are given by Equations 3.1 and 3.2. These equations are approximations for cylindrical probes in the OML regime, and are valid for specific values of  $V_p$ :

$$I_e = N_e A e 2\pi^{\frac{1}{2}} \left( \frac{kT_e}{2\pi m_e} \right)^{\frac{1}{2}} \left( 1 + \frac{eV_p}{kT_e} \right)^{\frac{1}{2}} \quad (V_p > 0) \quad (3.1)$$

$$I_i = AN_i q_i v_i \pi^{-1} \left( 1 + \frac{kT_i}{m_i v_i^2} + \frac{2eV_p}{m_i v_i^2} \right)^{\frac{1}{2}} \quad (V_p < 0) \quad (3.2)$$

Where the subscript  $e$  refers to electrons and the subscript  $i$  refers to an individual ion species.  $A$  is the probe surface area,  $e$  is electron charge,  $k$  is the Boltzmann constant,  $m$  is electron or ion mass,  $V$  is probe potential relative to spacecraft potential,  $T$  is electron or ion temperature,  $q_i$  is ion charge and  $v_i$  is the ion drift velocity in the spacecraft rest frame, where the ion flow is typically assumed perpendicular to the probe surface. In the technique outlined by *Brace* (1998), the spacecraft potential was taken as the inflection point between two regions referred to in this thesis as the  $T_e$  fit region and the electron saturation region. These regions are described in Section 3.4.2. This is equivalent to searching for a peak in the derivative of the measured I-V curve, as seen in Figure 3.2. This method is valid when only the cold bulk electron population is present; additional current sources must be first removed from the measured I-V curve before deriving  $V_{scp}$ . The electron temperature is derived from the  $T_e$  fit region using Equation 3.3, also from *Brace* (1998), which is applicable to cylindrical and spherical probes. Taking the natural log of Equation 3.3 yields a straight line whose gradient is proportional to  $\frac{1}{T_e}$ , thus allowing  $T_e$  to be derived independently of  $N_e$ .

$$I_e = AN_e e \left( \frac{kT_e}{2\pi m_e} \right)^{\frac{1}{2}} \exp \left( \frac{eV_p}{kT_e} \right) \quad (V_p < 0) \quad (3.3)$$

For the analysis of I-V curves measured in the terrestrial ionosphere, Equations 3.1 through 3.3 typically assume:  $T_i$  equal to  $T_e$ ,  $m_i$  equal to 16 AMU ( $O^+$ ) and  $v_i$  equal to the spacecraft velocity.

### 3.4 Langmuir probe measurements in ionospheres

The basic measurement technique for a Langmuir probe mounted onto a spacecraft and used to measure a planetary ionosphere is the same as that for a Langmuir probe in the lab. However, the presence of the spacecraft and sunlight now introduce several new sources of current that must be taken into account during the analysis of the measured I-V curves. Photoelectrons emitted by the spacecraft and probe itself are the most common sources of additional electron current, although hot electron populations can also be present. The most common source of additional ion current arises from the fact that planetary ionospheres are composed of multiple ion species that differ in relative abundance as a function of altitude.

A cartoon representation of the MAVEN spacecraft flying through the Martian ionosphere is depicted in Figure 3.3. The spacecraft is flying from right to left, as denoted by the arrow  $V_{sc}$ , which denotes spacecraft velocity. The brown box is the main spacecraft body; the two blue rectangles represent the solar panels; the gray circle is the communication antenna, and the LPW probes are mounted at the end of the two black booms. The light blue background represents the ambient plasma, the electron density and temperature of which the LPW probes are attempting to measure. The spacecraft generates a wake behind it, marked by the light brown region. The density at the center of the wake is  $\sim$  half that of the ambient plasma density; the edge of the wake is not an exact boundary, but its approximate extent is marked here by the dark blue curvy lines. The local plasma density transitions from the ambient value to that at the center of the wake across a finite region at the outer edges of the wake. The mounting points of the LPW booms and probes are chosen to maximize the likelihood that at least one probe will measure the ambient plasma and this is the case depicted in the figure. In the ionosphere, the ion thermal velocity is much smaller than the spacecraft velocity, and ions are essentially stationary with respect to the spacecraft and probe, colliding primarily with the forward facing surfaces of the spacecraft (in the solar wind, the ion velocity is much greater than the spacecraft velocity, but the solar wind flow is only in one direction, leading to the same effect). This leads to an angle of incidence, or attack, between the

LPW probes and the collected ion current. This angle of attack is marked by  $\theta_{sc,b}$ , where  $b$  is 1 or 2, for probe 1 or 2. Due to space limitations the figure only shows  $\theta_{sc,1}$ ;  $\theta_{sc,2}$  is also present and is usually different to  $\theta_{sc,1}$ . The yellow arrows represent solar EUV light that causes photoemission from the LPW probes and spacecraft surfaces. This light impacts the probes at angles  $\theta_{sun,1}$  and  $\theta_{sun,2}$ . Similar arrows exist for all spacecraft surfaces that are sunlit; the geometry of these is not known and so photoelectron emission from the spacecraft is assumed representable by a single, average term, as described in Section 3.4.1 below.

Additional electron and ion currents contribute to the measured I-V curve, making it difficult to extract the density and temperature information for the desired cold, bulk electron population. Thus, the removal of these additional current sources is typically important. The exact significance of each additional current source depends upon the Langmuir probe design, its location on the spacecraft, the spacecraft attitude, the specific spacecraft design itself, and the properties of the ionosphere being sampled. Section 3.4.1 below describes additional sources of current specific to the LPW instrument as it samples the Martian ionosphere.

There are three important potentials to consider when making Langmuir probe measurements on a spacecraft: the spacecraft ground (or spacecraft bus) potential, the spacecraft potential, and applied probe potential. Typically, spacecraft are designed such that their surfaces are conducting. These surfaces are grounded to the inner spacecraft bus. The scientific instruments are connected to this common ground, but some instruments, such as the Langmuir probe, require a floating potential. At all times, the potential between the spacecraft ground, and the Langmuir probe on MAVEN, are known. In this chapter, for all figures that are a function of potential on the horizontal axis: this is the potential between the probe sensor and spacecraft ground. The spacecraft potential, as discussed in Section 3.4.3.1, is the potential of the spacecraft with respect to the ambient plasma; for MAVEN, this the spacecraft ground with respect to the ambient plasma. The spacecraft potential typically varies throughout a spacecraft orbit depending on the local plasma environment and it cannot be explicitly controlled. An example of the effect of the spacecraft potential on measured I-V curves is shown in Figure 3.4. Panel A shows three theoretical I-V

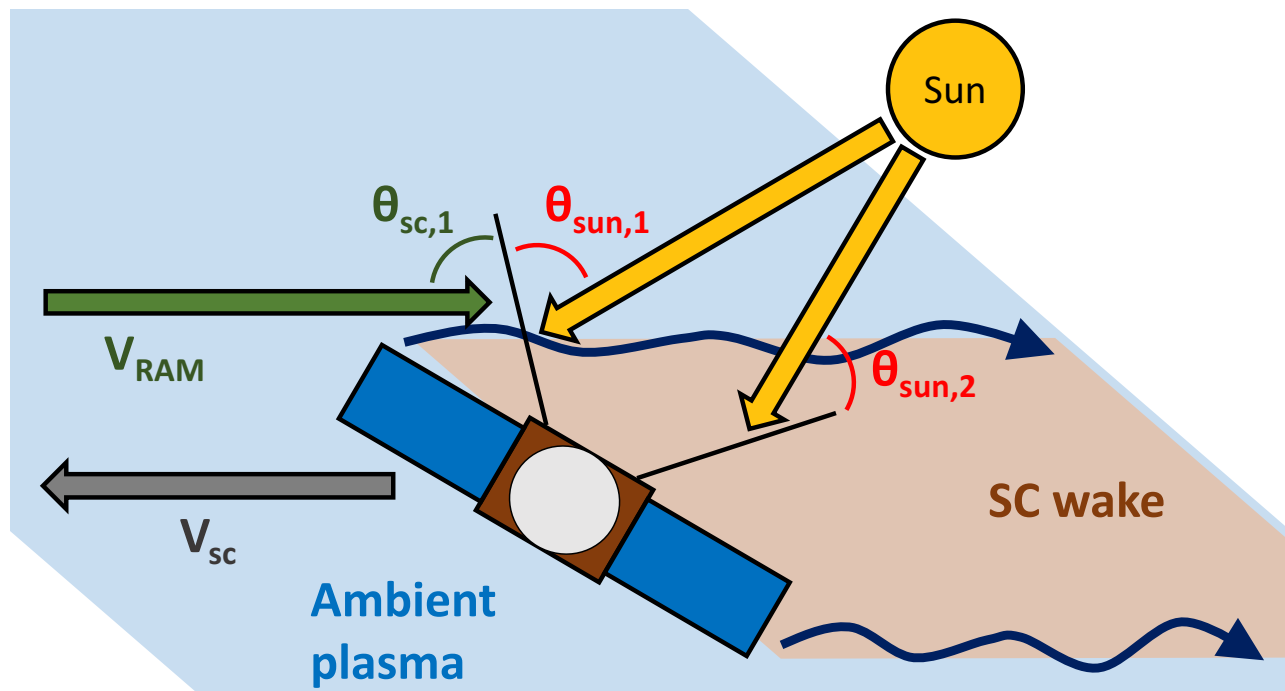


Figure 3.3: Cartoon representation of the MAVEN spacecraft traversing the Martian ionosphere. The spacecraft flies right to left at velocity  $V_{sc}$ . The ambient plasma surrounds the spacecraft except in the wake region, where the plasma density is roughly half that of the ambient plasma. Ions collide with the LPW probes at angles  $\theta_{sc,1}$  and  $\theta_{sc,2}$ ; sunlight strikes the LPW probes at angles  $\theta_{sun,1}$  and  $\theta_{sun,2}$ .

curves shown in green, black and red, corresponding to spacecraft potentials of +0.5 V, 0 V and -0.5 V, respectively. The horizontal axis voltages are with respect to the spacecraft ground. To first order, variations in spacecraft potential essentially shift the measured I-V curve in voltage space, although this becomes more complicated with the inclusion of multiple current sources such as photoelectrons. For the case of negative spacecraft potential, ambient electrons are retarded with respect to the spacecraft (and thus the probes), meaning that less electron current is collected, for any single probe voltage. The opposite is true for positive spacecraft potentials: more current is collected because a positive spacecraft potential attracts electrons. The corresponding derivatives are shown in panel B and these are also shifted in voltage space due to the spacecraft potential. Note that the peaks in these curves still correspond to the respective spacecraft potentials.

### 3.4.1 LPW specific electron and ion populations

Each of the electron and ion populations present within an LPW I-V sweep is assumed appropriately characterized by a density and temperature ( $N_e$  and  $T_e$ ). To first order, density affects the magnitude of the measured I-V curve for each population, whilst temperature affects the shape. Each ion species produces its own ion current. The inclusion of individual ion species severely complicates the fitting algorithm and instead, a single, average ion mass is assumed to represent the total ion current collected by the probes. Errors associated with this assumption are to first order negligible, as discussed in Section 3.5.5.3(5). The bullet points below describe each of the populations analyzed by the LPW fit algorithm; the terms  $I_{\text{subscript}}$  in each bullet point header denote the variable names given to each population during the I-V curve analysis, as found in Equation 3.27, for example.

- **Cold thermal electrons,  $I_e$ :** This is the electron population that LPW is designed to measure. Densities can be as large as  $\sim 10^6 \text{ cm}^{-3}$  and temperatures range from a few hundred K up to several thousand K, depending on spacecraft altitude. At periapsis the cold electron population makes up the bulk of the total electron population. The variables

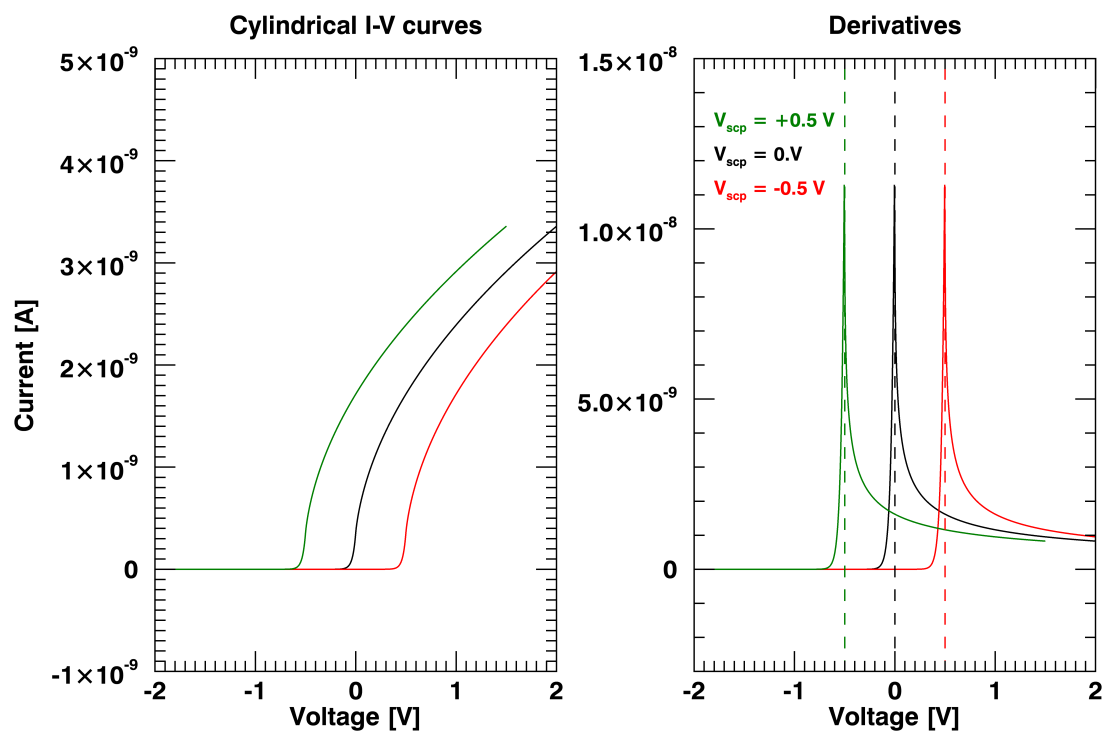


Figure 3.4: Panel A: Theoretical I-V curves for a cylindrical probe, under different spacecraft potential conditions. Panel B: Derivatives of panel A, where the vertical dashed lines mark the respective spacecraft potentials.

$N_e$  and  $T_e$  represent the cold electron density and temperature respectively.

- **Photoelectrons emitted by the spacecraft and boom,  $I_{\text{spe}}$ :** When the MAVEN spacecraft is in sunlight photoelectrons will be emitted from spacecraft surfaces and the LPW booms; these can subsequently be collected by the LPW sensors. The emission of spacecraft and boom photoelectrons from their respective surfaces are functions of solar EUV intensity (as a function of wavelength), angle of incidence of EUV light to the emitting surfaces, and the work function of those surfaces. These sources (spacecraft and boom) cannot be distinguished and as such their net effects are described by the single term,  $I_{\text{spe}}$ . At inner solar system bodies, when the spacecraft is in sunlight and in very low density plasma (i.e. at high altitudes), photoelectrons emitted by the spacecraft, boom, and probe (discussed next) are the dominant sources of electron current collected by the probe. Further, photoelectrons emitted from the spacecraft and booms are emitted relative to the spacecraft ground and not the ambient plasma potential. This means that the apparent spacecraft potential for  $I_{\text{spe}}$  is always at zero probe potential, regardless of the actual spacecraft potential. Thus, when large spacecraft potentials are present, the ambient electron population will be shifted in voltage space, and  $I_{\text{spe}}$  will be distinguishable from the ambient electron population. The analysis of I-V curves under such conditions allows an estimate of the spacecraft and boom photoelectron current to be determined. This population is given an empirically determined fixed temperature of 2.7 eV and a density that is proportional to the intensity of EUV light reaching the spacecraft. As the spacecraft passes through the Martian atmosphere, sunlight is absorbed as a function of decreasing altitude and thus  $I_{\text{spe}}$  also decreases with decreasing altitude. The LPW fit procedure utilizes a simple, spherical model of the neutral atmosphere to determine the intensity of EUV light reaching the spacecraft, which is described in Section 3.4.1.1. The guard and stub electronics (discussed in Section 3.4.3.7) mean that on MAVEN,  $I_{\text{spe}}$  is typically small compared to the photoelectron current emitted from the probes themselves,  $I_{\text{phe}}$ , which is

discussed next.

- **Photoelectrons emitted by the probe,  $I_{\text{phe}}$ :** When the LPW probes are in sunlight, photoelectrons are emitted from the probe surfaces and these contribute a negative current to the measured I-V curves (electron collection is defined as positive current). This process is depicted in Figure 3.3. Photoelectron emission from the probe is a function of the same parameters as for  $I_{\text{spe}}$ . The population is given a fixed temperature of 2.7 eV, based on the work function of the LPW probe surfaces. An estimate of  $I_{\text{phe}}$  is obtained from analysis of the ion side of an I-V sweep, measured in sunlight and very low plasma density conditions. This is because at positive probe potentials greater than 2.7 eV (on the electron side of the I-V sweep),  $I_{\text{phe}}$  photoelectrons are re-collected by the probe and contribute a net zero current. The intensity of sunlight reaching the probes also determines the size of  $I_{\text{phe}}$ ; the neutral atmosphere model described in Section 3.4.1.1 is used to calculate this intensity.  $I_{\text{phe}}$  is typically more important than  $I_{\text{spe}}$ .
- **Hot electrons,  $I_{\text{hot}}$ :** Hot electrons are high energy ionospheric electrons present in the Martian ionosphere. They are typically a product of photoionization of the neutral atmosphere and have characteristic energies of 10 - 30 eV. These energies are much greater than the potentials applied to the probes (which are usually +/- 5 V from spacecraft ground at periapsis) and to first order the hot electrons are unaffected by these probe potentials. As a result, the hot electron current collected by the probe is essentially constant as a function of probe potential and these hot electrons simply produce an offset in the measured I-V curve; they do not change the shape of it. Typical hot electron densities and temperatures are measured by the Solar Wind Electron Analyzer (SWEA) instrument onboard MAVEN (see Appendix A); the hot electron population is assigned an empirically determined constant temperature of 24 eV; an initial density of  $4 \text{ cm}^{-3}$  is assumed and this can be varied later within the fitting algorithm. Any instrumental offset current is also included in this term, as the two cannot be distinguished, and this is done in the LPW fitting algorithm.

Calibration of the LPW instrument has shown any offset currents to be less than 10 nA.

- **Ion current,  $I_{\text{ion}}$ :** The LPW fit procedure integrates the ion current using an average ion mass rather than dealing with individual ion mass species. Unlike for the above electron populations, the separate ion mass species have very similar temperatures and so can be modeled as an average population using an average ion mass and a single ion temperature,  $T_i$ , which is assumed to be equal to  $T_e$ . Recent modeling by *Matta et al.* (2014) has shown that different ion species above  $\sim 150$  km altitude at Mars can have temperature differences of factors of  $\sim 2 - 3$ ; these differences are significantly smaller than the differences in electron population temperatures outlined above, which can be 1 - 2 orders of magnitude in size. The increase in derivation accuracy that arises as a result of including multiple ion species lies within the current uncertainties; therefore, a single, average mass ion species is assumed in favor of a faster, less complex fitting algorithm.

#### 3.4.1.1 Neutral atmosphere model

The intensity of sunlight reaching the spacecraft strongly influences the photoelectron currents described above. As sunlight passes through the atmosphere, it is absorbed by the neutral constituents and thus its intensity decreases with decreasing altitude. A simple spherical model is utilized by the LPW fitting algorithm to estimate the intensity of EUV light reaching the spacecraft during each I-V curve measurement, so that photoelectron currents can be accounted for within the I-V curve analysis.

A static neutral atmosphere consisting of O and CO<sub>2</sub> (the two dominant neutral species in Mars' atmosphere) is assumed, based on atmospheric profiles from *Fox et al.* (1996). The integrated density of atmosphere that light must pass through to reach the spacecraft is then calculated, based on the spacecraft position. A cartoon representation of this is shown in Figure 3.5. Sunlight travels from right to left in the cartoon as marked by the orange arrows for three cases A, B and C. Above 400 km, the neutral density is assumed low enough such that absorption is negligible; this boundary

is marked by the outer, light blue circle in the cartoon. Below 100 km, 100% of the incident EUV light is assumed to have been absorbed; this boundary is marked by the dark blue circle in the cartoon.

Qualitatively speaking, cases A, B and C represent three different scenarios encountered by MAVEN. Case A shows MAVEN on the dayside of Mars, where distance A is relatively short and a significant amount of EUV light reaches the spacecraft. When MAVEN is eclipsed by the physical extent of the planet, no sunlight reaches the spacecraft, as depicted in case B. Case C shows when MAVEN is at the terminator or nightside of the planet, but is not eclipsed by the physical extent of the planet. Length C is much greater in this case and thus the intensity of EUV light reaching the spacecraft is typically small for such scenarios.

The intensity of EUV light at the spacecraft is calculated using Equations 3.4 and 3.5. The total integrated neutral density (ID) (assumed to be the sum of the O and CO<sub>2</sub> densities) is calculated as a function of distance along the ray path; at each point along the ray path between the spacecraft and the outer light blue circle shown in Figure 3.5, the altitude of the ray is calculated and the corresponding total neutral density is calculated. Equation 3.4 details this step:

$$ID = \int_a^b \left( N_{\text{O}} \exp\left(\frac{-alt}{H_{\text{O}}}\right) + N_{\text{CO}_2} \exp\left(\frac{-alt}{H_{\text{CO}_2}}\right) \right) \quad (3.4)$$

Where the parameters and their assumed values are described in Table 3.4.1.1. The integration is carried out over the column of atmosphere that lies between the spacecraft and an altitude of 400 km in the Sunward direction, as depicted by lines A, B and C in Figure 3.5.

The EUV intensity at the spacecraft is then calculated by Equation 3.5:

$$I_{\text{EUV}} = \exp\left(\frac{-ID}{IE}\right) \quad (3.5)$$

Where the value of IE is determined empirically to be  $1 \times 10^{20}$ . The Martian dayside plasma density has been shown to follow a Chapman function (e.g. *Fallows et al. (2015); Ergun et al. (2015a)*) and as such the peak in plasma density occurs when the EUV intensity reaches  $\frac{1}{e}$  of it's

Parameter	Value	Description
$N_{\text{O}}$ ( $\text{cm}^{-3}$ )	$1.28 \times 10^{11}$	Oxygen density at planet surface.
$N_{\text{CO}_2}$ ( $\text{cm}^{-3}$ )	$4.75 \times 10^{15}$	CO <sub>2</sub> density at planet surface.
$H_{\text{O}}$ (km)	26.78	Oxygen scale height.
$H_{\text{CO}_2}$ (km)	10.55	CO <sub>2</sub> scale height.
$a$	-	Lower column depth integration limit.
$b$	-	Upper column depth integration limit.

Table 3.1: Definition of parameters and assumptions used in Equation 3.4, and reference in Figure 3.5.

initial value. This fact is used to determine the value of IE: the ionization peak at the subsolar point lies between 125 km and 130 km (e.g. *Fallows et al. (2015)*; *Ergun et al. (2015a)*) and IE is set to match this. An example of the modeled EUV intensity at the subsolar point, as a function of altitude, is shown in Figure 3.6. A value of 0 means no EUV light reaches the spacecraft; a value of 1 means 100% EUV light reaches the spacecraft. It can be seen that the altitude range  $\sim 120$  km - 200 km is the most important for determining EUV intensity, and outside of this range the EUV intensity is essentially 0 or 1.

The neutral model assumes a spherically symmetric, static neutral atmosphere; these assumptions are to first order appropriate, but the Martian neutral atmosphere is known to be asymmetric in extent and to respond to solar inputs (e.g. *Mahaffy et al. (2015a)*; *Thiemann et al. (2015)*; *Andersson et al. (2016b)*). Thus, improvements to the model are possible. The most obvious is to use the now available, most recent atmospheric density profiles, as measured by the NGIMS instrument on board MAVEN (*Mahaffy et al., 2015a*). Data from the EUV monitor on MAVEN (an instrument that monitors the EUV input to the Martian atmosphere, see Appendix A) can also be incorporated into the model to validate the calculated EUV intensities. EUV data was not incorporated into the original model because data is not available during every periapsis pass: the EUV instrument must point at the Sun to acquire data and so measurement availability depends upon the spacecraft orientation during each periapsis pass. A method to account for these common data gaps at periapsis would need to be developed when incorporating EUV data into the model.

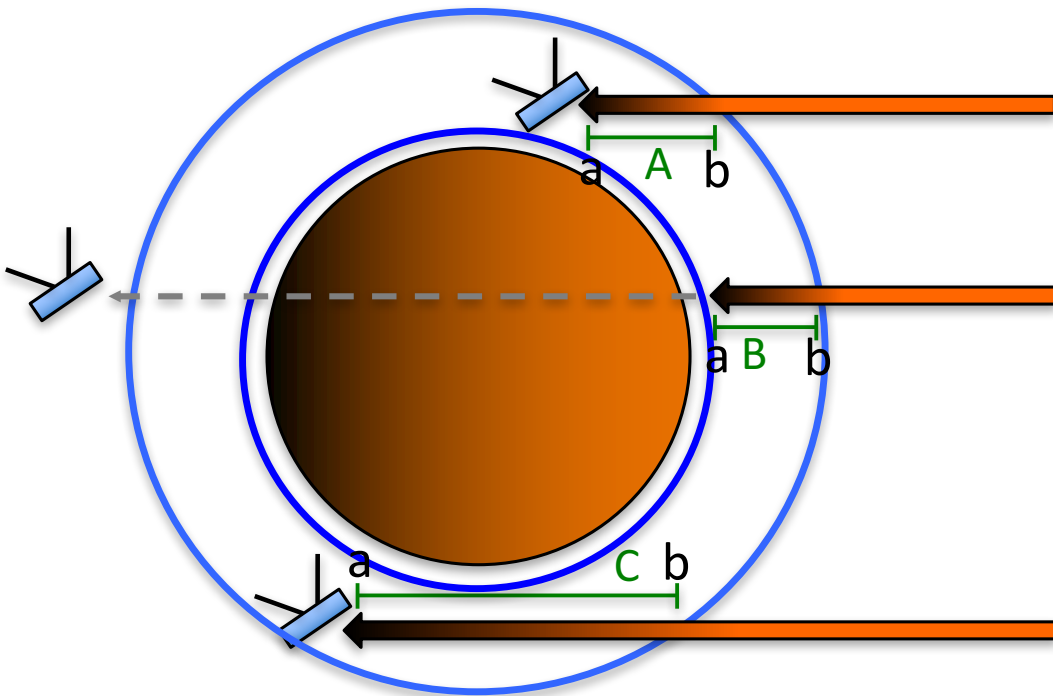


Figure 3.5: Cartoon depicting the method used to calculate the EUV intensity at the spacecraft as a function of position. EUV light is assumed to be absorbed between the inner dark blue and outer light blue circles (representing 100 km and 400 km altitudes respectively). The lower case letters  $a$  and  $b$  represent the lower and upper limits of integration in Equation 3.4 along the column depth in the Sunward direction.

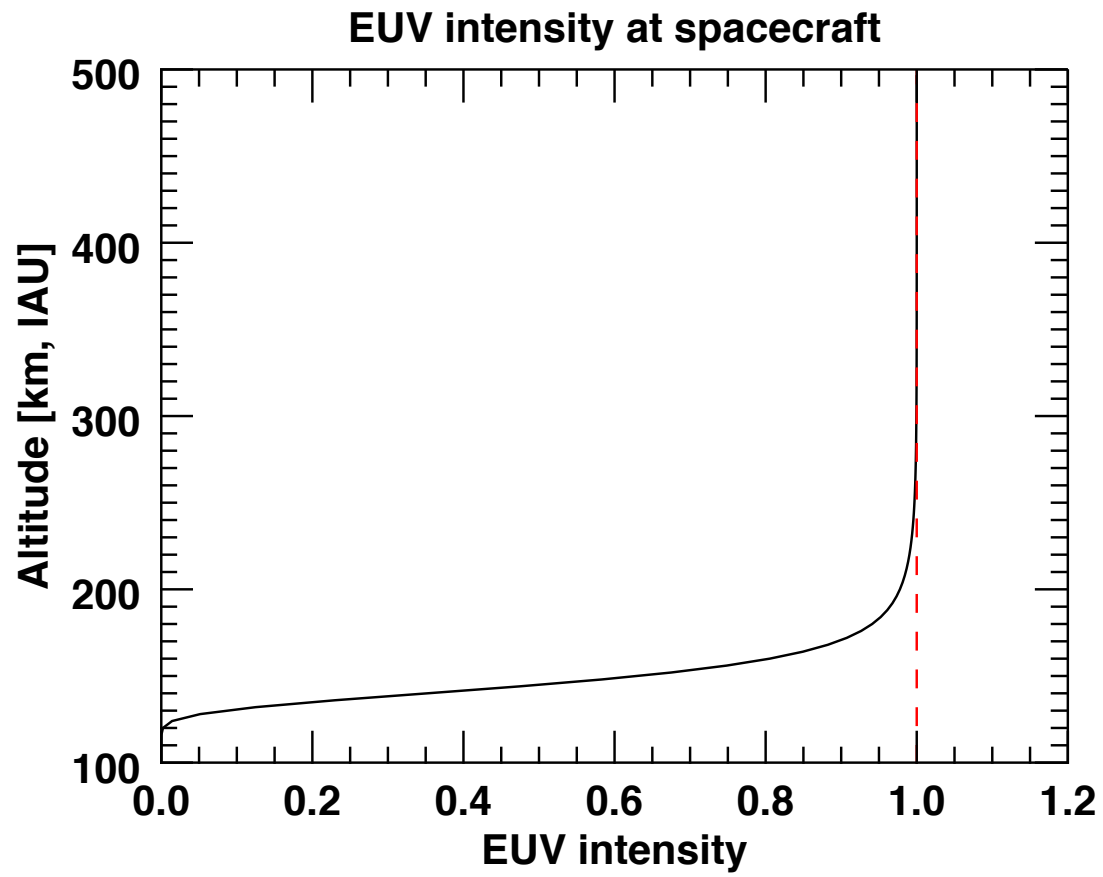


Figure 3.6: Modeled EUV intensity at the spacecraft, as a function of altitude at the subsolar point.

### 3.4.2 Example of an LPW I-V curve

An example LPW I-V sweep is shown in Figure 3.7. It was obtained close to the sub solar point at  $\sim 125$  km altitude. For the LPW instrument, positive current is defined as electron current collection and thus at positive potentials the probe collects electrons. This region is known as the electron collection region and is outlined in red in the figure; analysis of this region of the I-V curve allows a derivation of electron density to be made. When the probe is biased to negative potentials primarily ions are collected by the probe; this region is known as the ion collection region, outlined in blue in the figure. Analysis of the ion collection region allows a derivation of the ion density to be made. Assuming quasi neutrality, the ion and electron densities should be equal and this fact is used to verify and improve the LPW fit algorithm. The transitional region between the ion and electron collection regions is known as the electron retardation region, or  $T_e$  fit region; the electron temperature is derived from analysis of this region, which is outlined by green in Figure 3.7.

The range of potentials applied to the probe is determined such that all three of the above regions are aptly sampled. The resolution in voltage space of these measurements is determined, to first order, by telemetry restrictions: the number of total measurement points per I-V sweep depends on how much data can be sent back to Earth. The LPW instrument utilizes 128 measurements per I-V sweep. The width of the  $T_e$  fit region is proportional to the value of  $T_e$  itself.  $T_e$  is typically cold in the low Martian ionosphere (less than 1000 K below  $\sim 200$  km altitude) and because of this, I-V sweep measurements are made at greater resolution within the  $T_e$  fit region so that cold temperatures can still be resolved. The finest resolution in voltage space that the LPW instrument can achieve is 0.25 V. This is because variations in surface work function (which are discussed in Section 3.4.3.3) are on the order of 24 mV, and so finer resolution in applied potentials cannot be achieved. The instrumental measurement noise is about 1 nA, however, variations in the local plasma environment can occur on timescales much shorter than that of an I-V sweep, and so current measurement noise of 10 nA is typical. The theoretical lower temperature limit that the LPW instrument can measure is about 150-200 K and this is limited by the 24 mV variations in probe

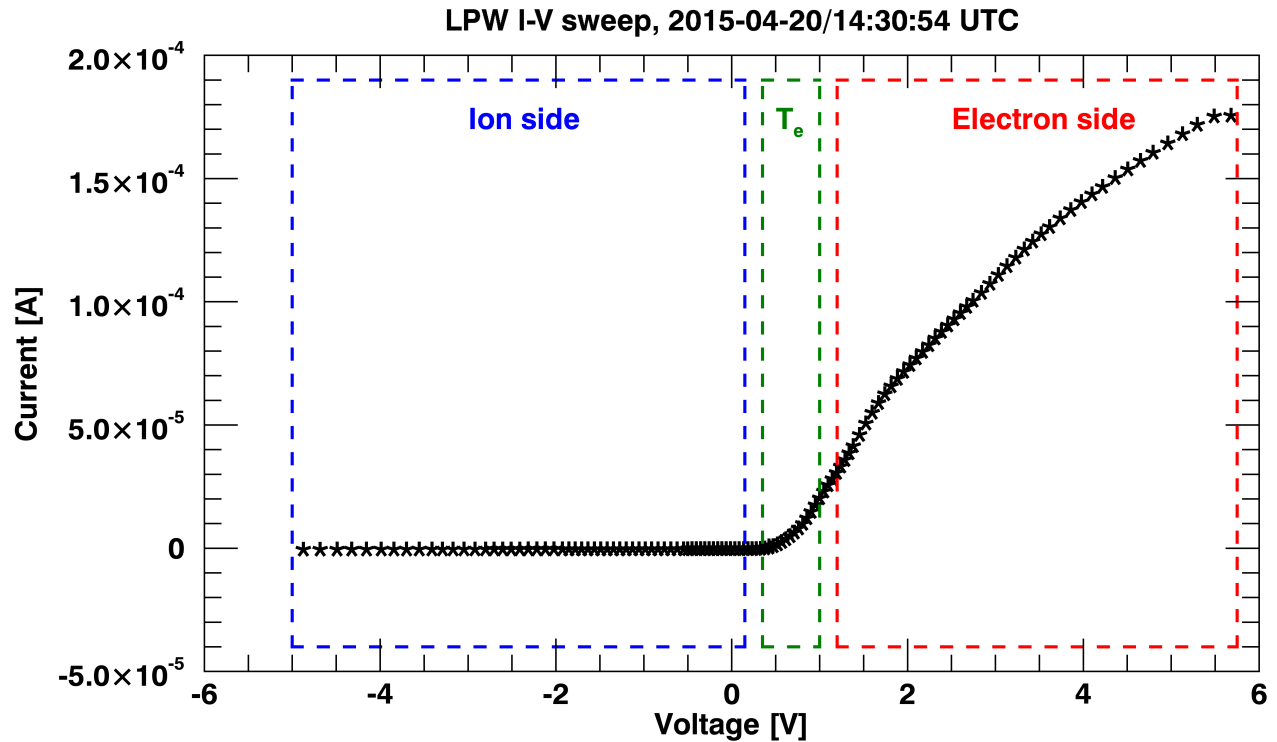


Figure 3.7: Example I-V sweep measured by the LPW instrument. The electron and ion collection regions are where electrons and ions respectively are the primary charges collected by the probe. These regions allow derivations of electron and ion density respectively. The  $T_e$  region is the region critical in determining the electron temperature. Positive current collection is defined as the collection of electrons. The derived  $N_e$ ,  $T_e$  and  $V_{scp}$  values were  $2.35 \times 10^5 \text{ cm}^{-3}$ , 0.05 eV (550 K) and 0.58 V respectively.

surface work function. Additional sources of current and complexities, as discussed throughout this chapter, mean that in reality the lower temperature limit measurable by LPW is about 500 K. The most negative and positive 2-3 potential measurements of the LPW I-V curves sometimes show instrumental effects when the applied potentials are set to default values prior to a change in instrument subcycle. These end data points are ignored during the fit process outlined in Section 3.5.

The LPW instrument was designed to measure dayside densities at Mars which range up to and above  $1 \times 10^6 \text{ cm}^{-3}$ . For  $N_e$  below about  $500 \text{ cm}^{-3}$ , photoelectron and hot electron currents can become significant compared to the ambient electron population, leading to greater uncertainties in the derived quantities. Uncertainties under high density conditions are typically less than 15-20%.

A single I-V curve is measured over a finite measurement time; thus, during the derivation of  $N_e$  and  $T_e$ , it is assumed that the ambient plasma conditions were constant during the entire I-V sweep measurement. The shortest time that the LPW instrument can measure a single I-V curve in is 1 s, and this is by design. There is a finite settle time required for the electronics to achieve the desired probe potential, and this limits how quickly the instrument can step between potentials. Thus, at it's highest measurement cadence, the LPW instrument can resolve scale structures in the ionosphere on length scales of  $\sim 4 \text{ km}$  or greater (this is also determined by the spacecraft periapsis velocity, about  $4 \text{ kms}^{-1}$  at periapsis). Much finer scale spatial structure has been observed in the Martian ionosphere and this is under sampled by the LPW instrument (e.g. Figure 8.1 in Chapter 8, this thesis). Figure 3.7 is used as the basis for the example figures shown throughout Section 3.5, which are typically zoom-ins to various regions of this I-V curve.

### 3.4.3 Additional complexities for space-bourne Langmuir probes

Langmuir probes mounted on spacecraft are subject to additional complexities and sources of error that do not usually arise in the lab. This section discusses complexities specific to the LPW instrument as a result of it being mounted on the MAVEN spacecraft. It is based on the informative discussion found in *Brace (1998)*.

### 3.4.3.1 Spacecraft potential ( $V_{\text{scp}}$ )

Potentials applied to Langmuir probes during the measurement of I-V curves are with respect to the spacecraft and not the ambient plasma. Thus, the spacecraft potential determines the range of potentials that must be applied to the probes to obtain a useable I-V curve. If an incorrect range of potentials is applied then one or more of the three critical regions (ion collection,  $T_e$  fit and electron collection) may not be sufficiently covered and some parameters may not be derivable from the I-V curve.

Spacecraft potential tends to become positive when the spacecraft is immersed in a very low density plasma in sunlight. Such conditions occur at high altitudes; the low density ambient plasma means that few ambient electrons or ions are collected by the spacecraft. Sunlight causes photoemission from spacecraft surfaces and under such conditions this photocurrent is significant compared to the ambient plasma currents. Thus, the spacecraft potential becomes positive so that some of these photoemitted electrons are drawn back to the spacecraft.

Negative spacecraft potentials tend to occur at low altitudes when the ambient plasma density is large. The electron thermal current is greater than the ion thermal current by a factor of  $\sqrt{\frac{m_i}{m_e}}$ , which is approximately 170 when  $O^+$  is the dominant ion species, and the spacecraft potential thus becomes negative to account for this. The spacecraft velocity at periapsis is about  $4 \text{ kms}^{-1}$  and this is significantly greater than typical ion thermal velocities of  $\sim 400 \text{ ms}^{-1}$ . Electron thermal velocities are close to  $100 \text{ kms}^{-1}$  at periapsis. Thus, electrons are collected essentially isotropically across all spacecraft surfaces, whereas ions are collected primarily on the forward facing surfaces. The large spacecraft velocity compared to the ion thermal velocity actually improves the amount of ion current collected, but not by enough to overcome the factor of  $\sim 170$  due to the differing ion and electron masses. Photoemission from spacecraft surfaces can still occur at low altitudes, but these currents are now small compared to the ambient current collection and do not play a major role in determining the spacecraft potential.

Within each mode of operation the LPW I-V curves are measured within a set voltage range.

During high density conditions the plasma temperature is typically cold and so the LPW sweep range is set to  $\pm 5$  V with respect to what is known as the dynamic offset potential: this is an automated potential offset that ensures that the  $T_e$  fit region is at the center of the measured I-V sweep. The instrument tracks the cross over voltage from negative to positive current collection in the current I-V sweep, and shifts the subsequent sweep to be centered upon this voltage.

#### **3.4.3.2 Boom and sensor**

The use of a boom is required to minimize the amount of disturbed plasma that the probe samples due to the presence of the spacecraft. The spacecraft potential can greatly influence the ambient plasma environment up to a few Debye lengths away from the spacecraft, where typical Debye lengths within Mars' ionosphere range from a few mm up to  $\sim$  a meter (see Figure 3.19). Thus, the LPW probes are mounted at the end of 7.1 m booms. Multiple probes can be flown not only for the sake of redundancy, but to also further minimize additional spacecraft effects, such as the wake. When the spacecraft and boom are in sunlight, photoelectrons will be emitted from them that can be collected by the probes. Extended booms help in reducing spacecraft photoelectrons being collected by the probes. Care must be taken in choosing the probe mounting points. They should be placed as far away from thruster nozzles as possible, for example, as these can lead to surface contamination, which is discussed below.

#### **3.4.3.3 Probe surface work function**

The probe surface work function influences the local surface potential that charged particles experience as they approach the probe surface. A uniform surface work function means that all charged particles experience the same probe potential as they approach the probe surface. A non uniform surface work function means that as charged particles approach the probe surface, the local potential experienced by each particle differs slightly, depending upon the section of probe surface that they are approaching. Variations in the surface work function of a probe can lead to substantial errors in the derivation of  $T_e$ . As an example, if the probe surface work function varies

by  $1k_bT_e$ , then the upper and lower  $1k_bT_e$  regions of the  $T_e$  fit will be smeared out; this arises because some parts of the probe surface are within the  $T_e$  fit region and some parts are still within the electron and ion collection regions. Work function irregularities can be a particular problem in low temperature plasmas such as the Martian ionosphere: the variations can then be of a similar magnitude or greater than the typical electron thermal velocity and the entire  $T_e$  fit region can be smeared out.

#### 3.4.3.4 Probe surface contamination

Probe surface contamination can be split into two categories: volatile and non-volatile contamination. Volatile contamination is temporary in that it can be removed from the probe surface under certain conditions. Non-volatile contamination is permanent: contaminating agents bond to the probe surface and cannot be removed. Surface contamination can arise at any point in the mission (during instrument construction, launch, and in flight) and occurs when unwanted contaminants are deposited on the probe surface. Such contaminants can range from dust and oils left on the probe as a result of being handled during construction of the instrument; the deposition of thruster gas during flight if the probe is mounted close to a thruster nozzle on the spacecraft, or contaminants within the planetary atmosphere binding to the probe surface during science operations. If the surface contaminants are poor conductors then this contamination can lead to a patchy work surface function as described above. Standard instrument practice is to perform cleaning prior to launch, but realistically this process will not be perfect.

The LPW probes were observed to suffer from volatile thruster contamination during the first 1-2 months of the primary science mission when several large, orbit adjustment firings, were undertaken during orbit capture. Similar contamination effects have been observed on previously flown Langmuir probes and various methods can be employed in flight in an attempt to remove such surface contamination. The Atmospheric Explorer (AE)-C, D and E Langmuir probes, for example, contained internal heating filaments in an attempt to ‘bake-out’ this contamination. Unfortunately, the temperatures reached were not quite high enough to be effective. The lack of success using

the bake out method, and the complexity of including heating filaments within the probes, led to the development of another method. The Dynamics Explorer (DE)-2 mission utilized ionospheric electrons to bombard the probe surfaces in an attempt to sputter off the contamination. The probe potentials were set to +150 V as the spacecraft traversed the high density ionosphere such that ionospheric electrons were accelerated to the probe surface; this method provided much better results. The Pioneer Venus Orbiter (PVO) mission spent 95% of its 24 hour orbit in the solar wind where the Langmuir probes were subject to bombardment by 1 keV solar wind protons. These proved similarly capable of cleaning the probes: neither of the LP probes on PVO showed signs of contamination over the 14 year mission.

The LPW probes do not possess internal heating filaments and as such the electron bombardment technique was utilized to remove volatile thruster contamination. The MAVEN spacecraft samples the solar wind for about 1 hour out of a  $\sim 4.5$  hour orbit period; at such times during the early mission the LPW probe potentials were set to their highest values, +90 V. The probe surfaces were subject to bombardment of high energy solar wind electrons and this proved able to remove the early science mission thruster contamination. The cleaning process took several orbits; it is likely that a single  $\sim 1$  hour cleaning period within the solar wind was not long enough to completely remove the volatile contamination.

The LPW instrument has also been observed to suffer from non-volatile contamination in the form of atomic oxygen (AO) contamination. For the first  $\sim$  nine months of the primary science mission, when MAVEN first started to sample the Martian ionosphere, the shape of the  $T_e$  fit region within the measured I-V curves was observed to evolve slowly over time for both probes. This led to complexities in deriving the spacecraft potential and electron temperature and the analysis method developed to account for this is discussed in Section 3.5. The contamination itself is thought to be a result of the high spacecraft velocity at periapsis relative to neutral oxygen in the atmosphere, which is equivalent to several thousand kelvin. At such high temperatures, atomic oxygen is thought to have permanently bonded to the probe surfaces in patches. The shape of the measured I-V curves stopped evolving after  $\sim 9$  months likely because by this point the probes were completely covered

by this contamination - oxygen could no longer reach the probe surface and the surface potential work function no longer changed over time. The operation of two independent Langmuir probes on MAVEN allowed for identification of this surface contamination. Measurements, and the evolution of, the  $T_e$  fit regions by the two LPW probes during these nine months were not identical; the ambient plasma conditions should be  $\sim$  constant over the length scale of the spacecraft and thus surface contamination was identified as the cause of these differences. This AO contamination is also discussed in Section 3.5.6 and *Ergun et al. (2015a)*.

### 3.4.3.5 Magnetically induced potentials

A Langmuir probe possesses a conducting surface and so as it (and the spacecraft) fly through any local magnetic fields the possibility of inducing a potential gradient within the probe exists. This effect can be significant for cylindrical probes whose length can be long enough such that the induced potentials are significant. The potential induced within the probe is of the order  $(\vec{B} \times \vec{v})L_p$ , where  $\vec{B}$  is the magnetic field vector,  $\vec{v}$  is the spacecraft velocity vector and  $L_p$  is the probe length. For cylindrical probes the length of the probe must thus be chosen such that these induced potentials are much smaller than the potentials to be applied to the probes during operation. When the induced potential is significant compared to the potentials applied to the probes, it can have the same effect as smearing out the  $T_e$  fit region as seen from surface contamination. The simplest solution, particularly in the terrestrial ionosphere where  $\vec{B}$  is strong, is to use short probes. Typical cylindrical Langmuir probe lengths are a few tens of centimeters. The Langmuir probe can also be aligned with  $\vec{B}$  or  $\vec{v}$  to reduce the induced potential, but this can be difficult and in the case of  $\vec{v}$  can lead to further distortion of the I-V curve from probe end effects. These are discussed in Section 3.5.4. In the case of LPW, the probes are relatively short (about 40 cm long), and Mars possesses no significant dipole magnetic field. Crustal magnetic anomalies observed at Mars are several orders of magnitude smaller than the Earth's dipole field strength and thus only small potentials are induced within the LPW probes that are insignificant compared to other sources of complexity noted in this section.

### 3.4.3.6 Instrument electronics

The electronics associated with a Langmuir probe are the components that apply potentials to the probes and measure the resulting currents. These components thus determine the accuracy of the measured I-V curves which in turn determine the quality of parameters derived from the measurements. Properties to consider include: to what precision can potentials be applied to the probes, what is the voltage settling time at each new potential, and to what degree of precision can the collected current be measured. The range of electron densities and temperatures that are to be derived also heavily influence these characteristics, as discussed in Section 3.4.2.

### 3.4.3.7 Probe and spacecraft design

The probe should be designed to cause minimal disturbance to the ambient plasma. Disturbances can arise simply from the probe being placed in the ambient plasma, but also through the operation of the instrument when observations are made. Typically, the smaller the physical size of a probe, the less likely it is to disturb the ambient plasma environment. There is thus a trade off between the level of disturbance caused by the probe, and the amount of current collected by the probe: a smaller probe causes less disturbance but also collects fewer charged particles, resulting in lower signal to noise.

The surface area of a Langmuir Probe must be small compared to that of the conducting area of the spacecraft it is mounted on, so that operation of the probe does not influence the spacecraft potential. Consider a probe biased such that it attracts electrons. The spacecraft must collect the same number of ions if the spacecraft potential is to remain unaffected. Because the electron thermal current is  $\sim 100$  times greater than the ion thermal current (again due to  $\sqrt{\frac{m_i}{m_e}}$ ), the Langmuir probe surface area needs to be a factor of  $\sim 100$  smaller than the spacecraft surface area that collects ions. When this surface area ratio is less than  $\sim 100$ ,  $V_{scp}$  will track potentials applied to the probe. As a rule of thumb, Langmuir probes are designed such that the spacecraft to probe collection area ratio is a few hundred, as additional complexities need to be considered.

The surface area ratio can vary depending upon the local plasma environment and spacecraft orientation: surfaces subject to sunlight, surfaces subject to the ion ram direction, and the local plasma density, for example, all influence the spacecraft current collecting surface area.

The instrument design can also be utilized to reduce unwanted sources of current reaching the probe. An engineering schematic of the LPW instrument is shown in Figure 3.8; the top configuration shows one of the booms in the stowed state; the bottom shows the deployed state. The probe is the cylindrical tip to the right of the instrument, referred to as the ‘whip’ in the figure. The left side of the instrument mounts to the spacecraft body. The guard contains the preamp and it is the cylinder located just below the probe. The guard surface is set to small negative potentials ( $\sim -5$  V) with respect to the probe to reflect photoelectrons emitted from the boom and spacecraft so that they are not collected by the probe. The stub is a disk that caps the end of the guard facing the probe; it is set to small positive potentials ( $\sim 1$  V) so that photoelectrons emitted by the stub itself are re-collected, and do not reach the probe.

### 3.5 The MAVEN LP fit algorithm

The fit algorithm used in the analysis of LPW measured I-V curves to derive  $N_e$  and  $T_e$  is described in detail here. At the core of the algorithm are expressions for the numerically integrated electron and ion currents collected by the probe, as described in Sections 3.5.1 and 3.5.2. The algorithm constrains variables in an empirically determined order and converges on final solutions by performing multiple iterations of the described procedures. The highly variable plasma environment at Mars, combined with in flight surface properties of the probes, led to difficulties in fitting the precise, multi-parameter analytical solutions outlined earlier in Equations 3.1 through 3.3, of the measured I-V curves. The LPW fitting algorithm developed differs significantly from any previously documented Langmuir probe analysis method. Discussion of the encountered complexities, and the solutions implemented to account for them, are detailed throughout this section. One of the most significant adaptations in the fitting algorithm is to account for variable sheath shape behavior that is observed. Although the probes themselves are cylindrical in shape, cylindrical and

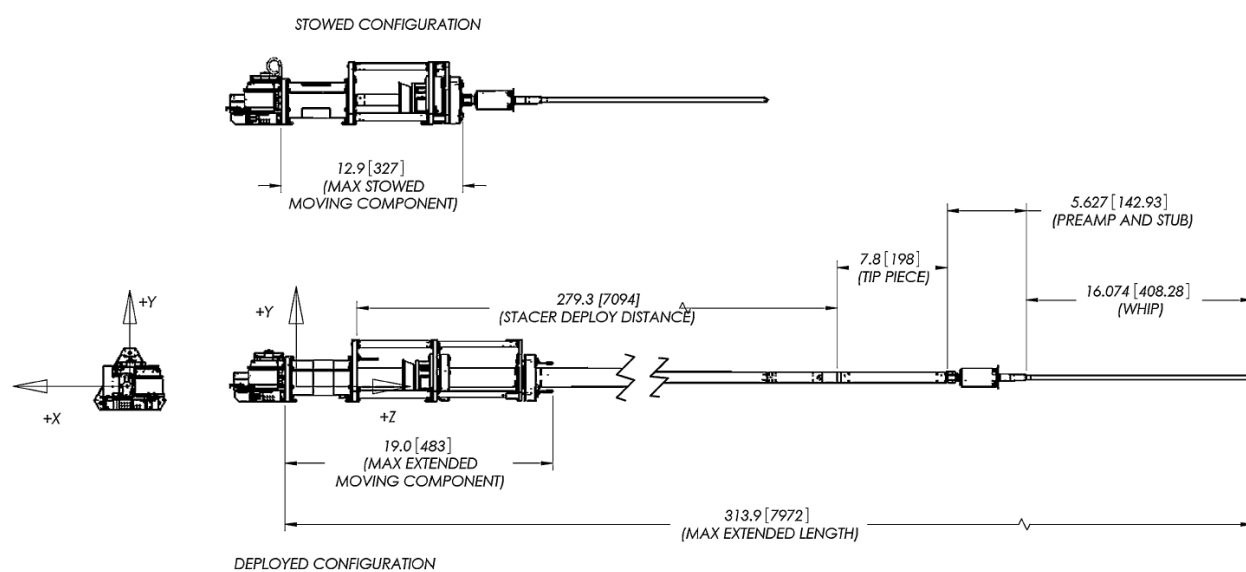


Figure 3.8: Engineering schematic of the LPW instrument, showing the boom deployment mechanisms and the attached probe. Figure taken from *Andersson et al.* (2014).

spherical sheath behaviors are observed, dependent upon the local plasma conditions at the time of measurement. Hints of similar effects have been observed before (e.g. on the AE-C, DE-2 and PVO missions (*Brace, 1998*)) but to my knowledge they have not been accounted for in such a detailed and comprehensive manor as the method presented here. These sheath complexities will effect any cylindrical Langmuir probe in general, but the plasma conditions and corresponding Debye lengths in Mars' ionosphere exaggerate this behavior.

When analyzing LPW I-V curves, the inclusion of variable sheath shape behavior, the large number of free parameters that determine the final form of an I-V sweep, and the range of values spanned, typically overwhelmed standard minimization routines. This lead to poor fits and in many cases there was no convergence to an optimum solution at all. Thus, the fitting algorithm developed for the LPW instrument not only allows the sheath shape to transition between cylindrical and spherical behaviors (based on the derived local plasma conditions at the time of measurement), it also constrains and optimizes fit parameters in an empirically determined order. This method produced a much more robust fitting algorithm, the implementation of which is described in Section 3.5.5. Expressions for the numerically integrated electron and ion currents are central to the LPW fitting algorithm; these are derived Sections 3.5.1 and 3.5.2 respectively. These expressions are derived for both cylindrical and spherical sheath shapes, with the net contributions from each determined, allowing for transitional behavior between the two. A flow chart summarizing the derivation of these expressions is presented in Figure 3.9, also referred to in the text as Flow Chart 1 (FC1). The numbers to the left in each box are used as references within the main text. A flow chart summarizing the LPW fitting algorithm is presented in Figure 3.12; this figure is not discussed until Section 3.5.5, but is referenced in the following section. I remind the reader that the figures presented in this section are zoom-ins of the example I-V curve shown in Figure 3.7; color schemes used to highlight various regions of the I-V curve are constant throughout the chapter. A summary of the variables found in this chapter can be found in Table D within Appendix D.

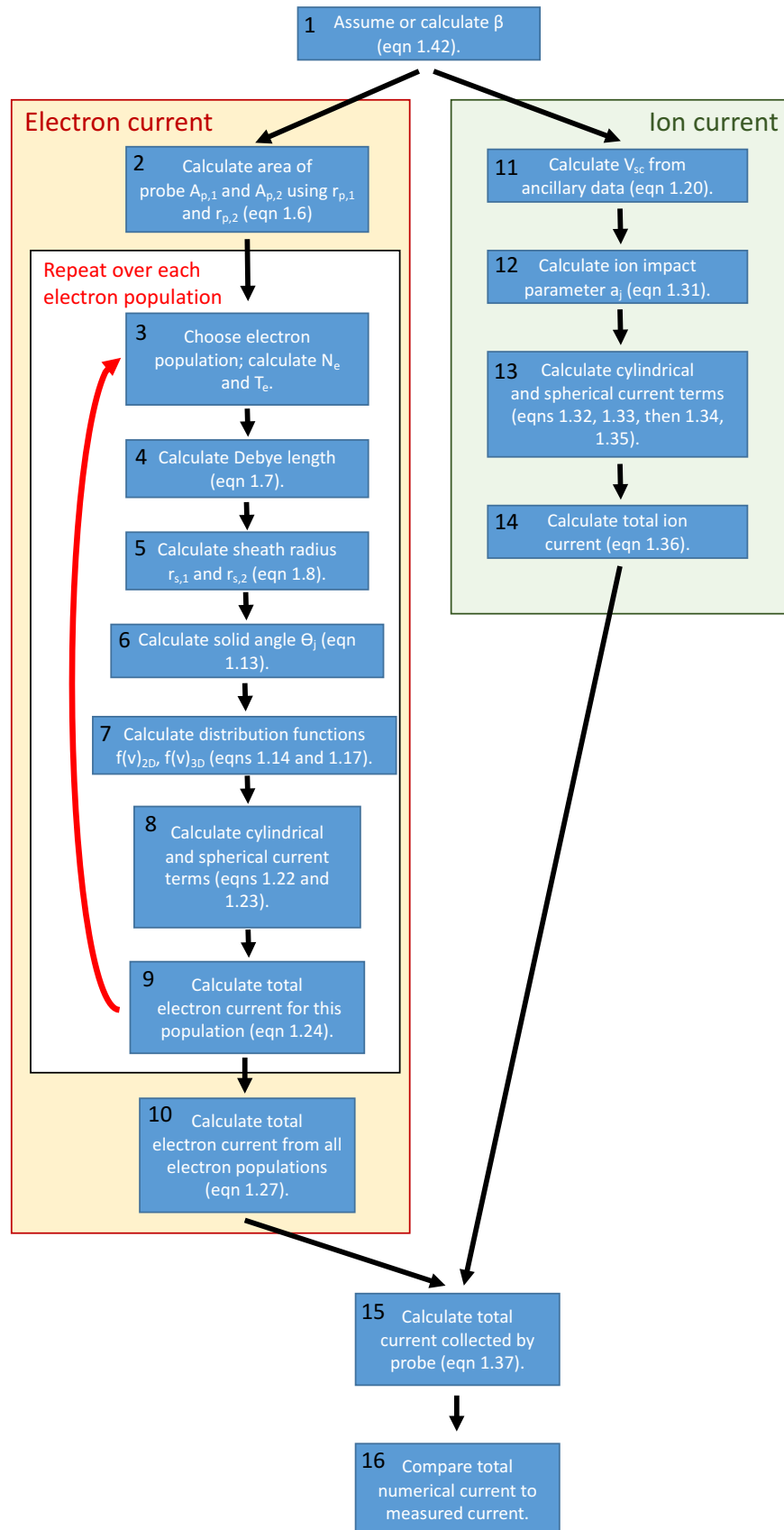


Figure 3.9: **Flow Chart 1 (FC1)**: Flow chart summarizing how the numerically integrated electron and ion currents are calculated, using expressions derived in Sections 3.5.1 and 3.5.2. Detailed discussion is given of each stage within the main text and is referenced using the numbers to the left in each box.

### 3.5.1 Derivation of the numerically integrated electron current

Expressions for the numerically integrated plasma current collected by the Langmuir probes are at the core of the LPW fitting algorithm. The numerically derived currents are based on initial estimates for various plasma parameters (such as electron density and temperature). General expressions for the numerically integrated plasma currents collected by a cylindrical probe are derived in this section, where FC1 provides an overview of these derivations.

- (1) **Assume initial value of  $\beta$ ; box 1 in FC1:** The behavior of the probe sheath, as a cylinder, sphere, or some combination, is parameterized by the variable  $\beta$ . The LPW software calculates current collection for two cases: a purely cylindrical sheath, and a purely spherical sheath. The parameter  $\beta$  quantifies the relative contributions of each case, as seen later in this section. When  $\beta = \frac{1}{2}$  the sheath is relatively small compared to the probe size and it is cylindrical in shape; when  $\beta = 1$  the sheath is large compared to the probe and can be approximated by a sphere; intermediate values of  $\beta$  represent transitional sheath behavior. Within the LPW fitting algorithm,  $\beta$  is initially assumed to be  $\frac{1}{2}$  to match the cylindrical shape of the probe itself, prior to being explicitly calculated in boxes 10, 18 and 23 in FC2. For these later boxes, the value of  $\beta$  is derived based on analysis of the asymptotic behavior of the electron saturation region of the measured I-V curve; this process is detailed in Section 3.5.5(4).
- (2) **Calculate surface area of probe; box 2 in FC1:** By assuming that the total probe surface area is identical for the cylindrical and spherical cases, the physical size of the LPW probe can be used to calculate the radius of the assumed spherical probe. The resulting radii of the cylindrical and spherical probes are thus different, and this difference is tracked in the fitting algorithm and following derivations by introducing the subscript  $j$ . Probe radius is denoted by the term  $r_{p,j}$ ; a purely cylindrical sheath is represented by  $j = 1$ ; a purely spherical sheath is represented by  $j = 2$ . Equation 3.6 is used to calculate the respective values of  $r_{p,1}$  and  $r_{p,2}$ :

$$A_p = 2\pi r_{p,1} L_p = 4\pi r_{p,2}^2 \quad (3.6)$$

The term  $L_p$  denotes the length of the probe, 0.408 m for LPW. For the cylindrical sheath case,  $r_{p,1} = 0.003175$  m (the actual radius of the LPW probe); for the spherical case,  $r_{p,2}$  is thus equal to 0.02546 m. Probe end effects are assumed negligible (as has typically been done with previous LP experiments) and these assumptions are discussed in Section 3.5.4.

- (3) **Calculate parameters associated with each electron population (Debye length and sheath radius); boxes 3, 4, 5 in FC1:** Boxes 3 through 9 in FC1 are repeated for each of the electron populations discussed in Section 3.4.1. These electron populations (spacecraft and probe photoelectrons, hot electrons, and the cold bulk population) have thermal velocities much greater than the spacecraft velocity at periapsis and so it is assumed that these electrons are collected isotropically across the probe surface. It is also assumed that each electron population is described by a unique electron density and temperature only; these are required inputs and are used to determine the Debye length,  $\lambda_D$ , for each population. For the following derivations, the cold, bulk electron population ( $I_e$ ) is used as an example. The derivations are identical for the other electron populations; the input values of electron density and temperature are the only things that change. The Debye length for each electron population is calculated using Equation 3.7:

$$\lambda_D = \sqrt{\frac{\epsilon_0 k_b T_e}{N_e e^2}} \quad (3.7)$$

Where  $\epsilon_0$  is the permittivity of free space,  $k_b$  is the Boltzmann constant,  $T_e$  is electron temperature in units of K,  $N_e$  is electron density in units of  $\text{m}^{-3}$ , and  $e$  is the elementary charge. The sheath radius (in units of m) is calculated using Equation 3.8. The minimum sheath radius is assumed to extend one Debye length from the surface of the probe; as probe potential increases, the sheath radius grows in size, dependent upon the temperature of the ambient population being considered.

$$r_{s,j} = \lambda_D \frac{eV_p}{k_b T_e} > (\lambda_D + r_{p,j}) \quad (3.8)$$

Where the subscript  $j$  again denotes the cylindrical ( $j = 1$ ) and spherical ( $j = 2$ ) sheath cases as discussed previously.  $V_p$  is the potential applied to the probe in units of volts, and  $r_{p,j}$  is the probe radius in units of meters. The ‘greater than’ symbol within Equation 3.8 means that the sheath radius is assumed equal to the larger of the two terms; thus, the minimum sheath radius is equal to one Debye length from the probe surface. Note that this derivation of sheath radius does not assume OML or sheath limited cases - the method allows for a transition between the two behaviors as it takes into account the local plasma environment through inclusion of  $\lambda_D$  and  $r_{p,j}$ .

- (4) **Calculate solid angle associated with electron population (box 6 in FC1):** A diagram representation of electron current collection by the probe is shown in Figure 3.10. Although the figure denotes the cross section of a cylindrical probe and sheath, similar arguments can be made for the spherical case that are discussed at the end of this bullet. I first deal with the cylindrical case, and as is typically done for cylindrical Langmuir probes, the probe is assumed infinitely long such that the third dimension can be integrated over and the problem reduced to two dimensions. The red circle represents the cross section of the probe of radius  $r_{p,j}$ . The outer green dashed circle represents a cross section of the sheath of radius  $r_{s,j}$ , in the orbit motion limited (OML) case where  $r_{s,j} \gg r_{p,j}$ . The blue dashed circle represents the sheath radius for the sheath limited case where  $r_{s,j} \not\gg r_{p,j}$ . The OML and sheath limited cases are described in Section 3.1. Considering the OML case first, suppose that an electron enters the sheath at point  $X_1$ , denoted by the black dot, with velocity  $v$ , denoted by the black arrow. If the probe is biased to positive potential  $\Phi$ , it will attract the electron; there is a certain range of trajectories that the electron can enter the sheath with such that this potential is large enough to draw the electron into the probe, depending upon its initial velocity. For each velocity, these trajectories lie within the solid

angle labelled  $\theta_j$ , which is subsequently a function of  $v$ . The yellow dashed line, labeled T, marks the most extreme attraction the electron can undergo and still be collected by the probe. This occurs at point X<sub>2</sub>, and it is important to note that at this point, the final electron velocity,  $v_2$ , is entirely in the  $v_y$  direction. The solid angle  $\theta_j$  is defined by Equation 3.9:

$$\sin\theta_j(v) = \frac{v_y}{v} = \frac{a_j}{r_{s,j}} \quad (3.9)$$

Where  $a_j$  is the impact parameter as labeled in the Figure, and  $\theta_j$  is a function of  $v$  and (as will be seen)  $\Phi$ . The value of  $\theta_j$  can be calculated using the conservation of energy and angular momentum of the electron at it's entry point on the sheath and point of collection at the probe:

$$\frac{1}{2}m_e v^2 + e\Phi = \frac{1}{2}m_e v_{2,y}^2 \quad (3.10)$$

$$r_{s,j}v_y = r_{p,j}v_{2,y} \quad (3.11)$$

Where  $v_y$  and  $v_{2,y}$  are the electron velocities (in units of  $\text{ms}^{-1}$ ) in the y direction at points X<sub>1</sub> and X<sub>2</sub> respectively;  $\Phi$  is the potential applied to the probe, and  $m_e$  is the electron mass (in units of kg).

Because  $v_{2,y} = v_2$  at point X<sub>2</sub>, Equation 3.10 can be rearranged to obtain an expression for  $v_2$ :

$$v_2 = \left( v^2 + \frac{2e\Phi}{m_e} \right)^{\frac{1}{2}} \quad (3.12)$$

The combination of Equations 3.9, 3.11 and 3.12 can be used to eliminate  $v_y$  and  $v_2$  to obtain an expression for  $\sin\theta_j(v, \Phi)$ , where it is seen that  $\theta_j$  is also a function of probe potential. The value of  $\theta_j$  can be obtained by taking the arcsin of Equation 3.13:

$$\sin\theta_j(v, \Phi) = \frac{r_{p,j}}{r_{s,j}} \frac{1}{v} \left( v^2 + \frac{2e\Phi}{m_e} \right)^{\frac{1}{2}} \quad (3.13)$$

Electrons with velocity  $v$  that enter the sheath outside of the solid angle  $\theta_j$  are not deflected enough to be collected by the probe. The same derivation can be carried out for the sheath limited case. Referring again to the cartoon Figure 3.10, the blue dashed circle (still labeled  $r_{s,j}$ ) represents a cross section of this much smaller sheath. The sheath limited regime means that  $r_{s,j}$  is almost equal to  $r_{p,j}$ ; the solid angle  $\theta_j$  will be larger and almost all of the electrons entering this much smaller sheath will be collected by the probe. Although not shown here so as not to overcomplicate the figure, the same arguments can be made and  $\theta_j$  calculated by use of Equation 3.13. I note again that  $\theta_j$  is a function of  $v$  and  $\Phi$ , and thus the attraction of electrons to, and the deflection of electrons away from, the probe are accounted for.

Although the spherical probe and sheath case must be dealt with in three dimensions, the expression for  $\theta_j$  in Equation 3.13 is also valid for this case and is discussed in bullet 6.

- (5) **Derive electron current collected by the probe (cylindrical case):** The derivation of the total electron current collected by the cylindrical probe is obtained by integrating the two dimensional electron distribution function, which is given by Equation 3.14:

$$f(v)_{2D} = n_e \left( \frac{m_e}{2\pi k_b T_e} \right) \exp \left( \frac{-m_e v^2}{2k_b T_e} \right) \quad (3.14)$$

The total electron current collected by the probe is obtained by integrating across all positive  $v_x$  velocities, as depicted in Figure 3.10. Because the electron thermal velocity is much greater than the MAVEN spacecraft velocity at periapsis, it is assumed that electron collection is isotropic across the surface of the probe and as such the contribution from the entire sheath is obtained by also integrating across the total sheath surface area:

$$I_{e,cyl}(v_x, v, \Phi, \theta_1) = \int_0^\infty 2qv_x v f(v)_{2D} \theta_1(v, \Phi) 2\pi r_{s,1} L_p dv \quad (3.15)$$

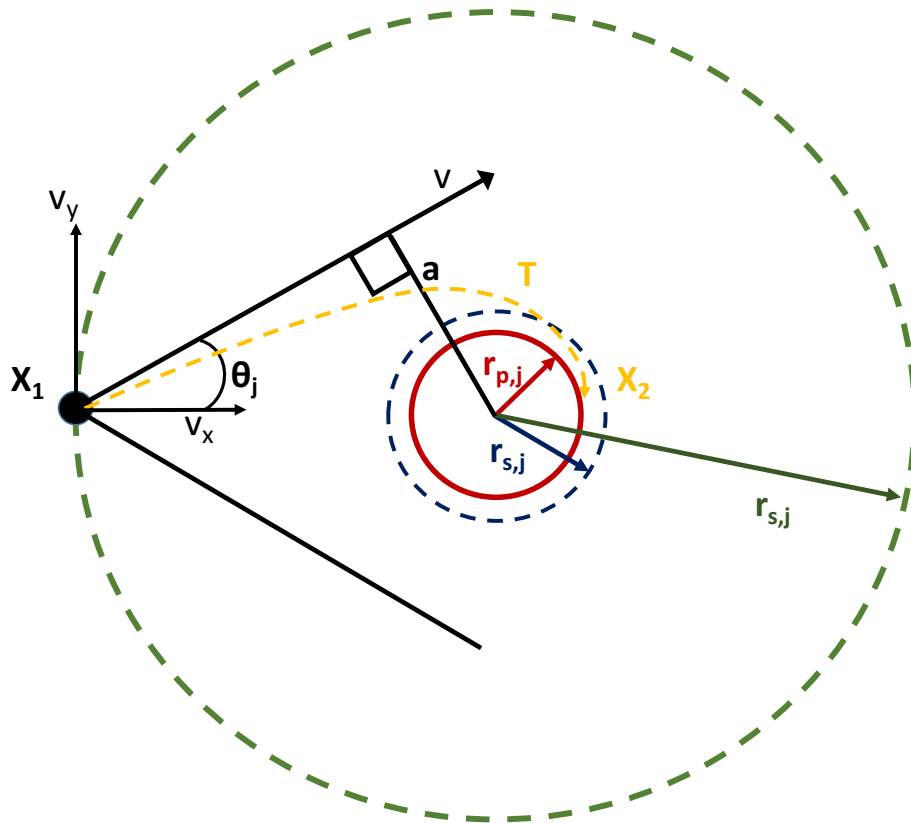


Figure 3.10: Cartoon representation of electron current collection by the LPW probes. The red circle marks the physical cross section of the probe; the blue and green dashed circles represent the sheath surface for the sheath limited and orbit motion limited cases respectively. The yellow dashed line marks the most extreme attraction an electron can undergo upon entering the sheath at point  $X_1$ , and still be collected by the probe, at point  $X_2$ . The parameter  $\theta_j$  shows the corresponding solid angle within which electrons are collected by the probe. Electron collection occurs from the entire sheath surface and so the contribution from point  $X_1$  must be integrated across the entire sheath surface area. More discussion is given in the main text.

The integral over the two dimensional distribution function,  $dv^2 = 2\pi v dv$ , has been replaced by  $2v\theta_1(v, \Phi)dv$ , because only electrons that lie within the solid angle  $2\theta_1$  will be collected by the probe, as depicted in Figure 3.10. The right most terms,  $2\pi r_{s,1}L_p$ , represent the surface area of the cylindrical sheath. Equation 3.9 is used to substitute for  $v_x$ , and the final expression for collected electron current for the cylindrical case is given by Equation 3.16. The numerical equivalent of this equation, and it's implementation within the LPW fitting algorithm, is discussed in bullet 7.

$$I_{e,cyl}(v, \Phi, \theta_1) = 4n_e q \left( \frac{m_e}{2\pi k_b T_e} \right) \pi r_{s,1} L_p \int_0^\infty v^2 \theta_1(v, \Phi) \cos \theta_1(v, \Phi) \exp \left( \frac{-m_e v^2}{2k_b T_e} \right) dv \quad (3.16)$$

- (6) **Derive electron current collected by the probe (spherical case):** Derivation of the collected electron current for the spherical probe and sheath case involves integration of the three dimensional electron distribution function, which is given by Equation 3.17:

$$f(v)_{3D} = n_e \left( \frac{m_e}{2\pi k_b T_e} \right)^{\frac{3}{2}} \exp \left( \frac{-m_e v^2}{2k_b T_e} \right) \quad (3.17)$$

The total electron current is again obtained by integrating across all positive  $v_x$  velocities, and the total sheath surface area:

$$I_{e,sph}(v_x, v, \Phi, \theta_2) = \int_0^\infty q v_x v^2 f(v)_{3D} 2\pi(1 - \cos \theta_2(v, \Phi)) 4\pi r_{s,2}^2 dv \quad (3.18)$$

The integral over the three dimensional distribution function,  $dv^3 = 4\pi v^2$ , has been replaced by  $2v^2\pi(1 - \cos \theta_2(v, \Phi))dv$ . In three dimensional velocity space, the solid angle  $\theta_2$  becomes a cone, whose end area, as projected onto the spherical velocity surface, is given by  $2\pi(1 - \cos \theta_2(v, \Phi))$ . The surface area of the spherical sheath is represented by the right most terms,  $4\pi r_{s,2}^2$ . Again, substituting for  $v_x$  using Equation 3.9 yields the final expression for the collected electron current for the spherical case:

$$I_{e,\text{sph}}(v, \Phi, \theta_2) = 8\pi^2 n_e q \left( \frac{m_e}{2\pi k_b T_e} \right)^{\frac{3}{2}} r_{s,2}^2 \int_0^\infty v^3 \cos\theta_2(v, \Phi) (1 - \cos\theta_2(v, \Phi)) \exp\left(\frac{-m_e v^2}{2k_b T_e}\right) dv \quad (3.19)$$

The numerical equivalent Equation 3.19, and its implementation within the LPW fitting algorithm, is also discussed in bullet 7.

(7) **Generate Maxwellian distribution function for a specific electron population;**

**box 7 in FC1; convert integrals to numerical solutions:** The final expressions for the total electron current collected by the cylindrical and spherical probe cases, as given in Equations 3.16 and 3.19, cannot be solved analytically. The LPW fitting algorithm thus solves numerical equivalents of these equations by generating a numerical distribution function for each electron population solved for. The numerical distribution function consists of  $N_v$  velocity steps and for the LPW fit procedure,  $N_v = 1000$ . This is chosen as a trade off between resolution in velocity space and the computational time taken to run the subsequent numerical integrations. Given an estimate of  $T_e$  as derived from boxes 8, 16 or 21 in FC2, Equation 3.20 is used to obtain the thermal velocity,  $v_{\text{th}}$ , of the population. A Maxwellian distribution function is then created for  $N_v$  velocities spanning  $0 < v < 10v_{\text{th}}$ , where the resolution in numerical velocity space is defined in Equation 3.21.

$$v_{\text{th}} = \sqrt{\frac{k_b T_e}{m_e}} \quad (3.20)$$

$$dv_n = \frac{10v_{\text{th}}}{N_v} \quad (3.21)$$

The two and three dimensional Maxwellian distribution functions are defined in Equations 3.14 and 3.17, and have been included explicitly in Equations 3.16 and 3.19. For the LPW fit algorithm,  $f(v)_{2D}$  and  $f(v)_{3D}$  are  $N_v = 1000$  element long arrays, corresponding to the 1000 values of  $v$  created.

Numerical equivalents to Equations 3.16 and 3.19 are given by Equations 3.22 and 3.23, where the integrals have now been replaced by summations over the numerical distribution function, and the value of  $\theta_j$  is calculated explicitly using Equation 3.13. These equations define the total electron current collected for a single probe potential  $\Phi$ ; for the case of LPW, there are 128 such potentials per I-V sweep.

$$I_{e,\text{cyl}}(v, \Phi, \theta_1) = 4n_e q \left( \frac{m_e}{2\pi k_b T_e} \right) \pi r_{s,1} L_p \sum_{v=0}^{N_v} v^2 \theta_1(v, \Phi) \cos \theta_1(v, \Phi) \exp \left( \frac{-m_e v^2}{2k_b T_e} \right) dv_n \quad (3.22)$$

$$I_{e,\text{sph}}(v, \Phi, \theta_2) = 8\pi^2 n_e q \left( \frac{m_e}{2\pi k_b T_e} \right)^{\frac{3}{2}} r_{s,2}^2 \sum_{v=0}^{N_v} v^3 \cos \theta_2(v, \Phi) (1 - \cos \theta_2(v, \Phi)) \exp \left( \frac{-m_e v^2}{2k_b T_e} \right) dv_n \quad (3.23)$$

- (8) **Calculate total electron current collected for a single electron population; boxes 8 and 9 in FC1:** The total electron current collected by the probe for a single electron population, shown in Equation 3.24, is a combination of the cylindrical and spherical contributions, as defined by Equations 3.22 and 3.23. Inclusion of the parameter  $\beta$  determines the relative contributions of each:

$$I_e(v, \Phi, \theta_j) = I_{e,\text{cyl}}^{2-2\beta} I_{e,\text{sph}}^{-1+2\beta} \quad (3.24)$$

It can be seen that for the two limiting cases of a cylindrical or spherical sheath we obtain the correct expression for  $I_e$ :

$$I_{e,\beta=\frac{1}{2}} = I_{e,\text{cyl}}^1 I_{e,\text{sph}}^0 \quad (3.25)$$

$$I_{e,\beta=1} = I_{e,\text{cyl}}^0 I_{e,\text{sph}}^1 \quad (3.26)$$

- (9) **Calculate total electron current collected from all electron populations; box 10 in FC1:** By repeating steps 4 through 8 for each of the electron populations described in Section 3.4.1, the total electron current collected by the probe, as a function of probe potential, is calculated using Equation 3.27:

$$I_{\text{total,e}} = I_e + I_{\text{pe}} + I_{\text{spe}} + I_{\text{hot}} \quad (3.27)$$

An individual LPW I-V sweep consists of 128 potential steps and as such, each of the terms in Equation 3.27, including  $I_{\text{total,e}}$ , is a 128 element long array. Note, that because the spacecraft and probe photoelectron density and temperatures are not varied within the LPW fitting algorithm, their respective currents ( $I_{\text{spe}}$  and  $I_{\text{pe}}$ ) are assumed constant within each I-V curve, but are still calculated using Equation 3.24. Once boxes 4, 5 and 6 have been processed in FC2, only the  $I_e$  and  $I_{\text{hot}}$  terms are varied in Equation 3.27, in order to obtain the best fit.

### 3.5.2 Derivation of the numerically integrated ion current

The ion current collected by the probe is calculated in a similar fashion to the electron current, with the major alterations that 1) the ion thermal velocity is much less than the MAVEN spacecraft velocity at periapsis, and 2) only a single ion species is assumed present, described by an average ion mass. Further discussion of the impacts of assuming a single, average ion mass are given in Section 3.5.5.3(5). The following derivation uses the ion current,  $I_{\text{ion}}$ , as the example.

- (1) **Calculate spacecraft velocity and ion impact parameter; boxes 11 and 12 in FC1:** MAVEN's periapsis velocity is about 4 kms<sup>-1</sup>; an O<sup>+</sup> ion at temperature 300 K has a thermal velocity of about 400 ms<sup>-1</sup>. Subsequently, ion collection occurs primarily on the side of the probe facing the velocity direction of the spacecraft; the probe can be thought of as sweeping through a sea of essentially stationary ions, an effect known as the ram effect. Because the LPW probes are mounted at an angle to the spacecraft body they are incident

to this stationary sea of ions at some angle of attack that depends upon the spacecraft orientation at the time of measurement. This angle of attack is depicted in Figure 3.3. The relative velocity between ions and the probe is defined by:

$$V_{sc} = V_{sc,abs} \cdot \sin\theta_{sc} \quad (3.28)$$

Where  $V_{sc,abs}$  is the absolute MAVEN spacecraft velocity and  $\theta_{sc}$  is the angle of attack between the LP probe surface and incident ions. The cartoon depiction of this ion current collection is shown in Figure 3.11. The red circle again depicts a cross section of the probe of radius  $r_{p,j}$  which is now moving with velocity  $V_{sc}$  in the direction indicated by the blue arrow. In the probe frame of reference, ions appear to flow in the opposite direction, as marked by the black arrows. The large green dashed circle shows the sheath at radius  $r_{s,j}$ . As for the electron case, the following derivation method does not assume OML or sheath limited conditions but rather allows transitional behavior to occur. Because of this, only one sheath radius is shown in Figure 3.11. Ions are still attracted to or repelled by the probe (depending on the potential applied to the probe) but the resulting deflection is much less than that for electrons due to the greater ion mass, and the large relative velocity between the spacecraft and the ions. The maximum attraction an ion can undergo upon entering the sheath, and still be collected by the probe, is depicted by the dashed yellow trajectory labeled T in the figure. It can be seen that ions entering the sheath between the two crosses marked  $X_1$  will be collected by the probe at point  $X_2$ . The resulting impact parameter is labeled  $a_j$  in the figure; unlike for electron current collection, we do not integrate about the entire surface area of the sheath - the large value of  $V_{sc}$  means that only ions entering between the two  $X_1$  points will be collected by the probe.

The conservation of energy and angular momentum can also be used to derive the impact parameter for both the cylindrical and spherical cases; Equations 3.29 and 3.30 can be used to eliminate  $v_2$ , obtaining an expression for  $a_j$ :

$$\frac{1}{2}m_i V_{sc}^2 + q\Phi = \frac{1}{2}m_i v_2^2 \quad (3.29)$$

$$a_j V_{sc} = r_{p,j} v_2 \quad (3.30)$$

$$a_j(\Phi) = \frac{r_{p,j}}{V_{sc}} \left( V_{sc}^2 + \frac{2q\Phi}{m_i} \right)^{\frac{1}{2}} \quad (3.31)$$

Where  $m_i$  is the average ion mass in units of kg;  $v_2$  is the ion velocity at point X<sub>2</sub> in Figure 3.11;  $q$  is the ion charge;  $\Phi$  is the potential applied to the probe; and  $r_{s,j}$  is the sheath radius, as determined using Equation 3.8. All velocities are in units of ms<sup>-1</sup>. Equation 3.31 is a function of probe potential  $\Phi$  and thus the attraction and repulsion of ions to the probe is accounted for. The ion temperature  $T_i$  and resulting ion thermal velocity have been assumed negligible compared to the spacecraft velocity.

- (2) **Calculate ion current collected per unit sheath area; box 13 in FC1:** Multiplication of the area that  $a_j$  projects onto the sheath surface, with the current density per unit area at the sheath, provides the total ion current collected by the probe. The current density at the sheath is assumed to be the current density of the ambient plasma. The ion current collected per unit area for the cylindrical and spherical sheath cases is calculated using Equations 3.32 and 3.33 respectively. These equations approximate current collection under the ram dominated flow:

$$J_{i,cyl}(N_i, V_{sc}, T_i, m_i, q) = -qN_i V_{sc} - \pi q N_i \sqrt{\frac{qT_i}{2\pi m_i}} \exp\left(\frac{-m_i V_{sc}^2}{2qT_i}\right) \quad (3.32)$$

$$J_{i,sph}(N_i, V_{sc}, T_i, m_i, q) = -qN_i V_{sc} - 4qN_i \sqrt{\frac{qT_i}{2\pi m_i}} \exp\left(\frac{-m_i V_{sc}^2}{2qT_i}\right) \quad (3.33)$$

Where  $N_i$  is the ion density in units of m<sup>-3</sup>, and  $T_i$  is assumed equal to  $T_e$  (in units of K). It is assumed that in the probe frame of reference, all ions travel at  $V_{sc}$  and so unlike

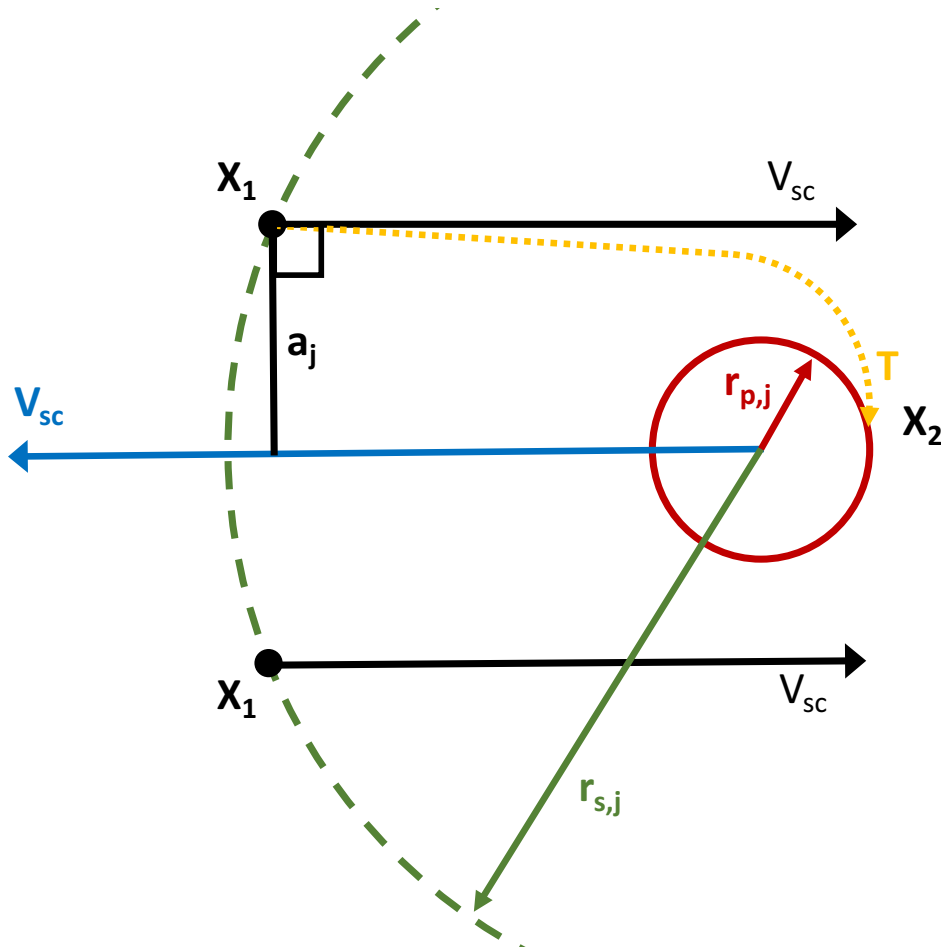


Figure 3.11: Cartoon representation of ion current collection by the LPW probes. The red circle marks the physical cross section of the probe; the dashed green line marks the sheath surface. The spacecraft velocity is much greater than the ion thermal speed at periapsis and so ions are collected purely from the RAM direction, denoted by the blue arrow. In the probe frame of reference, ions travel at the spacecraft velocity as marked by the black arrows. The yellow dashed line marks the most extreme deflection an ion can undergo upon entering the sheath at point  $X_1$ , and still be collected by the probe, at point  $X_2$ . Due to the large spacecraft velocity, ion collection occurs only between the two points labeled  $X_1$ , corresponding to the impact parameter  $2a_j$ . More discussion is given in the main text.

for electrons, an ion distribution function is not required - the single value of  $V_{sc}$  is used. The first terms in Equations 3.32 and 3.33 represent ram current collection per unit area of the forward facing probe surface. The second terms are empirical approximations to ion current collected at small, positive voltages, where ion current starts to be repelled from the probes.

- (3) **Calculate total ion current; boxes 13 and 14 in FC1:** The total ion current collected is calculated using Equations 3.34 and 3.35. As for electron current collection,  $I_{cyl,i}$  and  $I_{sph,i}$  are 128 element long arrays, representing the 128 potential steps in a single LPW I-V sweep:

$$I_{i,cyl} = J_{cyl} 2a_j L_s \quad (3.34)$$

$$I_{i,sph} = J_{sph} \pi a_j^2 \quad (3.35)$$

The respective contributions from the cylindrical and spherical terms are again obtained during the fitting process, where  $\beta$  has the same value as for the electrons, as obtained in Equation 3.24. Note that unlike for the electron current, we assume only a single ion population and the total ion current collected by the probe,  $I_{total,i}$ , is given by Equation 3.36:

$$I_{total,i} = I_{cyl,i}^{(2-2\beta)} I_{sph,i}^{(-1+2\beta)} \quad (3.36)$$

### 3.5.3 Total numerically integrated current

The total numerically integrated current collected by the probe is calculated by summing the total electron and ion currents, using Equation 3.37. This final step occurs in box 15 in FC1. Each of the terms  $I_{total,e}$  and  $I_{total,i}$  is a 128 element long array, representing the 128 potential

steps within an LPW I-V sweep. As such,  $I_{\text{total}}$  is also 128 elements long and a function of probe potential:

$$I_{\text{total}} = I_{\text{total,e}} + I_{\text{total,i}} \quad (3.37)$$

### 3.5.4 Probe end effects

The derivation of the collected electron and ion currents described above assumed that the cylindrical probe is infinitely long. The derivation of the cylindrical sheath area does not take into account end effects: current that can be collected at both ends of the cylindrical probe. This is a common assumption made in Langmuir probe theory (see the afore cited review articles) and leads to negligible errors when  $L_p \gg r_p$  during sheath limited conditions. Given the LPW sensor dimensions (40 cm by 0.635 cm), we expect this end current contribution to be negligible even under larger Debye length conditions. The stub and guard electronics are designed to prevent current collection at the end of the sensor attached to the boom, as discussed in Section 3.4.3.7, and so only the outward pointing end of the probe is susceptible to current collection.

Probe end effects tend to affect ion current collection to a greater extent than electron current collection, due to the non-isotropic nature of ion current collection over the probe surface. If the probe is flying such that its length is almost parallel to the spacecraft velocity (or ram) direction, the probe end is in fact the primary collection area for ions. Electrons are collected over the entire probe surface area. As depicted in Figure 3.3, the MAVEN spacecraft flies in an orientation at periapsis such that the probes are typically at an angle of  $\sim 45^\circ$  to the ram direction so that end effects are not significant for ion current collection. Although thought to be small, we note that these contributions are a source of error in the LPW fit algorithm.

### 3.5.5 Implementation of the LPW fit algorithm

The LPW fit algorithm is split into two main parts: firstly, initial estimates of key parameters are made by the analysis of certain regions of the measured I-V curve. The second part of

the algorithm refines these initial estimates and several other quantities in order to optimize the overall fit between the numerically integrated and measured I-V curves, based on the local plasma environment. A flow chart summarizing the LPW fit algorithm is shown in Figure 3.12, referred to as flow chart 2 (FC2) in the text. Numbers to the left of each box are again used as references within the main text.

#### **3.5.5.1 Data acquisition and calibration**

The measured I-V curves are calibrated during ground processing prior to detailed analysis. An important calibration step is the correction for changes in spacecraft potential during the measurement of a single I-V sweep. Ideally, spacecraft potential remains constant throughout the duration of each I-V sweep, so that the grounding of the LPW probe bias with respect to the ambient plasma also remains constant (probe potentials are applied with respect to the spacecraft, not the ambient plasma). If the spacecraft potential varies, so does this grounding level. When the grounding level changes, the potential felt by the ambient plasma due to the biased LPW probe also changes. One advantage of flying multiple Langmuir probes on a single spacecraft is that as one probe performs an I-V sweep, a second probe can monitor the spacecraft potential, and this happens with the LPW probes. This enables variations in spacecraft potential within I-V sweep measurements to be accounted for. Calibration at this stage also monitors and accounts for leakage currents due to aging components. Instrument dependent variations in gain are also accounted for.

The analysis of each I-V curve requires ancillary information such as spacecraft position, orientation, and velocity. I developed software that utilizes this ancillary information to generate look up tables that determine 1) the percentage of boom and probe surfaces that are in sunlight; 2) the angle of incidence sunlight strikes the boom and probe surfaces; and 3) the angle of attack between the probe surfaces and ionospheric ions. These parameters are shown in Figure 3.3. The ancillary information is obtained from the NASA Navigation and Ancillary Information Facility (NAIF).

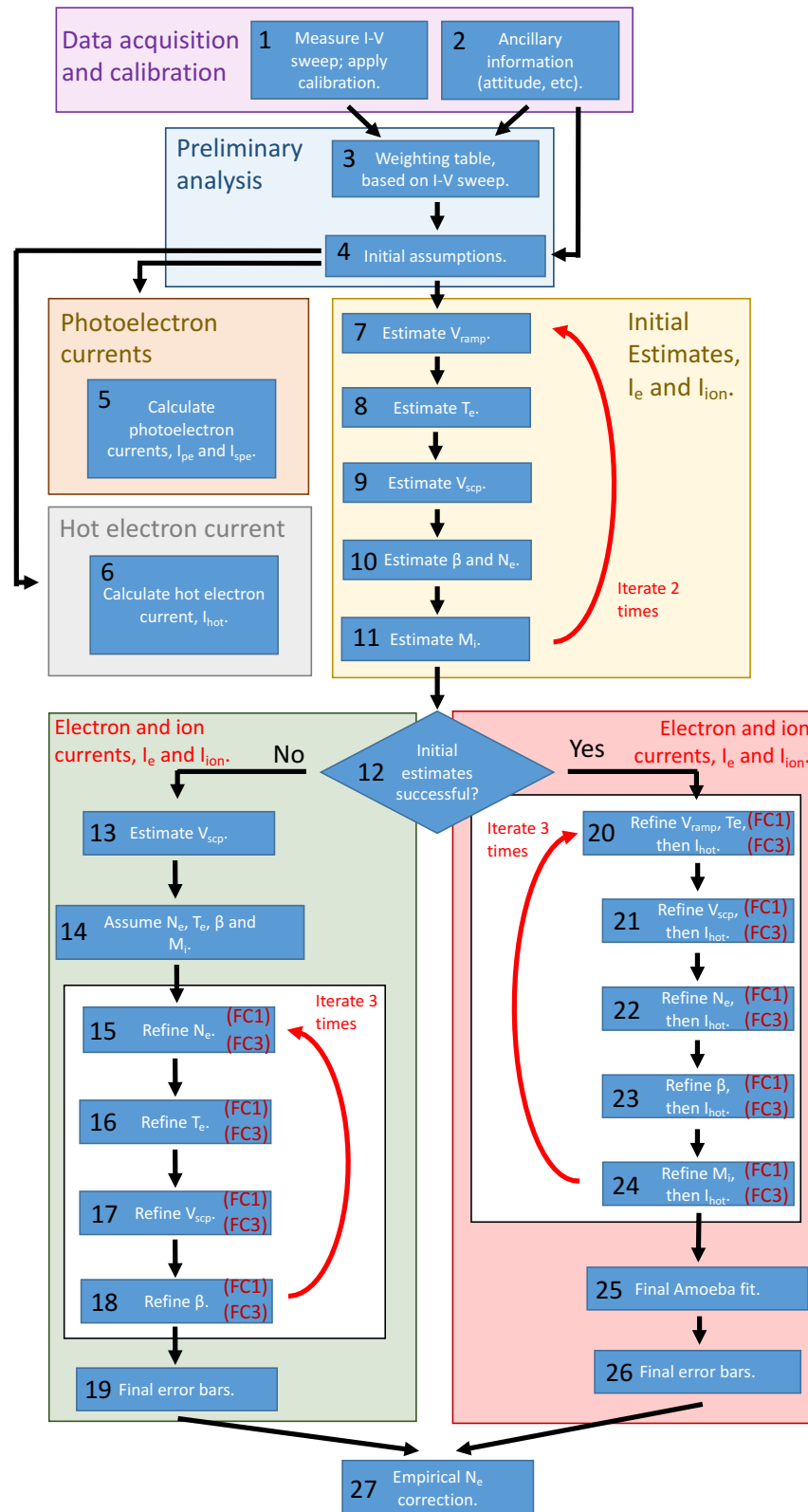


Figure 3.12: **Flow chart 2 (FC2)**: Flow chart summarizing the LPW fit algorithm. Detailed discussion is given of each stage within the main text and is referenced using the numbers to the left in each box.

### 3.5.5.2 Preliminary analysis

Preliminary analysis of each individual I-V curve is used to obtain several parameters that remain constant throughout the remainder of the fitting algorithm. Preliminary analysis occurs in boxes 3, 4, 5 and 6 of FC2. The LPW fit algorithm utilizes a weighting table to balance the relative contributions from the electron and ion sides of the measured I-V curve. The weighting table is designed to prevent the electron side dominating the fitting algorithm; this arises because the collected electron current is typically a few orders of magnitude greater than the collected ion current.

The weighting function is described by Equation 3.38 and the subsequent weighting table for the measured I-V sweep shown in Figure 3.7, is shown in Figure 3.13. The solid green and red, and dashed red, vertical lines show the parameters  $V_{\text{ramp}}$ ,  $V_{\text{scp}}$ , and the upper and lower bounds of  $V_{\text{scp}}$ , respectively. These parameters are discussed in detail in Sections 3.5.5.3(1) and 3.5.5.3(3).

$$W_{\text{swp},i} = \frac{I_{\text{max}} - I_{\text{data},i}}{I_{\text{max}}} \quad (3.38)$$

Where  $I_{\text{max}}$  is the maximum current measured for the I-V sweep being analyzed;  $I_{\text{data},i}$  is the measured current as a function of probe potential and  $i$  represents each of the 128 potential steps within one LPW I-V sweep. Equation 3.38 is applied to all I-V curves regardless of plasma conditions and spacecraft attitude, etc.

Further preliminary analysis involves calculating the photoelectron currents collected by the probe, in box 5 of FC2. This is achieved with the use of spacecraft ancillary data, such as spacecraft attitude and position. The intensity of EUV light reaching the spacecraft and booms is calculated assuming the neutral atmosphere model that is described in Section 3.4.1.1. Spacecraft and boom photoelectrons ( $I_{\text{spe}}$ ) are assigned an empirically determined constant temperature of 2.7 eV; probe photoelectrons ( $I_{\text{pe}}$ ) are also assigned a constant temperature of 2.7 eV that is determined from the surface properties of the LPW probes. The densities of these photoelectron populations are determined empirically as a function of EUV light intensity, as discussed in Section 3.4.1. The

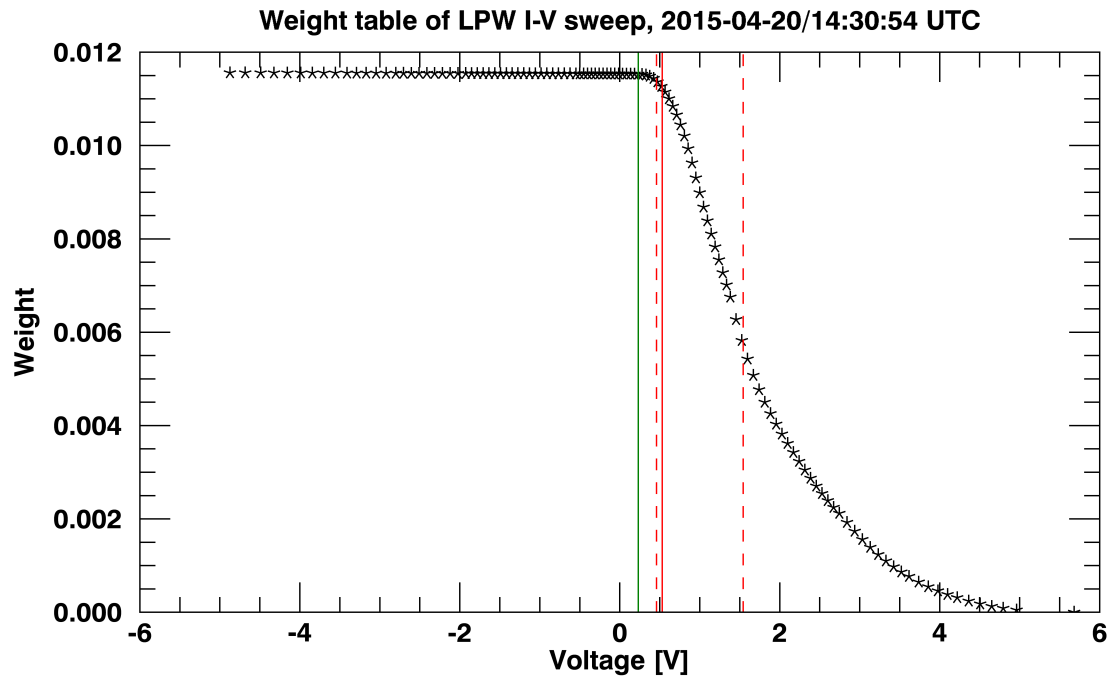


Figure 3.13: The weighting table corresponding to the I-V curve shown in Figure 3.7, used by the LPW fit software during the derivation of various parameters for this I-V curve. The horizontal axis is probe potential with respect to the spacecraft ground. The weighting table takes into account the fact that electron currents can be several orders of magnitude than collected ion currents, and prevents the electron side of the I-V curve from dominating the fit algorithm. The vertical lines mark  $V_{\text{ramp}}$ ,  $V_{\text{scp}}$ ; and the lower and upper bounds on  $V_{\text{scp}}$ , as described in Sections 3.5.5.3(1) and 3.5.5.3(3)

densities and temperatures for  $I_{\text{spe}}$  and  $I_{\text{pe}}$  are constant once set and are not allowed to vary within the LPW fitting algorithm.

An initial estimate of the hot electron population is also calculated during preliminary analysis, in box 6 of FC2. This population is assigned an empirically determined, fixed temperature of 24 eV. An initial density is assumed of  $4 \text{ cm}^{-3}$  and this is allowed to vary within the fitting algorithm; it is refined in boxes 20 - 24 in FC2. I remind the reader that the hot electron population is essentially an offset within the measured I-V curve due to its high temperature compared to the probe sweep range and the cold electron temperature, as discussed in Section 3.4.1.

### 3.5.5.3 LPW initial estimates

Initial estimates are achieved via the analysis of individual regions of each I-V curve. Boxes 7 - 11 in FC2 deal with these initial estimates: the probe potential at the point of transition from the ion current collection region, into the  $T_e$  fit region, is marked by  $V_{\text{ramp}}$ ; the spacecraft potential is denoted by  $V_{\text{scp}}$ ; the entire  $T_e$  fit region is identified; the parameter  $\beta$  is calculated; and an estimate of average ion mass  $M_i$  is obtained. These processes are detailed in this sub-section.

- (1) **Estimate  $V_{\text{ramp}}$ ; box 7 in FC2:** The parameter  $V_{\text{ramp}}$  is crucial to determining the electron temperature and spacecraft potential; it marks the region at which the measured I-V curve transitions from the ion current collection region into the  $T_e$  fit region. A zoom in of the I-V curve region surrounding  $V_{\text{ramp}}$  for the I-V curve shown in Figure 3.7, is presented in Figure 3.14. A straight line fit is performed on the most negative  $\frac{1}{3}$  of the I-V sweep, corresponding to the ion current collection region. The blue data points in Figure 3.14 show some of the points used in this fit (note that the horizontal axis does not span the entire ion fit region); the blue line shows the resulting fit.  $V_{\text{ramp}}$  is the point at which five consecutive data points show both ascending current values, and are greater in value than the blue fit line by at least three times the standard deviation of the data comprising the lower  $\frac{1}{3}$  I-V sweep.  $V_{\text{ramp}}$  is marked by the vertical green line in the Figures 3.13 and

3.14; the subsequent six green data points are used to estimate  $T_e$ , as discussed in the next bullet point.

- (2) **Estimate  $T_e$ ; box 8 in FC2:** Estimation of  $T_e$  is performed using several methods such that a best estimate with lower and upper bounds can be obtained using the six data points shown in green in Figure 3.14. Within the  $T_e$  fit region, current  $I$  is expected to be linearly proportional to the exponential of voltage,  $\exp(\frac{v}{T_e})$ , for cylindrical (and spherical) probes, assuming other sources of current are negligible, as discussed in Section 3.3. Thus, to obtain a first estimate of  $T_e$ , the first six data points only within the  $T_e$  fit region are used, for several reasons. Additional current sources are present within the LPW measured I-V curves, including the photoelectron and ion currents. These are not yet accounted for and so a simple first estimate is adequate at this stage. Second, contamination of the I-V curve from atomic oxygen exposure is thought to systematically increase derived  $T_e$  from higher voltage regions of the  $T_e$  fit region, as discussed in Section 3.5.6. Later refinement of  $T_e$  takes into account additional current sources, and utilizes a greater number of data points, as discussed in Section 3.5.5.4.

A zoom in of the green data points shown in Figure 3.14 are presented in Figure 3.15. Note that the vertical axis now shows the natural log of the measured current values and they are  $\sim$  linearly proportional to voltage, as expected in the  $T_e$  fit region. The black error bars show a 10 nA measurement uncertainty on each data point. The green line shows the fit described in the first bullet below. The red and blue lines show how this fit would change if  $T_e$  was varied by 20%. Thus, derivations of  $T_e$  to less than 20% are easily achievable assuming that measurement error is the only source of noise. Further sources of error are present and are discussed in Section 3.5.6, but typically the uncertainty in derived  $T_e$  is less than 20%.

- The first estimate of  $T_e$  is the simplest and is derived from a linear analytical difference straight line fit to the natural log current values of all six  $T_e$  fit points shown in green

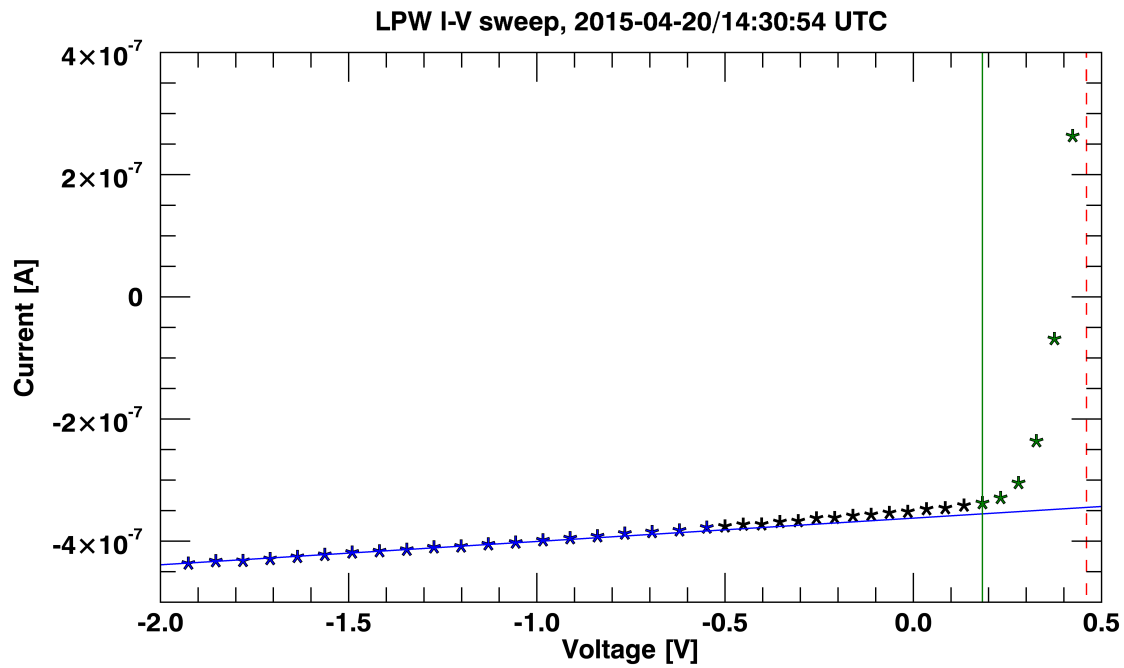


Figure 3.14: Zoom in of the  $V_{\text{ramp}}$  region. The blue line is a straight line fit to the blue ion side data (note the horizontal axis does not cover the entire ion current range); the green vertical line marks  $V_{\text{ramp}}$ , the transition into the  $T_e$  fit region. The first six data points within the  $T_e$  fit region (marked in green) are used to determine the initial estimate of  $T_e$ . The red dashed vertical line marks the lower limit to spacecraft potential, as calculated in bullet 3.

in Figure 3.14. This fit is shown as the green line in Figure 3.15.  $T_e$  is equal to the inverse value of the gradient of this fit; the natural log of Equation 3.3, for example, yields a straight line with gradient equal to  $\frac{e}{kT_e}$ . The derived value of  $T_e$  from this fit is labeled ' $T_e \text{ lad}$ ' in Figure 3.15. The red and blue lines in the figure show the corresponding fits when temperature is increased and decreased by 20%, respectively.

- A second estimate of  $T_e$  is obtained by fitting a straight line to neighboring pairs of points shown in Figure 3.15. The inverse of the gradient of each fit line again provides  $T_e$  and this method yields five 'sub values' of  $T_e$  (five neighboring pairs are possible from six data points). The statistical median of these five temperature values is used to obtain a second estimate of  $T_e$ , labeled ' $T_e \text{ med}$ ' in the figure. The smallest and largest temperatures derived from these five pairs of points are used as the lower and upper bounds for  $T_e$ , labeled ' $T_e \text{ low}$ ' and ' $T_e \text{ high}$ ' in the figure.
- A 'best estimate' of  $T_e$  is obtained from a weighted average of  $T_e \text{ lad}$  and  $T_e \text{ med}$ , and by taking into account  $T_e \text{ low}$  and  $T_e \text{ high}$ . The weightings depend on how well the data fit a straight line in each fit case; this best estimate is labeled ' $T_e \text{ best}$ ' in Figure 3.15.

- (3) **Estimate spacecraft potential; box 9 in FC2:** As discussed in Section 3.3, an estimate of spacecraft potential for cylindrical Langmuir probes can be obtained by searching for a peak in the derivative of the measured I-V curve. This method assumes no other sources of current are present; this is not true during this stage of the analysis as photoelectron and ion currents have not been removed from the measured I-V curve. Later refinements of spacecraft potential do account for such current sources.

The derivative of the I-V curve shown in Figure 3.7, is shown in Figure 3.16, where the symbol and color scheme is the same as for Figures 3.13, 3.15 and 3.17. The black data points show the derivative of the measured LPW I-V curve. Although an estimate for

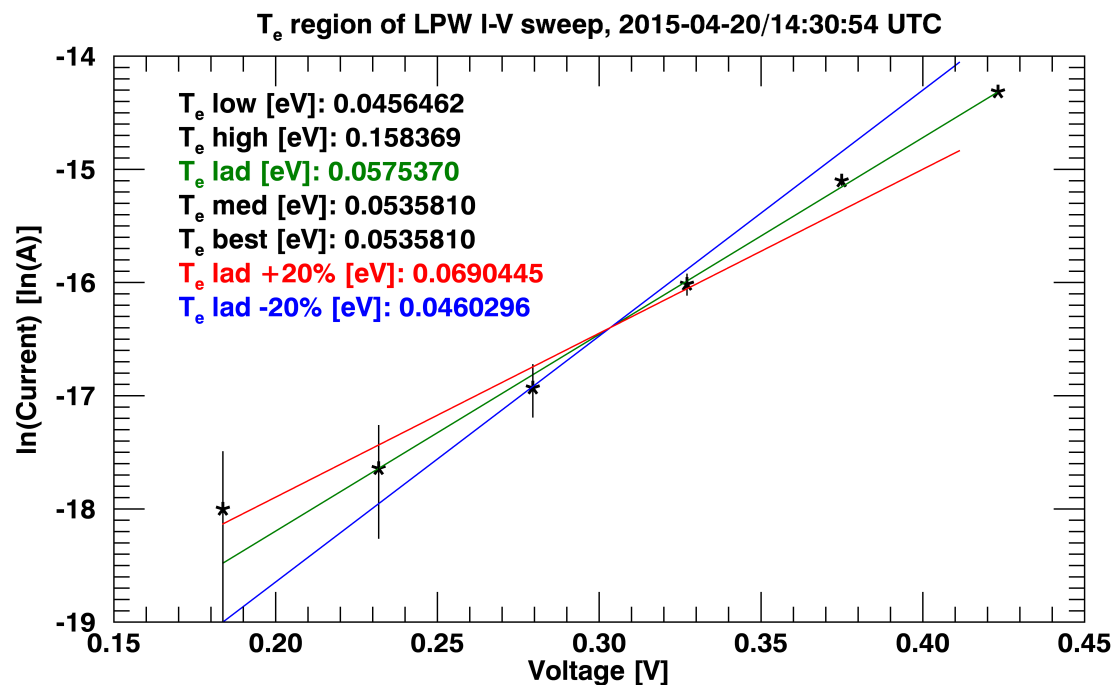


Figure 3.15: The six green data points from Figure 3.14 are plotted here and used to obtain an initial estimate of  $T_e$ . The natural log of measured current (shown on the vertical axis) is linearly proportional to probe potential within the  $T_e$  fit region; the green line shows a linear absolute difference fit to these data. The inverse of the gradient of this line is equal to  $T_e$ . Several estimates of  $T_e$  are obtained from these data; the values noted in the figure are described in the main text. The red and blue lines show how the green fit varies when  $T_e$  is increased or decreased by 20%, respectively.

density has not yet been made, the derivative of the theoretical electron current is shown by the purple line in the Figure after this fact, divided by a factor of 2, so that it can be displayed on the same figure, to aid in this discussion. For the purple curve presented, there is a clear peak at about 0.6 V; the measured derivative curve in black shows significantly different behavior. In particular, for this case, two peaks are observed at about 1 V and 1.5 V, and neither of these represent the true spacecraft potential (marked by the solid red line in the figure). The peak in the theoretical purple curve lies close to the true spacecraft potential; the small offset is likely because photoelectron and ion currents have not yet been taken in to account. The large disparities between the black and purple lines are due to atomic oxygen contamination of the Langmuir probes, as discussed in Section 3.5.6. The contamination is thought to distort the upper part of the  $T_e$  fit region, leading to these observed differences.

The presence of multiple peaks in the black curve leads to difficulties in determining  $V_{scp}$ ; the shape and number of peaks observed in the black line vary from I-V curve to I-V curve and therefore this section of the LPW fitting algorithm was developed to take this behavior into account. The algorithm places an upper bound to  $V_{scp}$  at the point of the right most peak in voltage space; a lower bound is placed five  $T_e$  above  $V_{ramp}$  (this lower bound was determined empirically). These lower and upper bounds are represented by the red dashed vertical lines in Figures 3.13, 3.14 and 3.16. Once lower and upper bounds have been defined, a first estimate of  $V_{scp}$  is produced from a weighted average of these bounds; the weighting takes into account the values of  $V_{ramp}$ ,  $T_e$ , the number of peaks found in the derivative curve, and their distance in voltage space from  $V_{ramp}$ .

I also bring to attention here the dip observed in the purple line at around 1 V. This dip should not be present in the theoretical derivative of the electron current and it is the result of incorrect sheath size assumption and calculation when deriving the numerically integrated electron current. This point is discussed in more detail in Section 3.5.6.

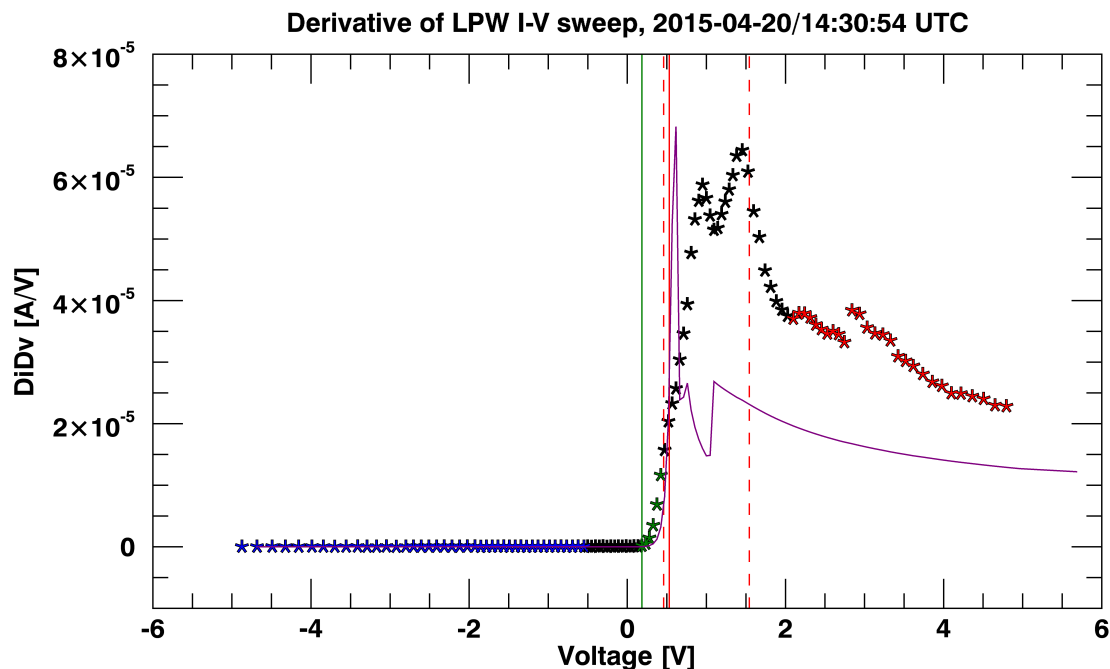


Figure 3.16: Derivative of the measure I-V curve shown in Figure 3.7 (black data points). The blue data points are used to determine  $V_{\text{ramp}}$  which is marked by the green vertical line. The six green data points are used to determine an initial estimate of  $T_e$ . The red data points mark the points used to determine the parameter  $\beta$  which is described in the main text. The purple line shows a theoretical derivative of electron current for this I-V sweep, divided by a factor of 2 so that it fits on the same plot. For ideal Langmuir probe behavior there is only one major peak in the derivative of measured current as seen in the purple line and this marks the location of  $V_{\text{scp}}$ . Atomic oxygen contamination of the probe surfaces, as discussed in *Ergun et al. (2015a)*, causes in some cases multiple peaks to be observed, complicating the derivation of  $V_{\text{scp}}$ . The solid red line marks an initial estimate of  $V_{\text{scp}}$ ; the two dashed red vertical lines mark the initial lower and upper bounds to  $V_{\text{scp}}$ .

(4) **Estimate  $\beta$  and  $N_e$ ; box 10 in FC2:** The parameter  $\beta$  quantifies whether the probe sheath behaves as a cylinder or sphere. It is derived from the electron collection region of the measured I-V sweep using data points that lie at voltages greater than  $V_{\text{scp,upp}} + 10.T_e$ , where  $V_{\text{scp,upp}}$  is the upper limit to spacecraft potential derived previously. A minimum of eight data points are required and the right most eight data points are always used regardless of how close to  $V_{\text{scp,upp}}$  they lie (the right most 3-4 points are not used as these sometimes show instrumental effects during mode changes). Under ordinary dayside periapsis conditions, 20 - 25 points typically satisfy the above criterion. The data points used to estimate  $\beta$  in Figure 3.7 are shown in red in Figures 3.16 and 3.17. Figure 3.17 shows the entire measured I-V curve for this example, and highlights the data points used to derive the various aforementioned quantities in their respective colors.

An expression for  $\beta$  is given by Equation 3.39; the full derivation of this is presented in Appendix C. This expression for  $\beta$  is used in box 10 of FC2.

$$\beta \approx \frac{dI_e}{d\Phi} \frac{\Phi}{I_e} \quad (3.39)$$

$\Phi$  is equivalent to the potential  $V_p$  of the measured I-V curve and hence all parameters in Equation 3.39 are measured during an I-V sweep:  $\Phi$  is the voltage at each sweep step;  $I_e$  is the measured electron current as a function of  $\Phi$ , and  $\frac{dI_e}{d\Phi}$  can be calculated from the measured I-V sweep. This expression for  $\beta$  assumes that the probe potential  $\Phi \gg T_e$  and that saturation of the electron current is not present. The shape of the I-V curve thus described by  $\beta$  is independent of density, temperature and spacecraft potential.

The evaluation of many individual LPW measured I-V curves under different plasma conditions demonstrates both theoretical cylindrical and spherical sheath responses in the LPW data set. An example of this change in sheath behavior is presented in Figure 3.18. The data are taken from the same inbound pass, spanning low to high (red to black) densities, where the black line is the I-V curve presented in Figure 3.7. Each curve is scaled by the

factors noted in the figure so that all five curves can be shown on the same plot (as density decreases with increasing altitude, collected current decreases, leading to the noted scaling factors). The figure focuses on the electron side of the I-V curve, and it can be seen that the shapes of the upper ends of these curves vary with altitude. As can be seen, the theoretical response is correlated to the Debye length of the plasma,  $\sqrt{\frac{T_e}{N_e}}$ .

A statistical analysis of a weeks worth of LPW I-V curves is shown in Figure 3.19. Data are taken from a MAVEN deep dip campaign, spanning dates 2015-04-17 UTC through 2015-04-23 UTC, which includes 38 periapsis passes, or just over 12,000 data points. The colorbar again references altitude, and covers the same range as the colorbar shown in Figure 3.18 so that direct comparison can be made between the two figures. Each data point represents a single LPW I-V sweep. The horizontal axis shows  $\lambda_D$ , calculated using the derived values of  $N_e$  and  $T_e$  for each individual I-V sweep; the vertical axis shows the corresponding value of  $\beta$  derived for each I-V sweep. Cylindrical behavior occurs when  $\beta = 0.5$  and spherical behavior occurs when  $\beta = 1$ . The figure clearly shows that as altitude decreases,  $\lambda_D$  decreases by several orders of magnitude and  $\beta$  approaches 0.5. Further discussion of this is provided in Section 3.5.6.2.

An initial estimate of electron density is obtained using Equation 3.40. The same data points used to derive  $\beta$  (the electron collection region) are used here. The derivation of Equation 3.40 is found in Appendix C. This equation is used to estimate  $N_e$  in box 10 of FC2.

$$I_e \approx A.n_e.e \left( \frac{T_e}{2\pi m_e} \right)^{\frac{1}{2}} \left( 1 + \frac{\Phi}{T_e} \right)^{\beta} \quad (3.40)$$

- (5) **Estimate  $M_i$ ; box 11 in FC2:** The final variable to be estimated is the average ion mass,  $M_i$ .  $M_i$  is initially assumed to be 16 AMU,  $O^+$ . An iterative procedure is used to improve this initial assumption by analyzing the ion side of the measured I-V curve. The numerical ion current is determined using Equation 3.36; all input parameters for this

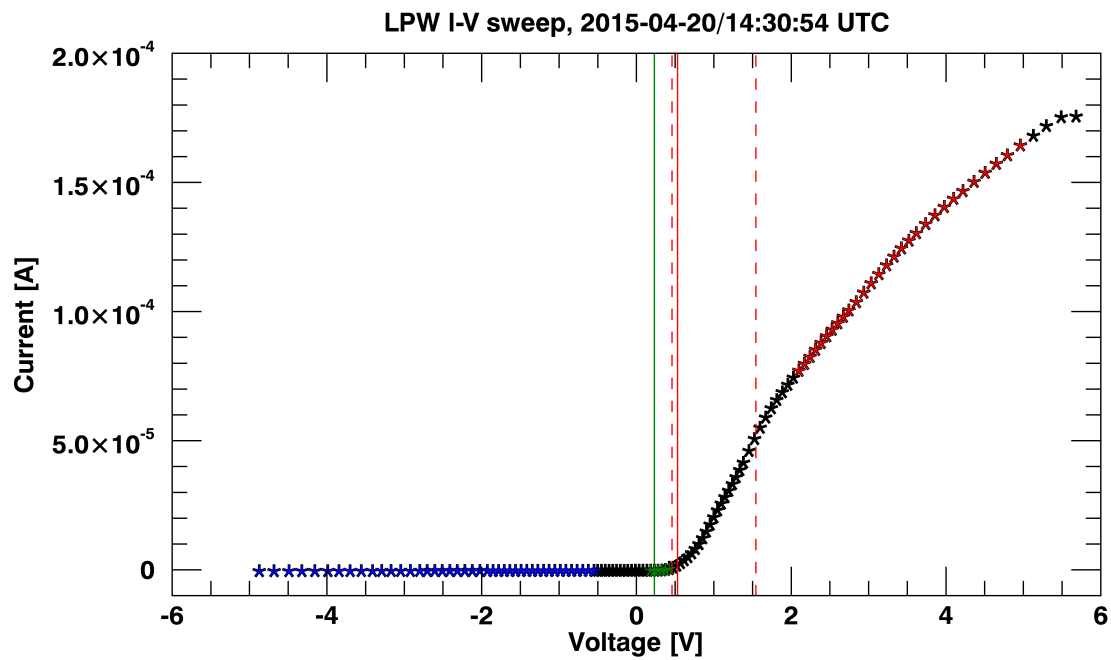


Figure 3.17: The example I-V curve shown in Figure 3.7. Blue colors mark data points used to determine  $V_{\text{ramp}}$ , which is marked by the green vertical line. The six green data points were used to obtain the initial estimate of  $T_e$ . The red data points were used to determine  $\beta$ . The solid red vertical line shows the initial estimate of  $V_{\text{scp}}$ ; the two red dashed lines show the initial lower and upper bounds on  $V_{\text{scp}}$ .

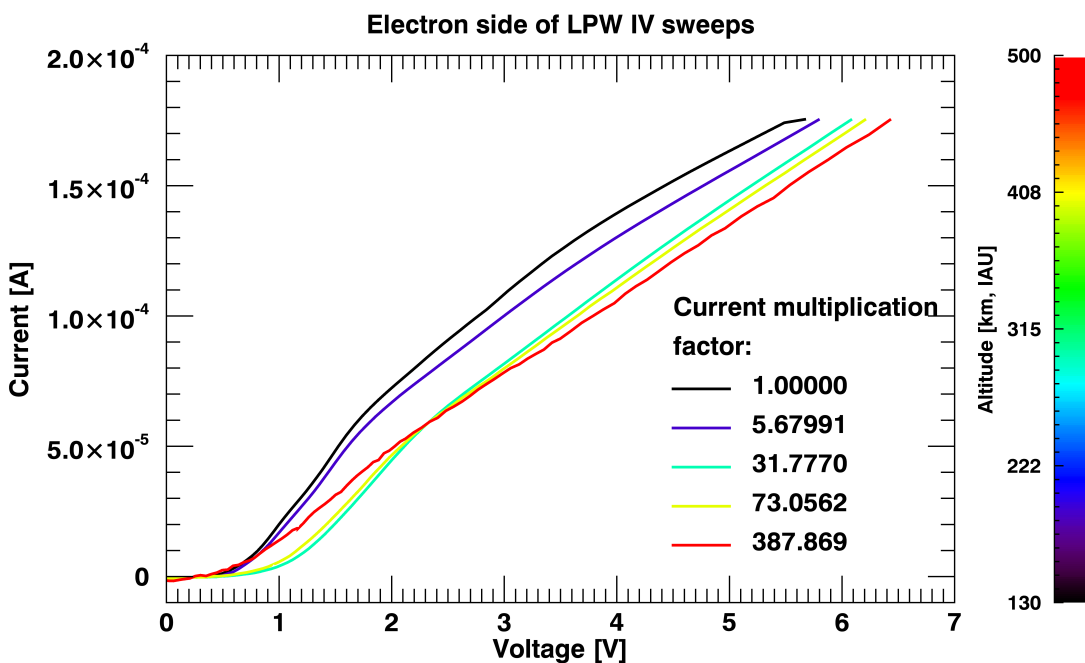


Figure 3.18: Individual I-V curves measured at different altitudes (marked by color) from the same periapsis pass as the I-V curve shown in Figure 3.7. The I-V curves have been multiplied by the noted factors so that they can be plotted on the same figure. The figure focusses on the electron collection region - the shape of the measured I-V curve here depends upon whether the probe sheath behaves as a sphere or cylinder. At high altitudes (low densities) the measured I-V curves show spherical behavior (the I-V curves are linear above about 2 V); at low altitudes (high densities) cylindrical behavior is observed (the I-V curves are no longer linear above 2 V).

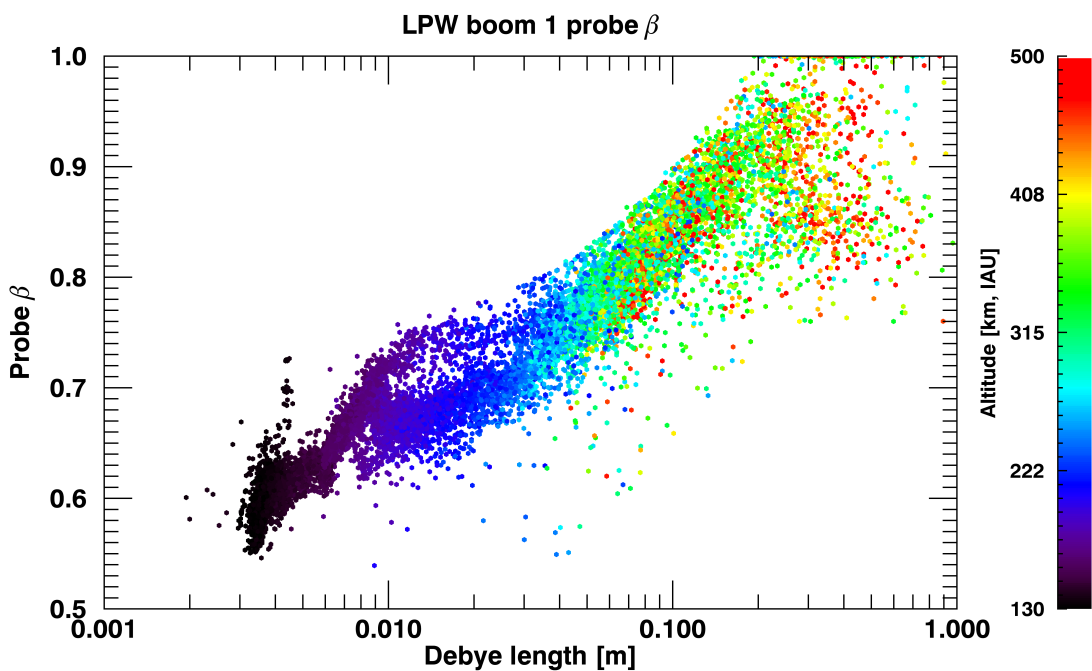


Figure 3.19: The parameter  $\beta$  derived from the LPW fit algorithm for a weeks worth of data, as a function of Debye length,  $\lambda_D$ .  $\lambda_D$  is calculated from the corresponding derived values of  $N_e$  and  $T_e$  from the LPW fit algorithm. Color shows the altitude at which each I-V curve was measured at. Cylindrical sheath behavior corresponds to  $\beta = 0.5$ ; spherical sheath behavior corresponds to  $\beta = 1$ .

equation have now been calculated at this step. The analysis focuses on the left most sixteen points on the ion side of the measured I-V curve: numerically integrated cold electron, photoelectron and hot electron populations (determined using Equation 3.24) are subtracted from the measured I-V curve, leaving just the ion current. A straight line is fit to both the numerically integrated and measured ion side data; the gradients of these two fit lines depend on  $M_i$ . Altering  $M_i$  by small amounts allows the gradient of the numerically integrated ion current to converge to that of the measured ion current. An iterative procedure similar to that outlined in Figure 3.22 is used to vary  $M_i$ . This procedure is performed twice; the lower and upper bounds to  $M_i$  are set at fixed values of 1 AMU (protons) and 44 AMU ( $\text{CO}_2^+$ ), based on the composition of the Martian ionosphere. This process assumes that the various numerically integrated electron populations are correct; subsequent iterations and refinement of these populations, and the initial parameter estimates, allows for convergence to the optimum value of  $M_i$ . An example of how  $M_i$  affects the ion current is shown in Figure 3.20. The black data points show the numerically integrated ion current based on the I-V curve shown in Figure 3.7; the different colored lines represent numerically integrated ion currents for different average  $M_i$ , as shown by the color bar (which has units of AMU). The value of  $M_i$  that contains decimal point precision is the final value converged upon by the LPW fit algorithm, which is used to numerically produce the black data points in this Figure.

The dayside Martian ionosphere is dominated by either  $\text{O}_2^+$  or  $\text{CO}_2^+$  (the cross over is at  $\sim 225$  km) and thus the approximation of an average ion mass is fairly robust for dayside conditions. The simpler, faster fitting algorithm, was chosen because the gain in fit accuracy when solving for multiple ion species on the dayside was within current uncertainties. The nightside ionospheric composition varies substantially more than the dayside, and at times significant proton densities are thought to exist. As can be seen from Figure 3.20, variation in average ion mass can lead to significant changes in collected current, particularly within

the  $T_e$  fit region. Thus, under nightside conditions, there may be increased uncertainty on the derived value of  $V_{\text{ramp}}$  and  $T_e$ . The composition of the nightside ionosphere as a function of altitude is not yet well constrained from observations due to the difficulty in obtaining reliable proton density measurements. It is thus not yet clear whether the presence of protons in the nightside ionosphere are a large source of error for the LPW derived quantities.

The statistical distribution of LPW derived average ion mass is shown in Figure 3.21, based on the same dataset used to produce Figure 3.19. The general trend is for average ion mass to increase with decreasing altitude, and this matches trends observed in statistical ion density profiles presented by *Benna et al.* (2015). Their study analyzed 8 months of species dependent ion density profiles as measured by the NGIMS instrument on MAVEN (see Appendix A).  $\text{O}_2^+$  was observed to be the dominant ion below about 300 km, and  $\text{O}^+$  was dominant above this.  $\text{CO}_2^+$  was the second most abundant ion below about 250 km. NGIMS cannot measure protons, but the STATIC instrument onboard MAVEN (again, see Appendix A) can, under certain plasma conditions (dependent upon, in particular, spacecraft potential). Protons have been observed to be a major constituent of the Martian ionosphere at higher altitudes, above  $\sim 400$  km.

The small number of  $M_i$  values that lie at 1 AMU and 44 AMU in Figure 3.21 are a result of the imposed lower and upper limits on  $M_i$ . Within the fitting algorithm, the initial average ion mass is assumed to be 32 ( $\text{O}^+$ ) and it is seen that essentially all data points move away from this initial value. A small number of points remain at this initial value as seen in the Figure; these points are associated with lower quality fits. The colorbar associated with Figure 3.21 depicts the number of days since the first measurement (2015-04-17/01:13:24 UTC) in the dataset.

- (6) **Iterate initial estimates:** The final steps within the initial estimate section of the LPW fit algorithm involve iterating bullet points 1 through 5 using these first round estimates

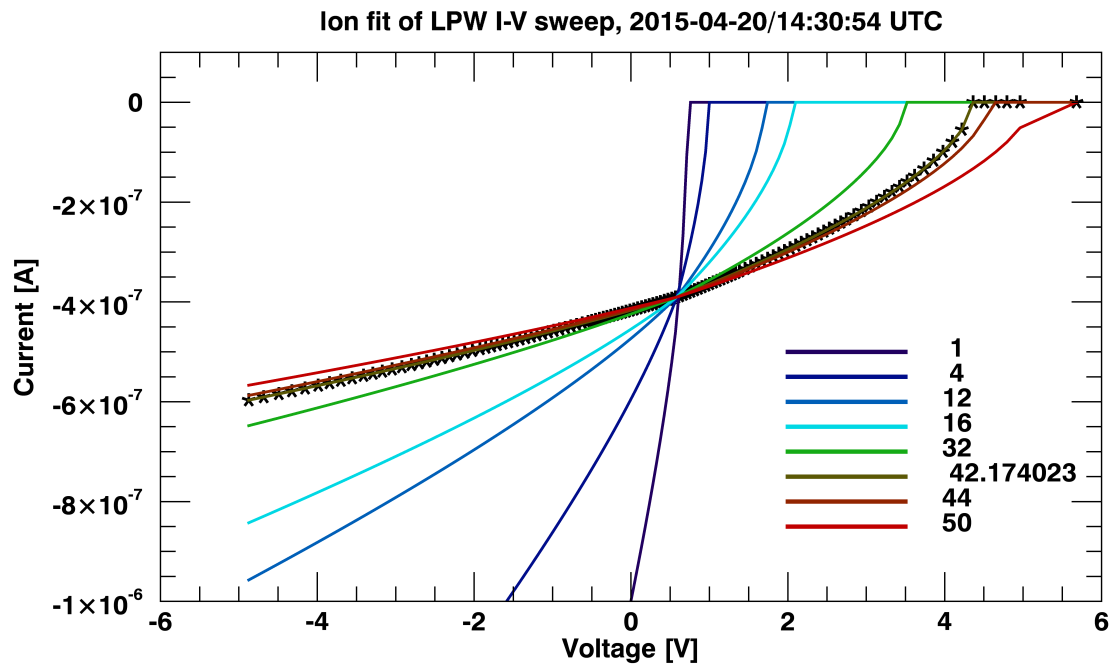


Figure 3.20: Zoom in of the ion saturation and  $T_e$  fit regions for the example I-V curve shown in Figure 3.7. The data are the numerically integrated ion currents as derived by the LPW fit algorithm for different average mass  $M_i$  values. The decimal precision mass value is the final value converged upon by the LPW fit algorithm and the black data points (and matching brown line) show these final numerically derived data points.

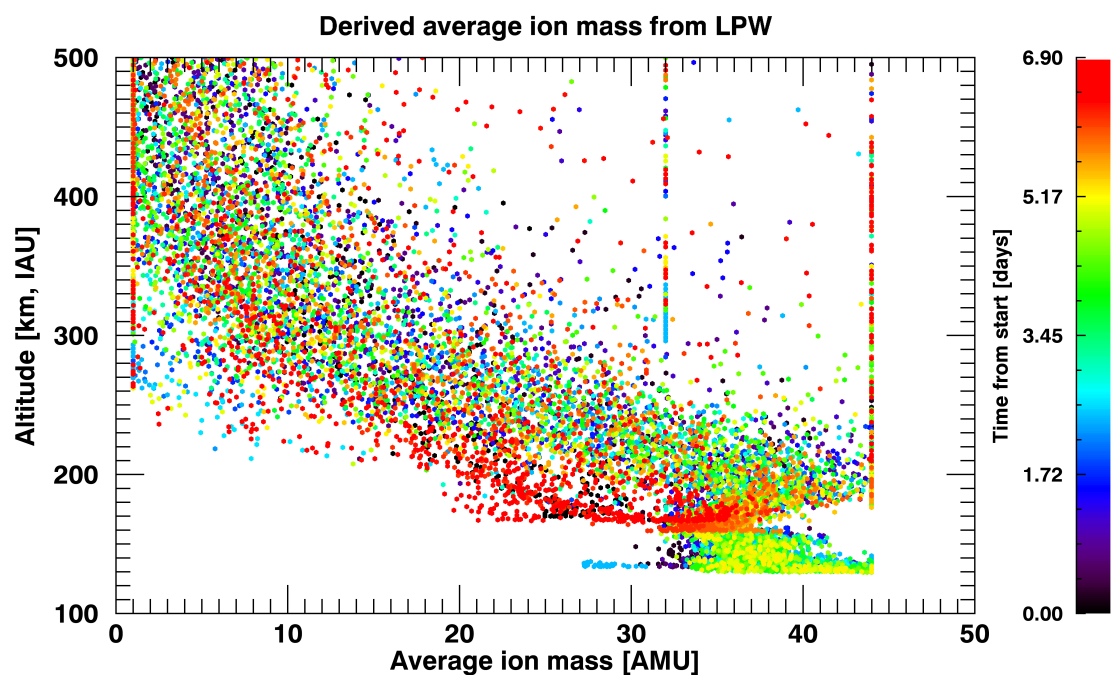


Figure 3.21: Statistical distribution of the LPW derived average ion mass as a function of altitude for the same data set used to produce Figure 3.19. The colorbar shows the time of measurement as a function of time elapsed (in days) from the first data point in the data set, 2015-04-17/01:13:24 UTC.

of  $N_e$ ,  $T_e$ ,  $V_{\text{scp}}$ ,  $V_{\text{ramp}}$ ,  $\beta$  and  $M_i$  as inputs at several of these stages. Iteration of these steps allows significant improvement of these initial estimates. When re-finding  $V_{\text{ramp}}$  and  $T_e$ , the numerically integrated ion current is now subtracted from the measured I-V curve as this current can significantly affect the  $T_e$  fit region. Note that the photoelectron, hot electron and offset currents are essentially constant as a function of probe potential (due to their high temperatures) and do not affect the shape of the  $T_e$  region, simply its offset. Subsequently, only the numerically integrated ion current is subtracted from the measured I-V curve upon iteration of these estimates. The number of iterations is a trade off between improvement in parameter values and computational run time; typically bullet points 1 through 5 are iterated twice; further convergence to optimal fit values is achieved within the refinement procedures that are discussed next.

#### 3.5.5.4 Refinement of variables

Refinement of fitted quantities occurs whether initial estimates were successfully obtained or not, however, the successful cases undergo more rigorous refinement and are more accurate. Initial estimates are deemed successful if all of the processes relating to boxes 7-11 in FC2 were successful. Initial estimates are typically unsuccessful during low density (less than  $\sim$  a few hundred  $\text{cm}^{-3}$ ) cases where the signal to noise is low. Under such conditions it can be difficult to identify  $V_{\text{ramp}}$  as the current noise is comparable in magnitude to the size of the ramp region itself. If  $V_{\text{ramp}}$  cannot be identified then initial estimates of the remaining parameters are also unobtainable from the fitting algorithm. For successful initial estimates, parameters can only be varied from their initial values by relatively small amounts, typically less than  $\sim$  50%. These constraints were empirically determined - when left unconstrained, in some cases the fit algorithm would ‘wander off’ in parameter space, leading to highly inaccurate fits. The following section details these refinement methods.

- (1) **Minimization function:** The ‘goodness of fit’ between the numerically integrated and

measured I-V curves is defined by the parameter  $ErrA$ . The LPW fit algorithm adopts a least squares fit type approach to minimize the quantity  $ErrA$ . This minimization function is called upon in boxes 6 and 7 of FC3, which is presented in Figure 3.22 and discussed next.

$$ErrA = \sum_i \frac{(I_{num,i} - I_{data,i})^2 W_{swp,i}}{norm} \quad (3.41)$$

Where  $I_{num,i}$  and  $I_{data,i}$  are the numerically integrated total current (Equation 3.37), and measured current, respectively, both as functions of sweep potential;  $W_{swp,i}$  is the sweep weighting table (an example is shown in Figure 3.13) and  $norm$  is a normalization factor to take into account the maximum current amplitude that varies from sweep to sweep. The quantity  $norm$  is defined as:

$$norm = \sum_i I_{data,i}^2 W_{swp,i} \quad (3.42)$$

- (2) **General refinement method for a single variable:** Convergence to the optimum set of fit quantities is achieved by refining each variable independently in an attempt to minimize the value of  $ErrA$ . The LPW refinement routines follow the steps outlined in Figure 3.22, which I refer to as flow chart 3 (FC3).
- (3) **Refinement order for successful initial estimates; boxes 20-24 in FC2:** The refinement of variables occurs in the following specific, empirically determined order, which yields the most accurate and reliable fit results. At each stage below, the named variable is refined using the method in FC3. The hot electron current is then refined in the same manner, before moving on to the next stage. The refinement of  $V_{ramp}$ ,  $T_e$  and  $M_1$  requires additional complexities, which are discussed here.

- (a)  $V_{ramp}$ ,  $T_e$ ,  $I_{hot}$  (**box 20 in FC2**).

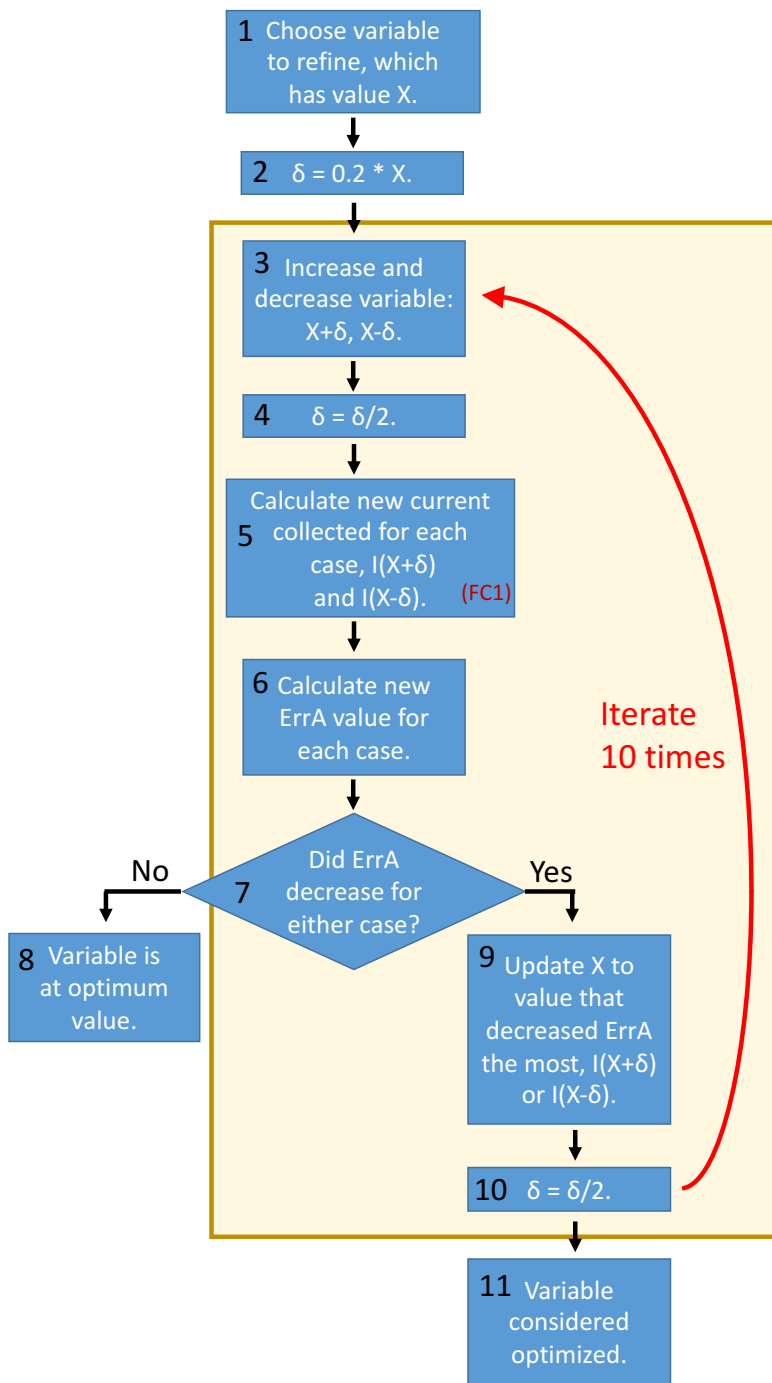


Figure 3.22: **Flow Chart 3 (FC3)**: Flow chart outlining the refinement procedure to optimize individual I-V curve parameters. This procedure is called upon by boxes 15-18 and 20-24 in FC2.

- (b)  $V_{\text{scp}}, I_{\text{hot}}$  (**box 21 in FC2**).
- (c)  $N_e, I_{\text{hot}}$  (**box 22 in FC2**).
- (d)  $\beta, I_{\text{hot}}$  (**box 23 in FC2**).
- (e)  $M_i, I_{\text{hot}}$  (**box 24 in FC2**).

The refinement process outlined by bullets 3a through 3e is repeated three times - again a trade off between the overall increase in fit quality and computational run time.

- (a) **Refinement method for  $V_{\text{ramp}}$  and  $T_e$ ; box 20 in FC2:** Because the derived value of  $T_e$  depends heavily on the derived value of  $V_{\text{ramp}}$ , both parameters are refined together. The numerically integrated ion, photoelectron and hot electron currents ( $I_{\text{ion}}, I_{\text{phe}}, I_{\text{spe}}$  and  $I_{\text{hot}}$ ) are subtracted from the measured I-V curve, leaving just the cold electron current ( $I_e$ ). This step is important because these subtracted currents change the shape of the measured I-V curve, which affects the identification of the  $V_{\text{ramp}}$  and  $T_e$  fit regions. A new estimate of  $V_{\text{ramp}}$  is then obtained using the same method described in Section 3.5.5.3. This allows a new estimate of  $T_e$  to be made using a modified method to that described in the same section. When refining  $T_e$ , the entire  $T_e$  fit region is now used, as opposed to just the first six points as is the case in Section 3.5.5.3. The  $T_e$  fit region spans a potential range based upon the maximum current measured for each particular I-V curve and this range is empirically determined using Equation 3.43:

$$V_{\text{ramp}} \rightarrow V_{\text{ramp}} + T_e \cdot (\log_{10}(I_{\text{max}}) < 6) \quad (3.43)$$

Where  $T_e$  is the latest estimate of electron temperature and  $I_{\text{max}}$  is the maximum current measured for each particular I-V curve. The factor that  $T_e$  is multiplied by has a maximum value of 6; this is imposed so that points affected by atomic oxygen contamination at higher potentials are not included. The  $T_e$  fit region, as

defined above, typically encloses 8-12 data points during high density ( $\gtrsim 5 \times 10^4 \text{ cm}^{-3}$ ) conditions. Under low density conditions (less than a few thousand  $\text{cm}^{-3}$ ), the  $T_e$  fit region typically consists of 5-6 data points. As before in Section 3.5.5.3, a linear analytical difference straight line fit is performed to the natural log of these current values; the inverse of the gradient provides  $T_e$ . Refined values of  $T_e$  typically differ by 10%-20% from the initial estimate, showing that the removal of  $I_{\text{ion}}$ ,  $I_{\text{phe}}$ ,  $I_{\text{spe}}$  and  $I_{\text{hot}}$  is important.

- (b) **Refinement method for  $M_i$ :** The refinement method for  $M_i$  is the same as that described in Section 3.5.5.3(5); the method outlined in FC3 is not used. This allows for just the ion current to be analyzed during  $M_i$  refinement, leading to more accurate results.
- (4) **Final refinement; box 25 in FC2:** A final refinement is performed once, at the very end of the fitting algorithm. A downhill simplex method (also known as the Amoeba function, *Nelder and Mead (1965); Press (2007)*) is used to converge upon a final minimum in parameter space based upon the quantities derived thus far. The function is highly constrained such that it does not run into the issues outlined in Section 3.3. Only four parameters are varied:  $N_e$ ,  $T_e$ ,  $V_{\text{scp}}$  and  $\beta$ . These parameters are allowed to diverge from their ‘input’ values by small amounts, determined empirically: upper and lower bounds on  $N_e$  are 5% and 15% respectively; 0% and 15% respectively for  $T_e$ ; 2% and 5% for  $V_{\text{scp}}$  respectively; and 4% for both bounds on  $\beta$ . This final step was included such that multiple parameters were varied simultaneously. The previous refinement steps vary one parameter at a time and the absolute minimum in parameter space may not be found using this method. Typically the Amoeba function refines the four parameters by amounts well within the empirical bounds stated above.
- (5) **Uncertainties in derived quantities; box 26 in FC2:** The LPW fit algorithm provides uncertainties, or error bars, for the derived quantities released to the LPW Level 2 Planetary

Data System (PDS) data set, namely  $N_e$ ,  $T_e$  and  $V_{\text{scp}}$ . These error bars relate to the uncertainty in the derived quantities, and not actual measurement uncertainty. Initial, large error bars are determined during the initial estimation of these quantities and these errors are reduced throughout the refinement process. Error bars for each of these three quantities are determined as follows:

- (a)  **$N_e$ :** Comparison is made between plasma densities derived from the cold electron and ion currents. Assuming quasi-neutrality,  $N_e$  should equal  $N_i$ ; when the two quantities are nearly equal, electron density error bars are small. If  $N_e$  and  $N_i$  do not match well, the corresponding error bars for  $N_e$  are increased. This method works well for plasma densities greater than about  $1 \times 10^3 \text{ cm}^{-3}$  when noise in the ion current is small. At lower densities noise on the ion side increases and  $N_i$  becomes more uncertain. The primary value reported by the LPW fit software is  $N_e$  - the larger measured electron currents make it less susceptible to noise - but when  $N_e$  and  $N_i$  don't agree, the error bars in  $N_e$  are increased. Typical error bars for  $N_e$  are  $<20\%$ .
- (b)  **$T_e$ :** Several methods are used to calculate  $T_e$  as outlined in Section 3.5.5.3. When these independent methods are in good agreement the error bars on  $T_e$  are reduced accordingly; disagreement in these methods leads to larger error bars. The weighting of each method and subsequent decision of 'agreement' has been determined empirically. The theoretical lower temperature limit that LPW can measure is about 150-200 K, as discussed in Section 3.4.2. In reality, additional sources of current and error mean that the LPW lower temperature limit is about 500 K (*Ergun et al.*, 2015a). As the derived value of  $T_e$  approaches this value at low altitudes, the lower error bar is extended to lower temperatures accordingly. The lower bound error can be as large as  $\sim 50\%$  when  $T_e$  lies between roughly 500 - 600 K; at higher  $T_e$  the lower error is usually  $\sim 20\%$ . The upper bound error is typically  $\sim 10\%$ .
- (c)  **$V_{\text{scp}}$ :** Adjustment of the spacecraft potential shifts the I-V curve in voltage space but

the shape of the curve itself does not change. This allows for an accurate determination of  $V_{\text{scp}}$ . If  $V_{\text{scp}}$  is incorrect then the numerically integrated  $T_e$  fit region will be offset from the measured  $T_e$  fit region in voltage space, resulting in a large *ErrA* value. Error bars for  $V_{\text{scp}}$  are empirically based on the final value of  $T_e$ ; a colder temperature results in a steeper  $T_e$  fit region and a more accurate determination of  $V_{\text{scp}}$  can be made. A higher temperature leads to a broader, less steep  $T_e$  fit region, making it harder to constrain the spacecraft potential.  $V_{\text{scp}}$  is typically determined to about 10% accuracy and this is consistent with measurements of  $V_{\text{scp}}$  made by other plasma instruments onboard the MAVEN spacecraft.

- (6) **Refinement order for unsuccessful initial estimates:** A simplified refinement method is used for unsuccessful initial estimates, and this is used in boxes 15-18 in FC2. Because one or more of the results from boxes 7-11 in FC2 yielded unsuccessful results, the following estimates are instead assigned. An estimate of  $V_{\text{scp}}$  is taken as the first data measurement that lies at a positive current value (box 13 in FC2). The following parameter values then assumed:  $N_e = 30 \text{ cm}^{-3}$ ;  $T_e = 1 \text{ eV}$ ;  $\beta = 0.9$  and  $M_i = 32 \text{ AMU}$  (**box 12 in FC2**). These estimates reflect the typical low density plasma conditions on the nightside and at high altitudes (typically above  $\sim 500 - 600 \text{ km}$ ) where unsuccessful initial estimates tend to occur. These parameters are refined in the above order, using the method outlined in FC3; up to three iterations are performed (**boxes 13 - 16 in FC2**). Error bars are set at 100% to represent the large uncertainties in these quantities (**box 17 in FC2**).

### 3.5.5.5 Empirical correction of derived $N_e$

This section refers to box 27 in FC2, and is the final step in the LPW fit algorithm. Statistical comparison of electron densities derived from analysis of LPW I-V curves with those derived from the LPW wave sounding measurements shows that the LP values are consistently higher than the wave sounding densities by about 10-20% for densities greater than  $\sim 2 \times 10^4 \text{ cm}^{-3}$ . At low densities,

below  $\sim 1 \times 10^3 \text{ cm}^{-3}$ , the LP derived densities are a similar factor lower than the wave sounding derived densities. This is shown in Figure 3.23A. The middle red dashed line shows the 1:1 ratio; the outer dashed red lines show 25% deviations from this. The middle purple line shows the median fit to the data; the outer purple lines show plus/minus one standard deviation from this fit. The waves derived densities are not continuous in nature due to the finite number of frequency bins that comprise the wave spectra. Data points are not shown between densities of  $1 \times 10^3 \text{ cm}^{-3}$  and  $2 \times 10^4 \text{ cm}^{-3}$  due to calibration complexities that I describe in detail in Chapter 6. An empirical correction is applied to the LP derived waves densities and this is shown in panel B. The blue lines mark the new median fit, and plus/minus a single standard deviation, of this corrected data. Considerable improvement is achieved at densities above  $2 \times 10^4 \text{ cm}^{-3}$ , where the LP measurements and derived quantities are most reliable. The correction factor that is applied to the LP derived  $N_e$  is a function of density and spacecraft potential. The data shown in Figure 3.23 are for spacecraft potentials between -7 V and -1 V.

The cause of this over and under estimation of LP derived  $N_e$  is likely due to incorrect estimation of probe sheath size for the LP derived densities, arising from varying spacecraft potentials. Incorrect sheath size estimation is discussed in Section 3.5.6 and so here I provide a brief explanation. The effect of varying spacecraft potential is demonstrated by the cartoon in Figure 3.24. The MAVEN spacecraft is depicted in each of the three cases, and the potentials applied to the LPW probes are the same for each case. Cases A, B and C depict large negative, medium negative and small negative spacecraft potentials. The corresponding potential surfaces are drawn about the spacecraft for each case. For case A, the spacecraft potential is much greater than the LPW probe potential, and the probe is enclosed within the spacecraft potential. This reduces the number of charged particles that are collected by the probe. Case B shows that with reduced spacecraft potential, the probe potential is now comparable in size and is able to ‘break through’ the spacecraft potential at the tip of the instrument booms. This enables greater current collection, despite the fact that the probe potential is the same as for case A. When the spacecraft potential is small, as in case C, the probe potential is now able to strongly influence the surrounding ambient

plasma. Current collection is further enhanced, despite the probe potential again being the same as for cases A and B. Thus, spacecraft potential affects the size of the probe sheath exposed to the ambient plasma and the empirical corrections to  $N_e$  are designed to account for this. The empirical correction algorithm applied in Figure 3.23 is discussed in more detail in (*Andersson et al.*, 2016a).

### **3.5.6 A summary of the complexities, sources of error, and implemented solutions, in the analysis of LPW I-V curves**

Throughout the derivation of the numerical equations utilized by the LPW fit algorithm, and the description of the fit algorithm itself, various assumptions, complexities and sources of error were discussed. This section provides more detail regarding these points, including the physical causes of such complications.

#### **3.5.6.1 Large sensor-to-spacecraft surface area ratio**

If the probe surface area is significant compared to the spacecraft current collection area than the potentials applied to the probe can influence the spacecraft potential. This is discussed in detail in Section 3.4.3.1. One reason that two Langmuir probes were flown on MAVEN is so that as one probe performs an I-V sweep, the second monitors the probe-to-spacecraft potential. Assuming a constant plasma environment during the I-V sweep measurement, spacecraft potential changes induced as a result of low spacecraft-to-probe surface area ratio can then be accounted for. Such changes in spacecraft potential are observed in the LPW data, and these are corrected for during the calibration of I-V sweeps, in box 1 of FC2. The probe-to-spacecraft potential measured by the second LPW probe is also used by some of the MAVEN particle instruments to minimize any effects that the LPW I-V sweep may have on their measurements.

#### **3.5.6.2 Probe size, sheath size, and $\beta$**

The assumption that the probe sheath shape can be modeled as a combination of cylindrical and spherical terms is somewhat ad-hoc and is likely one of the larger sources of error within the

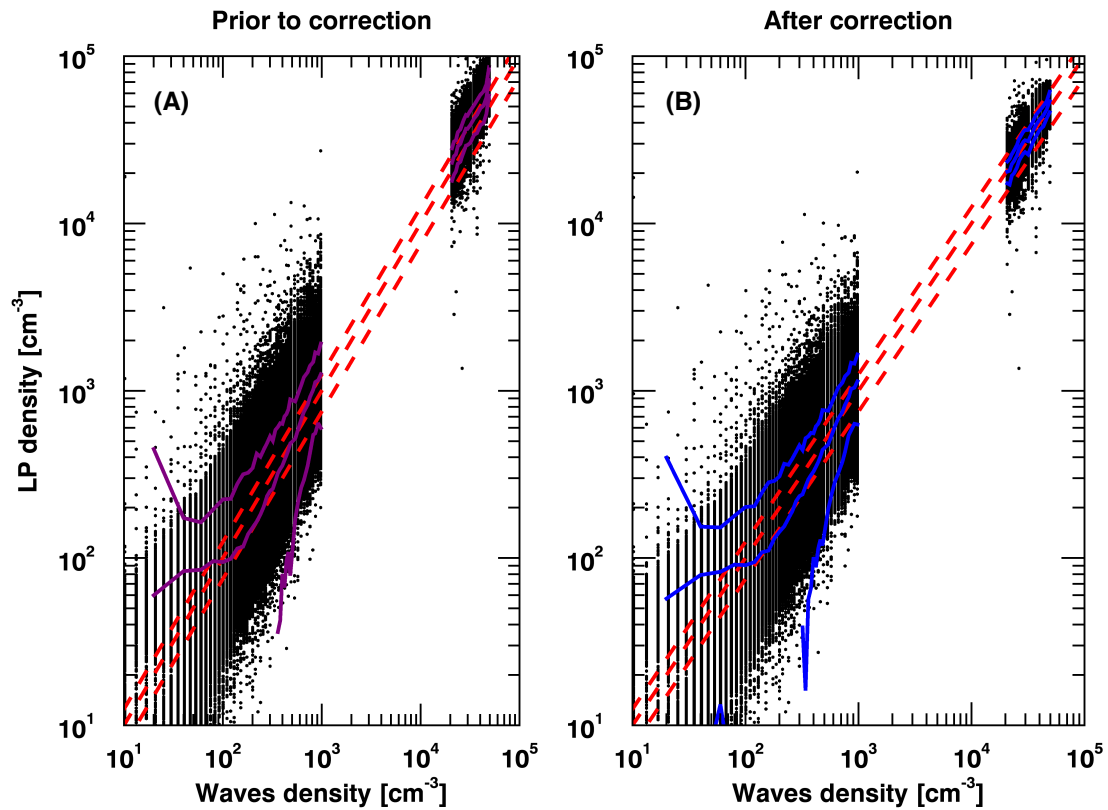


Figure 3.23: Panel A: LP derived and waves derived electron densities from the LPW instrument. The outer dashed red lines show plus/minus 25% from the 1:1 value (middle red dashed line). The middle purple line shows the median fit to the data; the outer purple lines show plus/minus one standard deviation from this. Panel B: as for panel A, but for the empirically corrected LP densities.

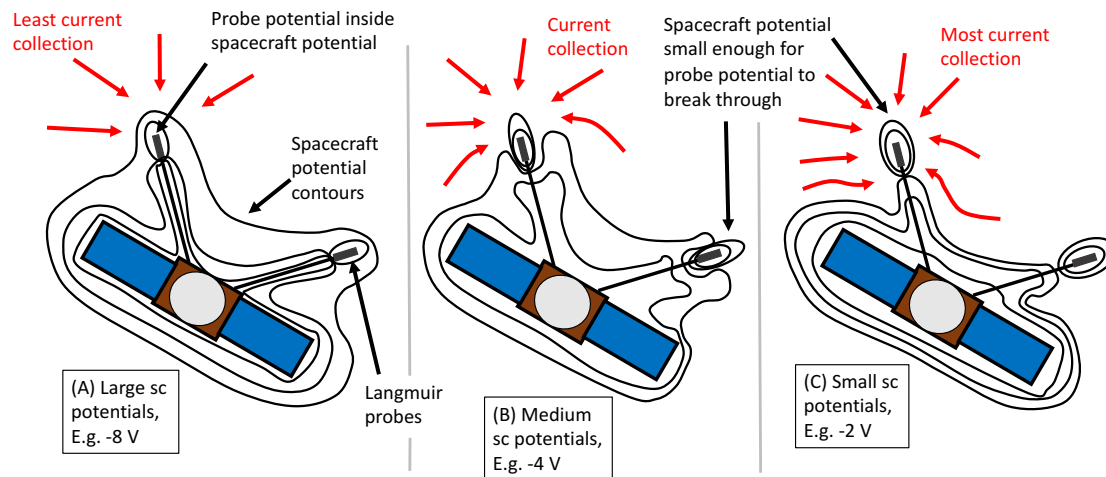


Figure 3.24: Cartoon depictions of large (case A), medium (case B) and small (case C) spacecraft potentials. As spacecraft potential gets smaller, the (constant) probe potentials are able to 'break out' of the spacecraft potential well, as seen in case C.

LPW fitting algorithm. It is assumed that the cylindrical and spherical cases share the same probe surface area and this results in a larger probe radius (and sheath radius) for the spherical case. This can lead to small inconsistencies between the cylindrical and spherical cases when the Debye length is comparable to the probe radius. Such inconsistencies are discussed in the following paragraph; as seen in Figure 3.19, the Debye length approaches the cylindrical and spherical probe radii at the lowest altitudes sampled by MAVEN, and this is where the largest inconsistencies are observed. I am still investigating these effects and how they effect quantities derived from the I-V curves. I aim to improve the fitting algorithm in early 2017 to account for these effects.

Evidence of such inconsistencies between the cylindrical and spherical sheath contributions is observed in Figures 3.16 and 3.27. The derivative of the theoretical electron current is shown as the purple line in Figure 3.16. There is a dip in this line at around 1 V that should not be present in the curve. The cause of this dip is observed in Figure 3.27, which shows the final fit solution for the same I-V sweep (and is discussed in Section 3.5.7). Between voltages of about 0.5 and 1 V in Figure 3.27A, the black line is noticeably higher than the measured data points and there is an inflection point at around 1 V. This inflection point causes the dip in the purple line in Figure 3.16. The overestimate of collected current between 0.5 V and 1 V in Figure 3.27 is likely due to an incorrect estimation of the probe and sheath size under small Debye length conditions. Further evidence of incorrect sheath size assumption comes from statistical comparisons between the LP and waves derived densities, as discussed in Section 3.5.5.5. Spacecraft potential likely also influences sheath size and is a source of error, as discussed below in Section 3.5.6.9.

The derivation of the parameter  $\beta$  was discussed in Section 3.5.5.3(4) and a simple thought experiment depicted in Figure 3.25 provides an explanation for the cylindrical and spherical sheath behavior observed as a function of Debye length. The red rectangles in Figure 3.25 represent the physical LPW probes for two cases, A and B. The green dashed lines represent the sheath for each case. Case A depicts the low altitude, high  $N_e$  case.  $\lambda_D$  is small compared to the probe radius,  $r_p$ , and subsequently  $r_s + r_p \ll r_s + \frac{L_p}{2}$ , where  $L_p$  is the physical length of the probe. Under these conditions, the probe sheath appears cylindrical, as seen in the cartoon figure. Case B shows

sheath behavior for high altitude plasma conditions:  $N_e$  is much smaller and subsequently  $\lambda_D$  is much larger than  $r_p$ . In this case,  $r_s + r_p \approx r_s + L_p$  and the sheath approaches a spherical shape. Thus, the range of plasma conditions experienced by the LPW probes leads to the cylindrical and spherical sheath behaviors observed during analysis of the measured I-V curves.

### 3.5.6.3 Probe end effects

The derivation of the numerically integrated electron and ion currents associated with cylindrical probes neglects probe end effects, as discussed in Section 3.5.4. Given the large ratio of LPW probe length to probe radius, these end effects should be negligible and have typically been assumed negligible on previously flown Langmuir Probes (e.g. *Brace (1998)*). Errors from probe end effects are thought to be much smaller than those due to incorrect sheath size estimation discussed above; the typical orientation of the LPW probes during periapsis passes is designed to reduce end effects by flying the probe surfaces at  $\sim 45^\circ$  to the ion ram direction.

### 3.5.6.4 Volatile surface contamination

Cleaning of the LPW booms was undertaken during the cruise phase of the early mission in an attempt to remove launch and cruise volatile contamination. The probes were set at +90 V (the maximum possible) so that high energy solar wind electrons were focused onto the probes. As the probes were stowed during the cruise phase, the I-V sweeps were overwhelmed by spacecraft photoelectron current, and so it is unknown how effective this cruise cleaning was. During mid-mission, just after Mars orbit insertion, the same cleaning technique was again applied when the spacecraft apoapsis was in the solar wind. Changes to the shape of measured I-V curves were observed after thruster firings; the above cleaning method was able to successfully remove these effects, as discussed in Section 3.4.3.

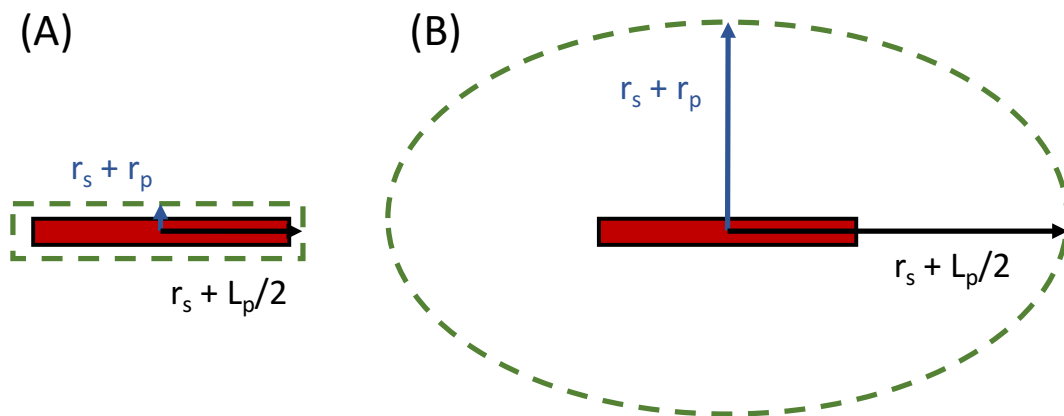


Figure 3.25: Cartoon depiction demonstrating why spherical sheath behavior is observed at large  $\lambda D$ . The red rectangles represent the LPW probes of physical radius  $r_p$  and physical length  $L_p$ . The dashed green lines represent the sheath surface. Case A is for a high densities when the Debye length is small, leading to a small sheath radius  $r_s$ . Case B is for a low densities when the Debye length is large and correspondingly  $r_s$  is large.

### 3.5.6.5 Non-volatile surface contamination - Atomic oxygen

AO contamination is discussed in *Ergun et al.* (2015a) and it reduces the current measured by the LPW probes at potentials close to and just above the spacecraft potential. This can be seen in Figure 3.27A. AO contamination does not significantly affect the derivation of  $N_e$  but it leads to difficulty in deriving  $V_{\text{scp}}$  and  $T_e$  using the method of identifying a peak in the derivative of the I-V curve. The analysis methods discussed here have been developed to account for this, and  $V_{\text{scp}}$  can still be converged upon with good accuracy, typically 10%-20%, as has been clarified with comparison to other instruments onboard MAVEN that are capable of measuring the spacecraft potential.

$T_e$  is slightly harder to constrain; the AO contamination leads to a slower response of the I-V curve close to  $V_{\text{scp}}$ , which reduces current collection by the probe at these potentials. This artificially lessens the gradient of the  $T_e$  fit region. A shallower slope in this region leads to a warmer derived  $T_e$ . The lowest points within the  $T_e$  fit region, those just after  $V_{\text{ramp}}$ , are least affected by this contamination and are subsequently highly weighted when deriving  $T_e$ , as can be seen in Figure 3.13. With this knowledge, the LPW  $T_e$  values are more likely an upper bound, particularly when  $T_e$  approaches the lower instrumental measurement limit of  $\sim 500$  K (*Ergun et al.*, 2015a). The lower uncertainty in  $T_e$  is thus lowered to reflect this.

During the first  $\sim 6$  months of MAVEN's primary science orbit, the measured I-V curves from each of the two LPW probes showed different behaviors. These characteristics also evolved differently over time. Because the two probes are identical, the evolution of each probe independent of the other allowed the culprit (AO contamination) to be identified, as discussed in Section 3.4.3.

The presence of multiple peaks in the derivative of the measured current, as a result of this AO contamination and as seen in Figure 3.16, can be (we believe incorrectly) interpreted as due to the presence of multiple cold electron populations. There can only be one value of spacecraft potential; thus, multiple, cold, bulk electron populations that demonstrate peaks in their derivative curves at different potentials, can only be explained if each population has a different potential

with respect to the spacecraft. This would require that they have undergone energization, by, for example, acceleration via electric fields. At periapsis, densities are so large that these cold, bulk populations will thermalize quickly via collisions with the neutral atmosphere and ions to a single temperature. We thus deem it highly unlikely that this is the correct interpretation of the observed multiple peaked derivative curves.

### 3.5.6.6 Sheath collapse

Sheath collapse is a phenomenon that may affect the tail end of the ion current a potentials close to  $V_{sep}$  within the  $T_e$  fit region. When the probe is biased to large negative potentials, ions are attracted to the probe and they flow through the probe sheath due to the ram effect; the sheath is large in size and it contains a large number of electrons to conserve charge neutrality. This is depicted in Figure 3.26A: the gray circle represents the probe cross section, biased at negative potentials. The gray arrow indicates the direction of spacecraft travel at the spacecraft velocity,  $V_{sc}$ . If the figure is in the probe frame of reference, then the Ions (the blue crosses) are not only attracted to the probe, but they appear to flow left to right due to the large spacecraft velocity with respect to the ion thermal velocity. There are  $\sim$  an equal number of electrons and ions within the sheath to conserve charge, the electrons of which are not shown here to keep the figure simple. As the probe potential is increased to small positive voltages there is a potential at which all ions are deflected from the probe, as depicted in Figure 3.26B. Because ions are deflected away from the probe, but the probe potential is not yet large enough to attract a significant number of electrons, the sheath size is small. If this transition between large and small sheath sizes is smooth, as shown by the red line in Figure 3.26C, the current collected by the probe is also smooth as a function of probe potential. If, however, the transition between sheath sizes is abrupt, as shown by the blue line in Figure 3.26C, there will be a spike in current collected at the probe potential of this transition. This is the sheath collapse effect and it occurs in the  $T_e$  fit region, leading to larger uncertainties in the derived value of  $T_e$ . This effect is not accounted for within the LPW fit algorithm and is not well understood. Modeling is thought to be the best approach in understanding it, and under what

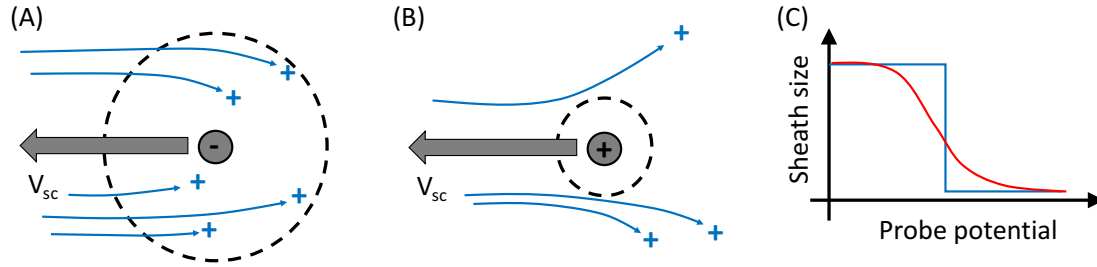


Figure 3.26: Cartoon representation of the sheath collapse effect. Panel A shows the probe biased at a large negative potential; ions are attracted to the probe and the sheath is large. Panel B shows the probe biased to a small positive potential; ions are deflected from the probe, but the potential is not yet large enough to attract a significant number of electrons and so the sheath is small. Panel C shows two possible behaviors for the transition between large and small sheath sizes: the red line represents a smooth transition; the blue a sharp one. Sheath collapse occurs under the sharp transition; there is a corresponding spike in current collected by the probe, leading to larger uncertainties in the derived value of  $T_e$ .

conditions it is (if at all) present. Large spikes of current collection within the  $T_e$  fit region are not obvious when inspecting individual I-V curves, and thus the errors caused by sheath collapse are thought to be small.

### 3.5.6.7 Ion temperature assumption

The ion RAM current is calculated using Equation 3.36 and assumes that  $T_i = T_e$ . In reality,  $T_e$  is slightly larger than  $T_i$ , typically by a factor  $<2$  at the exobase (e.g. *Dalgarno et al. (1963); Geisler and Bowhill (1965); Matta et al. (2014)*). Private communication with Jim McFadden, the primary investigator of the STATIC instrument on MAVEN, indicates that  $T_i$  can be even colder at times, close to the neutral temperature (although these ion temperature measurements are still under calibration). However, the true value of  $T_i$  is still negligible compared to the spacecraft velocity at periapsis and this assumption is appropriate.

### 3.5.6.8 Estimates of probe and spacecraft photoelectron, and hot electron, currents

For typical Langmuir probe analysis, errors in the estimation of the probe photoelectron, spacecraft photoelectron, and hot electron currents, produce errors in the derivation of  $N_e$ ,  $T_e$  and

$V_{\text{scp}}$ . At Mars, these populations typically have  $\sim$  constant temperatures that are large compared to that of the Martian cold electron population. For LPW and MAVEN, the probe, boom and spacecraft photoelectrons have temperatures of 2.7 eV, and hot electrons have temperatures between 10 and 30 eV (24 eV is empirically assumed in the LPW fitting algorithm). These temperatures are large compared to the ambient electron temperature of  $\sim 0.05$  eV at periapsis. As such, these warmer electron populations typically appear as offsets when compared to the cold electron current as a function of probe potential. These offsets do not affect the shape of the measured I-V curve, and thus at Mars, the errors in derived  $T_e$  associated with incorrectly estimating these warmer electron populations are small. Photoelectron currents can, however, impact the derivation of  $N_e$ , as to first order the current collected at large positive probe potentials is proportional to the ambient plasma density. At high altitudes when the ambient plasma density is low, the photoelectron currents can dominate and are thus important. At low altitudes, such as in Figure 3.27, the photoelectron current is negligible compared to the ambient electron density.

### 3.5.6.9 Large values of spacecraft potential

For large absolute values of spacecraft potential, when  $|V_{\text{scp}}| \gtrsim 6$  V, the LP derived electron density and temperature values possess large uncertainties. These uncertainties are because the theoretical numerically integrated currents used within the fitting algorithm do not account for the presence of the spacecraft. Thus, when the spacecraft potential becomes large, it starts to influence the current collected by the probes, which is not accounted for in the fitting algorithm. Such effects are depicted in Figure 3.24 and they must be investigated using simulations that have not yet been carried out. Large absolute values of  $V_{\text{scp}}$  are typically only observed during certain orientations of the MAVEN spacecraft that are flown infrequently at periapsis. These large potentials,  $\sim -15$  eV, arise due to the non conducting nature of the solar panels and resistiveness of the main antenna dish. The solar panels are fixed in position and point in the same direction as the antenna. When the spacecraft flies in an orientation such that these surfaces face forward, the collected ion current is small at periapsis. The collected electron current is still large, and the spacecraft potential thus

swings to large negative values. During more optimum spacecraft orientations at periapsis (which is the majority of cases),  $V_{\text{scp}}$  is typically steady at around -3 V.

The LPW instrument also applies a dynamic offset to the applied probe potentials to take into account variations of spacecraft potential. This offset is applied for several reasons: 1) Telemetry restrictions mean that each I-V sweep consists of 128 potential steps; thus, only a finite range in voltage space can be sampled per I-V sweep. 2) In order to obtain an accurate estimate of  $T_e$ , particularly at low temperatures as found in the Martian ionosphere, the  $T_e$  fit region must be sampled at high resolution in voltage space. Thus, high resolution measurements in voltage space are made at the middle  $\sim \frac{1}{3}$  of the applied potential range. The dynamic offset helps to center the applied potentials about the spacecraft potential so that these high cadence points overlap with the  $T_e$  fit region. This can be seen in Figure 3.7, for example.

#### **3.5.6.10 Secondary electron emission**

When high energy electrons ( $\gtrsim 100$  eV) impact the LP probe they can bounce off the probe surface instead of being collected. Further, this impact can cause the emission of additional electrons from the probe surface (the secondary electrons). Thus, instead of collecting a single, high energy electron, the probe may in fact emit several electrons under such conditions, resulting in negative current collection rather than positive. Secondary electron emission is not accounted for within the LPW analysis routines, however, it is thought to be a small source of error when measurements are made within the Martian ionosphere. Below  $\sim 400 - 500$  km altitude such high energy electrons account for a small, if not negligible, fraction of the electron population, as observed by the SWEA instrument onboard MAVEN. At higher altitudes, and particularly in the solar wind where the ambient electron density is low (a few  $\text{cm}^{-3}$ ) and electron energies can reach several keV, secondary electron emission is likely a more dominant source of error. The LPW instrument is designed to measure dense, low temperature plasmas, and as such errors are already large for measurements made at high altitudes: low signal to noise for measured currents is likely an equal, if not greater, source of error, as secondary electron emission is under such conditions.

### 3.5.7 Implementation on LPW data - a final fit example

The final fit converged upon by the LPW fit software, for the example IV sweep shown in Figure 3.7, is shown in Figure 3.27. The black data points are the measured current as a function of sweep potential. The colored curves show various numerically integrated currents: black shows the total current collected by the probe. Red shows the cold electron current (note that at positive potentials this is the bulk of the collected current and is almost identical to the total current shown in black at these potentials). Blue shows the ion current. Brown and purple show the photoelectron currents from the probe and spacecraft respectively; due to the high density, low temperature plasma conditions at periapsis, the photoelectron currents cannot be distinguished on the scales shown. Orange shows the hot electron current. The green data points mark the points used to determine the initial bounds for  $T_e$ . Panel A shows the entire I-V curve; panel B shows a zoom in on the  $T_e$  fit region.

The overall fit is very good. The ion and electron side currents match the data very well, seen in panels A and B. Atomic oxygen contamination affects current collection at potentials close to the spacecraft potential; in this case, between potentials of about 0.5 V to 2 V. This part of the curve has reduced weighting when iterating fit values, as shown in Figure 3.13. Subsequently, the numerically integrated current does not match the measured current within this potential range - the atomic oxygen contamination reduces current collection and this is seen in panel A. The fit is also very accurate within the  $T_e$  fit region - both the shape and absolute value of the  $V_{\text{ramp}}$  region matches the measured data very well, seen in panel B. The final fit parameters are shown in Table 3.5.7.

## 3.6 LPW wave sounding

As was discussed in Section 3.5.5.5, LPW wave sounding is used to calibrate the I-V sweep derived absolute electron density. Although wave sounding cannot be used to determine electron temperature, it can determine the absolute electron density to high precision, within about 6%-12%

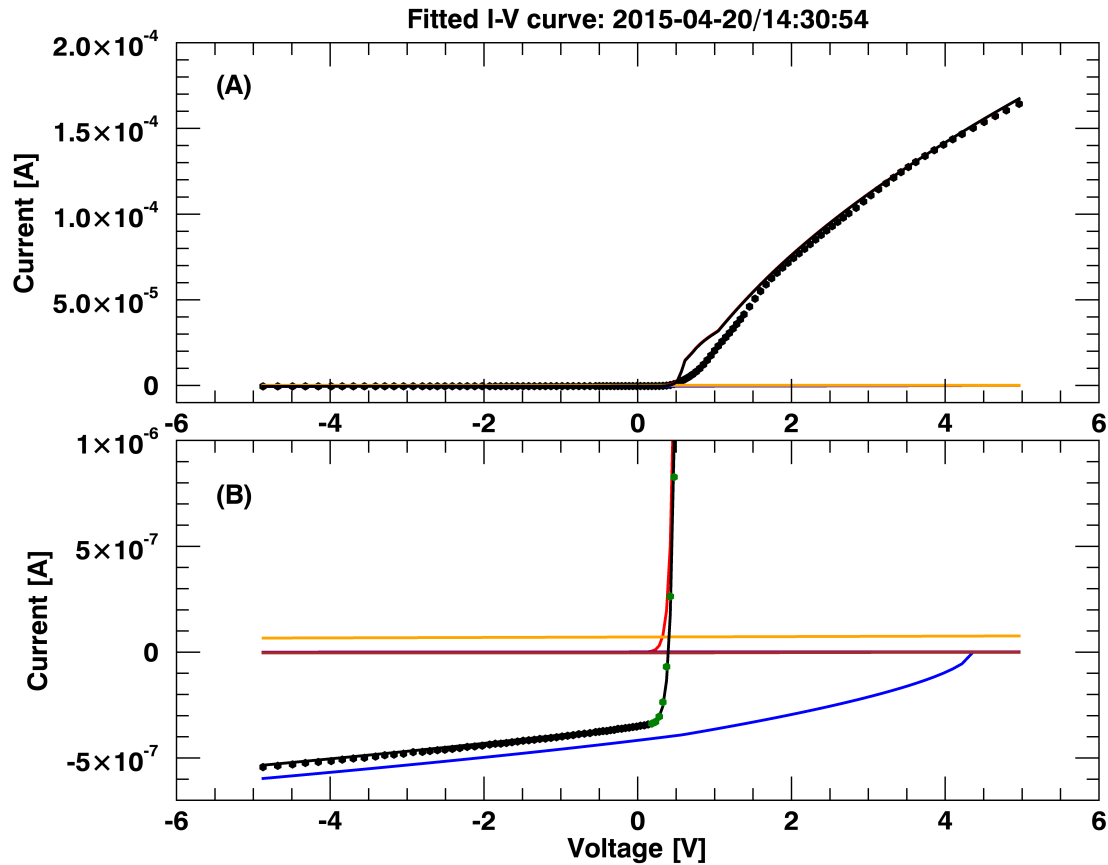


Figure 3.27: The final numerically integrated fit derived by the LPW fit software. The measured I-V curve is shown by the black data points. The colored curves show various numerically integrated currents: black the total current collected by the probe; red; blue the ion current; brown and purple the photoelectron currents from the probe and spacecraft respectively; orange the hot electron current. The green data points mark the points used to determine the initial bounds for  $T_e$ . Panel A shows the entire I-V curve; panel B shows a zoom in on the  $T_e$  fit region.

Fit quantity	Value	Lower limit	Upper limit
$N_e$ (cm <sup>-3</sup> )	2.38x10 <sup>5</sup>	1.79x10 <sup>5</sup>	2.62x10 <sup>5</sup>
$T_e$ (K)	560	316	680
$V_{\text{scp}}$ (V)	-0.58	-0.68	-0.48
$M_i$ (AMU)	42	7	44
$\beta$	0.60	0.52	0.70

Table 3.2: The final fit parameters derived by the LPW fit software for the I-V curve shown in Figure 3.7.

for LPW (*Andersson et al.*, 2014). When operating in waves mode, the LPW instrument measures the local plasma wave environment. The instrument emits a low power, broadband white noise signal that stimulates the local plasma frequency via resonance. The plasma frequency is also known as the Langmuir frequency, defined by  $\omega_L$ :

$$\omega_L^2 = \omega_{pe}^2 + 3v_{\text{the}}^2 k^2 \quad (3.44)$$

Where:

$$\omega_{pe} = \frac{ne^2}{\epsilon_0 m_e} \quad (3.45)$$

is the local plasma frequency,  $v_{\text{the}}$  is the electron thermal speed,  $n$  the local plasma density,  $e$  the electron charge and  $m_e$  the electron mass. Given the cold  $T_e$  observed in Mars' ionosphere (typically 0.1 to 0.3 eV, e.g. *Ergun et al.* (2015a)) the second term on the right hand side of Equation 3.44 is much smaller than the first term and can be assumed negligible.

Upper hybrid waves are expected to have frequencies of  $\omega_H$ :

$$\omega_H^2 = \omega_{pe}^2 + \omega_{ce}^2 \quad (3.46)$$

Where:

$$\omega_{ce} = \frac{eB}{m_e} \quad (3.47)$$

is the electron cyclotron frequency. The magnetic field strength  $B$  is typically  $< 50$  nT in the Martian ionosphere and rarely exceeds a few hundred nT; the electron cyclotron term is also small compared to the first term on the right hand side of Equation 3.46. Hence, the local plasma frequency  $\omega_L$  is proportional to  $\sqrt{N_e}$ .

A demonstration of the success of the LPW wave sounding measurements, and a statistical analysis of the first few months of this data set, has been carried out by *Andrews et al.* (2015). I present the caveats of this dataset, and a statistical study of the electromagnetic wave power distribution throughout Mars' magnetosphere, in Chapter 6 of this thesis.

### 3.7 Summary

The LPW fit algorithm has been described in detail; the expressions for the numerically integrated electron and ion currents collected by the probes are derived in Sections 3.5.1 and 3.5.2. The implementation of these expressions, and the overall fitting algorithm, are detailed in Section 3.5.5. The measured LPW I-V curves cannot be fitted using standard minimization routines that span a large parameter space - the large number of free variables, and the range in values over which they span, result in poor convergences. The analysis methods developed for the analysis of LPW I-V curves are described: initial estimates of important parameters are obtained by analyzing various regions of an individual I-V curve separately. The fitting algorithm enables a sequential derivation of the fit quantities in a much more constrained and robust manner, as discussed in Section 3.5.5. Refinement of the derived quantities, and comparison between the resulting numerically integrated, and measured, I-V curves, enables a convergence upon the optimum fit values. Many of the observed LPW probe characteristics and sources of complexity have been discussed in *Brace* (1998), for example.

## Chapter 4

### Summary of my publication work

#### 4.1 Paper 1: The first in-situ electron temperature and density measurements of the Martian nightside ionosphere

MAVEN is the first spacecraft to observe electron density and temperature in-situ on the nightside of Mars. I present statistical profiles of these quantities as a function of local time. Significant plasma densities of at least a few thousand  $\text{cm}^{-3}$  were observed below 200 km altitude at all nightside local times; analysis of plasma recombination rates shows that an ionization source is needed to sustain these high levels of density. One dimensional modeling using observed precipitating electron fluxes as input showed that precipitating electrons are able to sustain the observed nightside ionospheric densities, supporting conclusions drawn by earlier studies that precipitating electrons are likely an important source of the Martian nightside ionosphere. This paper is published in the journal Geophysical Research Letters (GRL).

#### 4.2 Paper 2: Magnetic and electric variations in the near Mars environment

The transfer of upstream solar wind energy into the Martian atmosphere is an important energy source that is likely able to significantly affect atmospheric escape rates. Electromagnetic variations within the Martian magnetosphere are studied in the form of statistical maps of magnetic and electric field wave power. The distribution of wave power varied with upstream solar wind conditions, highlighting regions important for the dissipation of energy throughout the Martian magnetosphere and how these are affected by upstream driving conditions. This paper has been

submitted to the Journal of Geophysical Research (JGR); I have received reviewer comments and will respond to them once this thesis is finished.

#### **4.3 Paper 3: Ion heating within a gradient magnetic field at low altitudes in the Martian ionosphere**

The energization of atoms and ions within the Martian atmosphere is important for escape to space. Sporadic, strong ion energization events are observed in the dayside Martian ionosphere below 400 km altitude. These ions have energies up to a few hundred eV - much greater than the typical cold ( $<10$  eV) ion energies observed in the Martian ionosphere at these altitudes. Analysis of these ions reveals ion conic behavior - evidence for parallel acceleration and perpendicular heating exist and these observations are the first conclusive evidence of such conics existing within the Martian ionosphere. This paper was submitted to the Journal of Geophysical Research in May 2016; reviewer comments were received in June 2016 with the recommendation of resubmission once they have been addressed. These comments will be addressed and the paper resubmitted in early 2017.

#### **4.4 Paper 4: Observations of the Rayleigh Taylor instability in Mars' ionosphere**

Ionospheric disturbances are observed below 200 km in the Martian ionosphere and in particular, quasi-sinusoidal signatures are observed in electron and ion density profiles, and the magnetic field strength and direction. Detailed analysis of one such event shows that the Rayleigh-Taylor instability is likely responsible for such disturbances, similar to the Equatorial Spread F (ESF) phenomenon frequently observed in the terrestrial equatorial ionosphere. A statistical analysis of 21 months worth of MAVEN data show that similar disturbances peak in occurrence at the Martian terminator, where top heavy ionospheric density profiles and horizontal magnetic fields are common. This paper has been submitted to the Journal of Geophysical Research and I am awaiting reviewer comments.

## Chapter 5

### The First In-Situ Electron Temperature and Density Measurements of the Martian Nightside Ionosphere

**First published:** 5<sup>th</sup> November 2015, Geophysical Research Letters

**Corresponding author:** C. M. Fowler, Laboratory of Atmospheric and Space Sciences, University of Colorado, Boulder, Colorado, USA 80303, christopher.fowler@lasp.colorado.edu.

**Authors:** C. M. Fowler<sup>1</sup>, L. Andersson<sup>1</sup>, R. E. Ergun<sup>1</sup>, M. Morooka<sup>1</sup>, G. Delory<sup>2</sup>, D. J. Andrews<sup>3</sup>, Robert J. Lillis<sup>2</sup>, T. McEnulty<sup>1</sup>, T. D. Weber<sup>1</sup>, T. M. Chamandy<sup>1</sup>, A. I. Eriksson<sup>3</sup>, D. L. Mitchell<sup>2</sup>, C. Mazelle<sup>4,5</sup>, B. M. Jakosky<sup>1</sup>

<sup>1</sup>Laboratory of Atmospheric and Space Sciences, University of Colorado, Boulder, Colorado, USA.

<sup>2</sup>Space Sciences Laboratory, University of California, Berkeley, California, USA.

<sup>3</sup>Swedish Institute for Space physics, Uppsala, Sweden.

<sup>4</sup>CNRS, Institut de Recherche en Astrophysique et Planétologie, Toulouse, France

<sup>5</sup>University Paul Sabatier, Toulouse, France

## 5.1 Abstract

The first in-situ nightside electron density and temperature profiles at Mars are presented as functions of altitude and local time (LT) from the Langmuir Probe and Waves (LPW) instrument on board the Mars Atmosphere and Volatile Evolution Mission (MAVEN) spacecraft. LPW is able to measure densities as low as  $\sim 100 \text{ cm}^{-3}$ , a factor of up to 10 or greater improvement over previous measurements. Above 200 km near vertical density profiles of a few hundred  $\text{cm}^{-3}$  were observed for almost all nightside LT, with the lowest densities and highest temperatures observed post midnight. Density peaks of a few thousand  $\text{cm}^{-3}$  were observed below 200 km at all nightside LT. The lowest temperatures were observed below 180 km and approach the neutral atmospheric temperature. 1D modeling demonstrates that precipitating electrons were able to sustain the observed nightside ionospheric densities below 200 km.

## 5.2 Introduction

The dayside ionosphere of Mars is primarily the product of photoionization of the dayside neutral atmosphere by solar EUV radiation that undergoes a complex set of photochemical reactions. Its shape, structure, and solar zenith angle (SZA) dependence are well described by a classical Chapman profile at low altitudes (*Chapman, 1931a*), (*Chapman, 1931b*). Comprehensive reviews of the Martian dayside ionosphere can be found in, for example, *Nagy et al. (2004)*, *Witasse et al. (2008b)* and *Withers (2009)*.

In contrast, the nightside ionosphere of Mars is less well understood. Radio occultations of the nightside ionosphere were made by the Mars, Mariner and Viking spacecraft in the 60's, 70's and 80's (see for example *Fjeldbo et al. (1970)*, *Savich and Samovol (1976a)*, *Lindal et al. (1979)*). *Zhang et al. (1990)* used this data set and found that around 60% of the radio occultation profiles between SZA  $90^\circ$  and  $125^\circ$  showed no detectable peak in electron density. The peaks that were observed typically lay between altitudes of  $\sim 140$  and  $180$  km with densities of  $\sim 5 \times 10^3 \text{ cm}^{-3}$ . It turns out that the nightside ionospheric densities were often too small to be detected by the radio

occultation method. Due to the relative orbital geometries of Earth and Mars radio occultations for SZA greater than  $\sim 125^\circ$  are not possible.

More recently, *Němec et al.* (2010) analyzed four years of nightside ionospheric data from the Mars Advanced Radar for Subsurface and Ionospheric Sounding (MARSIS) instrument on board the Mars Express spacecraft. Their dataset consisted of  $\sim 30,500$  ionograms, observed at SZA  $>107^\circ$  and altitude  $<1100$  km. They identified ionospheric echoes in  $\sim 9\%$  of these data, with peak densities less than  $2 \times 10^4 \text{ cm}^{-3}$ , and a lower limit to the peak altitudes of 100-150 km. Given that the lowest sensitivity of the MARSIS instrument is  $\sim 5 \times 10^3 \text{ cm}^{-3}$ , they were able to estimate that  $\sim 90\%$  of actual ionospheric density peaks (across all altitudes) are below this value. These ionograms were analyzed with respect to crustal magnetic field strengths and it was found that in weak crustal field regions ( $B < 20$  nT) the nightside ionosphere decreased with increasing SZA, up to  $\sim 125^\circ$ . They suggest that dayside plasma transport plays a crucial role for ionospheric formation in these regions. For strong crustal field regions ( $B > 20$  nT) they found no SZA dependence, but rather a dependence on magnetic field orientation relative to the surface. The nightside ionospheric occurrence rate was more than 4 times greater for near vertically aligned magnetic fields compared with horizontally aligned magnetic fields, suggesting the precipitating electrons (which can only enter the atmosphere when the magnetic field orientation allows it) could be a key ionization source for these regions.

With regards to modeling the nightside ionosphere and determining its source several suggestions have been put forth. *Verigin et al.* (1991) used magnetotail data from the HARP electron spectrometer onboard the Phobos 2 orbiter to investigate the effect of possible precipitating electrons. They showed that peak electron densities of a few thousand  $\text{cm}^{-3}$ , in agreement with previous observations of the nightside ionosphere, can be produced by the characteristic fluxes ( $\sim 10^8 \text{ cm}^{-2}\text{s}^{-1}$ ) and energies (tens eV) observed by the instrument. *Haider et al.* (1992) extended this work using HARP electron spectra from the magnetotail and plasma sheet and drew similar conclusions.

*Fox* (1993a) modeled upper limits to the nightside ionosphere using both precipitating elec-

trons (based on the HARP data) and a dayside transport model. They computed electron density peaks in the range  $\sim 1.5 \times 10^4 \text{ cm}^{-3}$  at altitudes of 159 to 179 km.

*Haider* (1997) used an analytical yield spectrum approach to model the chemistry of the major ions in Mars' nightside ionosphere. It was determined that the nightside ionosphere produced by precipitating magnetotail electrons agreed with Viking observations. Other sources of nightside ionization, such as plasma precipitation or horizontal plasma transport from the dayside, did not agree with the Viking profiles.

More recent modeling efforts by *Lillis et al.* (2009), *Lillis et al.* (2011) used a Monte Carlo approach to calculate the electron impact ionization rates in the nightside Martian ionosphere as functions of energy spectrum, pitch angle distribution (PAD) of precipitating electrons, magnetic field magnitude, and neutral density. They found that inclusion of the magnetic field gradients and PADs are essential in obtaining correct ionization rates within the Martian nightside ionosphere.

*Withers et al.* (2012) analyzed 37 electron density profiles obtained by the Mars Express Radio Science Experiment (MaRS) for SZA  $101^\circ - 123^\circ$  and concluded that profiles for SZA  $< 115^\circ$  showed trends consistent with the transport of dayside plasma. Above  $115^\circ$  these profiles were consistent with simulated plasma production by electron precipitation. A review of previous modeling efforts concluded that spatial variations in precipitating electron populations appear sufficient to account for the observed patchiness of the nightside ionosphere.

### 5.3 Data And Instrument Overview

The Mars Atmosphere and Volatile Evolution Mission (MAVEN) entered Mars orbit on September 22<sup>nd</sup> 2014 UTC. MAVEN is designed to study the upper atmosphere of Mars and as such carries a full suite of instrumentation that allows it to measure the magnetic, electric, neutral, charged particle and EUV environment (*Jakosky et al.*, 2015a). MAVEN is in an elliptical orbit about Mars with a periapsis of  $\sim 150$  km, apoapsis of  $\sim 6000$  km and orbit period of  $\sim 4.5$  hours. The orbit precesses about Mars such that all local times (LT) will eventually be observed, allowing in-situ measurements of all of the key plasma regions at Mars on the day and nightside.

The Langmuir Probe and Waves (LPW) instrument onboard MAVEN consists of two cylindrical Langmuir Probes, each at the end of a  $\sim 7$  m boom positioned on opposite sides of the main spacecraft body and separated by an angular distance of  $\sim 110^\circ$ . The instrument measures several quantities and for this study we focus on the results from the Langmuir Probe (LP) current-voltage (IV) sweeps (*Andersson et al., 2015*).

During one LP subcycle, the LPW instrument measures one IV curve from one of the probes, from which various plasma properties can be derived, including electron density ( $N_e$ ), electron temperature ( $T_e$ ) and spacecraft potential ( $V_{sc}$ ) (see for example *Mott-Smith and Langmuir (1926)*, *Allen (1992)*, *Brace (1998)*). A voltage is applied to one of the probes (1 or 2), and the resulting current to that probe measured. The voltage is sequentially stepped through 128 values, with the corresponding current measured at each step. The LPW fitting method is described in detail by *Andersson et al. (2015)* and *Ergun et al. (2015b)*. Densities as low as  $\sim 100 \text{ cm}^{-3}$  are measurable by LPW, which were not detectable by any previous remote sensing measurements. Currently, electron temperatures derived from the LPW instrument are thought to represent an upper limit to  $T_e$  due to sensor surface material characteristics and atomic oxygen surface contamination of the probes, particularly at  $T_e$  below  $\sim 0.15 \text{ eV}$  (1650 K). This should be taken into account for the remainder of this study and the reader is directed to *Ergun et al. (2015b)* for more information.

The data analyzed in this study span a time range of October 2014 through May 2015. MAVEN periapsis sampled the nightside of Mars during the months of approximately November 2014 through February 2015 with higher altitude measurements obtained on the nightside several months either side of this. MAVEN has not yet sampled the dayside extensively and these data are omitted for a later study once available. A case study of dayside electron density and temperature profiles is however available in *Ergun et al. (2015b)*.

For this study local time is referenced with respect to the Mars Solar Orbital (MSO) coordinate frame. We define noon (12 LT) as pointing directly from the center of Mars to the Sun; midnight (24 LT) is opposite to this. Dusk (18 LT) is in the positive Y MSO direction; dawn (6 LT) is in the negative Y MSO direction. The Sun is the main driver of the Martian ionosphere making

the MSO reference frame appropriate for this study. LT was used instead of SZA because SZA will divide data up using concentric rings as projected onto the planet. The lack of solar driving on the nightside means we may expect to see dawn-dusk asymmetries, which will average out when binned by SZA. It should be noted that the Z direction in the MSO frame is offset from the planet rotation axis by  $\sim 24^\circ$ .

We define nightside to lie between 18 LT through midnight to 6 LT and select all data for positive latitudes (i.e. the northern hemisphere, in MSO coordinates) within this range for altitudes below 600 km. Orbit coverage below 600 km for November through February is shown in Figure 5.1, where color represents altitude. Inbound orbits are to the south side of all periapses; outbound to the north. Because all observations within this study lie in the northern hemisphere, we assume that effects from crustal magnetic fields are small and are neglected here (eg *Acuña et al. (2001)*). At an altitude of 120 km the Sun does not set until an SZA of approximately  $105^\circ$ , which is equivalent to  $\sim 19$  LT. Hence this study spans both the “twilight” and nightside ionosphere.

After the removal of unreliable sweeps the data set consists of just over 87,000 individual IV sweeps. Extreme spacecraft charging and cases where the automated fitting software could not obtain reliable fit values constituted unreliable sweeps. Further, the data were “filtered” so that only the most confidently fitted values are presented here. These have been binned into 12 bins of 1 hour length, and 10 (20) km altitude bins for electron density (temperature).

## 5.4 Electron Density And Temperature Observations

### 5.4.1 Individual Orbit Profiles

An example of the electron density and temperature profiles from one nightside periapsis pass that occurred at the dawn terminator between 2014-12-02T22:09 and 2014-12-02T22:32 UTC are presented in Figure 5.2. The blue line represents the inbound part of the orbit and is on the nightside; red represents the outbound and is on the dayside. MAVEN approached periapsis from the southern magnetotail, crossing into the northern hemisphere before reaching periapsis.

Periapsis was approximately at the dawn terminator and the outbound leg of the orbit was close to the north pole on the dusk side of Mars in sunlight. This orbit has been highlighted in Figure 5.1 by the thick black line. The nightside profile shows large variability and dynamic behavior with electron densities two to three orders of magnitude lower than the dayside in this example. Representative error bars are shown at several altitudes by horizontal black lines.

#### 5.4.2 Statistical Profiles

The nightside median electron density and electron temperature profiles binned as functions of altitude and local time as described earlier are presented in Figures 5.3a) and 5.3b). Each line represents the median electron density or temperature for a certain local time, which is denoted by the line color. Dark red corresponds to 18 LT and is at dusk. Progressively lighter reds represent increasing LT, up to midnight (24 LT). Blue colors represent the dawn side, with light to dark blues representing 1 to 6 LT.

The electron density below  $\sim 200$  km statistically increases with decreasing altitude, with peaks in electron density of  $\sim 3 \times 10^3 \text{ cm}^{-3}$  or greater observed between 150 and 180 km for 18, 19 and 6 LT. These are most likely sunlit peaks and a result of EUV photo-ionization, although plasma transport across the terminator may play a role as well. This density altitude trend is not necessarily the case for individual orbits as shown in Figure 5.2. Above  $\sim 200$  km the statistically observed electron densities follow an almost vertical profile. Individual orbits show that above  $\sim 200$  km, significant structures and “blobs” of enhanced density over small altitude ranges are observed. The statistical result demonstrates that these structures and “blobs” do not appear to have any altitude dependencies.

At local times of 18 LT to  $\sim$  midnight the electron density decreases due to the lack of solar EUV and the effect of recombination. The lowest densities are observed just after midnight at local times of approximately 1 - 2 LT. After  $\sim 2$  LT electron density starts to increase again. At 6 LT the peak electron density is  $\sim 2 \times 10^4 \text{ cm}^{-3}$ , slightly larger than that at 18 LT. Due to the MAVEN orbit, observations made at dawn are at higher latitudes and closer to the pole than those

made at dusk. Differences in terminator flow at the pole versus mid latitudes may contribute to the observed profile differences at 18 and 6 LT.

At high altitudes ( $>200\text{-}300$  km) where the density is low ( $\lesssim 1000$  cm $^{-3}$ ), temperature increases ( $\gtrsim 0.15$  eV (1650 K)). The warmest temperatures are  $\sim 0.7$  eV (7700 K) and are observed at  $\sim 2 - 3$  LT above  $\sim 400$  km. The lowest temperatures ( $< 0.15$  eV (1650 K)) are observed below 200 km. Given that below  $T_e \sim 0.15$  eV (1650 K) the LPW  $T_e$  measurement is an upper limit, these temperatures could be as low as the expected neutral temperature of 200-300 K ( $\sim 0.02$  eV) (*Nier and McElroy, 1977*). An asymmetry between dawn and dusk temperatures exists for  $19 < \text{LT} < 5$ , with dawn temperatures being approximately 1.5 - 2 times warmer than at dusk.

## 5.5 Discussion And Modeling Effort

The dayside ionosphere is sustained primarily by the photo-ionization of neutral atoms by EUV sunlight (eg *Chapman (1931a,b)*; *Nagy et al. (2004)*; *Witasse et al. (2008b)*; *Withers (2009)*). This is naturally not the case on the nightside, and the rapid recombination of the ionospheric ions with free electrons rapidly reduces the densities of both. Analysis of ion composition from the Neutral Gass and Ion Mass Spectrometer (NGIMS) instrument onboard MAVEN shows that for  $45^\circ < \text{SZA} < 60^\circ$   $\text{O}_2^+$  is the dominant ion below  $\sim 300$  km and that  $\text{CO}_2^+$  is the second dominant ion below  $\sim 220$  km. Above 300 km  $\text{O}^+$  is the dominant ion (*Withers et al., 2015*). We assume that these profiles are constant up to SZA  $90^\circ$  (dusk) at which point we assume the ionosphere is no longer driven by solar EUV and evolves as observed in the LPW data. In Figure 5.4a) we show a simple simulation of the rate at which the plasma density drops once production ceases and as an example, initial  $\text{O}_2^+$  or  $\text{CO}_2^+$  densities of  $\sim 10^6$  cm $^{-3}$  are reduced to  $\sim 10^2$  cm $^{-3}$  after 12 hours. We assume a purely  $\text{O}_2^+$  or  $\text{CO}_2^+$  ionosphere and that the electron density ( $N_e$ ) is equal to the ion density ( $N_i$ ) for each case. The recombination rate is given by  $N_e \times N_i \times k_i$ . Recombination rate coefficients,  $k_i$ , were taken from *Fox and Sung (2001)*. Peak densities are observed between 150-180 km in Figure 5.3a) and here we simulate the ion density for this altitude range. An electron temperature of 300 K (0.02 eV) was hence assumed. The recombination rates for  $\text{O}_2^+$  and  $\text{CO}_2^+$

are inversely proportional to  $T_e$  and for comparison, an electron temperature of 1000 K (0.1 eV) resulted in densities of  $\sim 5 \times 10^2 \text{ cm}^{-3}$  after 12 hours.

The nightside ionospheric electron densities can have peak values of a few thousand  $\text{cm}^{-3}$  below  $\sim 200$  km even for late local times as shown in Figure 5.3. Given that these densities are a factor of 10 or more greater than those expected from recombination alone as shown in Figure 5.4 there is a clear need for an additional ion source to sustain the night side ionosphere. LPW has provided measurements of the low density ionosphere for the first time and as such two possible source processes are evaluated in this study.

First we assume quasi-neutrality and that the electron density loss at altitudes above 200 km, as the planet rotates, is returned to the ionosphere with a total ion density profile matching that of the electrons. Second we assume an electron precipitation source. The Combined Atmospheric Photochemistry and Ion Tracing (CAPIT) 1D photochemical model (*Andersson et al.*, 2010) was used to evaluate these possibilities within an assumed  $45^\circ$  magnetic field and a neutral collisionless atmosphere. The model solves key photochemical reactions for the major ion species (here  $\text{O}^+$ ,  $\text{O}_2^+$ ,  $\text{CO}_2^+$  and  $\text{N}_2^+$ ), with total initial ion density profiles matching those observed at 18 LT in Figure 5.3a).

### 5.5.1 Downward Flowing Ions

If all ions above 200 km were to flow downward into the ionosphere, could they sustain the ionosphere below this?  $\text{O}^+$ ,  $\text{O}_2^+$  and  $\text{CO}_2^+$  are the dominant ion species and as such each of three simulation runs assumed one of these ion species only with density profiles equal to the electron density profiles observed above 200 km at 18 LT in Figure 5.3. An infinite supply of downward flowing ions were available in the simulation that were able to charge exchange with neutrals via photochemical reactions to produce other ion species. We compare density profiles at 18 and 19 LT and assume that the density lost above  $\sim 200$  km must travel on average 300 km downward to reach an altitude of 200 km over the course of one hour. This constitutes a downward flow speed of  $\sim 80 \text{ km s}^{-1}$ .

Downward flowing  $O_2^+$  or  $CO_2^+$  ions at  $80 \text{ ms}^{-1}$  were unable to sustain the observed densities below 200 km due to frequent collisions with the neutral atmosphere and recombination. Downward flow speeds of  $800 \text{ ms}^{-1}$  could maintain a purely  $O_2^+$  or  $CO_2^+$  ionosphere at the density at which the infinite supply of ions enter the top side of the simulation. This flow speed is 10x greater than the data suggest, and the resulting ionospheric composition is incorrect. Downward flowing  $O^+$  ions at  $80 \text{ ms}^{-1}$  were able to sustain the observed densities however the resulting composition was incorrect, lacking any  $CO_2^+$  ions. Due to these disagreements with NGIMS observations, we deem it unlikely that downward flowing ions play an important role in sustaining the nightside ionospheric densities observed below 200 km.

### 5.5.2 Precipitating Electrons

An ion source was included to represent ionization via precipitating electrons. An electron energy spectrum as measured by the Solar Wind Electron Analyzer (SWEA) instrument (*Jakosky et al., 2015a*) on MAVEN was used to produce ionization rate profiles as input to the CAPIT code. A representative nightside spectrum observed at  $\sim 500 \text{ km}$  on 2014-12-05T05:11:59 UTC was used and is shown in Figure 5.4b). Pitch angle and energy distributions for downward flowing electrons as measured by SWEA were taken as inputs to the Mars Monte Carlo Electron Transport (MarMCET) model (*Lillis et al., 2009, 2011; Lillis and Fang, 2015*) to derive the ionization rate profiles used in this study. The neutral atmosphere for the MarMCET model was taken from the Mars Global Ionosphere-Thermosphere Model (M-GITM) (*Bougher et al., 2015a*) for equinox, equatorial, solar moderate conditions and is adequate for comparison purposes in this paper. Plasma transport processes were ignored.

The densities observed between  $\sim 19 - 5 \text{ LT}$  below 200 km were sustainable (and at some LT greater than the observed densities) when precipitating electrons were included and simulation results are shown in Figure 5.4c). The dashed green line shows the initial total ion density profile for one simulation run which was chosen to match the observed electron density profile at 18 LT. The dashed purple line shows the equilibrium density profile of the simulation run, which is

obtained after  $\sim 25$  minutes. Below  $\sim 170$  km the simulation profile is greater than the observed densities by a factor of up to  $\sim 10$ , depending on LT. The cause of this is thought to be the use of a constant precipitating electron source within the simulation. SWEA observations show large dynamic variations in energy flux and in some cases the observed spectra are sporadic in nature. As such, the constant precipitating source used here most likely causes an overestimate in the modeled nightside densities.

### 5.5.3 Electron Temperature

The anti-correlation between density and temperature is expected; at low altitudes the neutral and electron densities are high and collisions dominate, reducing the electron temperature to that of the neutral atmosphere. Above  $\sim 180$  km neutral densities decrease and collisions become less frequent. Electron temperature increases almost steadily above  $\sim 180$  km suggesting that plasma processes dominate here, heating the electrons. Comparison to dayside temperature profiles close to the sub solar point in *Ergun et al. (2015b)* shows that temperatures in the deep Martian tail (approximately  $22 < LT < 4$ ) above  $\sim 300$  km are greater than those on the dayside by factors of  $\sim 1.5$ -2. Current MAVEN coverage is limited and it will be interesting to see if this is true for all nightside LT and latitudes at a later time in the mission.

## 5.6 Conclusions

The first nightside electron temperature profiles at Mars are presented as functions of altitude and local time. Particular focus in this study was given to the corresponding nightside electron density profiles, which are the first in-situ electron density profiles to be measured on the nightside of Mars. The LPW instrument is able to resolve densities as low as  $\sim 100 \text{ cm}^{-3}$  and observed the low density, dynamic behavior of the nightside ionosphere.

The observed electron densities below  $\sim 200$  km are a factor of 10 or more greater than those expected if recombination alone were to act on the nightside of Mars and demonstrate the need for an ion source to maintain the nightside ionosphere. A collisionless version of the 1D CAPIT

code was used to investigate the effects of downward flowing ions and precipitating electrons to determine if either of these could maintain the observed ionosphere below 200 km. Downward flowing ion profiles were based on the observed electron densities after assuming quasi-neutrality. Ionization rates were calculated using the MarMCET code using measured electron energy spectra from the SWEA instrument on MAVEN.

Based on these simulations, downward flowing ions cannot sustain the ionosphere at the observed densities below 200 km due to frequent collisions with neutrals at these altitudes. Precipitating electrons appear to play an important role in sustaining the nightside ionosphere and were able to reproduce the observed nightside densities below 200 km. These latter findings are in agreement with previous conclusions drawn from analysis of earlier nightside datasets observed by previous missions at Mars.

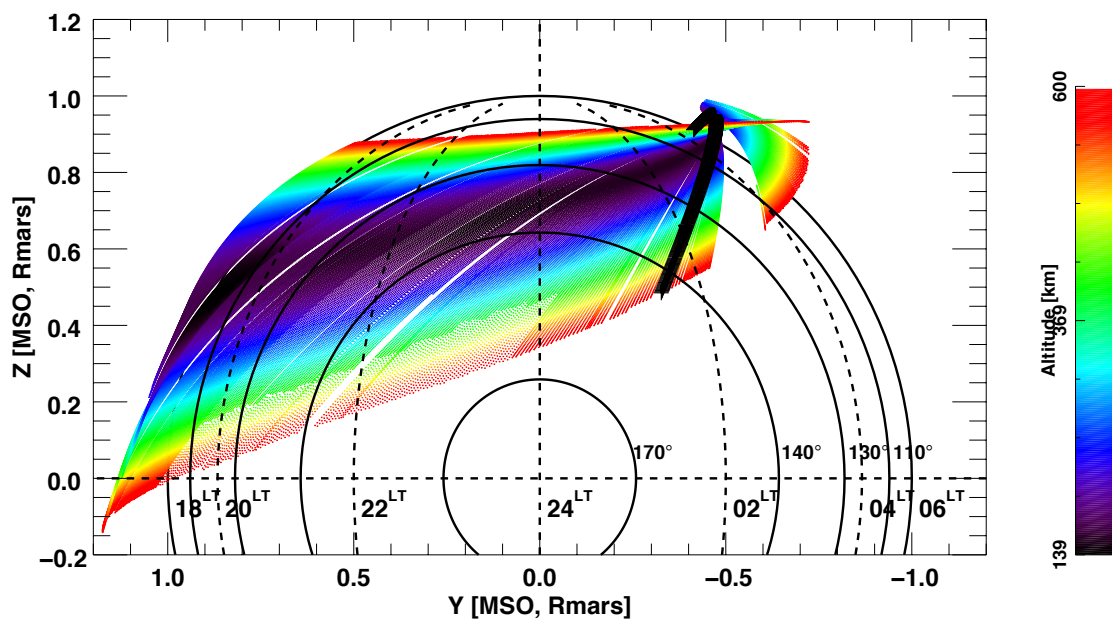


Figure 5.1: MAVEN orbit coverage for November 2014 through February 2015 in the MSO coordinate frame for altitudes below 600 km. Color represents altitude in km. Curved dashed lines represent the labeled local times as projected onto the Y-Z plane. Solid curved lines represent SZA as projected onto the Y-Z plane. The direction of travel for any individual orbit is in the +Z direction. The thick black line represents the orbit track corresponding to the electron density and temperature profiles shown in Figure 5.2.

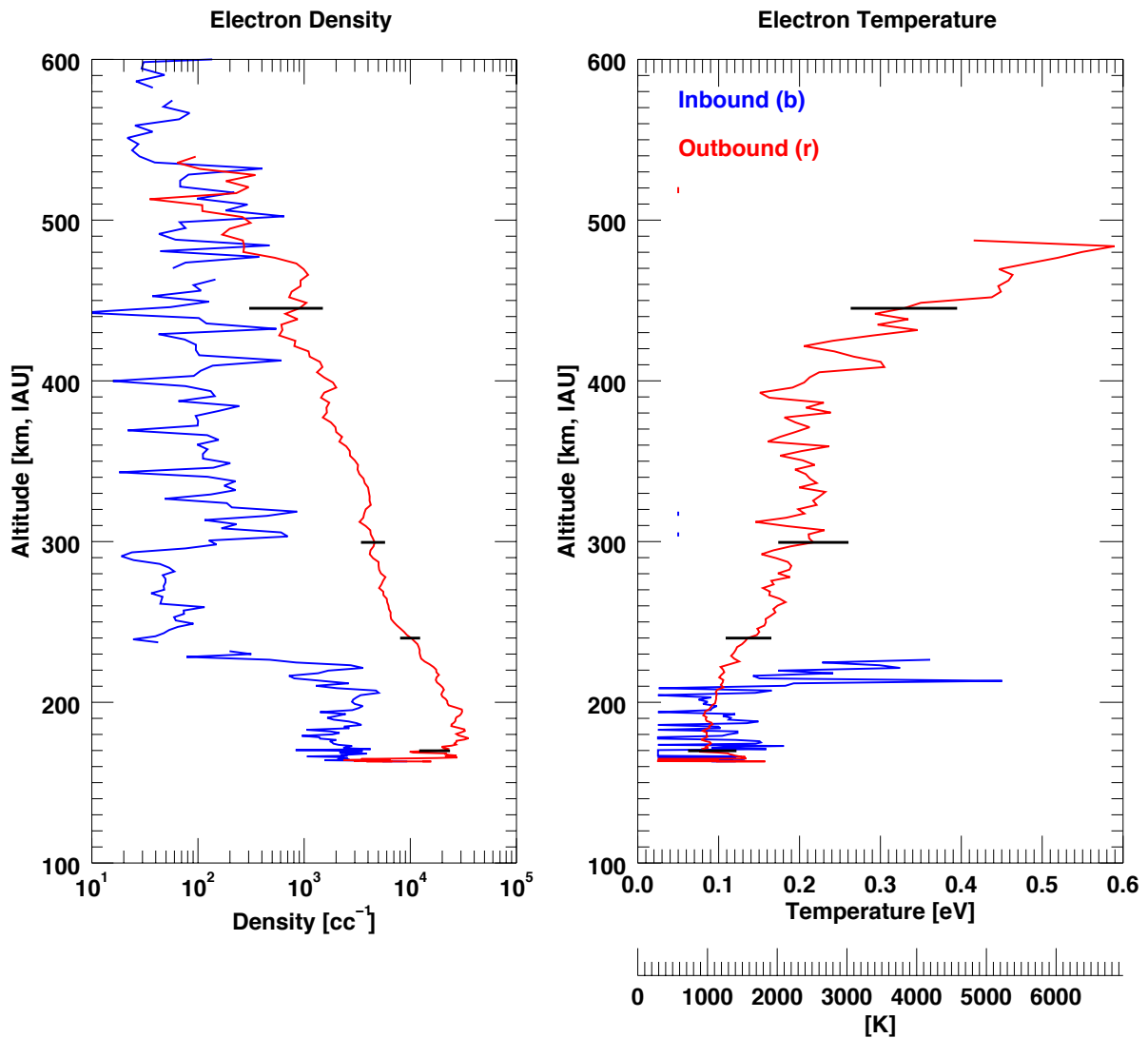


Figure 5.2: Altitude profiles of electron density (left) and electron temperature (right) for one periapsis pass between 2014-12-02T22:09 and 2014-12-02T22:32 UTC. The dawn terminator was approximately at periapsis. The inbound portion of the orbit is colored blue and is on the nightside. The outbound portion is colored red and is on the dayside. Representative error bars are shown as black horizontal lines. Altitude is calculated in the Mars IAU frame, which is referenced to the IAU 2000 Mars Areodetic ellipsoid. Reduced signal-to-noise ratios below densities of  $\sim 200 \text{ cm}^{-3}$  result in LP temperature measurement errors increasing to 100% or more and therefore such temperature measurements are omitted here.

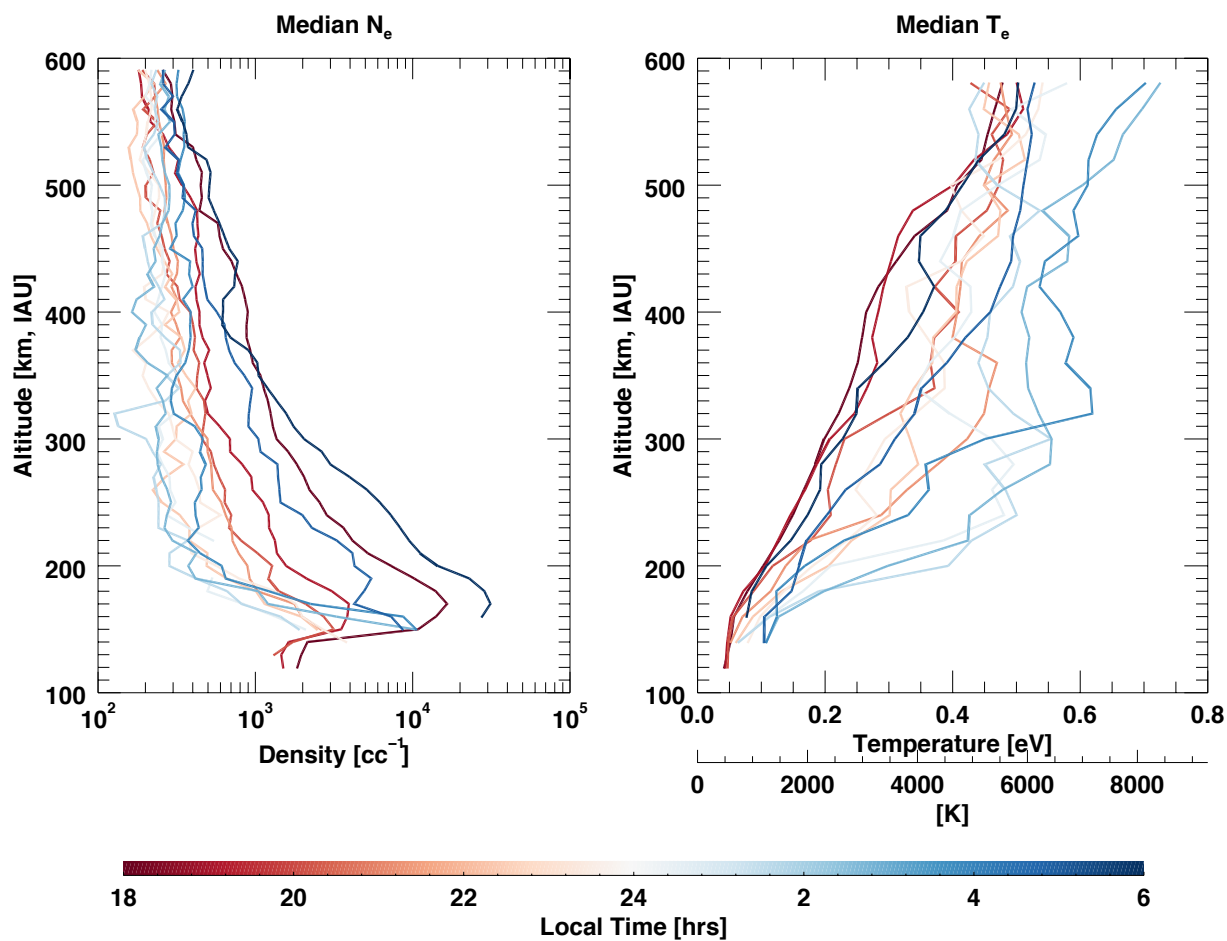


Figure 5.3: Statistical median altitude profiles of electron density (A, left) and electron temperature (B, right). Both binned as described in the text. A local time of 18 corresponds to dusk; 24 to midnight and 6 to dawn.

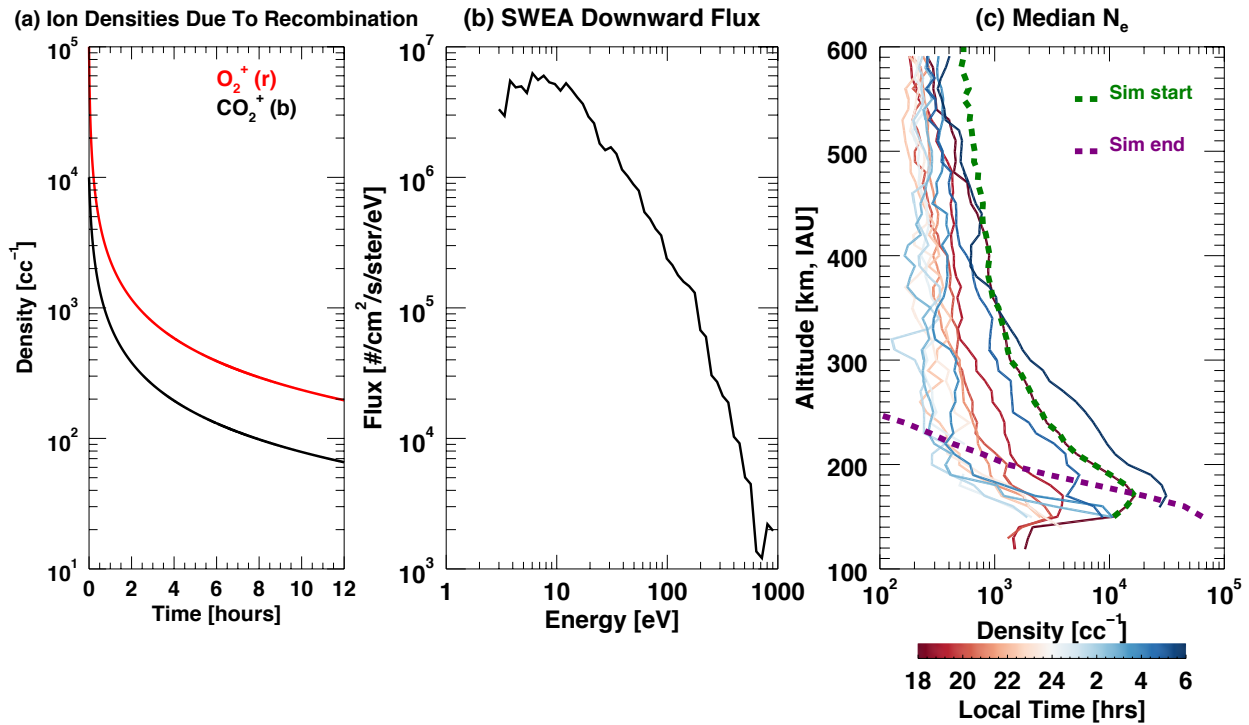


Figure 5.4: (a) Densities for  $O_2^+$  and  $CO_2^+$  ions based on recombination as a function of time. (b) Input spectrum for downward traveling precipitating electrons, as measured by SWEA at  $\sim 500$  km on 2014-12-05T05:11:59 UTC. (c) Median statistical electron densities as in Figure 5.3 with simulation results over plotted as dashed lines. Dashed green shows the input ion density profile; dashed purple shows the resulting equilibrium ion density profile that was obtained after  $\sim 25$  minutes of run time. Precipitating electrons were included as calculated from the SWEA spectrum shown in the middle panel.

## Chapter 6

### Electric and magnetic variations in the near Mars environment

**Submitted:** 31<sup>th</sup> August 2016, reviewer comments received 13<sup>th</sup> October, 2016, Journal of Geophysical Research: Space Science

**Corresponding author:** C. M. Fowler, Laboratory of Atmospheric and Space Sciences, University of Colorado, Boulder, Colorado, USA 80303, christopher.fowler@lasp.colorado.edu.

**Authors:** C.M. Fowler,<sup>1</sup> L. Andersson,<sup>1</sup> J. Halekas,<sup>2</sup> J.R. Espley,<sup>3</sup> R.E. Ergun,<sup>1</sup> D.J. Andrews,<sup>4</sup> J.E.P. Connerney,<sup>3</sup> B. Jakosky,<sup>1</sup>

<sup>1</sup>Laboratory of Atmospheric and Space Sciences, University of Colorado, Boulder, Colorado, USA.

<sup>2</sup>Department of Physics And Astronomy, University Of Iowa, Iowa City, IA 52242, USA

<sup>3</sup>NASA Goddard Space Flight Center, Greenbelt, MD 20771, USA

<sup>4</sup>Swedish Institute for Space physics, Uppsala, Sweden.

## 6.1 Abstract

We present statistical results of the electric and magnetic field wave power observed throughout the Martian magnetosphere by the Mars Atmosphere and Volatile EvolutioN spacecraft from the first 14.5 months of the mission. Wave power in several different frequency bands was investigated and the distribution of this wave power varied as a function of these frequency ranges. The Martian foreshock, bow shock, and magnetic pileup boundaries were observed in the data; lower frequency waves (0.01-0.1 Hz) showed enhancements of magnetic wave power within the sheath whilst higher frequency magnetic and electric field wave power (1-5 Hz, and 1k-5k Hz respectively) showed enhancements in power along the bow shock.

Upstream solar wind density and magnetic field strength were found to enhance electric field wave power by up to 25% along the bow shock and foreshock for lower frequency waves. Higher frequency waves showed similar enhancements driven by solar wind velocity. The upstream solar wind Alfvénic, sonic and magnetosonic mach numbers, and plasma beta, enhanced magnetic field wave power by up to 10% at the bow shock and foreshock. The solar wind interplanetary magnetic field cone angle strongly influenced electric and magnetic field wave power, causing increases of  $\sim 10\%$  at the quasi parallel shock and decreases by similar amounts at the quasi perpendicular shock. This leads to dawn-dusk asymmetries in wave power in the dawn-dusk plane.

Observations of waves within a planetary magnetosphere provide insight into the processes active during the transfer of energy from the solar wind to the planet.

## 6.2 Introduction

The lack of a significant intrinsic magnetic field at Mars and the subsequent interaction of the solar wind with the Martian ionosphere leads to an induced magnetosphere at the planet (e.g. Bertucci *et al.* (2011)). The Martian bow shock (BS) typically lies at a planetocentric distance of  $\sim 1.6$  Martian radii (e.g. Slavin *et al.* (1991); Vignes *et al.* (2000)) - much closer than, for example, the typical terrestrial BS location that lies at  $\sim 14.6$  Earth radii (e.g. Fairfield (1971)) as a result of

the Earth's large intrinsic magnetic dipole field. The magnetosphere of a planet facilitates energy transfer from the solar wind down to the upper atmosphere and ionosphere of the planet.

The first measurements of plasma waves at Mars were made by the Phobos 2 spacecraft (*Grard et al.*, 1989); the Plasma Wave System observed several plasma boundaries including the bow shock (BS), magnetosheath (MS) and a boundary termed 'the planetopause' (the boundary of the planetary obstacle to the solar wind). The planetopause is defined as a magnetic enhancement separating the shocked solar wind plasma from the colder heavier planetary plasma. These boundaries were observed to vary in position over multiple orbits. Within the planetopause the Plasma Wave System identified bursts of waves interpreted as whistler wave modes.

Wave activity in the region of the BS was reported by *Sagdeev et al.* (1990). They proposed that high frequency waves excited at the shock front were due to currents flowing along this front which were subsequently convected downstream to inside of the MS by the solar wind. Cold Martian ionospheric ions diffusing through the planetopause to the MS were thought to generate lower frequency waves observed close to the BS - MS boundary.

Proton cyclotron waves have been observed upstream of Mars by several studies. To the authors knowledge, *Russell et al.* (1990) were the first to report these observations, suggesting that the cause of these waves was the pick up of hydrogen from the hydrogen corona of Mars. *Russell et al.* (1990) also posed that waves observed within the moon Phobos' orbit plane were caused by the moon itself but conclusive evidence could not be ascertained. *Bertucci et al.* (2013) found correlations between observations of waves at the local proton cyclotron frequency made by the Mars Global Surveyor (MGS) spacecraft, and modeled densities of the hydrogen corona at Mars, further supporting the proposition that the Martian hydrogen corona can drive upstream proton cyclotron waves.

Empirical locations of the Martian bow shock have been calculated based on observations by the Mariner 4, Mars 2, Mars 3, Mars 5 and Phobos 2 spacecraft (*Slavin et al.*, 1991). The altitude of the Martian BS was not observed not vary with solar cycle, in contrast to what is observed at Venus. This was attributed to Venus' weak but significant intrinsic magnetic field. Similar analysis

has been carried out by other authors, for example *Vignes et al. (2000)*, who used data from the first year of the MGS mission to determine the empirical locations of the BS and magnetic pile up boundary (MPB). Their results agreed with previous analyses of Phobos 2 data and further confirmed the lack of solar cycle dependence of these boundary locations.

Low frequency (LF) waves have been observed by various authors using magnetic field data from the Mars Global Surveyor (MGS) spacecraft. *Brain et al. (2002)* observed waves upstream of the BS close to the local proton frequency whose amplitudes (occurrence) tended to decrease (increase) with increasing distance from the BS. They also observed whistler waves propagating upstream of the BS when MGS was magnetically connected to the BS. *Bertucci et al. (2004)* observed LF waves either side of the magnetic pileup boundary (MPB). Waves upstream of the MPB were found to be mirror mode waves whilst those downstream were large amplitude fast magnetosonic waves. *Espley et al. (2004)* observed LF compressional waves in the dayside sheath with frequencies many times less than the local proton frequency. These LF waves were much more varied in type on the nightside and were typically transverse with frequencies closer to the local proton frequency.

More recently, LF waves upstream of Mars observed by the Mars Volatile and Evolution (MAVEN) mission were analyzed by *Ruhunusiri et al. (2015)*. They found that Alfvén waves were dominant upstream and in the magnetosheath, with fast waves observed frequently near the BS and MPB. The occurrences of these Alfvén and fast waves varied with upstream solar wind dynamic pressure.

The relatively short mission lifetimes of the early Mariner, Mars and Phobos missions; the lack of a plasma wave instrument or magnetometer on the Mars Express spacecraft, and the Sun synchronous orbit of MGS, has meant previous observations of waves and plasma boundaries within the Martian magnetosphere have been limited in number, spatial, and temporal coverage. MAVEN is the first spacecraft to visit Mars carrying both a magnetometer and electric field instrument and to be in an orbit such that the entire magnetosphere will eventually be sampled.

We present here statistical maps of the magnetic and electric field wave power taken over

the first  $\sim 14.5$  months of the MAVEN mission throughout the Martian magnetosphere. The magnetosphere is seen to respond to various upstream solar wind drivers; the most influential of these are discussed here. The remainder of this paper is as follows: the data set used in this analysis is described in Section 6.3, including caveats of the electric field power spectra data set. Section 6.4 outlines the analysis method used in this study with regards to constructing the presented statistical maps. Statistical maps of electric and magnetic field wave power, and their responses to upstream solar wind drivers, are presented in Sections 6.5 and 6.6. A discussion of these results follows in Section 6.7 before conclusions are presented in Section 6.8.

### 6.3 Data

The MAVEN spacecraft reached Mars in September 2014 and achieved its final science orbit shortly thereafter (*Jakosky et al., 2015a*). Periapsis is typically at 150 km and apoapsis reaches approximately 6500 km in altitude. The elliptical nature of the orbit and subsequent precession about the planet means that MAVEN is able to sample the solar wind on a regular basis, obtaining upstream conditions that drive the downstream magnetosphere and ionosphere. Of interest to this study are data from the Langmuir Probe and Waves (LPW, *Andersson et al. (2014)*), Magnetometer (MAG, *Connerney et al. (2015)*) and Solar Wind Ion Analyzer (SWIA, *Halekas et al. (2015)*)

LPW consists of two  $\sim 7$  m booms separated by an angular distance of  $\sim 110^\circ$ . The instrument alternates between operating as a Langmuir probe measuring IV characteristics and operating as an electric field instrument measuring waves. The designed operation cycle consists of four sub cycles that are performed the same way regardless of measurement cadence. The four sub cycles for the nominal mission are: current-voltage (IV) measurement on boom 1, ‘passive’ (PAS) wave measurement, IV measurement on boom 2, ‘active’ (ACT) wave measurement. The difference between the PAS and ACT wave measurements is that prior to the ACT measurement a weak white noise broadcast (sounding) is performed, designed to stimulate waves at the local plasma frequency. Electric field power spectra are measured at cadences between 2 and 128 s depending on the instrument mode of operation. MAG is a fluxgate magnetometer that measures the vector magnetic

field at a rate of 32 Hz. SWIA is an electrostatic top hat analyzer that measures ion fluxes from 25 eV up to 25 keV. The coarse data used in this study cover a  $360^\circ \times 90^\circ$  field of view at a time resolution of 4 s.

LPW electric field wave spectra are available for the first  $\sim 14.5$  months of the MAVEN mission, from 2014-10-10 to 2015-12-09 UTC. Due to a change in instrument operation wave spectra are not available on a regular basis after these dates. The bulk of the Martian ionosphere is typically observed below 600 km and as such only data above 600 km were analyzed in this study. Taking into account this altitude range, the LPW data set consists of 3,308,714 spectra (1,415,620 active and 1,893,094 passive; Section 6.3.1 outlines the differences between the active and passive spectra). MAVEN orbit coverage was such that the spacecraft sampled the upstream solar wind for approximately 8.5 months of this data set, between roughly December 2014 to mid March 2015, and June 2015 to November 2015. Analysis utilizing the upstream solar wind drivers is subsequently limited to these time ranges, resulting in a total of 2,051,270 spectra (920,612 active and 1,130,658 passive) available for analysis. Before detailing the specifics of our analysis we first discuss the general properties of the LPW wave spectra and outline important caveats when analyzing this data set. As a side note, caveats for the LPW IV characteristics are discussed in a companion paper to be published in this issue (*Andersson et al.*, 2016c).

### 6.3.1 Description and caveats of the LPW wave spectra dataset

For the first  $\sim 14.5$  months of the MAVEN mission the LPW instrument operated in a mode such that electric field wave spectra were obtained along with IV characteristics. Here we discuss caveats of the wave spectra data products; discussion of the IV characteristics can be found in *Ergun et al.* (2015a); *Andersson et al.* (2014).

The LPW wave spectra are available from 10<sup>th</sup> October 2014 through till 9<sup>th</sup> December 2015, at which point a change in instrument operation mode meant that the sub cycles producing the wave spectra were no longer utilized on a regular basis. The electric field wave spectra are produced by measuring the potential difference as a time series between the two LPW booms,

which are separated by a distance of 12.68 m. The instrument measures the electric field the same way in both the PAS and the ACT sub cycles. Both sub cycles produce a 64 point electric field DC time series and for higher frequencies an onboard Fast Fourier Transform (FFT) is applied to three different frequency ranges: low ( $LF_{lpw}$ , 0.25 Hz - 496 Hz), medium ( $MF_{lpw}$ , 16 -  $3.2 \times 10^4$  Hz) and high ( $HF_{lpw}$ , 1 kHz - 2 MHz) frequencies. The subscript *lpw* denotes that these ranges apply to the LPW L2 spectra as apposed to the frequency ranges used for the study presented in Section 6.4 onwards in this paper. During the PAS sub cycle a burst system is available to record the largest amplitude electric field time series in the respective frequency bands. Due to telemetry constraints the availability of the burst time series data is limited. As mentioned the main difference between the PAS and ACT sub cycles is that for the ACT sub cycle low power white noise is broadcast just prior to capturing the electric field measurement. This white noise is broadcast to increase the probability of measuring the Langmuir (plasma) line and thereby obtain an absolute plasma density measurement. Typically multiple FFTs from the same subcycle are averaged during onboard processing when capturing the PAS  $MF_{lpw}$  and  $HF_{lpw}$  spectra and the number of FFTs averaged can be changed. For the ACT sub cycle only the first FFT after the white noise broadcast is recorded. This difference between ACT and PAS onboard processing can lead to slight differences between spectra captured at neighboring points in time. This is particularly true at high altitudes when the cadence of L2 spectra can be up to 128 s. An example can be seen just to the left of circle 2 in Figure 6.1A and B at approximately  $10^3$  Hz.

Example wave spectra, with to be discussed highlighted caveats, are shown in Figure 6.1. LPW wave spectra from ACT and PAS sub cycles are shown in panels A and B in Figure 6.1 respectively. Panel C shows the local electron density as determined by the local plasma line from the electric field waves measurement in black, and the Langmuir Probe derived density in red; panel D shows the percentage difference between these two quantities. ‘ $W_n$ ’ stands for waves derived electron density; ‘ $N_e$ ’ stands for Langmuir Probe derived density in this panel. The green and blue horizontal lines in panel C mark densities of  $1 \times 10^3$  and  $2 \times 10^4$   $\text{cm}^{-3}$ . The vertical black lines mark where the Langmuir Probe derived densities cross these values. Panel E shows the spacecraft

altitude in the International Astronomical Union (IAU) frame. The ACT and PAS spectra both span a frequency range of just below 1 Hz - 2 MHz but are composed of three separate, merged spectra spanning smaller frequency ranges.

### 6.3.2 Combining the $LF_{lpw}$ , $MF_{lpw}$ and $HF_{lpw}$ spectral ranges

The noise floor for each of the three individual frequency bands ( $LF_{lpw}$ ,  $MF_{lpw}$  and  $HF_{lpw}$ ) is frequency dependent. These three bands are combined to produce the L2 data products shown in Figure 6.1A and B. This noise floor is present in the form of three horizontal bands at constant frequency, close to  $\sim 500$  Hz,  $\sim 2000$  Hz and  $\sim 2$  MHz in the final L2 product and an example of this discontinuity is highlighted by circle 1 in Figure 6.1. The three individual frequency bands partially overlap in frequency space and the frequency bin sizes at these regions of overlap are different in size due to the quasi logarithmic scaling used in frequency space. As such, no further processing is carried out when the  $LF_{lpw}$ ,  $MF_{lpw}$  and  $HF_{lpw}$  spectra are combined; they are simply ‘cut’ and joined at empirically determined frequencies to produce the continuous spectrum in the L2 data products shown in Figure 6.1. When electric field waves are present the three separated frequency bands are well (but not perfectly) calibrated as shown by circle 2 in Figure 6.1 where there is no significant change in wave power across the two frequency bands at  $\sim 500$  Hz.

### 6.3.3 Flagging low quality spectra

Spectra of low quality have been removed resulting in ‘empty’ blocks within the final L2 spectra. Examples are highlighted by circles 3 and 4 in Figure 6.1, here shown by black blocks in the spectra. The degradation of spectra can arise for several reasons and we discuss the most important here. The primary source of spectra degradation arises from instrument induced DC electric fields. When wave spectra are captured, the instrument is operated as a ‘reverse Langmuir probe’. Rather than applying a voltage to one of the probes, and measuring the resultant current collected by that probe, a current is applied to both probes, and the resultant voltages on each measured. There is an optimum range of ‘bias’ currents that should be applied to each probe whereby voltage

is approximately proportional to the natural log of current and there is a corresponding unique voltage value that can be observed. This region is known as the ‘ramp’ or ‘electron temperature fit’ region on a Langmuir Probe IV curve (see for e.g. *Ergun et al. (2015a)*). If the applied bias current lies outside of this optimum range then voltage is almost constant with respect to current and there are many non-unique voltage values that can accompany this bias current value. Due to differences in the LPW probe surface characteristics these optimum bias currents are slightly different for each probe. If one, or both, of these applied bias currents lies outside of their optimum ranges then the corresponding measured voltages for both probes can swing to large values, typically inducing large instrumental DC electric fields that swamp any real ambient electric fields. The low density plasma environment at Mars makes this optimum bias current region narrower than on previously flown Langmuir Probes at Earth for example. The highly variable nature of the Martian plasma environment throughout a MAVEN orbit further increases the difficulty in applying the optimum bias currents at all times during one orbit. Subsequently the blank spectra marked by circles 3 and 4 in Figure 6.1 can be common, particularly during the early mission when calibration was ongoing. These large instrumental DC electric fields can be identified within the LPW ancillary data and are used to identify and flag these low quality spectral measurements.

Minor attitude control thruster firings typically occur on the outbound segment of each orbit. These events are recorded within MAVEN ancillary engineering data files which are used to identify thruster firing events within the LPW wave spectra.

LPW does not record wave spectra when capturing high cadence burst data but this happens less frequently than the inducement of instrumental DC electric fields and attitude control thruster firings. The lowest measured frequency bin for the LPW wave spectra usually contains noise and is typically not useful: the useable frequency range is subsequently quoted as upwards of  $\sim 1$  Hz. Additional noise can also be present below  $\sim 100$  Hz as is discussed in Section 6.3.6.

### 6.3.4 Wave sounding

The operation and onboard processing of the ACT and PAS measurements are identical with the difference of the weak white noise broadcast prior to the ACT measurements. PAS spectra are typically an average of multiple FFTs; ACT spectra consist of the single FFT processed immediately after a wave sounding. As stated above this sounding is an attempt to excite the local plasma line, allowing the local density to be derived with high accuracy. The instrument upper frequency range of 2 MHz limits the measurable upper density range to below about  $4 \times 10^4 \text{ cm}^{-3}$ . Circle 5 in Figure 6.1 demonstrates the plasma line observed in the ACT spectra. When comparing ACT and PAS spectra it is clear that the sounding is a success and is an important instrument capability. A review of the first wave sounding density measurements observed by LPW and MAVEN are presented by *Andrews et al.* (2015), who observed influences from local crustal magnetic fields that are consistent with previous observations at Mars. For the MAVEN mission the density values derived from the waves measurements are held as the ‘gold standard’ for all plasma density measuring instruments.

The LPW instrument unintentionally amplifies measured electric field signals for waves that have wavelengths close to the sensor size. This translates to amplified wave power at high frequencies and is only an issue at densities above  $\sim 1 \times 10^4 \text{ cm}^{-3}$  when the corresponding plasma frequency is high. The derived plasma density is a function of frequency and not signal amplitude. Somewhat fortunately this allows for an accurate determination of the local plasma line: the enhancement in measured power typically makes it easier to determine the local plasma line in the wave spectra. This effect occurs for the PAS and ACT sub cycles, resulting in amplified wave power at densities close to and above  $\sim 1 \times 10^4 \text{ cm}^{-3}$ . The effect is similar to that observed on the Polar satellite (*Kolesnikova et al.*, 2001; *Kolesnikova and Beghin*, 2001). Within the instrument the signal amplitude grows to the instrument limit and distortion / clipping of the signal occurs. This results in aliasing or ‘ghost peaks’ in the derived FFT wave spectra throughout the full frequency range of the instrument all the way into the LF range. Examples are highlighted in panels A and B in Figure 6.1 by circle 6; note the corresponding large electron densities in panel C. The dominant

wave power during these events remains in the local plasma line and so the local electron density can still be derived to high accuracy.

For densities greater than  $\sim 4 \times 10^4 \text{ cm}^{-3}$  the plasma line lies above the instrument frequency range. The effect of signal amplification still occurs and aliasing and ghost peaks are still present in the derived FFT wave spectra despite the absence of the real local plasma line. Such densities are typically only encountered close to the sub solar point at low altitudes and can be identified based on spacecraft position. If the corresponding LP derived electron density is available, this can be used as a further proxy to identify times when the density approaches  $\sim 4 \times 10^4 \text{ cm}^{-3}$ . During these time periods, when density approaches or is greater than  $\sim 4 \times 10^4 \text{ cm}^{-3}$ , the waves derived density should not be used as the density lies outside of the instrument measurement range.

### 6.3.5 Effects of the spacecraft wake

The LPW instrument is one of the first to demonstrate an effect produced by the spacecraft wake as a result of the large dynamic range of different plasma conditions encountered by the MAVEN spacecraft. Langmuir waves prefer low density regions and they can accumulate in density cavities (e.g. *Ergun et al. (2008); Malaspina (2010)*). The sounding feature of the LPW instrument is designed to excite Langmuir waves and circle 5 in Figure 6.1 demonstrates this. As the Debye length of the local ambient plasma shortens it approaches the characteristic size of the spacecraft and spacecraft wake. The density in the spacecraft wake is a factor of  $\sim 2$  lower than the ambient plasma and as a result of the sounding, Langmuir waves accumulate in the spacecraft wake cavity and have much larger power than the non trapped waves in the ambient plasma. In panel C of Figure 6.1 the density measured by the LP is compared to that derived from the waves measurements. Below densities of  $\sim 1 \times 10^3 \text{ cm}^{-3}$  and upwards of  $2 \times 10^4 \text{ cm}^{-3}$  the two methods agree very well, within  $\sim 25\%$ . Between the horizontal lines L1 and L2 the density derived from the waves measurements is lower by a factor of up to  $\sim 2$ . This effect may exist on other missions but there are key aspects that have allowed the MAVEN mission to identify this: (1) the spacecraft is flying through a plasma where the Debye length is comparable to the spacecraft size, (2) multiple instruments measure the

plasma density allowing density gradients to be compared, and perhaps most importantly (3) due to the signal amplification discussed above the LPW instrument measures the true density at small Debye lengths. Clear evidence of spacecraft wake effects can be seen from the anomalous density jump before and after crossing line L2 in panel C of Figure 6.1. None of the other plasma density measuring instruments on the spacecraft observe such a density jump, indicating that the Langmuir waves before and after this jump have two different sources with a density difference of  $\sim 2$ . This is explained by the Langmuir waves that are observed between lines L1 and L2 originating from within the spacecraft wake. There are times when the Langmuir waves originating from the spacecraft wake and ambient plasma appear to co-exist. Most importantly the waves derived density provides a baseline for the minimum ambient plasma density and between  $\sim 1 \times 10^3$  and  $2 \times 10^4 \text{ cm}^{-3}$  the waves derived densities may be up to a factor of  $\sim 2$  lower than the true ambient plasma density.

### 6.3.6 Low frequency noise

The LPW subcycle prior to the waves measurement ends with setting the probe that has just performed an IV sweep to the spacecraft potential. When the waves measurement starts the potential on this sensor then floats to the ambient plasma potential and this coupling between the sensor and ambient plasma to achieve equilibrium takes time. The onboard FFT neglects the first two data measurements to account for this ‘equilibrium settling time’. However, under certain plasma conditions this settling time is longer than expected and as a result a DC signal is present at the start of the electric field time series measurement. When present the onboard FFT of this DC signal produces a significant, low frequency signal in the power spectrum. Ground data processing blocks out some such times (as seen by circle three in Figure 6.1) but the filter is set modestly such that if single LF spectra are removed, neighboring spectra should be treated with caution. Plasma conditions together with spacecraft illumination in the central Martian magnetotail often exhibit these conditions.

At high densities the ACT subcycle can contain low frequency instrument noise which has been confirmed within the LF time series data. The signature within the onboard FFT can manifest

itself as near constant power present below frequencies of  $\sim 100$  Hz. This noise varies in strength; an example is highlighted by circle 7 in Figure 6.1A. This noise can be identified when comparing ACT and PAS wave spectra.

The cadence between the individual wave spectra in the L2 data product depends on the operation mode of the LPW instrument which varies as a function of MAVEN's altitude. Typically, higher resolution data is available at periapsis, at a cadence of 2s. At higher altitudes the resolution in time becomes coarser (due to telemetry restrictions and subsequently changes in instrument mode) and spectra are typically available every  $\sim 128$  s above 2000-3000 km, depending on the exact instrument mode being run at the time.

## 6.4 Analysis method

This study utilized data from several instruments on board MAVEN. The LPW wave spectra are typically the most constrained in cadence and so MAG and SWIA measurements were paired to the LPW data set. For each LPW spectral measurement, the closest MAG and SWIA measurements in time were paired to this. MAG data were required to lie within 5 s of an LPW wave spectral measurement; SWIA data had to lie within 180 s. The lower constraint for SWIA arises because the LPW wave spectra are averaged onboard over a cadence of 128 s at apoapsis; typically SWIA measures at 4 s cadence but occasional data gaps are present. The lower timing restraint helps reduce the number of gaps in the final data set. In this example, a single LPW spectrum is an onboard average of multiple spectra taken over 128 s; we thus deem any errors that arise from the lower LPW-SWIA timing constraint as comparable to or less than any errors introduced in the LPW spectra due to the onboard averaging of multiple spectra. Solar wind parameters for the second part of the data analysis were calculated as an average value for each orbit when MAVEN sampled the solar wind. These parameters were also paired to LPW spectral measurements, and were required to lie within 5 hours of each other. MAVEN's orbit is approximately 4.5 hours long and we assume that the solar wind does not change significantly over the course of one orbit. See *Halekas et al.* (2016) for more information on how the upstream solar wind parameters are

calculated.

Statistical maps were generated from this dataset as a function of MAVEN position in the Motional Solar wind Electric field (MSE) frame. The rotation into the MSE frame assumed that solar wind velocity lay entirely in the radial direction outwards from the Sun. Aberration due to Mars' orbital motion about the Sun was not taken into account, leading to an error in solar wind velocity direction of  $\sim 4^\circ$ , which was deemed negligible for this study. Statistical maps were compiled in the three planes: X-Z, X-Y and Y-Z. Instead of simply compressing the third axis within each map, a more accurate binning method was used. The Y-Z map was split into four sections, based on dividers at  $45^\circ$  to the  $Z = 0$  line. The boundaries were labelled north (N), south (S), dawn and dusk, as shown in panel A in Figure 6.2. Subsequent maps in the X-Z and X-Y planes utilized data only from the N and S, and dawn and dusk sections, respectively, as shown in Figures 6.2b and 6.2c. Data in the Y-Z map utilized data between  $-1 < X < 1.5 R_{\text{mars}}$ .

These maps were produced for several frequency ranges for the magnetic and electric field wave spectra. The frequency ranges are defined as: ultra low frequency (ULF): 0.01 - 0.1 Hz; low frequency (LF): 1 - 5 Hz; medium frequency (MF): 5 Hz, high frequency (HF): 1k - 5kHz. The MF range is the single frequency bin closest to 5 Hz in the power spectra; the ULF, LF and HF frequency ranges typically span  $\sim 4 - 5$  frequency bins in the power spectra. The measurement cadence of MAG and LPW are such that wave spectra are available for both within the LF and MF frequency ranges. Magnetic field spectra are available in the ULF range and electric field spectra are available in the HF range. Justifications for these frequency ranges are discussed in Section 6.4.1.

Further statistical maps were generated based on upstream solar wind conditions. The distributions of several solar wind parameters (listed below) were split into quartiles. Statistical maps of the corresponding wave powers were compiled for the high and low solar wind conditions, separately. Dividing the high condition map by the low condition map produces the fractional change between the two sets of solar wind conditions. Values of one mean no change; values greater than one mean that wave power was greater for high solar wind conditions. Values less than one mean

that wave power has decreased for high solar wind conditions. The solar wind parameters explored were: proton density ( $N_{sw}$ ), the variation (standard deviation) of proton density ( $N_{sw}STD$ ), magnetic field strength ( $B_{sw}$ ), variation of magnetic field strength ( $B_{sw}STD$ ), proton velocity ( $V_{sw}$ ), variation of proton velocity ( $V_{sw}STD$ ), Alfvénic mach number ( $V_a$ ), sonic mach number ( $M_s$ ), magnetosonic mach number ( $M_{ms}$ ), proton beta (Beta) and IMF cone angle to the solar wind velocity ( $-B_x$ ,  $+B_x$ ). The IMF cone angle was split in to two sub parameters, that where the solar wind was parallel to the solar wind flow ( $-B_x$ ) and that where it was anti parallel to the solar wind flow ( $+B_x$ ). More detailed description of these solar wind parameters can be found in *Halekas et al.* (2016).

#### 6.4.1 Example spectra

An example of the electric and magnetic field power spectra for one MAVEN orbit at Mars are shown in Figure 6.3. Panels A and C show the ACT and PAS electric field power spectra respectively. Panels B and D show the corresponding electric field time series for the ACT and PAS power spectra, from which these spectra were derived from. It should be noted that the onboard measured electric field time series is measured at a much higher cadence - the time series shown here (which is the data product transmitted from the spacecraft to Earth) is an averaged, 64 point per spectral measurement, time series. The DC component has not been removed. Panel E shows the magnetic field power spectrum, which has been derived using wavelet analysis of the time series magnetic field data shown in panel F. Panel G shows the spacecraft altitude in the IAU reference frame.

The orbit is approximately in the dawn-dusk plane, spanning  $\sim 4.5$  hours with periapsis occurring at just after 14:00 UTC. The inbound section is on the dawn, sunlit side of Mars, in the southern hemisphere of the planet. Up until about 13:30 UTC MAVEN is in the solar wind, as visible by the relatively calm magnetic field in panel F. The magnetic field strength is a few nT and shows little variation. This is mirrored in the magnetic field power spectrum in panel G and the electric field power spectra in panels A and C also show relatively calm conditions.

At around 13:30 UTC the electric and magnetic field data show disturbed features. The magnetic field power spectrum shows a brief increase in power of several orders of magnitude across the entire frequency range, before measuring strong wave power all the way through periapsis. This enhancement in wave power is the bow shock - the brief burst of wave power prior to the more continuous power measured is most likely the bow shock moving back across the spacecraft in response to changing upstream solar wind conditions. Based on the spacecraft position and orbit trajectory it crossed the bow shock at an oblique angle,  $\sim 45^\circ$ . The bow shock is also visible in the data.

MAVEN observes the high frequency electric and magnetic field wave powers as it crosses the bow shock. As the spacecraft approaches periapsis, wave power at higher frequencies drops off, as can be seen in panels A, C and E. Periapsis occurs just past the dusk terminator in the northern hemisphere. There is very little electric field wave power observed in panels A and C during periapsis but strong magnetic field wave power is observed at low frequencies below  $\sim 0.1$  Hz, seen in panel E. The observed magnetic field strength of 20 - 40 nT through periapsis means that the gyro frequencies of heavier ions ( $O^+$  and above) are at and below this frequency range - on the order of  $<0.05$  Hz. The large spacecraft velocity ( $\sim 4 \text{ km s}^{-1}$ ) at periapsis means that it is not possible to tell whether these low frequency waves are due to the gyro motion of heavy ions about the local magnetic field, or an artifact of the spacecraft traveling through the large scale changing magnetic field topology. It is most likely a combination of the two - this study utilizes data above 600 km altitude where the effects of localized crustal magnetic fields and field aligned currents (at times a large contributor to the large scale magnetic field topology) are deemed negligible for this study.

The outbound segment of the MAVEN trajectory passes across the nightside of the planet in the northern hemisphere, from dusk to dawn. Between  $\sim 14:30$  and  $15:30$  UTC MAVEN is in the magnetotail - the magnetic field power spectrum shows lower amplitude waves across a wide range of frequencies. The 'bulge' in both electric and magnetic field wave power at roughly 15:30 UTC is most likely MAVEN exiting the magnetotail and crossing the bow shock. Once the MAVEN is

back in the solar wind, the magnetic and electric field data in panels A, C and E quieten down, appearing very similar to the start of the orbit.

There are several sporadic ‘blips’ of electric field wave power observed at higher frequencies, between  $\sim 10^2$  and  $10^3$  Hz, observed with a slight preference at the bow shock and in the upstream solar wind. The measurement cadence of the MAG time series data prevents confirmation of the existence of these high frequency bursts in the magnetic field data.

We note that several of the electric field wave spectra caveats discussed in Section 6.3.1 are observed here; the stimulated plasma line at frequencies greater than  $\sim 10^4$  Hz at periapsis in panel A; vertical black lines denoting poor data in panel C; and the three horizontal bands in panels A and C marking the frequencies at which the LF, MF and HF spectra have been merged into a single product.

Here we discuss the chosen frequency ranges as outlined in Section 6.4 using Figure 6.3 as an example. In the upstream solar wind, when the magnetic field is typically a few nT, wave power around 0.05 Hz is close to the proton cyclotron frequency. In the magnetosheath, where magnetic field strengths of  $\sim 20$  nT are more common, the proton cyclotron frequency is closer to  $\sim 0.3$  Hz. Wave power in the ULF (0.01 - 0.1 Hz) range is thus typically associated with heavier ion cyclotron frequencies, although the proton cyclotron frequency can occur in this frequency range in the upstream solar wind. We do not chose a lower frequency range as this would involve analysis of time series data spanning longer than 100 s. MAVEN’s apoaapsis velocity is  $\sim 1.5$  kms<sup>-1</sup> and spatial effects would likely start to affect the observed power spectra. The LF (1 - 5 Hz) range was chosen as this is the lowest frequency range that the LPW instrument can sample at; this range typically samples above the proton cyclotron frequency except in cases where the magnetic field is particularly strong,  $\sim 60$  nT. The magnetic field strength can reach values close to this in the magnetosheath, as seen in Figure 6.3F. The LF range thus most likely samples harmonics of the proton cyclotron frequency. The MF (5 Hz) range was chosen because electric field wave power tends to fall off quickly at frequencies greater than this when the spacecraft is in the solar wind. The most intense wave power within the bow shock and magnetosheath tends to peak close to this

frequency as well. These features can be seen in panels A and C of Figure 6.3. The HF (1k - 5k Hz) frequency range is at the typical electron cyclotron frequency with a wave power that is much more sporadic in nature as can be seen in Figure 6.3A and C.

Finally we note a possible source of error accompanying this analysis method related to the identification of ‘real waves’ versus ‘single events’. As an example, waves in the local magnetic field are typically required to possess some number of oscillations to be classified as a real wave (e.g. *Brain et al. (2002); Espley et al. (2004)*). If MAVEN crosses a plasma boundary that has a spatial scale similar to, say, a 5 Hz wave in the magnetic field, then this single boundary crossing will appear as wave power in the 5 Hz band of the magnetic field power spectra. The same argument holds for the electric field power spectra. Given the difficulty associated with reliably identifying plasma boundaries in an autonomous manner (and indeed the number of plasma boundaries and regions observed in this study) we do not attempt to correct for this source of error.

## 6.5 Statistical Maps

### 6.5.1 Electric and magnetic wave power

Statistical maps in the MSE frame of electric field wave power for the LF, MF and HF frequency ranges are shown in Figures 6.4, 6.5 and 6.6 respectively. Each figure is split into three panels: panel A shows the X-Z frame; panel B shows the X-Y frame; panel C shows the Y-Z plane. We remind the reader that the binning method used is described in Section 6.4 and Figure 6.2. Empirical boundaries for the BS and MPB as determined by *Vignes et al. (2000)* are over plotted in panels A and B. Panel C shows circles at altitudes 400, 1000 and 2000 km from the Martian surface to give a sense of scale. Only bins that contained at least 10 data points have been used, with most bins typically containing a few thousand data points. The colorbars used in Figures 6.4, 6.5 and 6.6 all span three orders of magnitude, but start at different values, so that features can be observed in each frequency range. The LF range contains the most wave power, with the MF and HF ranges containing  $\sim 3 - 4$  orders of magnitude less power. We also note that the HF range in

Figure 6.6 shows the statistical mean wave power as apposed to the statistical median wave power. Inspection of individual power spectra shows that wave power in the 1k - 5k Hz range is sporadic in nature; when the median is used to bin the data a ‘blank’ map is obtained showing little wave power and no structure. Using the mean produces the map shown here; further discussion of the importance of this is left for later.

Wave power shown in Figure 6.4 does not show any obvious structure and does not follow the BS or MPB - it appears ‘smeared’ over the Martian magnetosphere. The largest wave powers are observed in the upstream solar wind and in the Martian magnetotail. The enhanced wave power in the tail is most likely contamination in the LF band, as discussed in Section 6.3.6. Wave power in the MF spectrum shows more structure, with a peak in wave power along the BS, as shown in Figure 6.5. Wave power decreases in the upstream solar wind, although there is some spill over from the BS into the upstream region - the upper edge of the BS is not sharp. Downstream of the MPB wave power decreases, again with some overspill from the sheath. Wave power along the BS peaks at the sub solar point. The enhanced wave power in the central magnetotail is again likely due to LF noise and represents the upper limit to wave power there. The HF wave power shown in Figure 6.6 shows the most structure, with the greatest power observed along the BS, peaking at the sub solar point. The upstream edge of the BS still shows overspill of wave power into the foreshock, but the lower boundary of the MPB is much clearer and sharper compared to the LF and MF ranges. In the flanks of the magnetotail, wave power is generally small but patches of enhancement exist close to planet in the central tail region. There is no obvious asymmetry in electric field wave power distribution in the Martian magnetosphere in the MSE frame, for all three of the frequency ranges shown here.

Statistical maps of the magnetic field wave power are shown for the ULF, LF and MF frequency ranges in Figures 6.7, 6.8 and 6.9 respectively. These maps follow the same layout as those for the electric field power spectra except that all three figures were produced using the statistical median of the data, and the colorbar for the MF range covers two orders of magnitude only. The Martian magnetosphere is clearly visible in Figure 6.7, with magnetic field wave power peaking in

the sheath. The majority of wave power is at the sub solar point with significant power present in the foreshock. There is also significant wave power throughout the magnetotail; the inner MPB is visible although this boundary is not sharp in the flanks of the tail. Clear structure is present in the LF frequency range shown in Figure 6.8 with wave power again peaking at the sub solar point and along the BS, as apposed to within the sheath for the ULF range. The majority of wave power is at the BS and within the sheath - there is little power in the tail region. The inner MPB is now clear and fairly sharp. Wave power in the MF frequency range shown in Figure 6.9 is again structured, with wave power focused along the BS and outer sheath regions. Peak wave power is again at the sub solar point. The MPB is visible, but wave power falls off within the inner sheath region before reaching this boundary, particularly in the flanks of the sheath.

## 6.6 Wave power as a function of upstream solar wind drivers

As discussed in the Section 6.4 the statistical distribution of electric and magnetic field wave powers throughout the Martian magnetosphere were analyzed with respect to twelve upstream solar wind parameters (also outlined in Section 6.4). Here we present the upstream solar wind drivers that produce the largest variations in electric and magnetic field wave power. Due to space limitations we show statistical maps of the variability in wave power with respect to the upstream driver in the plane that showed the most interesting results; Figures 6.10 through 6.17 subsequently show the dawn-dusk (X-Y) plane only.

### 6.6.1 Electric field: $N_{sw}$ , $B_{sw}$ and $V_{sw}$

The electric field wave power was most influenced by the upstream solar wind proton density, magnetic field strength and proton velocity, and examples of this are shown in panels A, B and C of Figures 6.10, 6.11 and 6.12. The solar wind parameters are labeled in parentheses above each plot. The Figures show the LF, MF and HF ranges respectively. Increased solar wind density enhances electric field wave power by up to  $\sim 25\%$  compared to low density conditions for the LF and MF ranges, as shown in Figures 6.10A and 6.11A. In the LF range, enhancements are generally

observed throughout the entire magnetosphere, with little obvious structure. The MF range shows smaller enhancements,  $\sim 15 - 20\%$ , that appear more structured, particularly at the foreshock, BS and sheath, although a decrease in wave power of  $\sim 10\%$  is observed at the sub solar sheath. The upstream magnetic field strength also tends to enhance wave power throughout the magnetosphere for the LF and MF ranges. Solar wind velocity produces the smallest enhancements overall and in fact shows decreases close to  $25\%$  along the dawn flank of the magnetosheath in the LF range. Figure 6.10C shows a slight enhancement of wave power at the sub solar point within the LF sheath, which is not obvious for the MF range shown in Figure 6.11C.

Electric field wave power in the HF range, presented in Figure 6.12, shows opposite trends to the LF and MF ranges. Enhancements in solar wind velocity produce the greatest enhancements in wavepower, with peaks of enhancement observed at the foreshock and BS. There is also a dawn dusk asymmetry, with enhancements in wave power observed within the dawn magnetosheath and decreases in power observed along the inner edge of the dusk magnetosheath. Enhancements are of a similar size to the LF and MF ranges,  $\sim 20\%$ . The solar wind magnetic field causes slight enhancements of wave power in the foreshock and at the sub solar point within the magnetosheath. Decreases in wave power are observed in the flanks of the magnetosheath. Upstream solar wind density tends to decrease wave power throughout the magnetosheath and in the foreshock by  $\sim 10\%$ . Wave power in the magnetotail stays more or less constant.

Electric field wave power was also influenced by the upstream mach number parameters,  $M_a$ ,  $M_{ms}$ ,  $M_s$  and Beta. For the LF and MF ranges, increases along the BS and into the foreshock were observed, at levels smaller than those in Figures 6.10, 6.11 and 6.12,  $<10\%$ . The HF range showed a stronger dependence on these parameters, with enhancements close to  $20\%$  at the BS. Overall these parameters influenced the electric field wave power to a lesser extent than  $N_{sw}$ ,  $B_{sw}$  and  $V_{sw}$  and as such we do not show those maps here.

### 6.6.2 Magnetic field: $M_a$ , $M_{ms}$ , $M_s$ and Beta

Contrary to the electric field wave power, the magnetic field wave power was most influenced by the upstream mach numbers,  $M_a$ ,  $M_{ms}$ ,  $M_s$  and Beta. Examples are shown in Figures 6.13, 6.14 and 6.15. ULF wave power shows enhancements of  $\sim 6\%$  evenly distributed along the outer edge of the BS and into the foreshock. Magnetosonic mach number ( $M_{ms}$ ) produces the largest influence on ULF wave power, causing increases in wave power throughout the entire magnetosphere.  $M_a$ ,  $M_s$  and beta show decreases in wave power of a few percent within the sheath and tail regions.

LF wave power shows similar behavior to the ULF range, as shown in Figure 6.14. Enhancements are larger,  $<10\%$ , and are still distributed evenly across the outer edge of the BS and foreshock. Wave power in the tail region shows no significant change between high and low conditions, and wave power still decreases in the sheath by a few percent for  $M_a$ ,  $M_s$  and beta.  $M_{ms}$  appears to produce a dawn dusk asymmetry in the sheath, with enhancements in wave power observed at dusk and decreases observed at dawn.

MF wave power shows similar enhancements to the ULF range, 5-6%. Wave power is still distributed evenly across the BS, with enhancements now observed along the inner edge of the BS and into the sheath. Wave power in the tail still shows no significant change with these upstream drivers. The sheath typically shows decreases in wave power by a few percent, except at the outer sheath edge where increases across the BS are present. The magnetosonic mach number causes a possible dawn dusk asymmetry in the sheath although this is not as clear as it is for the LF range.

### 6.6.3 IMF cone angle

Parallel and anti-parallel solar wind IMF produced asymmetries in wave power in the dawn-dusk plane for electric and magnetic field wave powers across all frequency ranges except for HF in E. These asymmetries are shown for the electric field MF and magnetic field LF ranges in Figure 6.17. These ranges showed the greatest asymmetries; the remaining frequency ranges showed similar behaviors but with smaller enhancements and are not shown here. Panels A and C show

the ratio of electric field wave power for parallel ( $-B_x$ ) and anti-parallel ( $+B_x$ ) IMF compared to perpendicular IMF, respectively. Panels B and D show the same for the magnetic field wave power. The electric and magnetic field wave powers show the same asymmetries in the dawn-dusk plane. Wave power is enhanced at dawn for parallel IMF as seen in panels A and B: the sheath and BS show enhancements, with the peak enhancement in the foreshock. Wave power decreases at dusk for parallel IMF, with decreases observed in the dusk sheath, BS and foreshock. This behavior is opposite for the anti-parallel IMF cases, shown in panels C and D.

## 6.7 Interpretation and discussion

The lack of obvious structure observed in the electric field LF range (Figure 6.4) compared to the ULF range for magnetic field (Figure 6.7) can be explained by examination of the individual power spectra shown in Figure 6.3. Constant ACT and PAS wave power is present below  $\sim 5$  Hz for almost the entire orbit as seen in panels A and C; only below about 500 km altitude does this low frequency wave power drop off. By comparison, panel E shows significant variation in the magnetic field power spectrum across the entire frequency range and for the entire orbit. Although noise can be present in the LPW spectra below  $\sim 100$  Hz, this noise (outlined by circle 7 in Figure 6.1) does not appear to be present for the majority of the example orbit shown in Figure 6.3, especially above altitudes of 400 - 500 km. As such, it is unclear why there is no obvious structure throughout the sheath and BS regions in Figure 6.4. The lack of structure and relatively large wave power in the tail is however likely a result of low frequency noise. An additional automated flagging routine was used in this study to identify this noise not removed by ground processing. By eye inspection (not shown here) showed that this routine was able to flag noise to  $\sim 90\%$  reliability throughout the majority of the magnetosphere. This routine was least reliable in the central magnetotail region and because of this we do not discuss the tail region further with respect to the LF electric field power spectra.

Electric field wave power in the HF range was observed much more sporadically than in the MF range, but when present, this HF power was comparable to that in the MF range, as seen

in Figures 6.5 and 6.6. This suggests that electron driven waves occur more sporadically in the Martian magnetosphere than ion driven waves, but when present, are able to contribute comparable amounts of power.

Various plasma boundaries are visible in the electric and magnetic field power spectra. Electric field wave power in the LF range shows no obvious structure and the cause of this is not obvious. Electric field wave power tends to peak along the BS in the MF and HF ranges and is most likely associated with particle reflection at the shock. In contrast, the magnetic field ULF wave power shows obvious structure. The BS is clearly defined, although wave power peaks within the sheath rather than along the BS. The dissipation of solar wind energy requires heating and thermalization of electrons and ions in the sheath region downstream of the shock, which are the likely cause of this observed wave power (e.g. *Bale et al. (2005)*). Magnetic field wave power in the LF and MF ranges is greatest along the BS, peaking at the sub solar point. This wave power is again most likely associated with the motion of reflected ions at the shock: over and under shoots are observed in the time series magnetic field data at the shock and may be the cause of these higher frequency waves. The peak in wave power at the sub solar point is not surprising due to the parallel nature of the shock normal to solar wind velocity here.

The BS is not always a sharp boundary within these statistical maps, most likely due to variation in upstream solar wind conditions which are known to influence the locations of the various Martian plasma boundaries (e.g. *Brain et al. (2005)*; *Edberg et al. (2009a,b)*; *Halekas et al. (2016)*). Proton cyclotron waves are known to exist upstream of the BS at Mars (e.g. *Russell et al. (1990)*; *Bertucci et al. (2013)*; *Brain et al. (2005)*) and are the probable cause of upstream wave power observed in the ULF frequency range. ULF wave power upstream of the BS is approximately an order of magnitude greater than that in the LF and MF ranges. *Brain et al. (2002)* also observed upstream propagating whistler waves thought to be generated within the sheath region. These waves lay between 0.4 and 2.3 Hz in their study, corresponding roughly to the LF frequency range used in this study. Wave power upstream of the BS observed in Figure 6.8 may hence be attributed to these whistler waves. We also note that the statistical wave power amplitudes observed by *Brain*

*et al.* (2002) in the 0.04 - 0.1 Hz range used in their study agree well with those observed in the ULF range in this study. Wave power in the *Brain et al.* (2005) study peaked within the sheath, also seen in this study.

The MPB is observed in the electric and magnetic field power spectra. There is again variation in the location of this boundary, most likely caused by varying upstream solar wind conditions. Typically, wave power falls off downstream of the MPB, leaving the tail region fairly devoid of wave power. The ULF magnetic field power shows a decrease in wave power downstream of the MPB but within the tail region this is  $\sim 2$  orders of magnitude greater than for the LF and MF ranges here. This may be related to large scale structures such as current sheet crossings, which lie outside the scope of this work. *Espley et al.* (2004) analyzed magnetic field data from the MGS spacecraft and concluded that oscillations below the local proton frequency decreased in amplitude downstream of the MPB and within the magnetotail region, agreeing with results from this study. *Bertucci et al.* (2004) also used MGS magnetometer data, observing similar ULF waves either side of the MPB, seen in this study as well.

The enhancements in electric field wave power in the LF range at the sheath and shock shown in Figure 6.10, produced by large  $N_{sw}$ , may be a result of the increased thermal energy carried by the solar wind in these cases and the subsequent dissipation of this additional energy. Enhanced  $V_{sw}$  reduces wave power in the flanks of the sheath and in the foreshock for the LF range; a possible explanation is that the wave modes produced in the LF range are unable to propagate upstream as  $V_{sw}$  increases.

Enhanced wave power is observed at the shock and foreshock in the MF range in Figure 6.11A, as may be expected with enhanced solar wind thermal energy. It is unclear why wave power in the sheath decreases in this case; perhaps reflection of particles at the shock is more important for energy dissipation than thermalization within the sheath, for this frequency range.

In contrast to the lower frequency ranges,  $V_{sw}$  drives enhanced electric field wave power at the sheath, shock and foreshock in the HF range, shown in Figure 6.12C. It is clear that there is an impressive increase in energy dissipation across the shock region for these higher frequency waves.

It is known that the nature of energy dissipation varies with mach number (*Bale et al., 2005*) and this may be evidence of greater energy dissipation upstream of the shock due to increased particle reflection there. It is not clear why there is a significant decrease in wave power within the sheath in the HF range in Figure 6.12A with no accompanying increase in wave power at the BS and / or foreshock. Increased solar wind density should lead to a greater dissipation of enhanced solar wind thermal energy in sheath, BS or foreshock, which does not appear to be the case here.

Opposite to electric field wave power, magnetic field wave power is most influenced by various upstream solar wind mach numbers. Figures 6.13 through 6.15 show enhancements of wave power at, and upstream of, the BS, and decreases in wave power within the sheath. The width of the shock front and the nature of energy dissipation are again dependent on upstream mach number (e.g. *Bale et al. (2005)*) and these figures most likely show the results of different physical processes acting at the shock. We suggest that for higher upstream mach numbers a greater number of particles are reflected at the shock front; the observed increase in wave power there is a result of the motion of these particles. For lower mach numbers, fewer particles are reflected at the shock and thermalization within the sheath is the primary process for dissipating the incident solar wind energy, leading to enhanced wave power there. Plasma beta correlates with  $M_a$  and  $M_{ms}$  (not shown here) and so it is not surprising that it shows similar behavior to these two drivers. Upstream mach numbers were observed to influence electric field wave power as well, but to a much smaller extent than  $N_{sw}$ ,  $B_{sw}$ , and  $V_{sw}$ . Electric field wave power in the HF range shows the most structured responses to upstream mach numbers (Figure 6.16), with behavior similar to the magnetic field power described above. We suggest the same reasoning to explain these responses.

The IMF cone angle influences the electric and magnetic field wave power by similar amounts,  $\sim 10\%$ . Wave power increases at the quasi-parallel foreshock (the magnetic field is approximately parallel to the shock normal) and decreases at the quasi-perpendicular foreshock (the magnetic field is approximately perpendicular to the shock normal). For the coordinate system shown in Figure 6.17, the quasi-parallel shock corresponds to  $+Y$  for  $+B_x$ , and  $-Y$  for  $-B_x$ . This asymmetry in wave power is to be expected: for a quasi-perpendicular shock reflected ions gyrate about the immediate

upstream magnetic field. They gain energy via the solar wind electric field (equal to  $-\vec{V}_{\text{sw}} \times \vec{B}_{\text{sw}}$ ) and are subsequently able to penetrate the shock potential and thereafter are convected downstream through the shock. In the case of the quasi-parallel shock the magnetic field is  $\sim$  parallel to the solar wind velocity and the reflected ions are able to travel a much greater distance upstream before being convected back to the shock front (e.g. *Burgess et al. (2005b)*). Hence, we expect wave power to be distributed over a much larger area upstream at the quasi-parallel shock, as is observed here.

## 6.8 Conclusions

A statistical study of  $\sim 14.5$  months of electric and magnetic field wave power spectra observed by the MAVEN spacecraft has produced a much more comprehensive study of wave power distribution within the Martian magnetosphere than has previously been possible. Wave power from several frequency bands was analyzed, enabling statistical maps of this wave power distribution to be created. Upstream solar wind parameters were used to determine the response of this wave power within the Martian magnetosphere to these various drivers. Caveats of the LPW wave power spectra are discussed in this paper. The key conclusions from this statistical study are as follows:

- (1) The lowest frequency ranges contained the most wave power for the electric and magnetic field spectra. Various plasma boundaries are clearly evident in the statistical maps, including the magnetic pile up boundary (MPB), magnetosheath (MS), bow shock (BS) and foreshock. Enhancements in wave power at these boundaries show regions important for the dissipation of solar wind energy incident to the planetary obstacle. Enhancements observed in the sheath most likely represent thermalization of electrons and ions in this region. Enhancements at the BS and foreshock are likely caused by the reflection of particles at the shock and subsequent asymmetric particle distributions. Magnetic field wave power in the ULF (0.01 - 0.1 Hz) range is largest in the sheath, suggesting that the thermalization of electrons and ions is the key energy dissipation mechanism for waves close to the local

proton frequency here (*Bale et al.*, 2005). Magnetic field wave power is largest at the BS for the LF (1 - 5 Hz) and MF (5 Hz) ranges, suggesting that reflection of ions is an important dissipation mechanism for these higher frequency waves. The magnetic field is known to ‘over and under shoot’ immediately downstream of a collisionless shock causing higher frequency oscillations in the magnetic field there. These oscillations may also contribute to the observed wave power at the BS in the LF and MF ranges. The distribution of electric field wave power is similar in the MF and HF (1k - 5k Hz) ranges to that in magnetic field LF and MF ranges. There is no obvious structure in electric field wave power in the LF range.

- (2) Various upstream solar wind parameters were observed to drive the distribution of electric and magnetic field wave power throughout the magnetosphere of Mars, in particular within the MS, BS and foreshock regions. Solar wind density and magnetic field enhanced electric field wave power at the BS and foreshock in the LF and MF ranges. It is suggested that this is caused by additional solar wind thermal energy being dissipated through the reflection of ions at the BS. Increased solar wind velocity reduced the electric field wave power at the BS and foreshock in the LF and MF ranges, thought to be caused by the inability of these waves to propagate upstream as the solar wind velocity increases. In contrast, wave power increases at the BS and foreshock in the HF range, suggesting waves in this frequency range are able to propagate upstream even with increased solar wind velocity.
- (3) The magnetic field power spectra were most influenced by various solar wind mach numbers, causing changes of 6 - 9%. For the ULF, LF and MF ranges, greater Alfvénic, Sonic and Magnetosonic mach numbers, and plasma beta, led to enhanced wave power at the BS and foreshock, and reduced wave power within the MS. It is suggested that this is caused by the greater number of particles reflected at the shock for a greater mach number. Thermalization within the sheath becomes less important for energy dissipation. Upstream mach numbers produced similar behavior in the electric field power spectra but these changes

were smaller than for solar wind density, magnetic field and velocity, <20%.

- (4) The IMF cone angle and resulting quasi parallel or perpendicular shocks were observed to produce asymmetries in the distribution of electric and magnetic field wave power in the dawn - dusk plane. Wave power increased by  $\sim 10\%$  at the quasi parallel shock and decreased by a similar amount at the quasi perpendicular shock. The underlying magnetic field topology is thought to cause this: reflected ions at the quasi parallel shock are able to propagate upstream much easier than for the quasi perpendicular case, resulting in greater wave power further upstream of the quasi parallel shock.

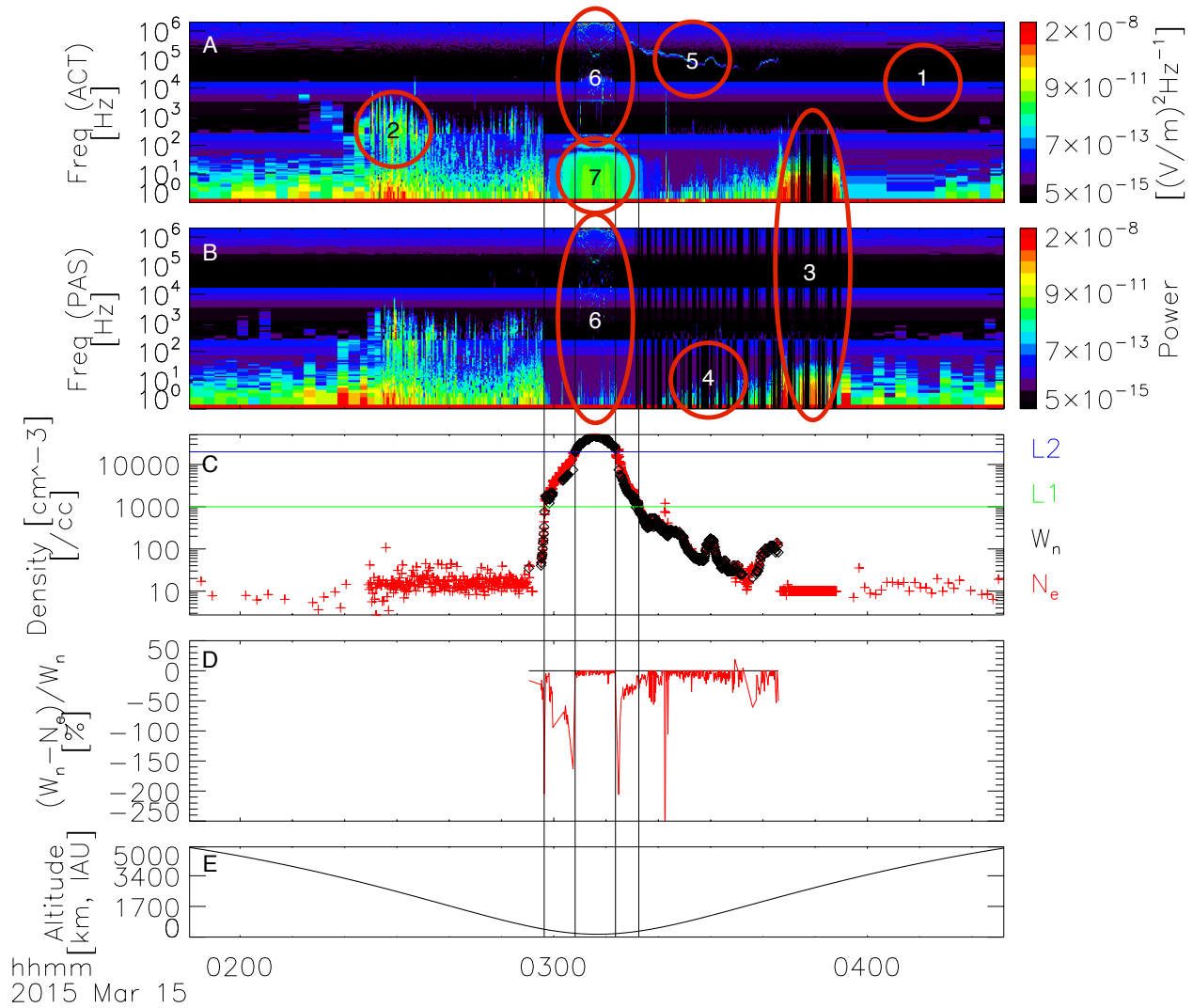


Figure 6.1: Highlighted caveats of the LPW wave spectra that are discussed in the text. Panels A and B show the ACT and PAS wave spectra; panel C shows the local electron density derived from the LPW wave sounding measurements in black and the Langmuir Probe in red. Panel D shows the percentage difference between these quantities. Panel E shows the spacecraft altitude. The lines L1 and L2 mark densities of  $1 \times 10^3$  cm<sup>-3</sup> and  $2 \times 10^4$  cm<sup>-3</sup> respectively. The four vertical black lines mark where the Langmuir Probe derived densities in Panel C cross these values.

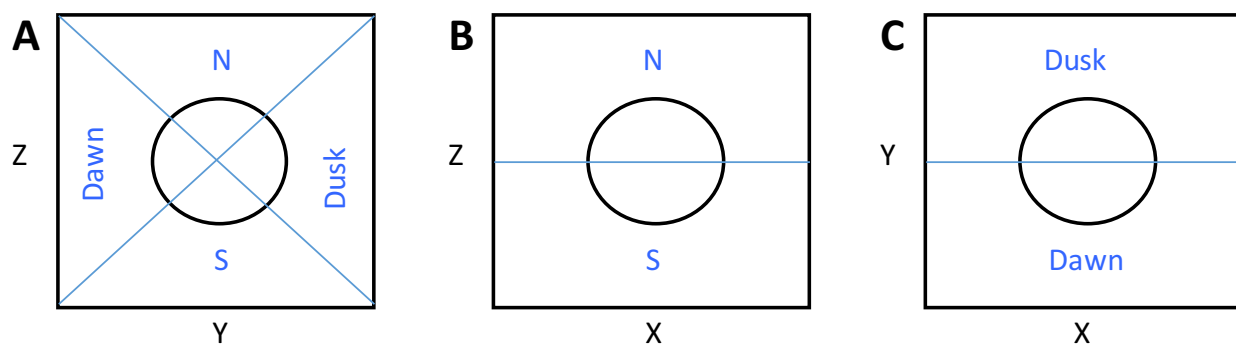


Figure 6.2: Cartoon diagram of the binning method used to produce statistical maps in this study. Panel A shows the Y-Z plane cut into four regions - north (N), south (S), dawn and dusk. Data from these regions are used to produce the maps shown in panels B and C, looking at different planes. This system is used for both the MSO and MSE frames at Mars. Only data between  $-1R_M < 1.5 R_N$  is used when creating the statistical map shown in panel A.

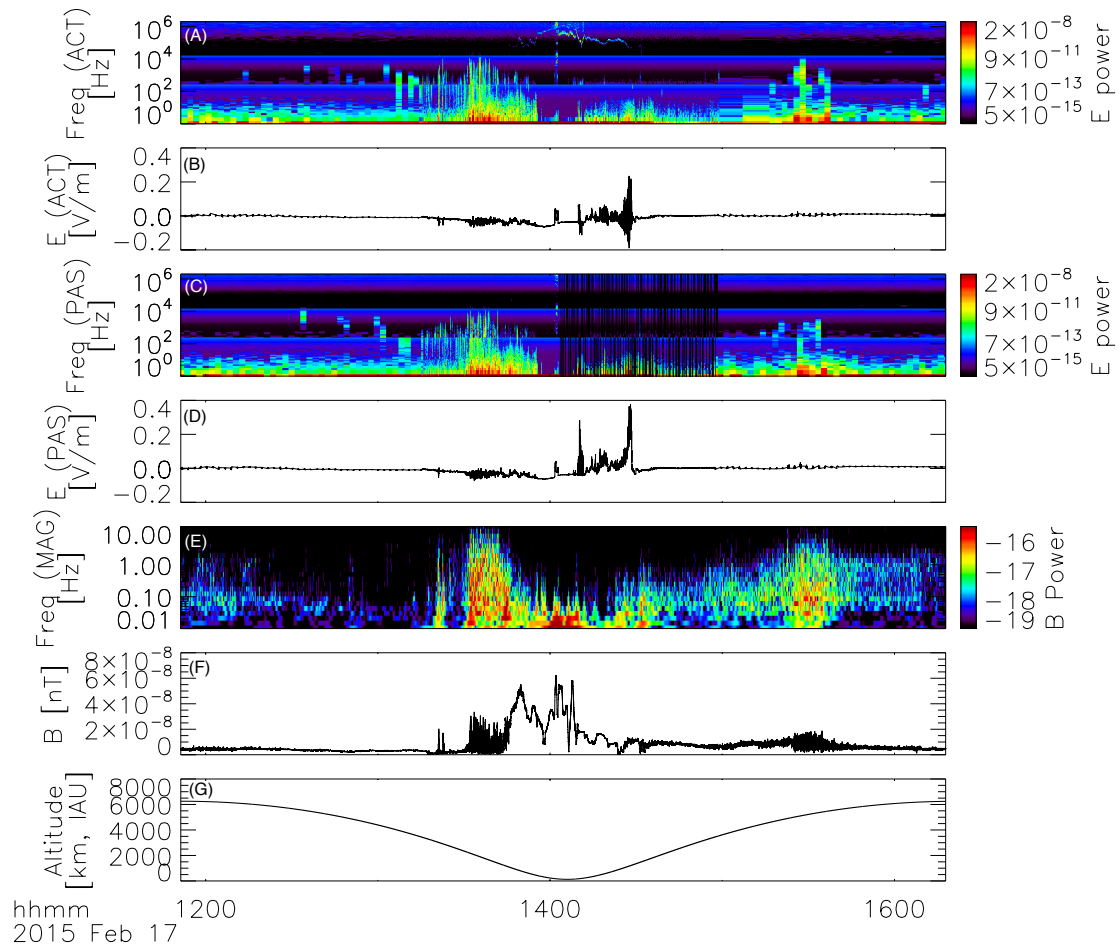


Figure 6.3: Example electric and magnetic field wave power spectra for one orbit about Mars. Panels A and C show the ACT and PAS electric field power spectra respectively. Panels B and D show the time series electric field data from which these spectra were derived from. Panels E and F show the magnetic field power spectrum, and the corresponding time series magnetic field data, respectively. Panel G shows the spacecraft altitude in the IAU frame. E power has units of  $V^2m^{-2}Hz^{-1}$ . B power has units of  $T^2Hz^{-1}$

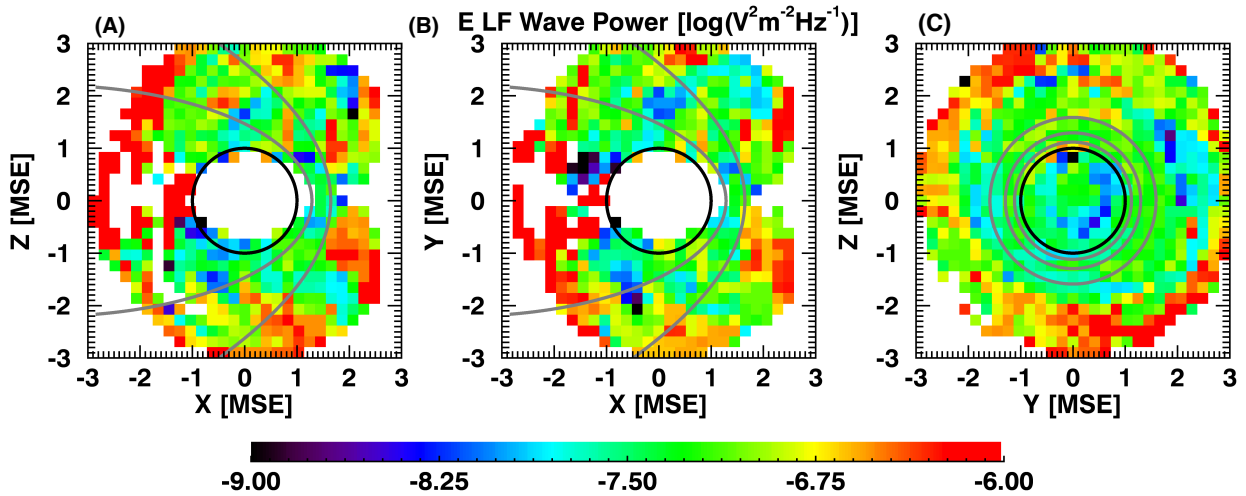


Figure 6.4: Statistical maps of LF (1-5 Hz) electric field wave power in the MSE frame. Panels A, B and C show the X-Z, X-Y and Y-Z planes respectively.

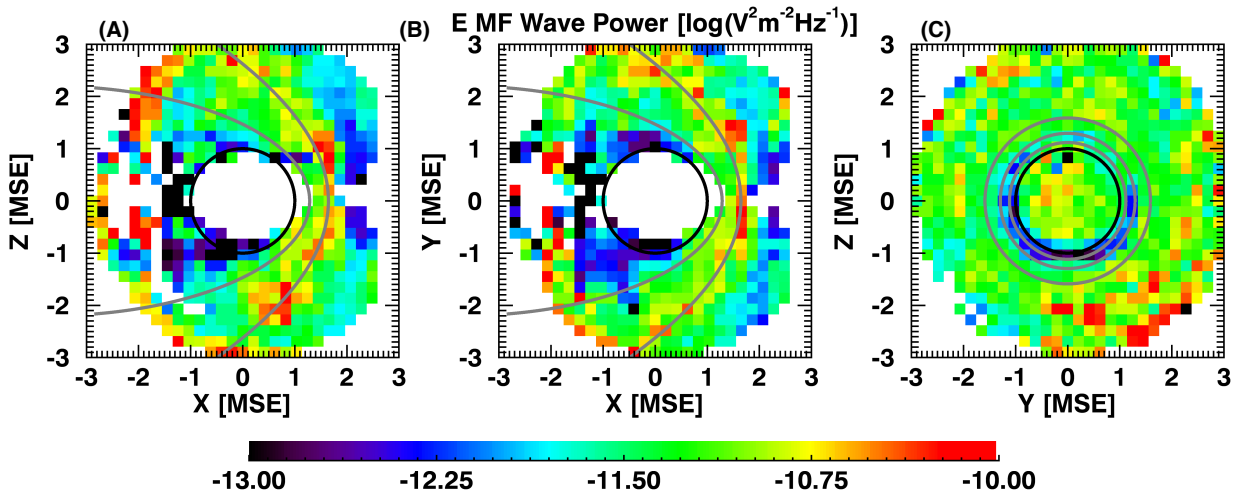


Figure 6.5: Statistical maps of MF (5 Hz) electric field wave power in the MSE frame. Panels A, B and C show the X-Z, X-Y and Y-Z planes respectively.

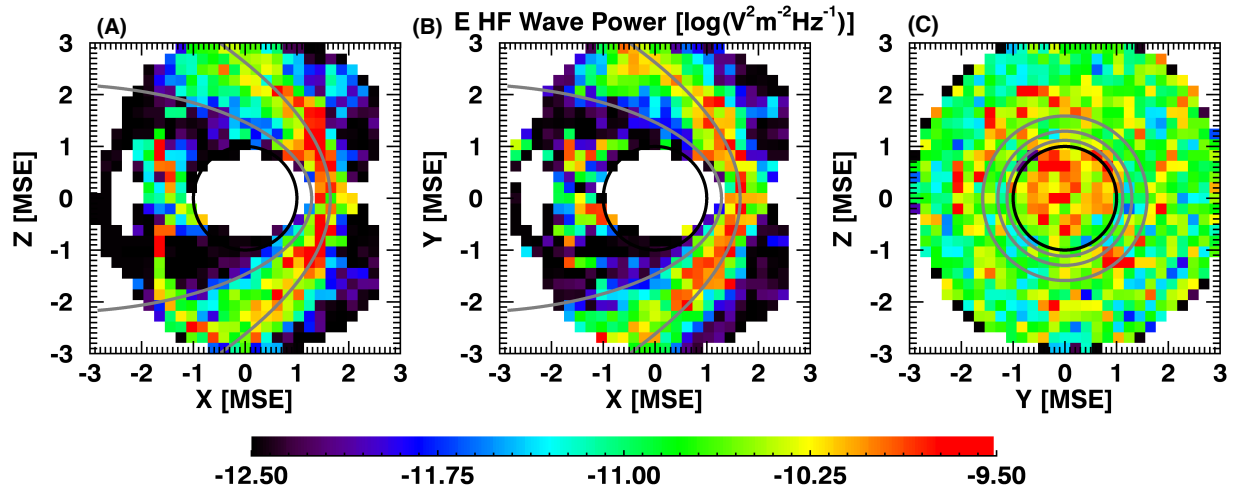


Figure 6.6: Statistical maps of HF (1k - 5k Hz) electric field wave power in the MSE frame. Panels A, B and C show the X-Z, X-Y and Y-Z planes respectively. Note that due to the sporadic nature of electric field wave power in the HF range the statistical mean has been used to produce this map rather than the statistical median.

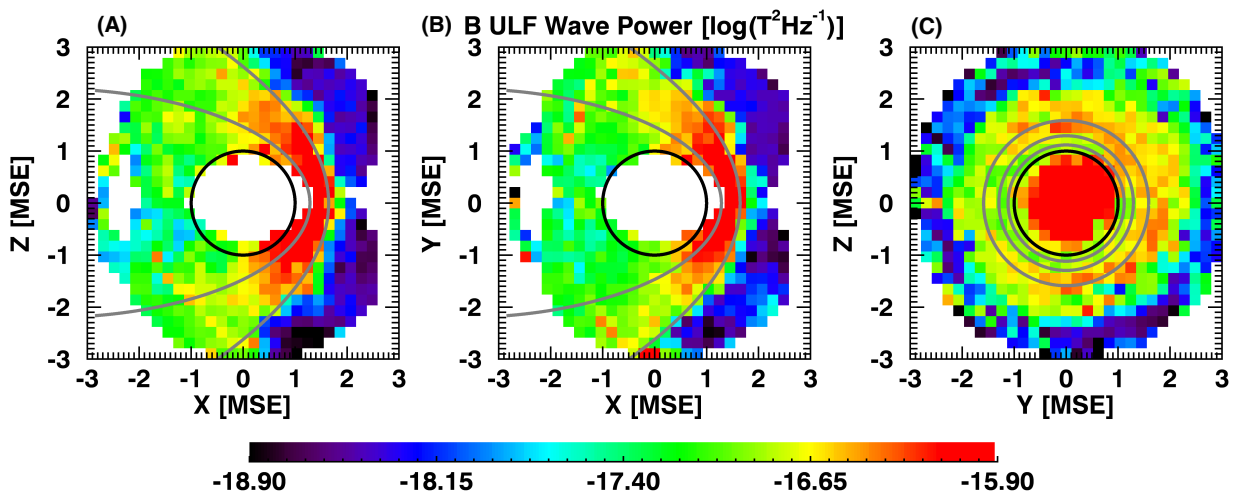


Figure 6.7: Statistical maps of ULF (0.01 - 0.1 Hz) magnetic field wave power in the MSE frame. Panels A, B and C show the X-Z, X-Y and Y-Z planes respectively.

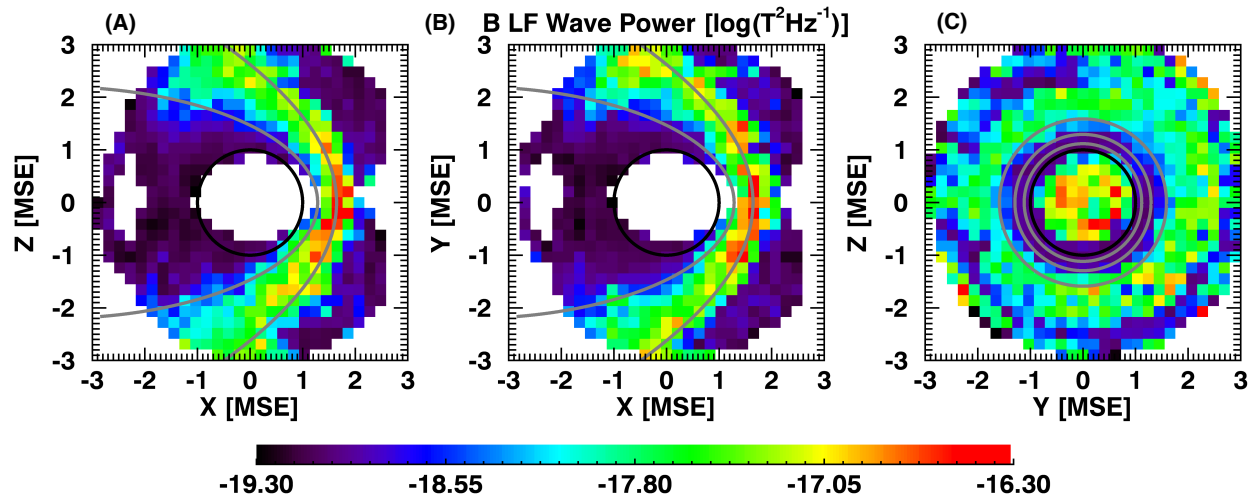


Figure 6.8: Statistical maps of LF (1 - 5 Hz) magnetic field wave power in the MSE frame. Panels A, B and C show the X-Z, X-Y and Y-Z planes respectively.

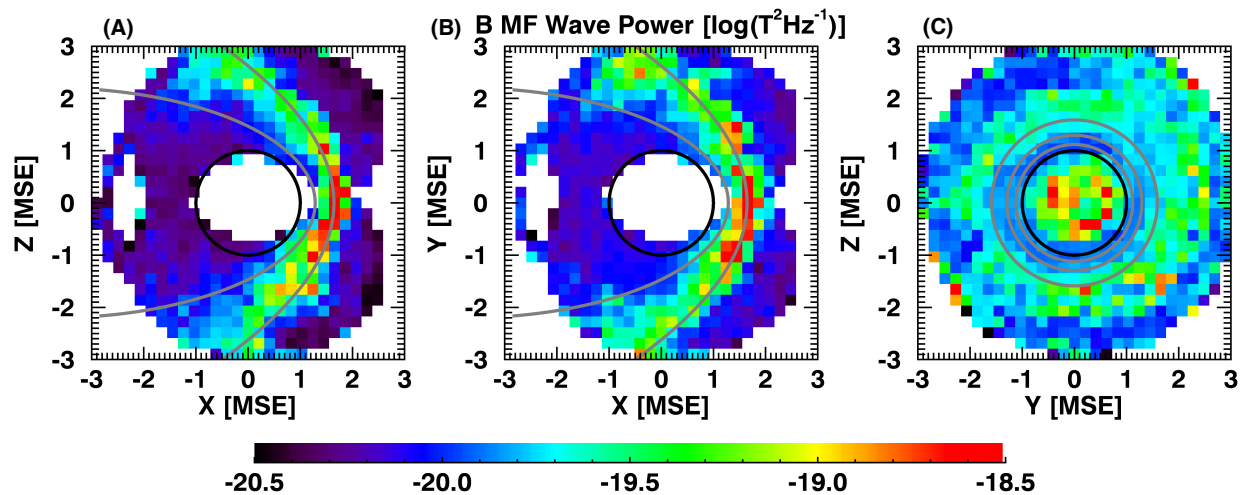


Figure 6.9: Statistical maps of MF (5 Hz) magnetic field wave power in the MSE frame. Panels A, B and C show the X-Z, X-Y and Y-Z planes respectively.

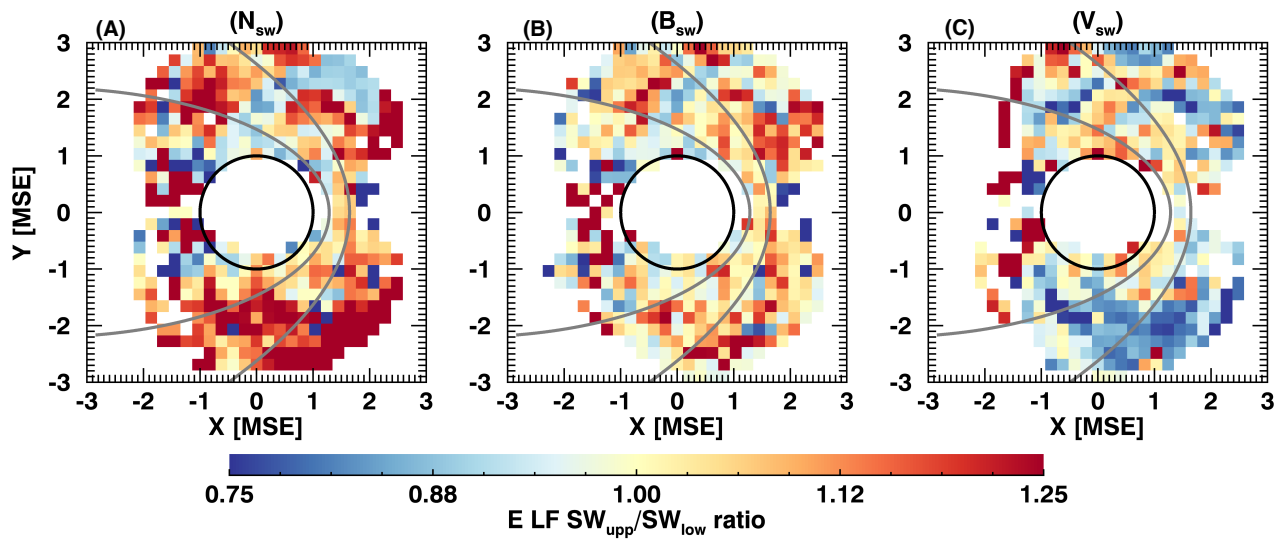


Figure 6.10: Ratio of electric field wave power in the LF (1 - 5 Hz) range for upper to lower quartiles of solar wind upstream drivers. Panels a, b and c show ratios for upstream solar wind proton density, magnetic field and proton velocity.

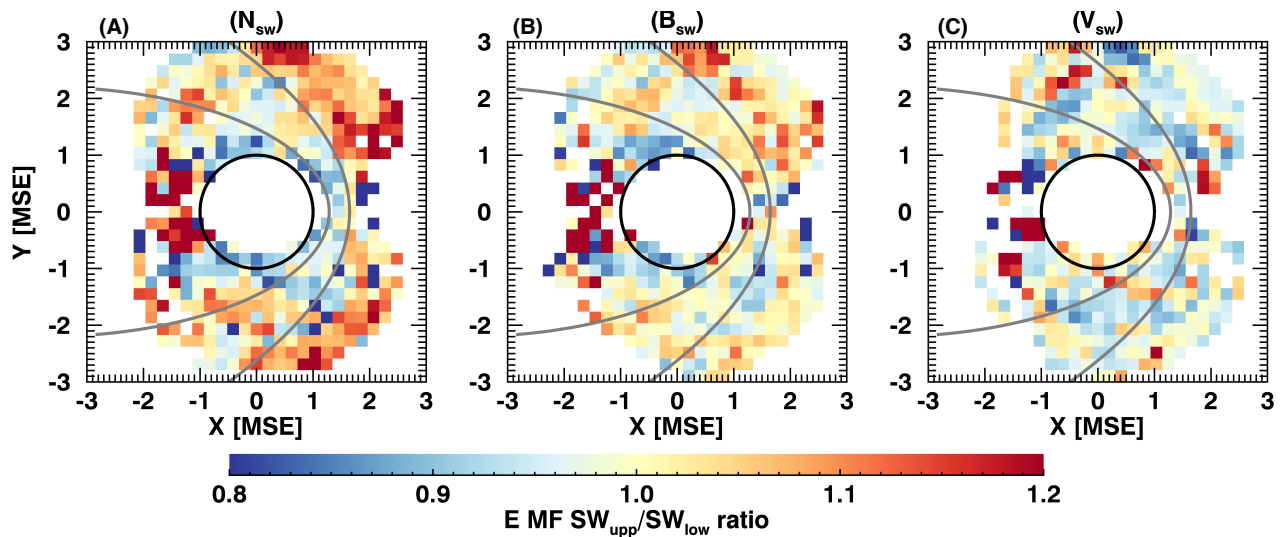


Figure 6.11: Ratio of electric field wave power in the MF (5 Hz) range for upper to lower quartiles of solar wind upstream drivers. Panels a, b and c show ratios for upstream solar wind proton density, magnetic field and proton velocity.

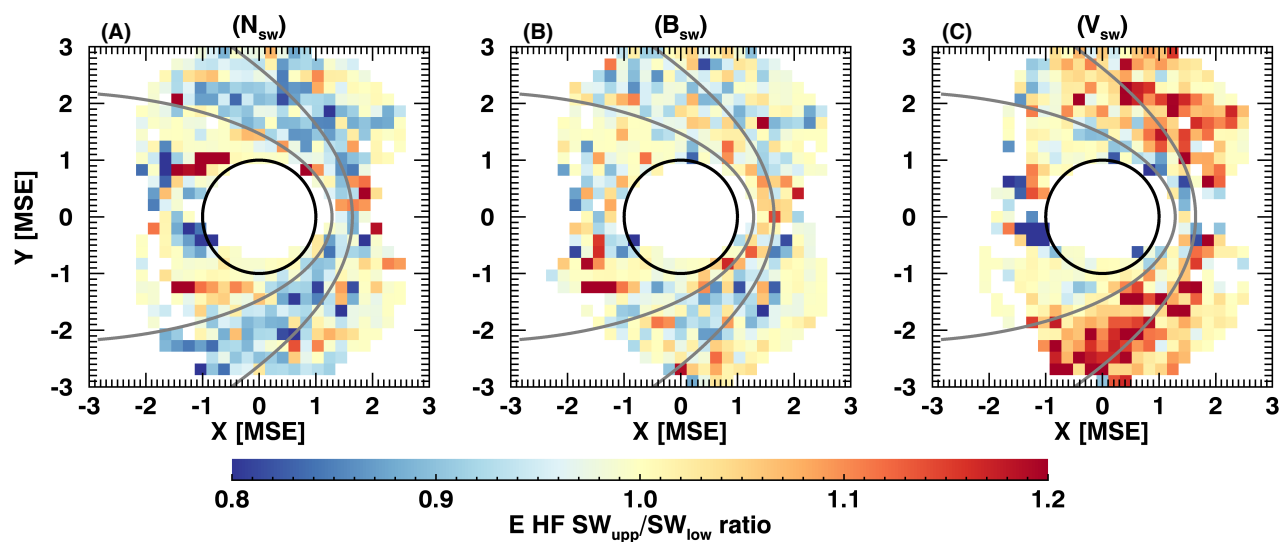


Figure 6.12: Ratio of electric field wave power in the HF (1k - 5k Hz) range for upper to lower quartiles of solar wind upstream drivers. Panels a, b and c show ratios for upstream solar wind proton density, magnetic field and proton velocity.

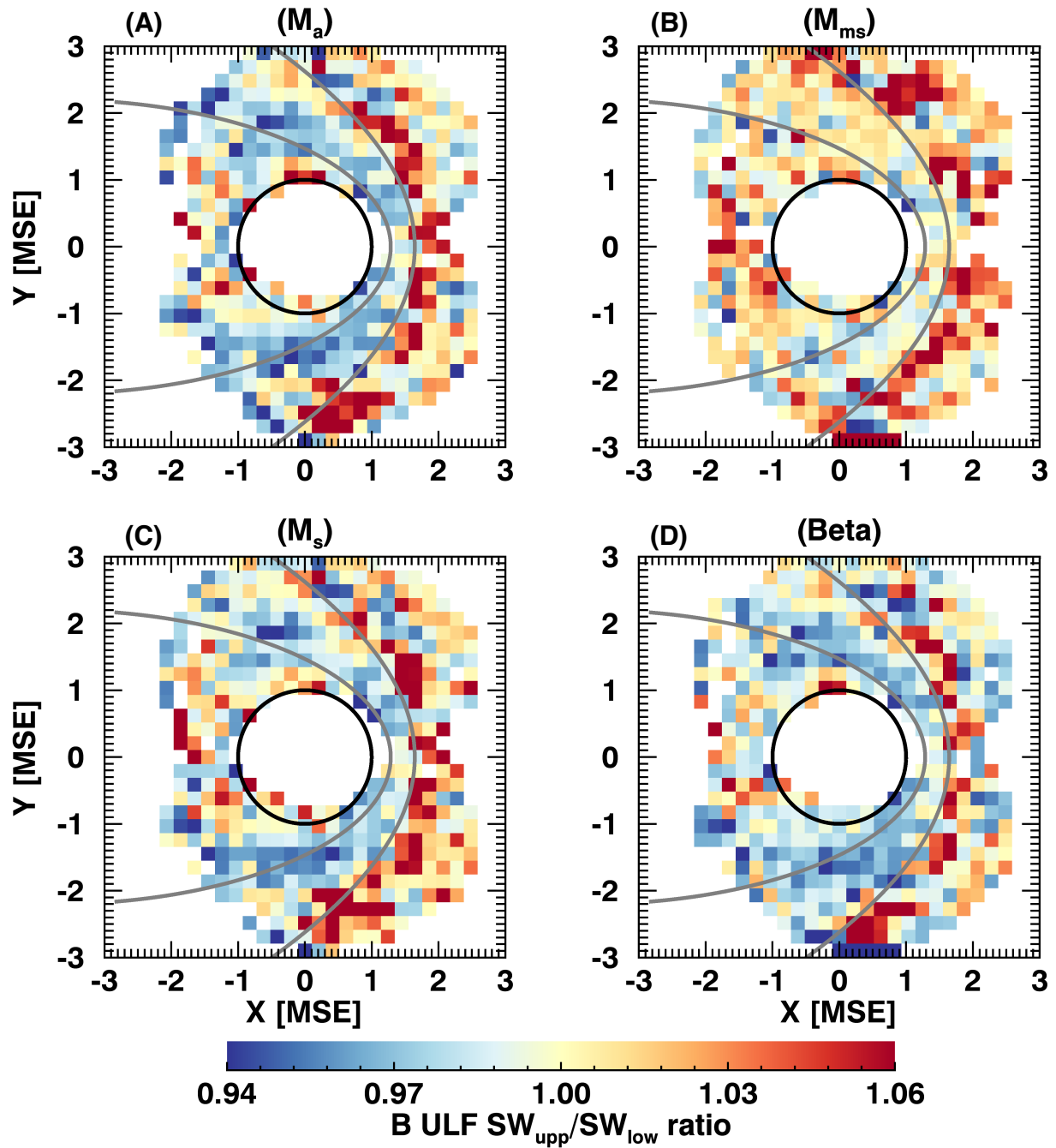


Figure 6.13: Ratio of magnetic field wave power in the ULF (0.01 - 0.1 Hz) range for upper to lower quartiles of solar wind upstream drivers. Panels a, b, c and show ratios for upstream Alfvén mach number ( $M_a$ ), magnetosonic mach number ( $M_{ms}$ ), sonic mach number ( $M_s$ ) and proton beta (beta), respectively.

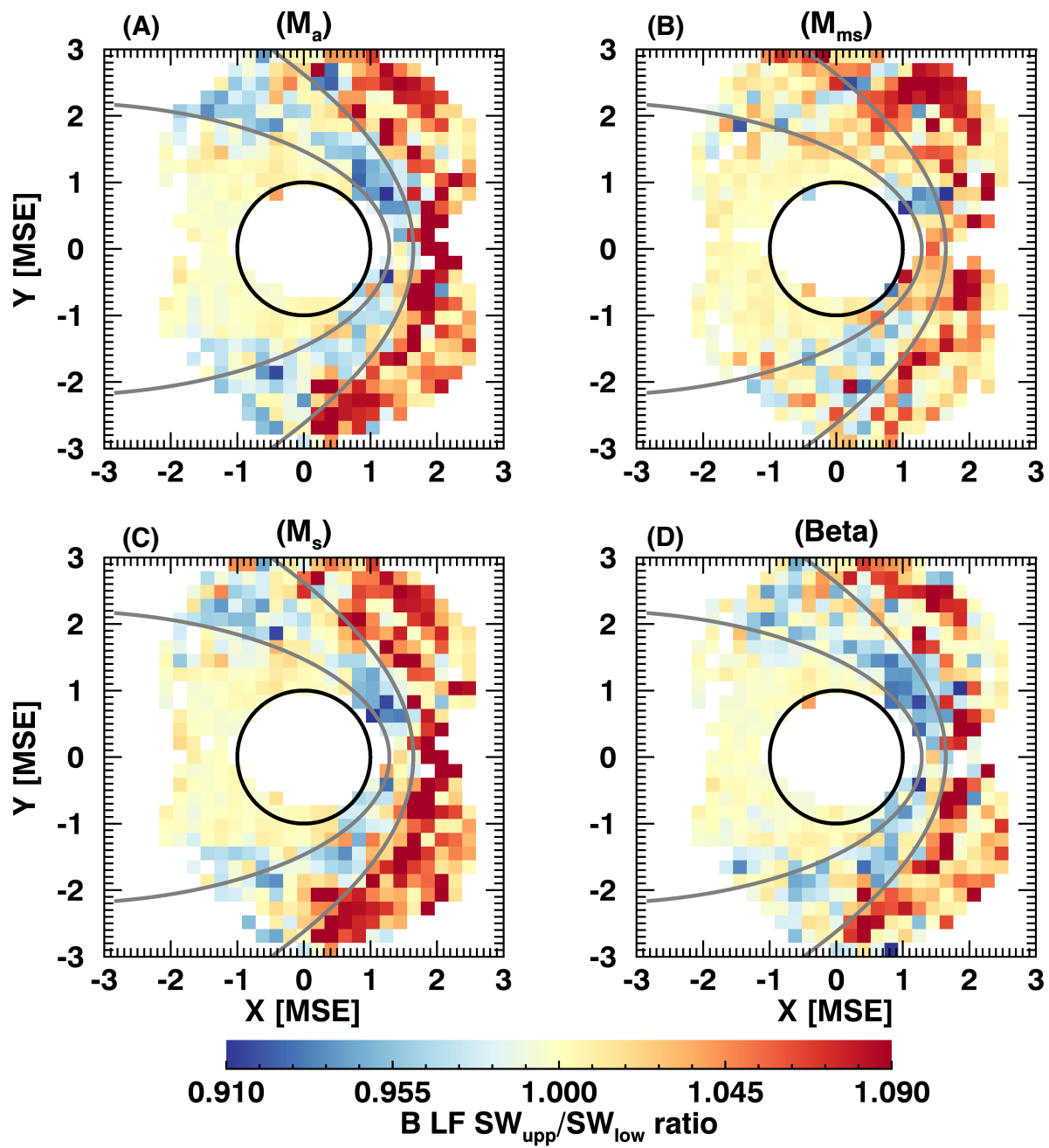


Figure 6.14: Ratio of magnetic field wave power in the LF (1 - 5 Hz) range for upper to lower quartiles of solar wind upstream drivers. Panels show the same upstream drivers as in Figure 6.13.

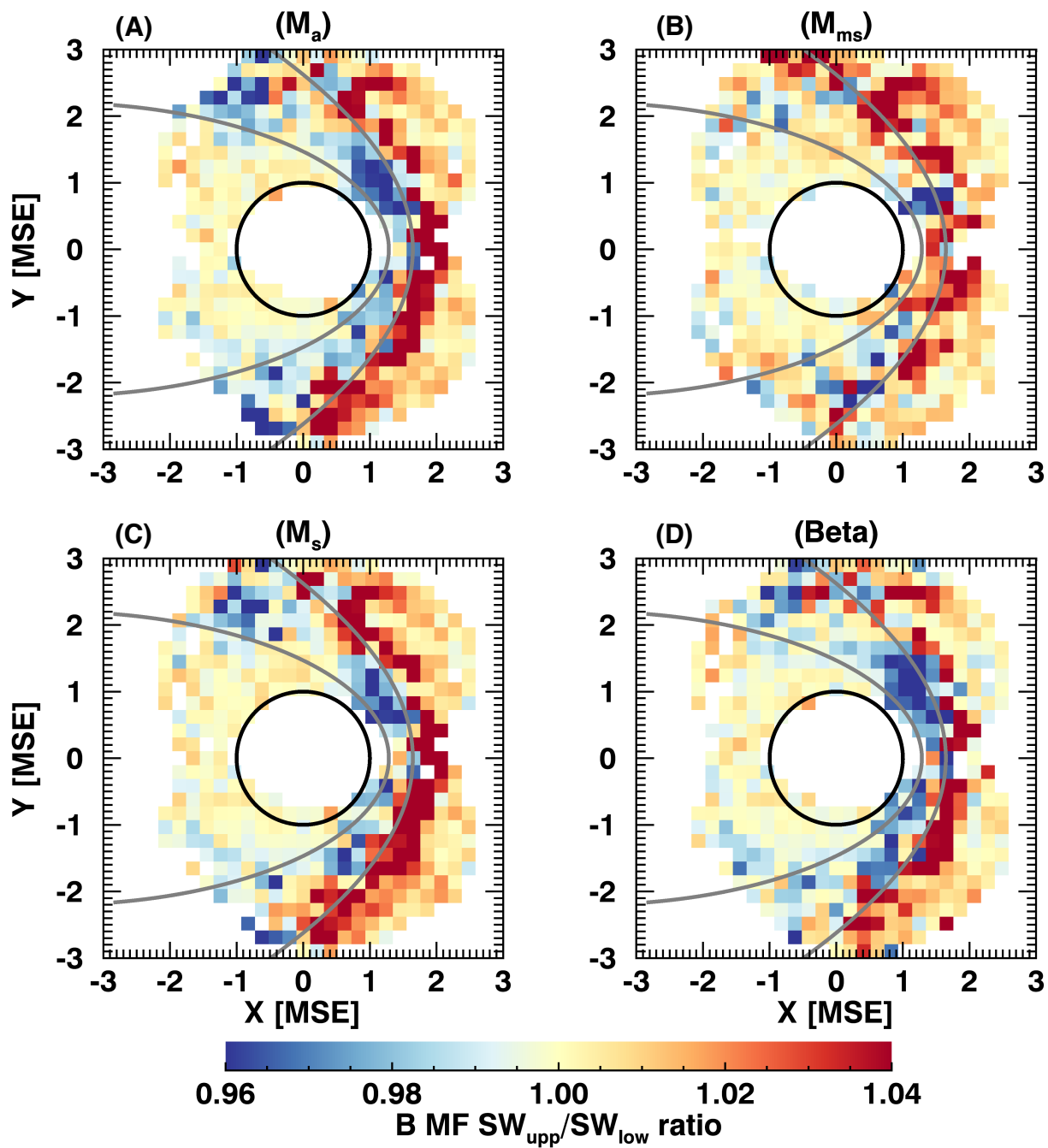


Figure 6.15: Ratio of magnetic field wave power in the MF (5 Hz) range for upper to lower quartiles of solar wind upstream drivers. Panels show the same upstream drivers as in Figure 6.13.

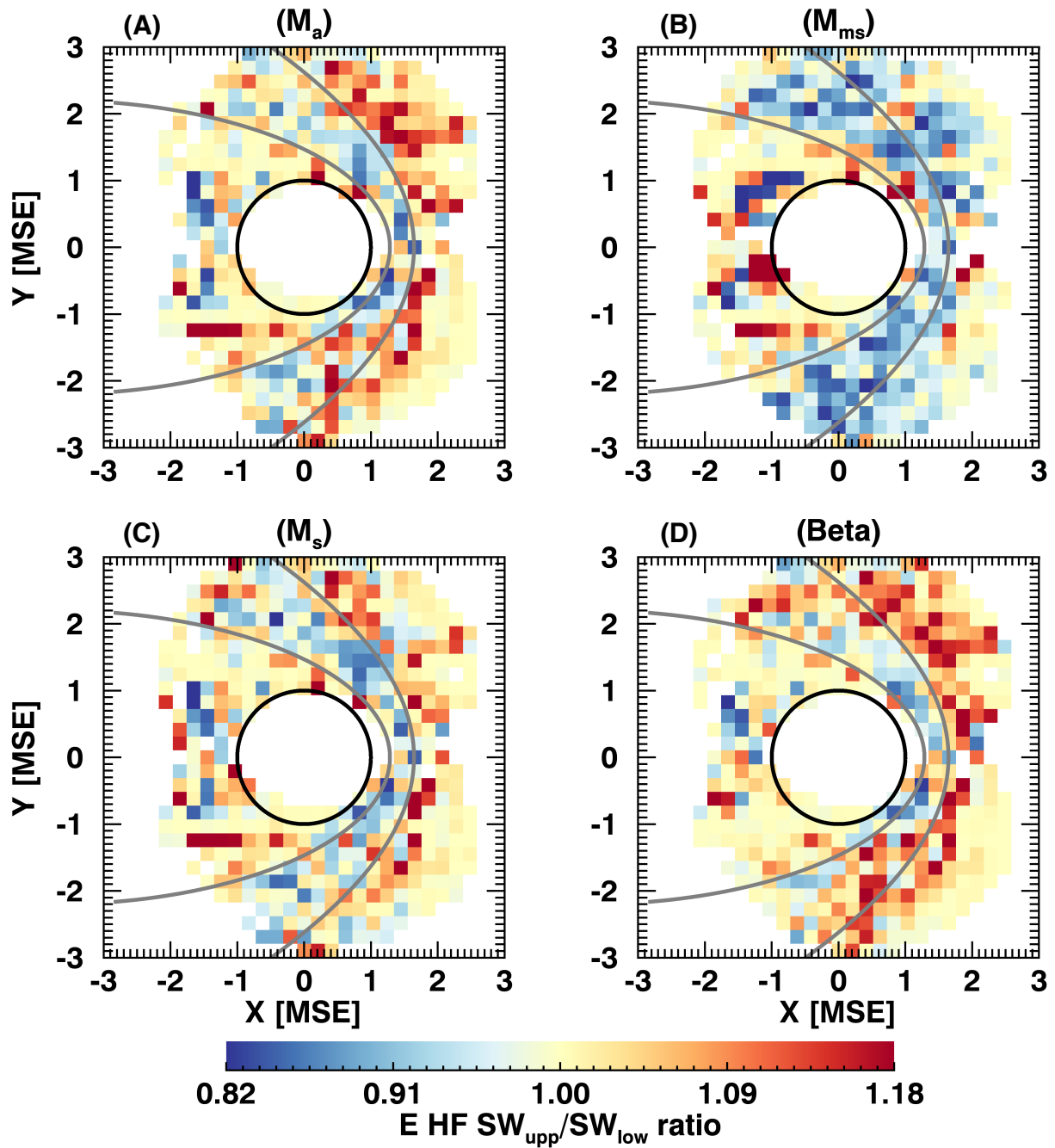


Figure 6.16: Ratio of electric field wave power in the HF (1k - 5k Hz) range for upper to lower quartiles of solar wind upstream drivers. Panels show the same upstream drivers as in Figure 6.13.

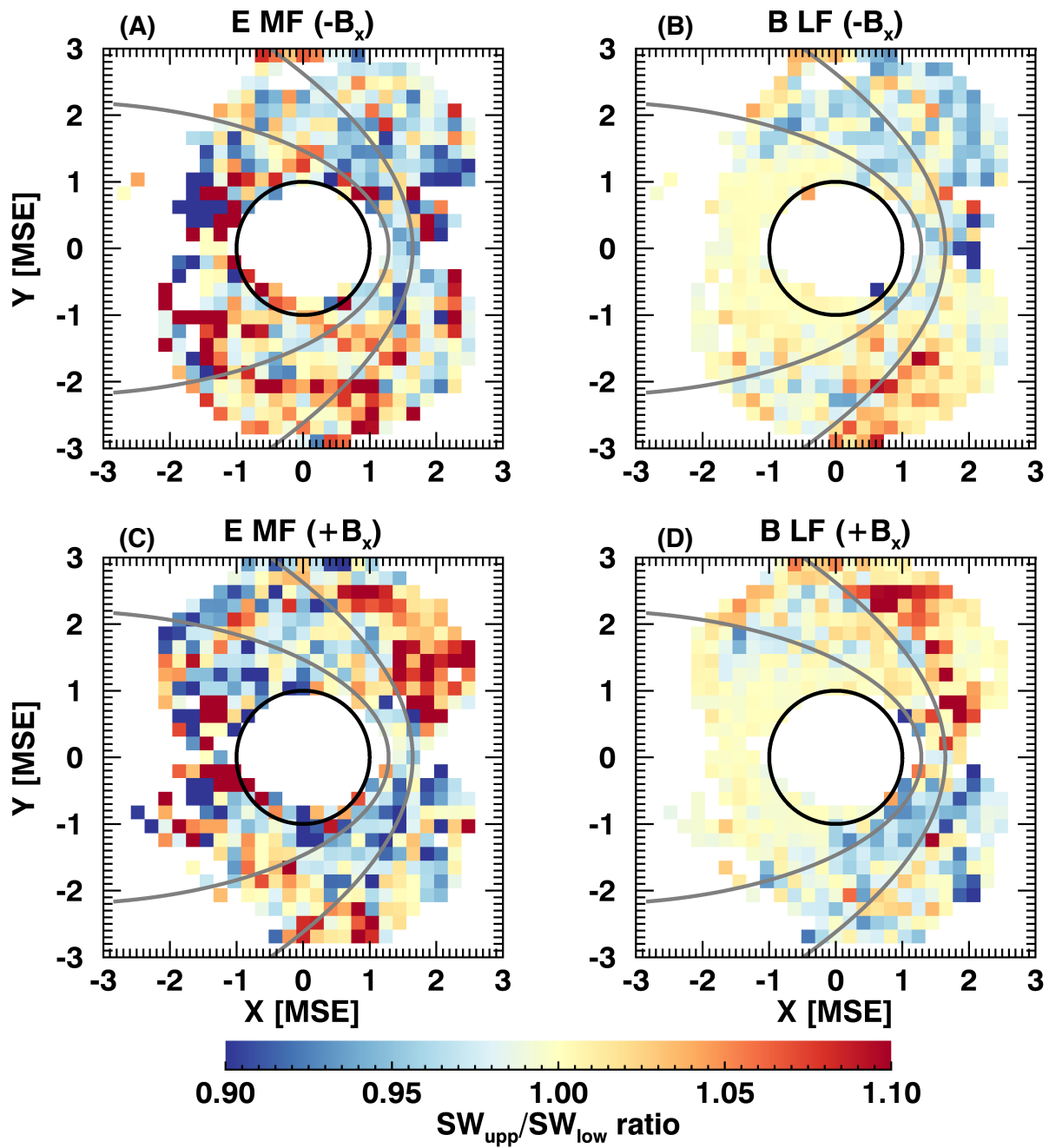


Figure 6.17: Panels a and c show the ratio of electric field wave power in the MF (5 Hz) range, for parallel ( $-B_x$ ) and anti-parallel ( $+B_x$ ) IMF directions. Panels b and d show the ratio of magnetic field wave power in the LF range for  $-B_x$  and  $+B_x$  IMF directions.

## Chapter 7

### Ion heating within a gradient magnetic field at low altitudes in the Martian ionosphere

**Submitted:** May 2016, Journal of Geophysical Research; reviewer comments received June 2016; to be resubmitted early 2017.

**Corresponding author:** C. M. Fowler, Laboratory of Atmospheric and Space Sciences, University of Colorado, Boulder, Colorado, USA 80303, christopher.fowler@lasp.colorado.edu.

**Authors:** C. M. Fowler<sup>1</sup>, J. McFadden<sup>2</sup>, T. Hara<sup>2</sup>, L. Andersson<sup>1</sup>, J. E. P. Connerney<sup>3</sup>, J. Espley<sup>3</sup>, R. E. Ergun<sup>1</sup>, D. L. Mitchell<sup>2</sup>, C. Mazelle<sup>4,5</sup>

<sup>1</sup>Laboratory of Atmospheric and Space Sciences, University of Colorado, Boulder, Colorado, USA.

<sup>2</sup>Space Sciences Laboratory, University of California, Berkeley, California, USA.

<sup>3</sup>NASA Goddard Space Flight Center, Greenbelt, MD 20771, USA

<sup>4</sup>CNRS, Institut de Recherche en Astrophysique et Planétologie, Toulouse, France

<sup>5</sup>University Paul Sabatier, Toulouse, France

## 7.1 abstract

The MAVEN spacecraft has observed energetic ions on the dayside of the Martian ionosphere below 400 km. For the first time at Mars ion conics are unambiguously identified demonstrating that ion heating and magnetic field gradients can play an important role for atmospheric loss at Mars. This work focuses on events where evidence of parallel acceleration, perpendicular heating, and magnetic mirroring are present, resulting in significant ion energization and transport. For the event analyzed in detail, the spacecraft was moving parallel to the magnetic flux tube and the observations suggest that a bottle neck type magnetic field topology is present, causing the observed ion conics. A statistical study shows that energetic ion events within a magnetic bottle like topology are rare. The observed events are most likely to occur between altitudes of 250 and 300 km, a critical region for eroding the Martian ionosphere by plasma processes. Since this study only included significantly heated ions, one can expect that this process is also active at altitudes below 250 km.

## 7.2 Introduction

The climate of Mars is known to have changed dramatically over the course of the planet's history. Many studies have shown that Mars was once a much wetter planet, where liquid water was present on the surface and the atmosphere was much thicker than it's present day counterpart. See, for example, the review by *Jakosky and Phillips* (2001). It is thought that a significant contributor to this climate change is the loss of atmosphere to space: atmospheric gases with energies greater than the gravitational potential of the planet can escape the gravity field of Mars. Jean's escape, photochemical escape, sputtering loss and charge exchange are thought to be some of the key escape processes for both neutral and charged particles, although the relative importance of these has yet to be determined (*Chassefière and Leblanc*, 2004). The loss of charged particles to space can be particularly complex - the energy gain to reach escape velocity via electromagnetic interactions can be through a single instantaneous process, or many different processes occurring over longer

time periods. Therefore, the magnetic field topology is important as this can prevent high-energy, charged particles escaping by redirecting them back into the atmosphere.

The most critical altitudes for energization of charged particles are at, and just above, the exobase, where ion densities are high and collisions with the neutral atmosphere start to become insignificant. At Mars the exobase is located at  $\sim 180 - 200$  km (*Haider and Mahajan, 2014*) and ions there typically have energies of a few eV or less (*Hanson et al., 1977*). Ion energization in the same region at Earth is observed as bulk upwelling (e.g. *Pollock et al. (1990)*) and as ion heating (e.g. *Ungstrup et al. (1979)*). Ion heating - ions gaining energy perpendicular to the magnetic field direction in a collisionless plasma - can be caused by many different processes (e.g. *André and Yau (1997)*). At Earth in the auroral regions there is often a lot of energy available for heating and energization of charged particles is usually limited by the number of ions available to heat. Ions tend to leave the energization regions quickly, resulting in low density regions. It is therefore very difficult to correlate which exact energization mechanism(s) heated the ions, since ions are quickly removed from regions where energization mechanisms are active and efficient. Despite this, statistical studies at Earth have shown that low frequency broad band heating is the most common mechanism to energize  $O^+$  (*André et al., 1998; Norqvist et al., 1998*).

The effect of ion heating is most easily observed away from the heating region. Even if heated ions do not have any initial parallel velocity, when subject to heating in a magnetic field gradient topology - such as in the Earth's auroral regions - ions will move towards the weaker magnetic field region due to the magnetic mirror force. Ion distributions are then observed as ion conics: a well studied distribution that can provide information on what processes are, or have been, active on a magnetic flux tube (for example *Ungstrup et al. (1979); Chang et al. (1986); André et al. (1988)*). If ions are subject to localized heating, prior to moving through a gradient magnetic field, their pitch angle as a function of total ion energy will be constant for all energies. If ions are subject to a broader heating region spread out within a gradient magnetic field, their distribution will be more 'U' shaped, where ion pitch angle varies with total ion energy. Finally, if a parallel electric field is present (localized or over a broad region) the observed ion conics will be shifted in the

parallel direction to a non-zero value for the lowest ion energies. Hence analyzing ion distributions provides substantial information as to the processes active on a magnetic flux tube and how the loss of charged particles from an atmosphere is driven.

Energetic ions interpreted as heated ions have been observed at Mars previously (*Lundin et al.*, 1989, 1990, 2004). These observations by the Mars Express (MEX) spacecraft were made above 300 km (a limitation due to the spacecraft orbit). The lack of magnetic field information on this mission has prevented these observations being uniquely associated with perpendicular heating. In addition, it was also not possible to evaluate the importance of magnetic field topology, and its ability to enhance parallel velocity (and subsequently escape), from these observations. It is therefore still unclear if these observed warm ion populations are a result of ion heating prior to, or whilst subject to, a gradient magnetic field. Such a two step process could be an efficient loss path for ions at Mars. Of particular interest is if this two-step process can occur close to the exobase where significant ion densities exist.

This paper presents observations made by the Mars Atmosphere and Volatile Evolution (MAVEN) mission that strongly support these earlier interpretations of MEX data. MAVEN carries a complete plasma package and makes measurements all the way below the exobase to  $\sim 150$  km on regular basis. This paper demonstrates for the first time that ion conics exist at Mars, and that energetic ion events can be observed associated with gradients in magnetic field topology. In Section 7.3 the data and mission are described followed by an event analysis in Sections 7.4, 7.5 and 7.6. A statistical study of similar events is presented in Section 7.7. A discussion and summary of the observations are made in Sections 7.8 and 7.9, respectively.

### 7.3 Data

The MAVEN mission (*Jakosky et al.*, 2015a) entered Mars orbit on 22<sup>nd</sup> September 2014. The spacecraft is in a 4.5 hour elliptical orbit with a typical periapsis altitude of around 150 km. This study utilizes data from the Suprathermal and Thermal Ion Composition (STATIC, *McFadden et al.* (2015)), Magnetometer (MAG, *Connerney et al.* (2015)), Langmuir Probe and Waves

(LPW, *Andersson et al.* (2014)) and Solar Wind Electron Analyzer (SWEA, *Mitchell et al.* (2016)) instruments. STATIC is an electrostatic top hat analyzer that uses time of flight to determine ion mass. Electrostatic deflectors give the instrument a  $360^\circ \times 90^\circ$  field of view and is able to measure energies down to below 1 eV up to several keV. Due to ongoing instrument calibration at energies below  $\sim 5$  eV, we do not state absolute fluxes here. STATIC has a measurement cadence of 4 s at periapsis for the data presented in this study. MAG is a fluxgate magnetometer that measures the vector magnetic field at a rate of 32 Hz. LPW consists of two  $\sim 7$  m booms separated by an angular distance of  $\sim 110^\circ$ . Electric field power spectra are measured at a cadence of 2 s for the data presented here. SWEA is a hemispherical electrostatic analyzer that measures electron fluxes from a few eV up to several keV. It has a  $360^\circ \times 120^\circ$  field of view provided by electrostatic deflectors and a time resolution of 4 s.

#### 7.4 Event

Highly energetic ions were observed by the MAVEN spacecraft close to periapsis on the 4<sup>th</sup> May 2015 at approximately 12:20 UTC. The MAVEN orbit track for this orbit is shown in Figure 7.1. The time period during which high energy ions were observed ('the event') is marked by the thicker purple line on the inbound part of the orbit, spanning an altitude range of approximately 550 - 300 km. Periapsis lies close to the sub solar point, at solar zenith angle (SZA) of approximately  $20^\circ$ . The event lies at slightly larger SZA, roughly  $45^\circ$ .

Plasma data from several instruments on board MAVEN are presented in Figure 7.2, providing evidence that these energetic ions were subject to parallel acceleration and perpendicular heating within a gradient magnetic field. The inbound portion of the periapsis spans altitudes below 1000 km. Periapsis occurs at 164 km altitude at  $\sim 12:30$  UTC, and the outbound portion of the periapsis is shown up to altitudes of approximately 250 km. The altitude profile is shown in panel J and is referenced to the International Astronomical Union (IAU) 2000 Mars Areodetic ellipsoid. An ion energy spectrogram for all mass species as measured by the STATIC instrument, corrected for spacecraft potential (as measured by LPW), is shown in panel A. The ion mass distribution as

observed by STATIC is shown in panel B. Electron density and temperature as measured by the LPW instrument are shown in panels C and D respectively. The total magnetic field strength and the corresponding magnetic field power spectrum are shown in panels E and H respectively. The cone angle between the spacecraft velocity vector and magnetic field vector is shown in panel F. Values of  $0^\circ$  and  $180^\circ$  represent parallel and anti-parallel spacecraft velocities to the magnetic field respectively and a value of  $90^\circ$  represents perpendicular travel to the flux tube. The cone angle between the spacecraft radial position vector and the magnetic field vector is shown in panel G. Values of  $0^\circ$  and  $180^\circ$  mean that the magnetic field is aligned vertically to the planet surface, where  $0^\circ$  is upward and  $180^\circ$  is downward. A value of  $90^\circ$  means the magnetic field is aligned horizontally to the surface. Dashed lines have been added to panels F and G at  $45^\circ$ ,  $90^\circ$  and  $135^\circ$  to aid the reader. The electric field power spectrum as measured by LPW is shown in panel I.

The observed energetic ions in panel A are marked by the black vertical lines and are characterized by significant energy fluxes at energies greater than 10 eV up to several hundred eV. The instrument mode during periapsis is such that energies above 1000 eV are not sampled. Typical ionospheric energies of less than  $\sim 10$  eV are observed outside of the event. The plasma composition during the event is fairly typical of the entire periapsis pass - the primary species being  $O^+$ ,  $O_2^+$  and  $CO_2^+$ , with a fair amount of protons also present. A clear drop in electron density by a factor of  $\sim 10$  is observed at the center of the event, at approximately 12:20 UTC. There is a corresponding increase in electron temperature. The magnetic field strength either side of the observed energetic ions reaches  $\sim 55$  nT and a minimum of  $\sim 30$  nT is observed at the center of the event. Although not shown here, this minimum in magnetic field strength is not caused by localized crustal magnetic field sources (*Acuna et al.*, 1999). There is evidence of wave activity throughout the entire periapsis pass and this is verified in the magnetic field power spectrum in panel H. Periapsis shows the strongest wave power and this is observed at the lowest frequencies,  $\sim 0.1$  Hz. The inbound part of the orbit, times leading up to about 12:25 UTC, shows more modest wave power at frequencies below  $\sim 1$  Hz. The outbound part of the orbit, times later than  $\sim 12:35$  UTC, shows wave power at slightly higher frequencies - between 0.1 and 1 Hz. At the observed

magnetic field strengths, waves at frequencies  $< 1$  Hz are comparable to the ion gyro frequencies for the heavier ions, namely  $O^+$  and heavier. When energetic ions are observed, in particular  $\sim 12:20:30$  to  $12:21:00$  UTC, MAVEN flies almost anti-parallel to the magnetic field as shown in Figure 7.2F. The magnetic field is aligned more or less horizontal to the planet surface during this time period and the importance of this is discussed in Section 7.6. Electric field wave power is present at the same time energetic ions are observed. Due to the instrument mode the electric field spectrum is more suited for analyzing higher frequency waves and is unable to resolve frequencies below  $\sim 1$  Hz.

## 7.5 Ion velocity distributions

Analysis of ion velocities with respect to the local magnetic field can yield important information on the nature of any acceleration and heating processes that are, or have, acted on the plasma. In order to achieve good signal to noise the event analyzed in this study was split up into five segments of equal length, each approximately sixty seconds long. These segments are labeled 0 through 4 and are shown in Figure 7.3. During each segment the local magnetic field direction varied by less than  $15^\circ$  and the spacecraft potential varied by less than 1 volt, allowing for averaging of the data. Ion distributions from the lowest altitudes at which energetic ions were observed are presented in Figure 7.4. These correspond to segment 4 in Figure 7.3, spanning altitudes 340 - 300 km. To put the observed energetic ions into context we also show ion distributions from similar altitudes and location two periapses later when energetic ions were not observed, Figure 7.5. Non energetic ions are observed during every periapsis pass, however the STATIC observation mode and orientation relative to the local magnetic field mean that coverage in velocity space can be poor at times. The coverage in Figure 7.5 allows for a clear demonstration of the differences between energetic and non energetic ion distributions, as discussed below.

$O^+$  and  $O_2^+$  ion distribution functions are shown in panels A and B of Figures 7.4 and 7.5. The jagged contours are a result of not smoothing the data - this allows for important features to remain observable. Data has been transformed to the Mars frame by accounting for the spacecraft

velocity and spacecraft potential. The ion distributions are presented with respect to the local magnetic field, where positive parallel velocity is along the magnetic field and the perpendicular velocity direction is cross track ( $-\vec{V} \times \vec{B}$ ). We only show positive perpendicular velocity where the spacecraft body is not obstructing the instrument field of view. Color represents the average distribution function and the color bars within each figure are to the same scale so that ion species can be directly compared. The black vertical lines mark zero velocity in the parallel direction. Due to ongoing instrument calibration ion distributions observed below  $\sim 2\text{-}3 \text{ km s}^{-1}$  are uncertain and so we ignore these regions in our analysis - these regions are small and do not affect our conclusions. The black crosses represent the data points within velocity space. During this periapsis the instrument mode was such that the electrostatic deflectors provided four azimuthal measurements for each of the sixteen toroidal sectors, resulting in sixty four data points spanning velocity space. The average spacecraft potential for the time period covered by Figure 7.4 was  $-3.3 \text{ V}$ ; two periapses later for Figure 7.5 it was  $-11.8 \text{ V}$ .

The core populations for  $\text{O}^+$  and  $\text{O}_2^+$  in Figure 7.4 have bulk velocities of approximately  $9$  and  $7 \text{ km s}^{-1}$  respectively. In contrast, both species have close to zero bulk parallel velocity in Figure 7.5. Ions that have been significantly heated in the perpendicular direction are present in Figure 7.4 but not in Figure 7.5.

## 7.6 Interpretation and discussion of ion data

The large scale magnetic field topology shown in Figure 7.2G shows that the magnetic field is roughly horizontal to the planet surface for the duration of this periapsis. Given that this periapsis pass occurs on the dayside at relatively small to moderate SZA, we expect this behavior due to the draping of magnetic field lines around the dayside of the planet. There are several instances outside of the times when energetic ions are observed when the magnetic field topology is more vertically aligned, such as at times between  $12:16:20 - 12:18:30 \text{ UTC}$  and  $12:27:30 - 12:30:00 \text{ UTC}$ . These more vertical fields are caused by localized crustal magnetic fields (not shown here). Figure 7.2F shows that MAVEN travels roughly parallel to the magnetic field for most of the analyzed event,

suggesting that the spacecraft samples plasma from the same flux tube. The observed gradients in magnetic field suggest a magnetic bottle like topology is present.

The ion distributions presented in Figure 7.4 show evidence of acceleration and heating. The parallel bulk velocities of  $O^+$  and  $O_2^+$  vary by a factor close to  $\sqrt{2}$ , suggesting that the ions were subject to a parallel acceleration process that imparts the same energy independent of mass. The bulk of the ions are traveling along the magnetic field, away from the planet. The extended tail populations for both ion species in the perpendicular direction suggest a perpendicular heating mechanism is present and these features are known as ion conics (*André and Yau, 1997*). These conics appear curved in velocity space suggesting perpendicular heating within a gradient magnetic field. We suggest that the ion populations observed in Figure 7.4 have undergone a two step energization process: firstly they are subject to parallel acceleration that imparts equal energy independent of mass; these populations are then subject to perpendicular heating whilst traveling in a gradient magnetic field, in the form of a magnetic mirror, that produces the observed conics.

To test these interpretations we look in more detail at the observed conics and their corresponding pitch angle distributions as a function of total ion velocity in Figure 7.4. The magnetic field gradient required to produce these observed pitch angles is evaluated. The ion distributions shown in Figure 7.4 were interpolated to a grid of resolution of  $1 \text{ km s}^{-1}$ ; the observed conics show up as peaks in the distribution function and these are mapped as functions of pitch angle and total ion velocity, shown in Figure 7.6. The observed conics are represented by the black horizontal lines in the figure; panels A and B show  $O^+$  and  $O_2^+$  respectively. The uncertainty in exact conic location is accounted for by extending each black line across a  $15^\circ$  range in pitch angle. The red lines in the figure show modeled pitch angles as functions of total ion velocity, pitch angle and magnetic field strength ratio,  $B_r$ . A simple model was used whereby starting populations of  $O^+$  and  $O_2^+$  were given parallel and perpendicular velocity distributions matching those observed in Figure 7.4. These populations were subject to magnetic mirror forces of varying  $B_r$ , producing the red lines in Figure 7.6. The range of  $B_r$  shown in the figure spans 0.64 to 0.84 from left to right, in increments of 0.02. As pitch angle approaches zero, the red lines approach the respective

bulk parallel velocities of each ion species. Observed pitch angles (the black lines) located at 5 km s<sup>-1</sup> total ion velocity lie below the bulk parallel velocities of both ion species and so the modeled pitch angles (red lines) do not cross through them. The modeled pitch angles for  $B_r$  between 0.64 and 0.84 can produce the observed ion conics. These values of  $B_r$  agree well with magnetic field observations of the event: a minimum of 30 nT up to a maximum of 55 nT results in a range of  $B_r$  of  $\sim 0.55$  up to 1.

If the proposition that the ion populations observed in Figure 7.4 have undergone an initial parallel acceleration is correct then electrons should be observed having been decelerated in the same direction along the magnetic flux tube. Electron spectrogram data from the SWEA instrument is shown in Figure 7.7. Electrons traveling parallel and anti parallel to the magnetic field are shown in panels A and B respectively. The horizontal axis is UTC time, the vertical axis is energy and the color represents energy flux. The color scales are the same so that direct comparison between the two panels can be made. At times before 12:15 UTC in panel A, and for approximately 12:26:30 - 12:26:40 UTC in panel B, no data exist (denoted as black across all energies). This is due to the orientation of the magnetic field with respect to the SWEA instrument being such that parallel and anti parallel traveling electrons were outside of the instrument field of view.

Ionospheric electrons are identified from the presence of CO<sub>2</sub> photo electron lines nominally located at  $\sim 23$  and 27 eV (*Frahm et al.*, 2006). Ionospheric photoelectrons travel parallel to the magnetic field during the time period of interest, between 12:15 and 12:25 UTC, as seen by a peak in energy flux at approximately 20 eV in Figure 7.7A. This indicates that one end of the magnetic flux tube is well connected to the Martian ionosphere. There is a lack of clear ionospheric photoelectron peaks in panel B during this same time period, suggesting that the other end of the flux tube is either not connected to the Martian ionosphere, or that the plasma traveling in this direction has been subject to plasma processes. Photoelectrons are present in panel B at times before  $\sim 12:17$  UTC, suggesting that at earlier times the flux tube was connected to the ionosphere at both ends, or that MAVEN was sampling different flux tubes at these times.

When energetic ions are observed, two completely different electron populations are observed

moving in opposite directions along the magnetic field. The potential below the spacecraft can therefore not be determined by comparing similar but oppositely traveling electron populations, as has been done for the polar wind at Mars (*Collinson et al., 2015*). The photoelectron lines at 23 and 27 eV can also be used to determine the potential beneath the spacecraft. The energy resolution of the SWEA instrument at the relevant energies is however coarse and therefore only large potentials can be identified. During times of significant spacecraft charging, the photoelectron lines can be shifted to lower energies where higher energy resolution measurements are made. For this event the spacecraft potential was not large enough for this to happen and the interpreted parallel potential that the ions were subject to is less than the energy resolution SWEA can provide for this event.

## 7.7 Statistics of similar events

An automated software routine was written to identify events similar to the one shown in this article. There were three broad criteria that had to be satisfied for an event to be flagged: 1. The event must occur below altitudes of 600 km. 2: The observed average ion energy flux must be above a specified threshold of  $1 \times 10^7$  eV (eV cm<sup>2</sup> s sr)<sup>-1</sup> for energies between 10 and 50 eV. 3: The total magnetic field strength must show a minimum during the event.

The software analyzed approximately one years worth of data from 2014-10-08 to 2015-11-31 and utilized primarily ion energy spectrogram data as shown in Figure 7.2A. Each periapsis was analyzed separately; a sliding window five time steps (20 seconds) long was used to average the energy flux observed between 10 and 50 eV in the ion data. If this average energy flux was greater than the specified threshold then that time step (and subsequently periapsis) was flagged as a potential energetic ion event. The magnetic field data was not analyzed in this first step due to the complexities of reliably finding a minimum in large scale magnetic field strength using an automated routine. The energy flux threshold was specified so that events of similar magnitude to that presented in this study would be identified. The automated routine flagged 448 periapses - these were inspected by eye to confirm the existence of energetic ionospheric ions coinciding with a minimum in magnetic field strength. Thirty one events were confirmed from this analysis method.

The large number of false positives arose due to the upper altitude limit of 600 km. Solar wind plasma is often observed at altitudes below this and the automated routine cannot distinguish between this and ionospheric plasma. Inspection by eye eliminates this problem.

The confirmed events were located almost exclusively on the dayside of Mars, distributed approximately uniformly across the dayside of the planet. The distribution of these events with respect to altitude is shown in Figure 7.8. Altitude is referenced to the IAU frame. If an energetic ion event that meets the above three criteria is observed, it is most likely to occur at altitudes between 250 and 300 km. There is a sharp decrease in likelihood below  $\sim 200$  km, with a low probability tail extending out to 600 km.

## 7.8 Interpretation and discussion of statistical data

When an energetic ion event was observed, it was most likely to occur between 250 and 300 km altitude. In a gradient magnetic field ions will be accelerated towards the weaker magnetic field strength - in the 31 observed cases this was out of the ionosphere. When observed by MAVEN, energization and mirroring of ions have already been active in space and time, indicating that these processes occur at even lower altitudes in the Martian ionosphere. Significant ion densities exist at 250 - 300 km altitudes and the region is relatively collisionless meaning that energized ions do not lose their energy through collisions with the neutral atmosphere. Below  $\sim 200$  km altitude the atmosphere at Mars becomes highly collisional - ions collide frequently with the neutral atmosphere and thermalize over very short timescales. This is the most probable cause of the sharp drop in distribution function seen in Figure 7.8 below 200 km.

The small number of events observed in just over a years worth of data show that energetic ion events and strong ion heating similar to that shown here are rare at current day Mars. A gradient magnetic field topology will enhance ion outflow through perpendicular heating. A bottleneck magnetic field topology will trap ions with the largest pitch angles; the high altitude mirror point would reflect ionospheric ions back down to encounter any heating region(s) for a second (or greater) time. In such a situation the bottle neck topology would provide larger than normal heated ions.

These events may have contributed significantly to the loss of Martian atmosphere if they occurred more frequently in the past.

## 7.9 Conclusions

During a periapsis pass on the 4<sup>th</sup> May 2015 at approximately 12:20 UTC, the MAVEN spacecraft observed energetic ions up to several hundred eV at low altitudes in the Martian ionosphere. Analysis of the magnetic field topology suggests that MAVEN flew almost parallel to a flux tube and observed a minimum in magnetic field strength during the event. We interpret this to be a gradient magnetic field, indicating the presence of a magnetic bottle like field topology.  $O^+$  and  $O_2^+$  ion distributions in the Mars frame have bulk parallel velocities that differ by a factor close to  $\sqrt{2}$  suggesting a parallel acceleration mechanism that imparts equal energy independent of mass. Curved ion conics are present for both ion species, with tail populations possessing large velocities in the perpendicular direction, relative to the local magnetic field. These are interpreted as evidence of perpendicular heating within a gradient magnetic field. We suggest a two stage energization process: ions are initially subject to a parallel electric field, before being subject to perpendicular heating within a gradient magnetic field and reflection by a magnetic mirror. A simple pitch angle model shows that the observed magnetic field gradients can produce the observed ion conics. Based on the electron distributions shown here the fluxtube on which the observed ions and electrons were traveling along was either not connected to the atmosphere, or the observed ions were traveling tailward away from the atmosphere. These energetic ions will easily escape the planet if the flux tube is connected to the solar wind.

A statistical study containing just over a years worth of data found 31 confirmed similar energetic ion events in the presence of a minimum in magnetic field strength. These events were distributed roughly uniformly across the dayside of Mars, with only one event occurring on the nightside of the planet. When an energetic ion event was observed, it was most likely to occur between altitudes of 250 - 300 km, an important altitude range when considering plasma loss to space at Mars. The observed ions were most likely energized below this altitude region but their

largest energy gain was between 250 and 300 km due to the lower collision frequency with the neutral atmosphere here. If more frequent in the past then these events may have been able to remove significant amounts of the Martian ionosphere, contributing to the extreme climate change that the Red planet has undergone throughout it's history.

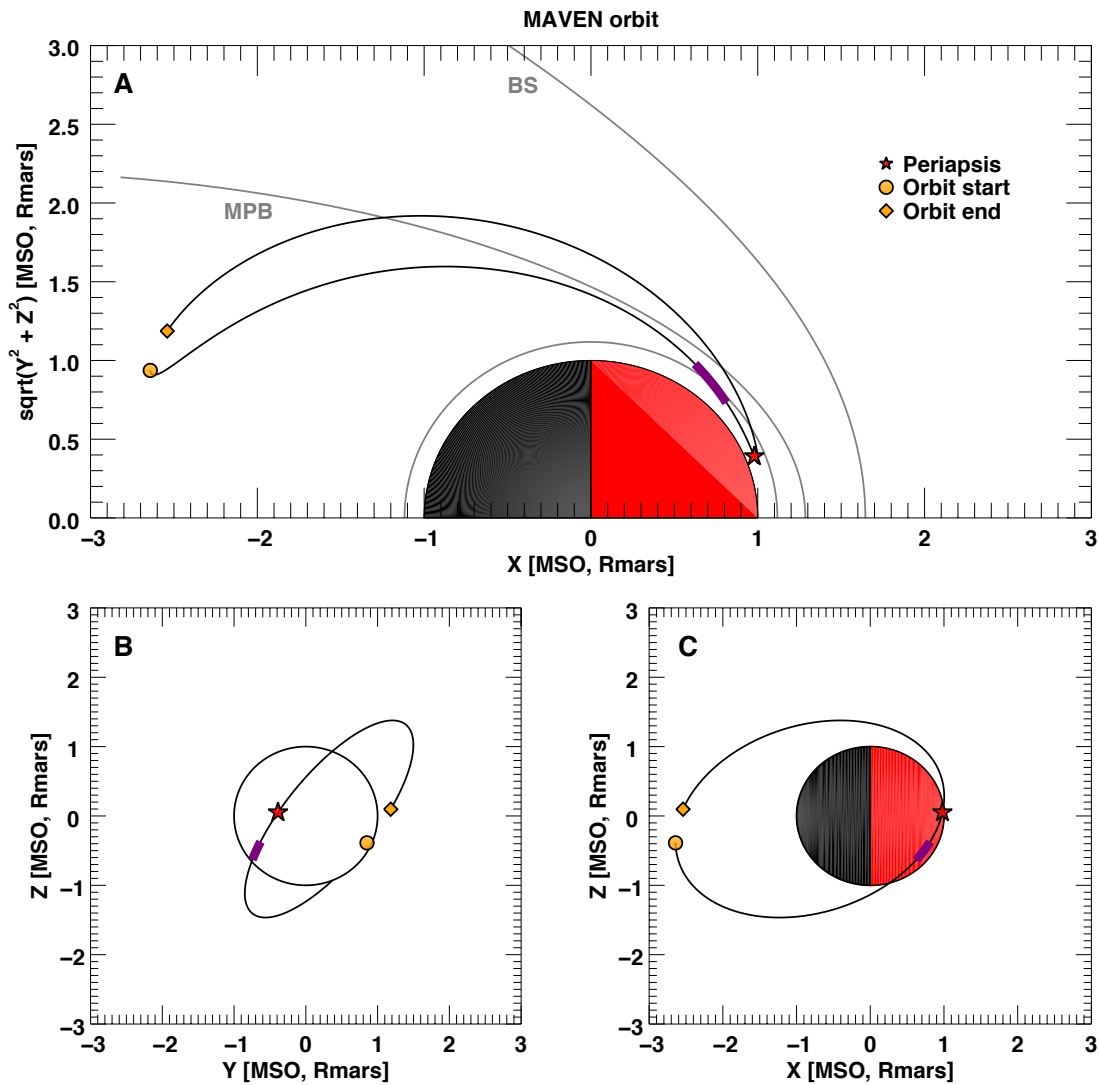


Figure 7.1: The MAVEN orbit trajectory in the Mars Solar Orbital (MSO) frame for May 4<sup>th</sup> 2015 between approximately 10:00 to 15:00 UTC. (A) is in cylindrical coordinates, (B) and (C) show the orbit from different perspectives in the MSO frame. All axes have units of Mars radii. The grey conics in (A) represent the empirical Bow Shock (BS) and Magnetic Pileup (MPB) plasma boundaries as derived by *Vignes et al.* (2000). The grey semi-circle represents an altitude of 400 km, the approximate extend of the Martian ionosphere. The heating event is marked by the thick purple line.

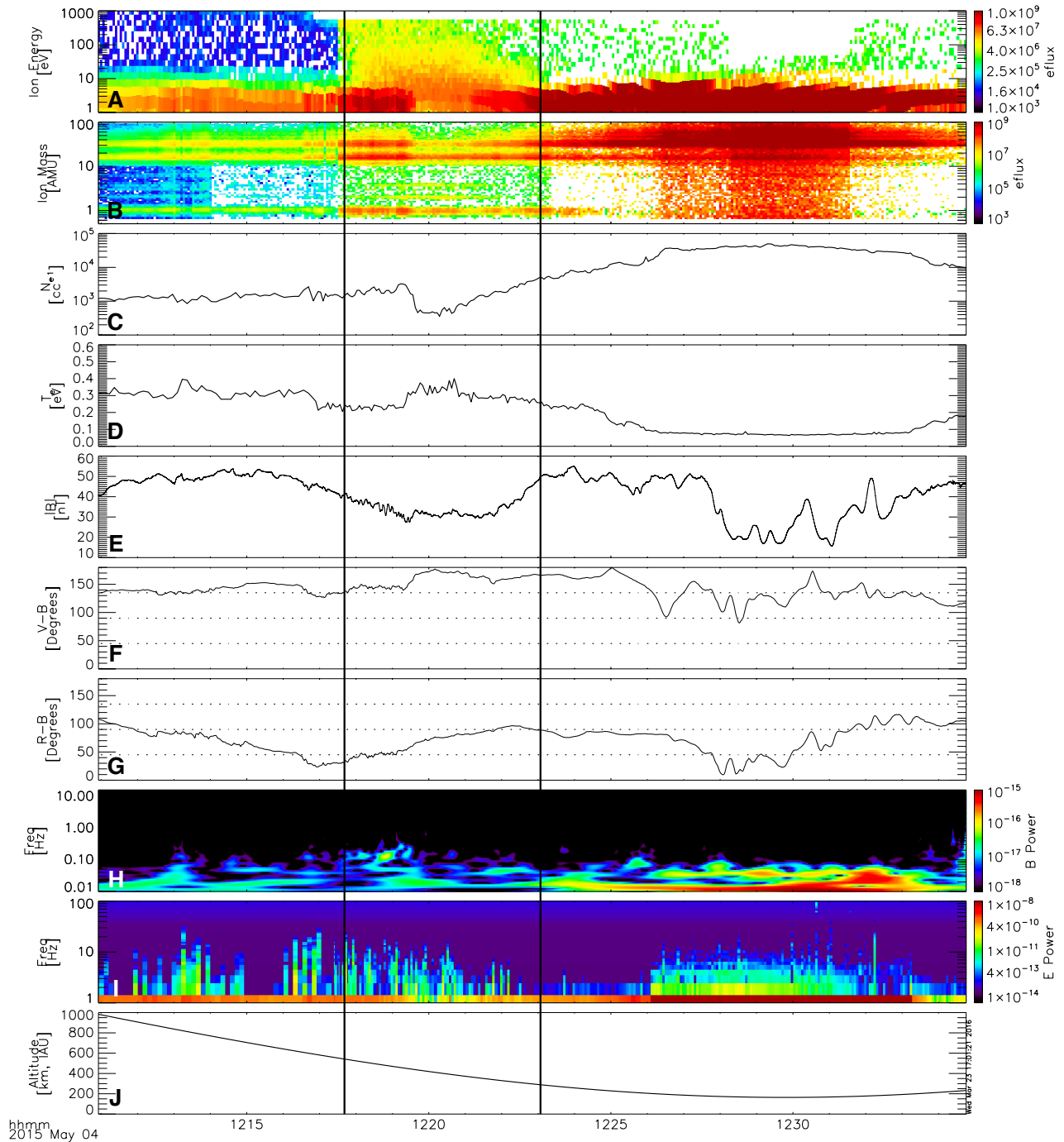


Figure 7.2: Panel A: ion energy spectrogram for all mass species, corrected for spacecraft potential. Panel B: ion mass distribution. Panels C and D: electron density and temperature respectively. Panel E: total magnetic field strength. Panel F: cone angle between the spacecraft velocity vector and magnetic field vector. Panel G: cone angle between the spacecraft radial position vector and the magnetic field vector. Panel H: magnetic field power spectrum. Panel I: electric field power spectrum. Panel J: altitude profile as referenced to the International Astronomical Union (IAU) 2000 Mars Areodetic ellipsoid. Energy flux has units of [eV (eV cm<sup>2</sup> sr)<sup>-1</sup>].

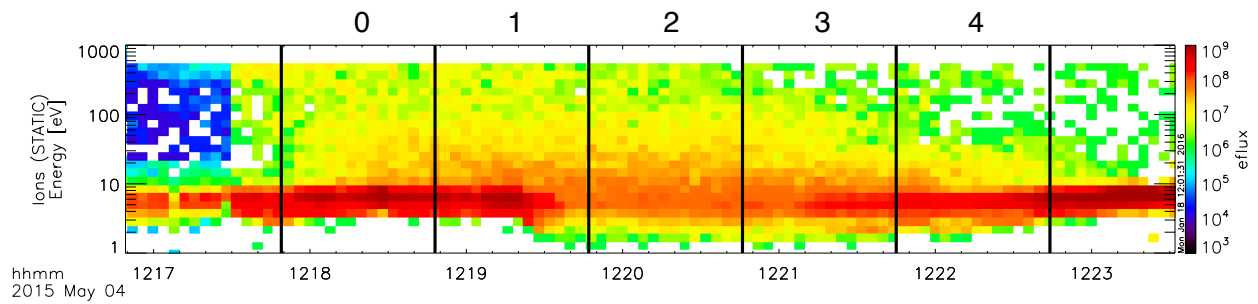


Figure 7.3: Spectrogram data showing energetic ions for all mass species. The analyzed ion distributions are averaged over the five segments shown in the figure, labeled with the numbering at the top of the panel.

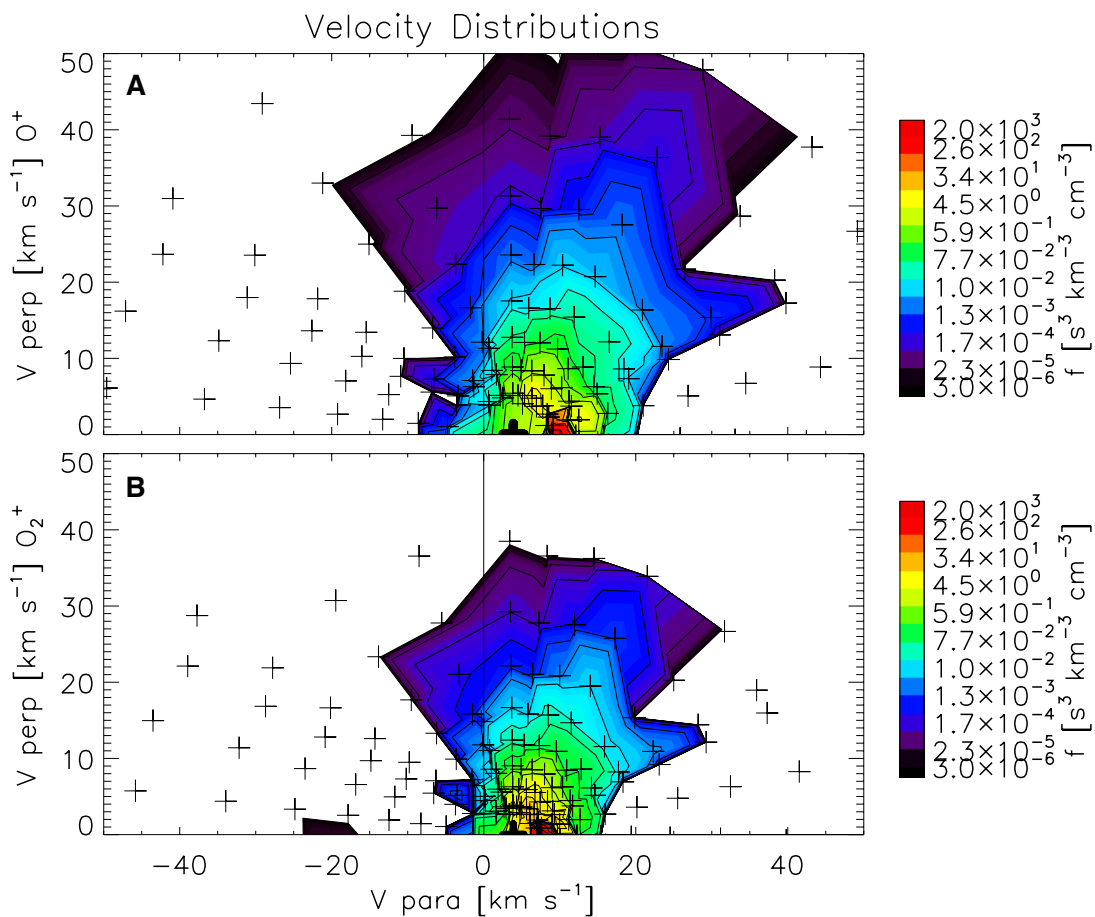


Figure 7.4: Panels A and B: distribution functions of  $O^+$  and  $O_2^+$  ions when energetic ions were observed. Data is averaged between 12:21:45 and 12:22:44 UTC from segment 4 in Figure 7.3 and is presented in the Mars frame. Positive parallel velocity is in the magnetic field direction. Only positive perpendicular velocities are shown due to spacecraft contamination at negative velocities.

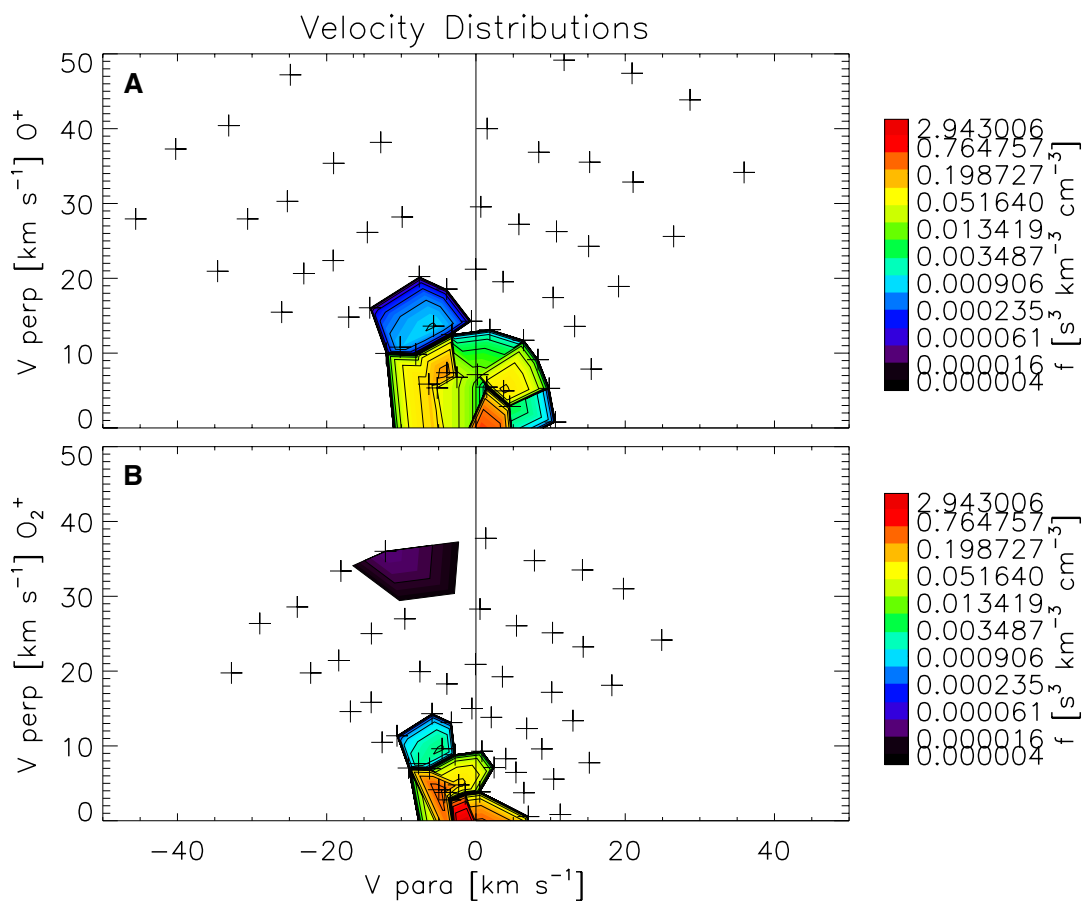


Figure 7.5: More typical non energetic ions observed at periapsis. The figure format is the same as Figure 7.4. Data is averaged from two periapses later between 21:21:00 and 21:22:00 UTC.

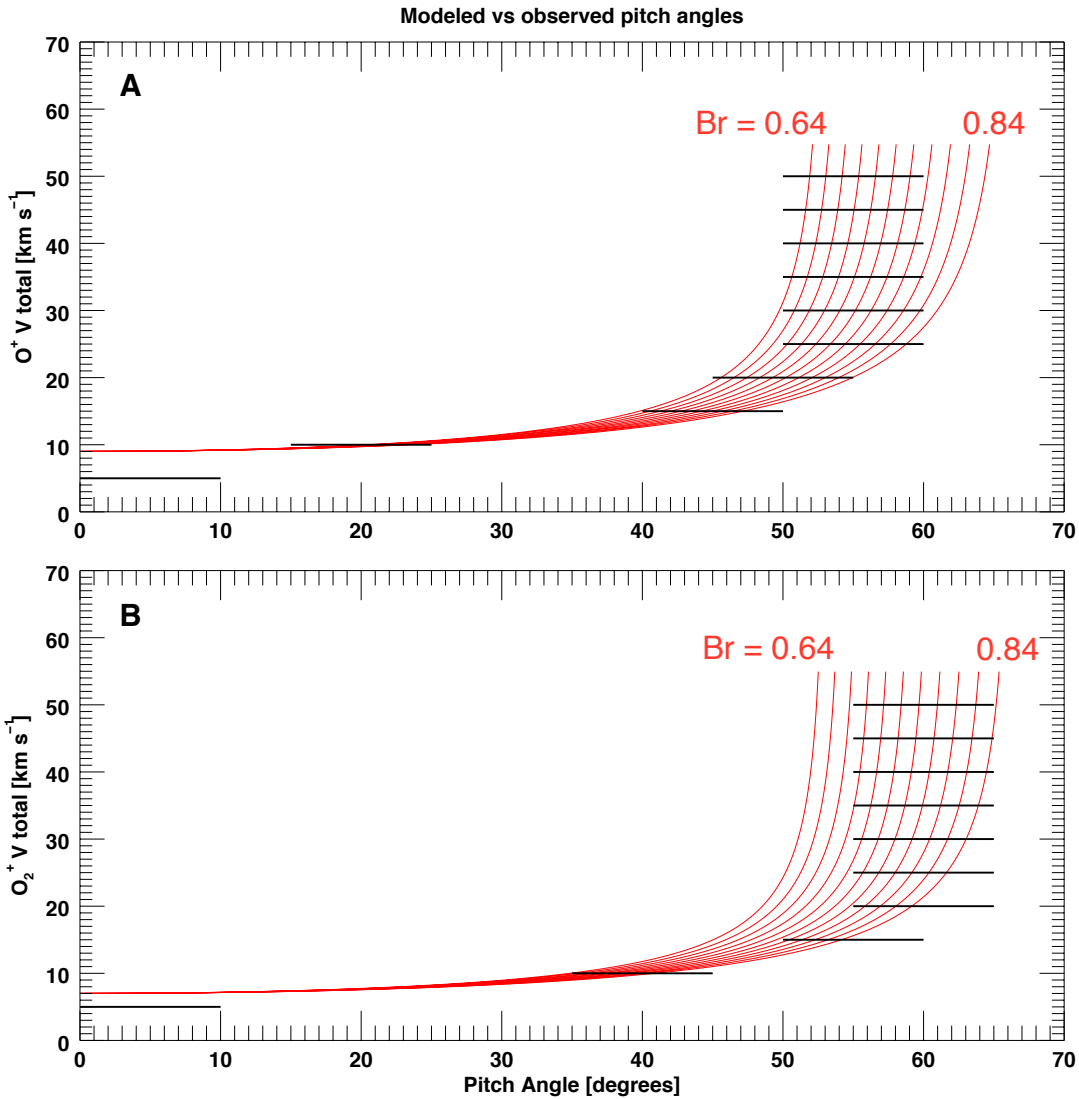


Figure 7.6: Observed ion pitch angles for different ion velocities compared to what a simple magnetic mirror would produce. Panels A and B show data for O<sup>+</sup> and O<sub>2</sub><sup>+</sup> respectively. The black lines show the measured pitch angle distributions obtained from analysis of Figure 7.4. Red lines show modeled pitch angle distributions resulting from the magnetic mirror force at various magnetic field strength ratios,  $B_r$ .

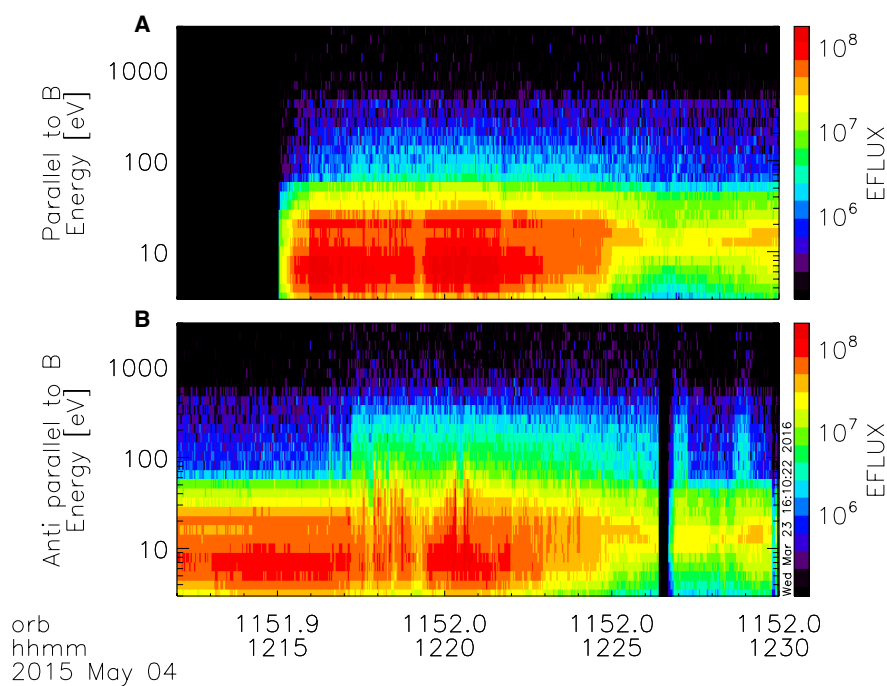


Figure 7.7: Electron fluxes demonstrating photoelectrons are leaving the planet parallel to the magnetic field (panel A) during the time that energetic ions are observed. No photo electrons are observed moving towards the planet anti-parallel to the magnetic field (panel B) during the same time period. This suggests that one end of the magnetic flux tube is well connected to the deep Martian ionosphere; the other end is not.

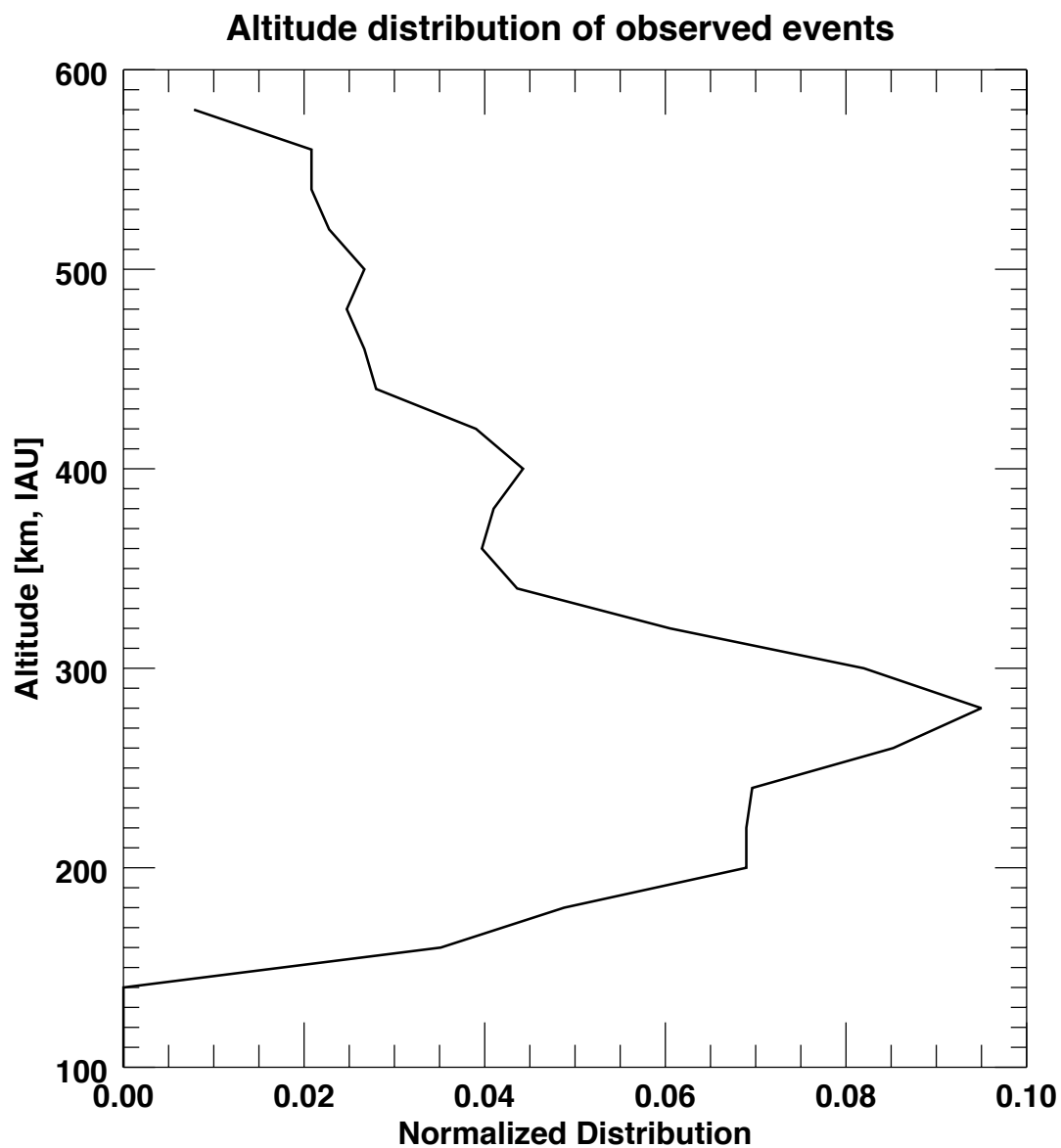


Figure 7.8: The distribution of the 31 observed energetic ion events as a function of altitude. Events full filled three criteria: 1. They occur below 600 km altitude. 2: Ionospheric ions are observed between energies 10 - 50 eV with average energy fluxes greater than  $1 \times 10^7$  eV  $(\text{eV cm}^2 \text{ s sr})^{-1}$ . 3: A minimum in magnetic field strength is present when energetic ions are observed. All events are confirmed by eye.

## Chapter 8

### Observations of the Rayleigh-Taylor instability in Mars' ionosphere

**Submitted:** 6<sup>th</sup> October 2016, awaiting reviewer comments, Geophysical Research Letters

**Corresponding author:** C. M. Fowler, Laboratory of Atmospheric and Space Sciences, University of Colorado, Boulder, Colorado, USA 80303, christopher.fowler@lasp.colorado.edu.

**Authors:** C. M. Fowler,<sup>1</sup> L. Andersson,<sup>1</sup> S.R. Shaver,<sup>1</sup> R. Lillis,<sup>2</sup> M.E. Usanova,<sup>1</sup> J. Espley,<sup>3</sup> R.E. Ergun,<sup>1</sup> J. McFadden,<sup>2</sup> P.R. Mahaffy,<sup>4</sup> J.E.P. Connerney,<sup>3</sup> M. Benna,<sup>3,5</sup>, M. Elrod,<sup>6</sup> D.L. Mitchell,<sup>2</sup> C. Mazelle,<sup>7,8</sup> B.M. Jakosky,<sup>1</sup>

<sup>1</sup>Laboratory of Atmospheric and Space Sciences, University of Colorado, Boulder, Colorado, USA.

<sup>2</sup>Space Sciences Laboratory, University of California, Berkeley, California, USA.

<sup>3</sup>Planetary Magnetospheres Lab, NASA Goddard Space Flight Center, Greenbelt, MD 20771, USA.

<sup>4</sup>Planetary Environments Laboratory, Code 699, NASA Goddard Space Flight Center, Greenbelt, Maryland, USA.

<sup>5</sup>CRESST, University of Maryland, Baltimore, Maryland, USA.

<sup>6</sup>Planetary Environments Laboratory, NASA Goddard Space Flight Center, Greenbelt, Maryland, USA.

<sup>7</sup>CNRS, Institut de Recherche en Astrophysique et Planétologie, Toulouse, France.

<sup>8</sup>University Paul Sabatier, Toulouse, France.

## 8.1 Abstract

Ionospheric disturbances associated with horizontal magnetic field below 200 km altitude are observed at Mars. Plasma density modulations of up to 200% are observed during such events and are correlated with fluctuations in magnetic field. The observed fluctuations are Doppler shifted and represent spatial structures at the 15-20 km length scale. Similar disturbances are observed at Earth and are thought to be caused by the Rayleigh-Taylor (R-T) instability. Analysis of one such event at Mars using R-T theory shows that the Martian ionosphere can be R-T unstable. At Earth such disturbances occur primarily at the equatorial dusk and nightside ionosphere and are known as Equatorial Spread F (ESF). This paper shows that the disturbances at Mars are most likely to be observed just past the dawn and dusk Martian terminators. ESF disrupts communication signals in the terrestrial ionosphere and such effects may be present in the Martian ionosphere.

## 8.2 Introduction

The Rayleigh-Taylor (R-T) instability is a plasma instability that arises when a heavy fluid is supported over a lighter one. Typical theoretical approaches invoke a horizontal magnetic field that supports a heavy plasma above a vacuum. Small perturbations in the topside plasma density can lead to the onset of the instability; gravity acts to pull the plasma downward while magnetic tension opposes this. The R-T instability is the primary driver of equatorial dusk and nightside ionospheric disturbances in the terrestrial ionosphere (*Fejer and Kelley, 1980*). These disturbances are known as Equatorial Spread F (ESF) and are characterized by large irregularities and depletions in electron density, wave-like ion density structures and vertical ion flows (e.g. *Szuszcwicz et al. (1980)*; *Hoegy et al. (1982)*; *Raghavarao et al. (1999)*; *Singh et al. (1997)*).

Conditions at Earth's equatorial dusk ionosphere are favorable for supporting the R-T instability. The Earth's dipole magnetic field produces a horizontal magnetic field there preventing the vertical transport of magnetized plasma. Zonal winds mean that the dusk equatorial ionosphere is subject to an upward directed induced electric field that raises the ionosphere (*Schunk and Nagy,*

2009). These conditions, and a lack of photoionizing light at low altitudes, lead to a top heavy ionosphere. The initial seed perturbations that drive the R-T instability and ESF in the terrestrial ionosphere are thought to be caused by gravity waves that produce localized enhancements in neutral and plasma densities (*Singh et al.*, 1997). Typical length scales of ESF density structures have been observed to span sub-kilometer up to several hundred kilometer scales (*Mathews et al.*, 2001; *Singh et al.*, 1997). A multitude of physical processes acting within the ESF region are thought to cause this range of length scales (*Kelley et al.*, 1982)

*Fejer and Kelley* (1980), for example, present a comprehensive review of ESF, including examples of in-situ and ground observations and a discussion of the physical processes that drive the phenomenon. Extensive theoretical work has also been reported relating to the onset of ESF and the relevant plasma instabilities acting, for example, *Cunnold* (1969); *Ott* (1978); *Russell and Ott* (1979); *Mitchell et al.* (1985); *Huang et al.* (1994).

Observations of similar ESF-type disturbances in the Martian ionosphere have to this authors knowledge not been reported before. The geometry at the Martian terminator is such that ionizing sunlight cannot reach below altitudes of about 120 km (*Withers et al.*, 2012). Mars does not possess a global dipole magnetic field and the planet-solar wind interaction produces ‘draped magnetic fields’ that typically lead to horizontal magnetic field topologies on the dayside and at the terminators of the planet (*Bertucci et al.*, 2003). At first glance conditions are thus suitable for an R-T like instability to form at the Martian terminator and we present here observations of what we believe to be this phenomenon acting in the Martian ionosphere. The data analyzed in this study are described in Section 8.3 and a single event is analysed in Section 8.4. A statistical study of similar events is shown in Section 8.5. We discuss our observations in Section 8.6 before concluding in Section 8.7.

### 8.3 Data

The Mars Atmosphere and Volatile Evolution (MAVEN) spacecraft is a dedicated aeronomy mission with the primary science goals of understanding the physical processes that act

within the Martian atmosphere and to evaluate how the Martian atmosphere itself has evolved over time (*Jakosky et al.*, 2015a). This study utilizes data from several instruments carried by MAVEN, namely the Langmuir Probe and Waves (LPW (*Andersson et al.*, 2014)), Magnetometer (MAG (*Connerney et al.*, 2015)); Neutral Gas and Ion Mass Spectrometer (NGIMS, *Mahaffy et al.* (2015a,b); *Benna et al.* (2015)) and Solar Wind Electron Analyzer (SWEA, *Mitchell et al.* (2016)) instruments.

LPW consists of two  $\sim 7$  m booms separated by an angular distance of  $\sim 110^\circ$ . Current-voltage (I-V) characteristics are measured at a cadence of 1 s for the data presented here. Due to the instrument mode of operation, I-V characteristics were measured for the first 3 seconds out of every 4; an I-V characteristic was not measured on the fourth second. The local electron density ( $N_e$ ), electron temperature ( $T_e$ ) and spacecraft potential ( $V_{sc}$ ) are derived by analysis of the measured I-V characteristics (*Ergun et al.*, 2015a). MAG is a fluxgate magnetometer that measures the vector magnetic field at a rate of 32 Hz. NGIMS utilizes a mass quadrupole filter that only allows ions of a specific mass to charge ratio ( $m/z$ ) to reach a pulse counting detector. The instrument is able to measure multiple  $m/z$  values in quick succession, and is able to measure both neutral and ion species during the same periapsis pass. The measurement cadence for any one species is typically around 2.6 s, but this can vary depending on the number of species being measured on any given periapsis pass. SWEA is a hemispherical electrostatic analyzer that measures electron fluxes from a few eV up to several keV. It has a  $360^\circ \times 120^\circ$  field of view provided by electrostatic deflectors and a time resolution of 4 s.

## 8.4 Event

During equatorial terminator periapsis passes MAVEN frequently observes ionospheric disturbances below 200 km in altitude. Quasi-periodic fluctuations in magnetic field and ionospheric density are observed spanning  $\sim 10$  seconds up to several minutes in time series data. Time series plasma data from such a disturbance is shown in Figure 8.1; periapsis for this orbit was at the pre-dawn equatorial terminator at approximately 2016-01-04/21:05 UTC. Panel A shows the

LPW I-V characteristics; the SWEA suprathermal electron energy flux is shown in panel B; the 3D magnetic field in the Mars Solar Orbital (MSO) frame is shown in C; the magnitude of the 3D magnetic field is the black line in panel D and the modeled crustal magnetic fields are shown as the red line in panel D (*Acuna et al.*, 1999; *Morschhauser et al.*, 2014). The MSO frame is defined as positive X pointing along the Mars-Sun line, towards the Sun; Y points opposite to Mars' orbital motion, and Z completes the system. The high frequency ( $\gtrsim 0.1$  Hz) variation in the total magnetic field strength shown as black in panel D is shown in panel E. The angle between the 3D magnetic field and the vertical direction is shown in panel F; values of  $0^\circ$  and  $180^\circ$  denote upward and downward pointing field respectively;  $90^\circ$  signifies horizontal magnetic field with respect to the planet's surface. Horizontal lines at  $45^\circ$ ,  $90^\circ$  and  $135^\circ$  have been added to the panel to aid the reader. The LPW I-V characteristic derived local  $N_e$  and  $T_e$  are shown in panels G and H respectively. The spacecraft altitude in the International Astronomical Union Mars planetocentric (IAU-Mars) reference frame is shown in panel I. The solar zenith angle (SZA) and position coordinates in the MSO frame are printed underneath the bottom panel, in units of degrees and Mars radii respectively. Negative SZA denote dawn; positive dusk. The three colored regions labeled R1, R2 and R3 are discussed in Section 8.6. The dominant neutral and ion density altitude profiles are shown in Figure 8.2B.  $\text{CO}_2$  was the dominant neutral species below about 165 km. Above this, O dominates.  $\text{O}_2^+$  was the dominant ion below 180 km;  $\text{O}^+$  dominates above this. Quasi-periodic fluctuations in magnetic field and plasma density that are the subject of this study occur below approximately 150 km, in the  $\text{CO}_2$  and  $\text{O}_2^+$  dominated atmosphere. They are observed between approximately 21:03:00 UTC and 21:05:30 UTC. The magnetic field fluctuations are observed in Figure 8.1C and D, and are of the order of 1-3 nT amplitude as presented in Figure 8.1E. The fluctuations in plasma density are observed by the LPW and NGIMS instruments as seen in Figures 8.1G and 8.2B. The mainly horizontal motion of the spacecraft and collisional nature of the atmosphere (see Figure 8.2A and corresponding text) at periapsis means that these magnetic and density fluctuations are likely standing structures that are observed at approximately the local proton frequency ( $\sim 0.3$  Hz). When Doppler shift is taken into account due to the spacecraft motion ( $\sim 4 \text{ km s}^{-1}$  at periapsis)

these fluctuations have length scales of 15-20 km.

The magnetic field is horizontal during the event, shown in Figure 8.1F, and appears to contain very little contribution from the localized crustal magnetic fields. When the magnetic field is no longer horizontal, before about 21:02:40 UTC and after about 21:06:30 UTC (when more significant crustal magnetic fields are present) the high frequency fluctuations in magnetic field are not present. Electron density can vary by up to 200% during these fluctuations, as made evident by the linear axis scaling in Figure 8.1G. These fluctuations are also present in the measured I-V characteristics from LPW (Figure 8.1A) and the measured ion density from NGIMS (Figure 8.2B), confirming that these variations in electron density are real and are not a result of poor fitting during analysis of the I-V characteristics for this event. There is no obvious variation in electron temperature (Figure 8.1H), suggesting that the same plasma population is present throughout the event. Large, unstable values of spacecraft potential can degrade ion and electron plasma measurements; the spacecraft potential was essentially constant throughout this periapsis pass at a value of  $\sim -2$  V. Electrons measured by the SWEA instrument in Figure 8.1B are produced from photoionization of the neutral atmosphere; the observed lack of significant energy flux after  $\sim 21:02$  UTC suggests a lack of photoionizing light at such times.

The small patches of suprathermal electrons observed on the outbound portion of the orbit, just after 21:07 and 21:08 UTC in Figure 8.1B, are most likely precipitating electrons, or patches of ionization caused by precipitating electrons. These are a known source of the Martian nightside ionosphere and are not discussed further here (e.g. *Verigin et al. (1991)*; *Haider et al. (1992)*; *Fox (1993a)*; *Lillis et al. (2009, 2011)*; *Lillis and Fang (2015)*; *Fowler et al. (2015)*).

Various parameters for the inbound segment of this event are shown in Figure 8.2. The majority of the event was observed on the inbound portion of the orbit; due to space limitations we do not show the outbound segment here. Panel A shows the collision frequencies (derived using *Schunk and Nagy (2009)*) of  $O_2^+$  and electrons, with neutral  $CO_2$ , in dashed blue and red respectively. Corresponding gyrofrequencies about the measured local magnetic field are shown in solid blue and red respectively. The  $CO_2$ ,  $O_2^+$  and electron densities are shown as the black, blue

and red lines respectively in panel B. The  $O_2^+$  and electron densities have been multiplied by a factor of  $5 \times 10^5$  so that all three lines can be plotted on a linear scale within the same plot. The percentage variation of these three profiles are shown in panel C, where the colors match those in panel B. The variation in magnetic field is shown in panel D; this is the same data as shown in Figure 8.1D but plotted as an altitude profile. Close inspection of the variation in ion and electron densities showed a strong, but not perfect, correlation with the oscillations in magnetic field strength (not shown here). The electron density profile for this event is shown as the red line in panel E. The black, blue, green and purple lines show electron densities from four neighboring orbits where ionospheric disturbances were not observed.

The electron gyrofrequency is always at least a factor of  $\sim 3-4$  greater than the electron- $CO_2$  collision frequency as seen in Figure 8.2A and as such the electrons are magnetized throughout the entire periapsis pass.  $O_2^+$  on the other hand is unmagnetized below about  $\sim 163$  km. The ion and electron density profiles in panel B show similar variations across all altitudes and exhibit large fluctuations across small (a few km) altitude ranges when the fluctuations in magnetic field are present. These density fluctuations are  $\sim 50\%$  for  $O_2^+$  and up to almost  $200\%$  for the electrons (panel C). In contrast, the neutral  $CO_2$  density profile shows very little variation,  $<10\%$ . Differences in ion and electron densities are due to differences in measurement cadence and integration time: NGIMS density measurements for a single species are taken over a fraction of a second; for the instrument mode in operation here the LPW I-V characteristics were measured over 1 second. The large amplitude fluctuations in magnetic field strength are observed below about 144 km altitude (panel D). Above this, the variation in magnetic field strength is small, about 0.1 nT, which is the typical instrument noise level (*Connerney et al., 2015*). The electron density profile for this event (the red line in Figure 8.2E) does not stand out in any obvious way from the neighboring passes that did not show ionospheric disturbances. All five density profiles show large variability due to the terminator location of periapsis.

## 8.5 Statistical Study

Events similar to those shown in Figure 8.1 were identified from 21 months of MAVEN data, spanning November 2014 through July 2016 below altitudes of 200 km. Events were identified purely by the variation in magnetic field strength as shown in Figure 8.1D and E, and were required to exist for at least 20 s to avoid false detections from sudden changes in magnetic field strength which are typically associated with crustal magnetic fields. In total 142 events were found by an automated routine; these were confirmed by eye. The normalized distribution of these events with respect to SZA is shown by the black line in Figure 8.3A (i.e. the black line shows the fraction [number of separate orbits where at least one event was observed for this SZA bin] / [the total number of separate orbits that passed through this SZA bin]). Negative SZA are on the dawn side of Mars, positive on the dusk side. The red line shows the total number of orbits that sampled each SZA bin and it can be seen that few measurements currently exist at the subsolar point and close to midnight. The black error bars are the statistical  $\sqrt{N}$  errors, where N is the number of detected events in each SZA bin. There are clear peaks in occurrence just past the dawn and dusk terminators, at  $\sim \pm 90^\circ$ - $110^\circ$ . The peaks in occurrence at small absolute SZA are partly a result of low number statistics; three orbits, all from 2015-04-23 UTC, comprise the spike at  $-10^\circ$  to  $0^\circ$  SZA. The outbound density profiles for these three orbits are shown as the colored lines in panel C. The gray dots show density profiles from 6 days either side of this UTC day. The colored profiles show significantly more variation, and reduced densities at high altitudes, than the majority of the gray orbits. This is an unexpected location to observe such drastic variation in electron density and more profile measurements are required before the importance of these highly variable profiles can be quantified. The distribution of magnetic field angles throughout the 142 identified events is shown in panel B. The vertical green line marks horizontal field; the two blue lines enclose 75% of the distribution. The error bars are again  $\sqrt{N}$ .

## 8.6 Discussion

At Earth, zonal winds transport neutrals and ions from day to night across the terminator. At equatorial dusk, these flows and the horizontal dipole magnetic field produce an upward directed induced electric field that lifts the ionosphere to higher altitudes. In combination with a lack of photoionizing sunlight at lower altitudes, a top heavy ionosphere forms where conditions are favorable for the onset of the R-T instability (e.g. *Schunk and Nagy (2009)*). The lack of a dipole magnetic field at Mars means that there is, to first order, no upward pointing induced electric field at the terminator. Draped magnetic fields can, however, transport dayside ionospheric plasma across the terminator (*Lundin et al., 2008*). These draped fields point tailward and are typically horizontal, preventing the vertical transport of magnetized plasma. Combined with a lack of photoionizing light at low altitudes, conditions become favorable for the onset of the R-T instability. Magnetic field draping occurs at all local times explaining why the R-T instability is observed at dawn and dusk in this study; the induced electric field at Earth points downward at dawn, meaning that the ionosphere is more likely to be R-T stable there.

The neutral atmosphere is not directly affected by the magnetic field and is free to move vertically in response to gravity, pressure gradients and any other forces present. Gravity acts to pull the ionosphere downward and is opposed by the tension force produced by the horizontal magnetic field. Gravity waves have been observed in the Martian atmosphere (e.g. *Yigit et al. (2015)*) and we suggest that, as at Earth, these seed an R-T like instability producing ‘fingers’ of ions diffusing downward; although the unmagnetized ions collide frequently with the neutral atmosphere their net motion is downward. To conserve quasi-neutrality electrons follow the ions; as they are magnetized they drag the magnetic field with them. As MAVEN flies through these finger-like structures, quasi-sinusoidal fluctuations in plasma density and magnetic field are observed. The magnetic field fluctuations observed in Figure 8.1C show that the largest variations are in the  $B_y$  component in the MSO frame; given the periapsis location for this orbit, variations in the  $B_y$  plane are mostly in the vertical direction with respect to the planet’s surface. Since the ions are

unmagnetized the magnetic field fluctuations cannot be the result of an electromagnetic wave and thus they are Doppler shifted structures in the ionosphere.

The linear growth rate of the RT instability as derived in *Ossakow* (1981) and *Sultan* (1996) is given by Equation 8.1:

$$\gamma = -\frac{g}{\nu_{\text{in}}} \frac{1}{n_0} \frac{\partial n_0}{\partial h} - R \quad (8.1)$$

Where  $\gamma$  has units of  $\text{s}^{-1}$ ,  $g$  is gravity (positive upward),  $\nu_{\text{in}}$  is the ion-neutral collision frequency between  $\text{O}_2^+$  and  $\text{CO}_2$ ,  $n_0$  is the background (or average) electron density,  $h$  is altitude and  $R$  is the local chemical recombination rate. Positive  $\gamma$  implies an RT unstable system and typical values of such unstable conditions in the terrestrial ionosphere are a few  $10^{-3} \text{ s}^{-1}$  (*Sultan*, 1996).

To test whether the observed ionosphere presented in this study is unstable to the RT instability  $\gamma$  was calculated for the three regions R1, R2 and R3 as labelled in Figure 8.1. The parameter  $g$  was taken as  $-3.5 \text{ ms}^{-2}$ ,  $\nu_{\text{in}}$  was read from Figure 8.2A,  $n_0$ ,  $\partial n_0$  and  $\partial h$  were calculated from the observations in Figure 8.1, and  $R$  was calculated based on the  $\text{O}_2^+$  recombination rate given in *Fox and Sung* (2001). The values of  $\gamma$  in regions R1, R2 and R3 are  $-2.6 \times 10^{-2}$ ,  $2.3 \times 10^{-3}$  and  $3.9 \times 10^{-3} \text{ s}^{-1}$  respectively. Thus, region R1 is stable to the RT instability but regions R2 and R3 are unstable and possess similar growth rates to those calculated for the terrestrial ionosphere. Equation 8.1 assumes a horizontal magnetic field and this is true for regions R2 and R3. Somewhat vertical field is present during region R1 and this may explain why this region appears R-T stable.

The statistical distribution of similar events shown in Figure 8.3A further supports the interpretations of this study. The peaks in occurrence are just past the dawn and dusk terminators, between  $\sim \pm 90^\circ$ - $110^\circ$ . At a Martian ionospheric altitude of 120 km the Sun sets at  $\sim 105^\circ$  SZA (e.g. *Withers et al.* (2012)) and as such a top heavy ionosphere can be produced at these SZA. The large spike in occurrence  $+130^\circ$ - $140^\circ$  SZA in panel A has been confirmed by eye; it may suggest an asymmetry in the occurrence of these disturbances between the pre- and post-midnight

locations. As the dayside ionosphere rotates through dusk the lowest altitudes stop receiving sunlight first and ionization no longer occurs there. When present, horizontal magnetic field prevents the vertical transport of magnetized plasma leading to a top heavy ionosphere that can persist until pre-midnight (*Fowler et al.*, 2015). At post midnight, the high altitude ionosphere has not yet formed due to its passage through the nightside. The number of events in this dusk bin is relatively small ( $\sim 10$ ) and so this explanation is not conclusive.

The few observed events close to the subsolar point in Figure 8.3A occur under highly disturbed ionospheric conditions as seen by the colored lines in Figure 8.3C. MAVEN cannot sample the solar wind whilst periapsis is close to the subsolar point but the reduced ionospheric densities suggest upstream conditions are driving the dayside ionosphere for these orbits. The highly variable profiles provide small regions of top heavy ionosphere which do not typically occur at these SZA; solar EUV can reach well below 130 km altitude here to provide ionization (e.g. *Ergun et al.* (2015a)). The R-T instability could thus be common at the subsolar region despite these EUV conditions, but more observations are required to confirm this.

The distribution of magnetic field angles during the 142 identified events shows that horizontal field is the most likely orientation during such disturbances (Figure 8.3B). Vertical magnetic field allows vertical transport of magnetized plasma and prevents the accumulation of a top heavy ionosphere, a primary cause of the R-T instability. This distribution of magnetic field angles is similar in shape to the distribution of all magnetic field angles observed by MAVEN below 200 km altitude. This confirms that the identified events do not occur often under vertical magnetic field conditions, and that horizontal magnetic field is a required, but not exclusive, condition to observe such disturbances. Indeed, a top heavy ionosphere is at the very least also required and this is not taken into account when solely analyzing the observed magnetic field angle. Accounting for a top heavy ionosphere is difficult - MAVEN flies almost horizontal at periapsis and so the measured  $N_e$  profiles are not truly vertical profiles. The similar, highly variable electron density profiles shown in Figure 8.2E demonstrate this difficulty - only the red profile showed R-T behavior but it does not stand out from the others in any obvious way. Modeling of the onset of the R-T instability

by *Ossakow* (1981) also shows that in the terrestrial ionosphere it can take 15-20 minutes for the instability to fully develop, given a horizontal magnetic field. Thus, the magnetic field angle, density profile and time history of the magnetic field topology must all be considered.

Neutral winds have also been proposed to drive significant density variations in the Martian ionosphere through collisions with ions. Neutral winds are known to exist at Mars (e.g. *Bougher et al.* (2015b) and references therein), and will drive ionospheric currents in a collisional regime. *RiOUSSET et al.* (2014) investigated the signatures produced by such winds using an electrodynamic model. By including an arcade like magnetic field topology they were able to produce density fluctuations on the scale of hundreds of kilometers. Given the much shorter length scales of magnetic field fluctuations observed in this study (approximately 15-20 km) and the likely lack of any strong crustal magnetic field sources (Figure 8.1D), we deem this explanation unlikely.

For ESF events observed in the terrestrial ionosphere, vertical ion drifts of  $\sim 100 \text{ ms}^{-1}$  are typically observed (e.g. *Hoegy et al.* (1982)). The Suprathermal and Thermal Ion Composition instrument (STATIC, *McFadden et al.* (2015)) onboard MAVEN is able to determine the direction of ion flows but the deviation of ion flow resulting from the observed disturbances is below the noise limit of the instrument. The NGIMS instrument is able to measure neutral wind direction but the measurement cadence during this mode is unable to resolve the small structures observed in this study. Thus, verification of the flows associated with these disturbances is difficult.

## 8.7 Conclusions

Strong ionospheric disturbances have been observed at low altitudes in the Martian ionosphere that are characterized by large fluctuations in plasma density and magnetic field. Such disturbances are characteristic of the ESF phenomenon observed in the terrestrial ionosphere; ionospheric conditions at the times of these disturbances at Mars match those at Earth and analysis of one such event using linear R-T instability theory shows the ionosphere to be unstable just prior to and at the time of disturbance. A statistical analysis of similar events observed throughout 21 months of MAVEN data further support these interpretations; events are primarily observed at the dawn and

dusk terminators, where the lack of photoionizing EUV light at low altitudes combined with typically horizontal draped magnetic fields allow a top heavy ionosphere to form. The draped magnetic fields not only prevent vertical transport of magnetized plasma but also transport plasma from the dayside across the terminator, augmenting the top heavy ionosphere. At Earth, cross terminator winds coupled with the horizontal dipole field at the equator induce an upward pointing electric field at dusk that lifts the ionosphere to higher altitudes; a lack of photoionizing light at lower altitudes leads to a top heavy ionosphere. The induced electric field points downward at dawn, leading to an R-T stable ionosphere there.

These disturbances of the Martian ionosphere may have implications for future communication systems at Mars, particularly for ground based assets that will require communication through the ionosphere. At Earth, variations in signal strength and phase (known as scintillations) can cause a loss of signal (e.g. *Basu et al. (2002); Bernhardt et al. (2014)*). These scintillations are caused by changes in the refractive index of the propagation medium, which is proportional to electron density (*Kintner et al., 2004*). Kilometer scale features in the terrestrial ionosphere are known to cause such effects (*Groves et al., 1997*) and similar scales were observed in this study. The thinner extent and lower absolute density of the Martian ionosphere may reduce these effects but by how much is unknown.

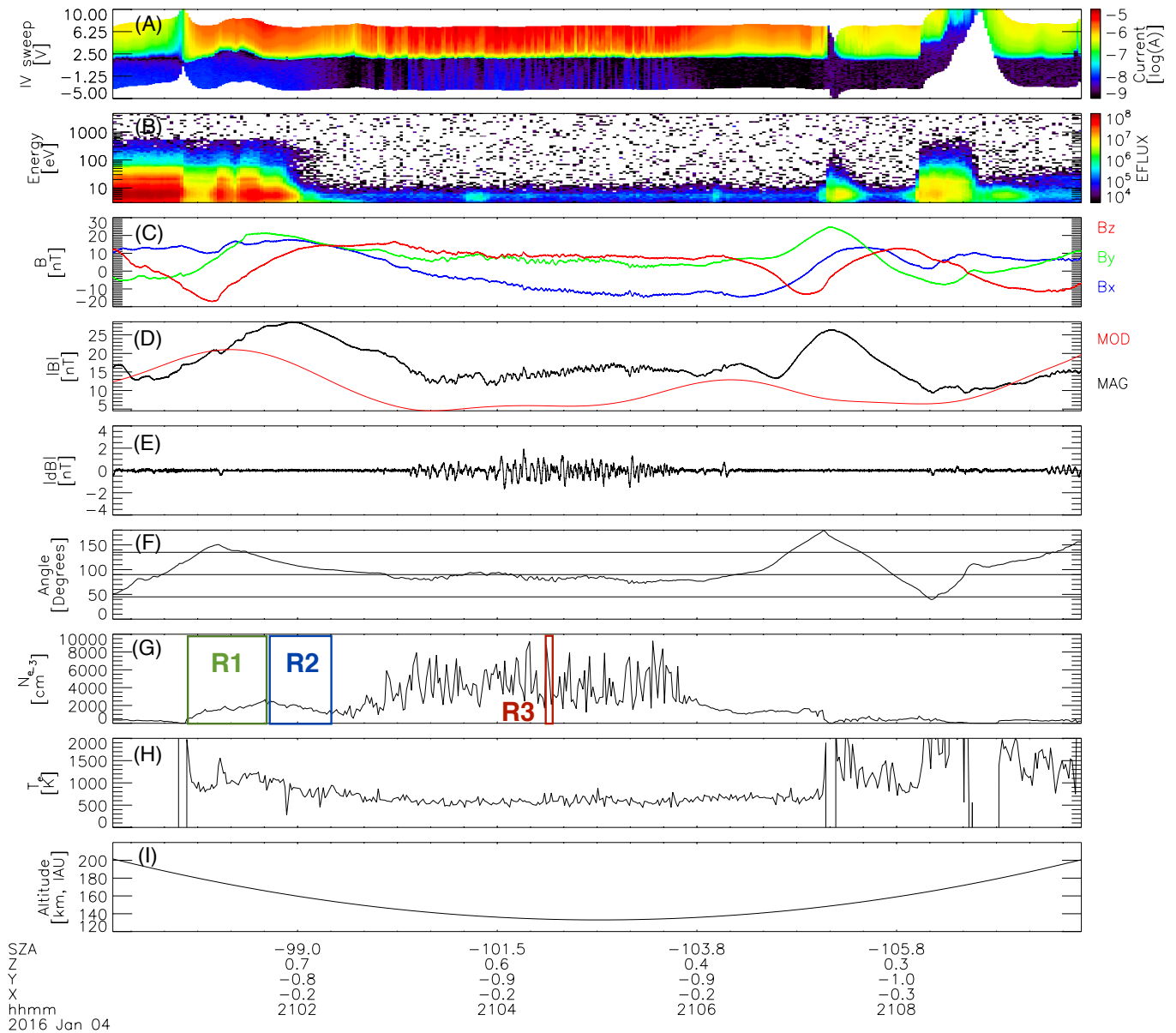


Figure 8.1: Time series plasma data for the studied event. Panels are: A: LPW I-V characteristics. B: SWEA suprathermal electron energy flux. C: 3D magnetic field in the MSO frame. D: total magnetic field strength (black) and modeled magnetic crustal fields (red, *Morschhauser et al.* (2014)). E: high frequency variation in magnetic field. F: angle between magnetic field and vertical direction. G:  $N_e$  from LPW. H:  $T_e$  from LPW. I: Altitude in the IAU-Mars frame. The fluctuations in magnetic field and electron density mark the region of interest, between 21:03:00 and 21:05:30 UTC

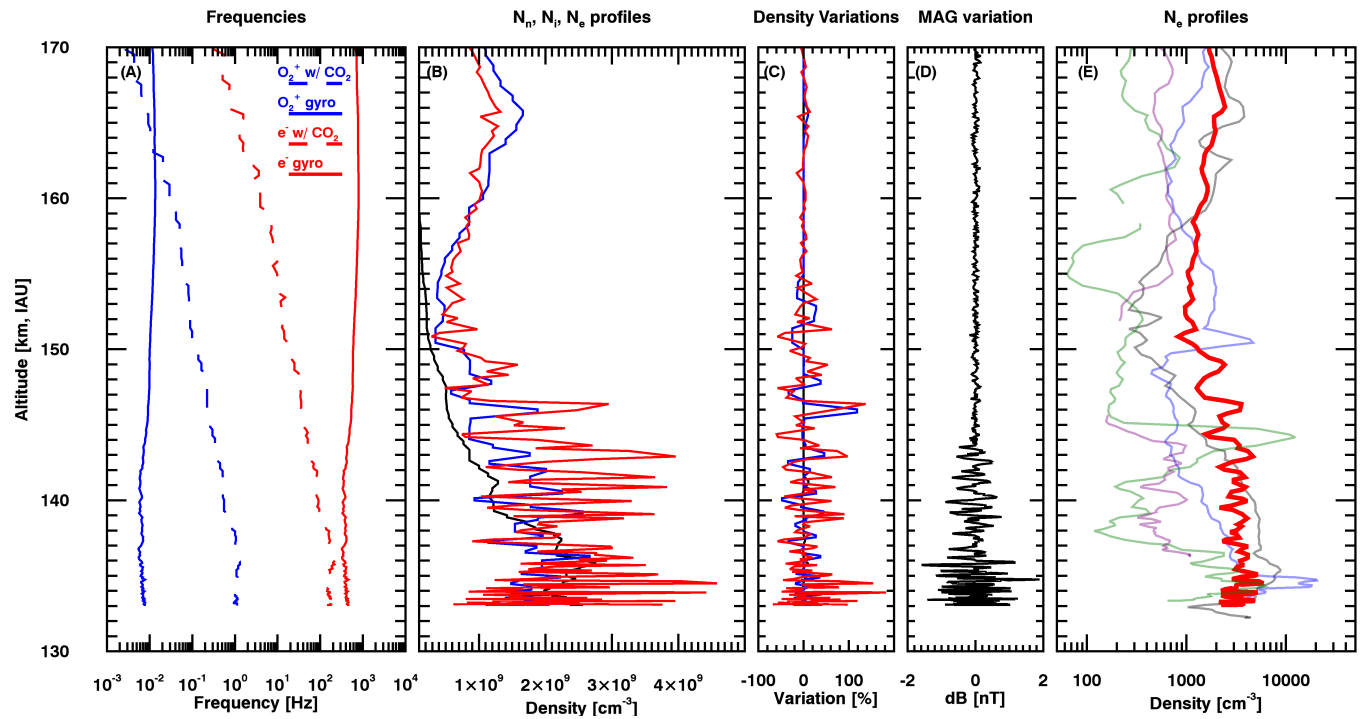


Figure 8.2: Various parameters for the inbound segment of the orbit shown in Figure 8.1. Panels are: A: Collision and gyrofrequencies for the species labeled in the plot. B: Neutral  $CO_2$  density (black), ion and electron density (blue and red respectively, both scaled by  $5 \times 10^5$ ). C: The percentage variation of the species shown in panel B. D: The high frequency variation in magnetic field. E:  $N_e$  for this event (red);  $N_e$  for neighboring orbits where fluctuations in magnetic field and plasma density were not present (lighter colors).

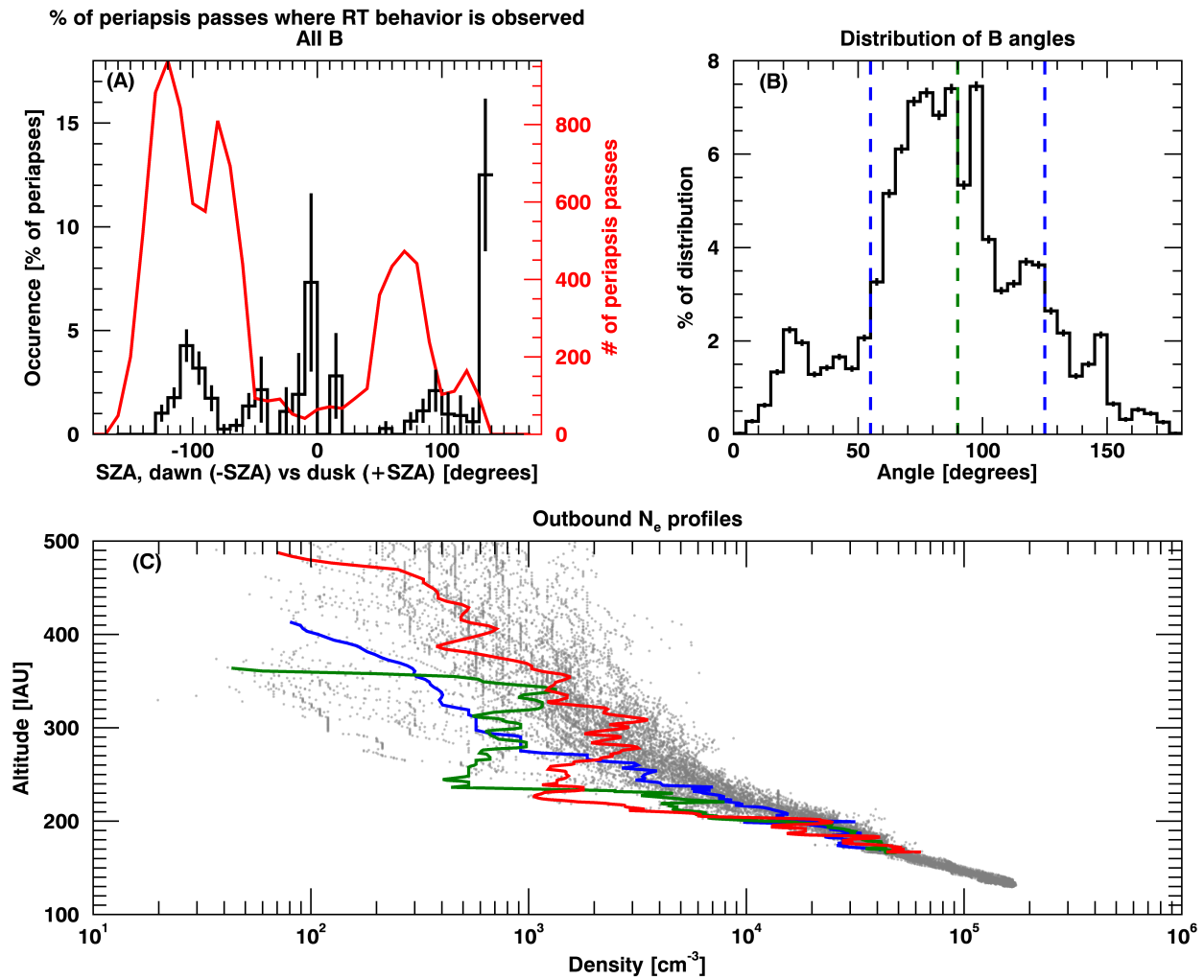


Figure 8.3: Statistical analysis of events similar to those shown in Figure 8.1. Panel A: the normalized distribution of events (black) and the total number of orbit samples (red) as functions of SZA. Panel B: the distribution of magnetic field angles for the events shown by the black line in panel A;  $90^\circ$  is horizontal,  $0^\circ$  and  $180^\circ$  are vertical field. Panel C:  $N_e$  profiles for the three events that comprise the spike in occurrence at  $-10^\circ$  to  $0^\circ$  in the black line in panel A (colored lines). The gray dots show density profiles for  $\sim 25$  orbits either side of these events.

## Chapter 9

### Future Work

In the immediate future I will wrap up the final loose ends of this thesis. Responding to reviewer comments for papers 2, 3 and 4 will be a top priority. It is also important to share with the scientific community the gains in understanding that have been achieved through the operation and analysis of LPW data. I plan to write up Chapter 3 as an independent manuscript, to be submitted to a peer reviewed journal. The reality of flying a scientific instrument in space is always different to what was expected on the ground. The discovery of, and methods developed to account for, the various complexities and non-ideal behaviors of the LPW instrument, will be of substantial value for the design, construction, and analysis of future Langmuir probes. There are still improvements to be made to LPW fitting algorithm. In particular, the estimation of the probe sheath size, modeling of the sheath collapse issue, and the influence of spacecraft potential, are all areas that will not only improve the fitting algorithm, but further our knowledge of the physical processes acting during the collection of current by a spacecraft mounted Langmuir probe in general. Improving the estimation of the sheath size is likely the easiest improvement that can be made to the LPW fitting algorithm. Modeling of the probe sheath, and in particular modeling of the spacecraft potential influence, will require substantial model development to simulate the various potentials affecting the collection of current by the Langmuir probes.

I stated in Chapter 3 that the theoretical lower electron temperature limit that the LPW instrument can measure is 150-200 K, and that the actual limit is about 500 K. The LPW team has been considering the idea of attempting to extract lower temperatures from the LPW data by using

an ‘after-the-fact’ empirical correction. This idea is still in its infancy, and will likely require some form of modeling effort and comparison to neutral and ion temperatures derived by the NGIMS and STATIC instruments, but it is a very worthwhile goal to achieve. Currently, LPW temperature measurements close to 500 K act as an upper limit; electron temperature significantly impacts and drives many of the photochemical processes active in the Martian atmosphere, for example, and thus improvements in temperature derivations will influence our understanding of other processes that drive the Martian atmosphere. More accurate electron temperatures will also help to constrain models of the electron temperature, many of which utilize assumptions made in the Viking days (the 1970s and 80s). There is still large uncertainty as to what a ‘typical’ electron density profile actually looks like at low altitudes when the temperature is cold (below 500 K); it is thus difficult to know which dominant physical processes are acting that determine this (unknown) temperature profile.

One of the major science goals of the MAVEN spacecraft is to extrapolate current day atmospheric escape rates back in time to obtain an estimate of the total amount of atmosphere and water lost to space from the planet throughout Mars’ history. The MAVEN team has started to focus on this goal, but many complexities still remain and solving each of them is likely to be difficult. Electron density and temperature have been shown able to strongly influence the escape to space of Martian atmosphere - the dependence of the rate of dissociative recombination of  $O_2^+$  on  $T_e$ , and the ambi-polar electric field, are two such examples. Thus, not only understanding and constraining the effects of electron density and temperature on escape to space are important, but understanding the drivers of electron density and temperature themselves are also vital. There are many questions that need answering; below I list a few of these:

- (1) How do variations in the neutral density and temperature affect  $T_e$  on an orbit by orbit basis? Are these effects significant? We have already observed statistical changes in  $T_e$  that are linked to statistical differences in neutral density (*Andersson et al.*, 2016b).
- (2) Can ion density and temperature significantly affect  $T_e$  as it does at Earth? The ‘elec-

tron temperature morning overshoot' in the terrestrial ionosphere is driven by heating and cooling (in)balances between electron-neutral and electron-ion collisions, for example.

- (3) Are large, episodic events such as solar flares and CMEs important for driving the electron density and temperature profiles, and subsequent atmospheric escape?
- (4) The nightside ionosphere has not been investigated as thoroughly as the dayside due to its highly variable and complex nature (and the lack of comprehensive observations up until the MAVEN mission). What are the most important nightside ionization sources? How sporadic or continuous are they in nature? Can the highly variable density profiles be predicted or correlated to certain drivers? Are there significant effects on the corresponding electron temperature profiles and how will these effect escape to space?
- (5) What impacts will the observed Rayleigh-Taylor instability have on the Martian ionosphere and how will these affect future human activities on Mars? I observed this instability acting at the subsolar point, a location that should be very stable to the R-T instability. How often does this occur? What causes this?

The MAVEN mission has, and still is, producing an incredibly rich dataset that is able to describe the neutral, plasma, electric, magnetic, and solar EUV environments of the Martian atmosphere. Such a dataset at Mars is unprecedented; MAVEN is the first mission to be able to do this, and it will likely be the last for a long time. New insights into the evolution of the Martian climate will shed light on planetary evolution in general, and perhaps aid in our search for habitable planets outside of our solar system.

## Bibliography

- Acuna, M., J. Connerney, P. a. Wasilewski, R. Lin, K. Anderson, C. Carlson, J. McFadden, D. Curtis, D. Mitchell, H. Reme, et al. (1998), Magnetic field and plasma observations at Mars: Initial results of the Mars Global Surveyor mission, *Science*, *279*(5357), 1676–1680.
- Acuna, M., J. Connerney, R. Lin, D. Mitchell, C. Carlson, J. McFadden, K. Anderson, H. Rème, C. Mazelle, D. Vignes, et al. (1999), Global distribution of crustal magnetization discovered by the Mars Global Surveyor MAG/ER experiment, *Science*, *284*(5415), 790–793.
- Acuña, M., J. Connerney, P. Wasilewski, R. Lin, D. Mitchell, K. Anderson, C. Carlson, J. McFadden, H. Rème, C. Mazelle, et al. (2001), Magnetic field of Mars: Summary of results from the aerobraking and mapping orbits, *Journal of Geophysical Research*, *106*(E10), 23,403–23,408.
- Allen, J. (1992), Probe theory: the orbital motion approach, *Physica Scripta*, *45*(5), 497.
- Andersson, L., R. Ergun, and A. Stewart (2010), The combined atmospheric photochemistry and ion tracing code: Reproducing the Viking lander results and initial outflow results, *Icarus*, *206*(1), 120–129.
- Andersson, L., R. Ergun, G. Delory, A. Eriksson, J. Westfall, H. Reed, J. McCauly, D. Summers, and D. Meyers (2014), The Langmuir Probe and Waves (LPW) instrument for MAVEN, *Space Science Reviews*, pp. 1–26.
- Andersson, L., R. E. Ergun, G. T. Delory, A. Eriksson, J. Westfall, H. Reed, J. McCauly, D. Summers, and D. Meyers (2015), The Langmuir Probe and Waves (LPW) instrument for MAVEN, *Accepted manuscript number SPAC-D-14-00089R1*.
- Andersson, L., C. Fowler, T. Chamandy, R. Ergun, A. Eriksson, G. Delory, D. Andrews, A. Woodson, and J. Connerney (2016a), Electron temperature and density profiles from the Martian ionosphere: a statistical study, *Journal of Geophysical Research*.
- Andersson, L., C. Fowler, and et al (2016b), Diurnal variations in electron temperature in the Mars ionosphere, *Geophysical Research Letters*, *Submitted, under peer review*.
- Andersson, L., T. Chamandy, C. Fowler, R. Ergun, A. Eriksson, G. Delory, D. Andrews, A. Woodson, J. Connerney, and B. Jakosky (2016c), Electron and Density Profiles of the Martian Ionosphere: A Statistical Analysis, *Journal of Geophysical Research: Space Physics*, *This Issue*.
- André, M., and A. Yau (1997), Theories and observations of ion energization and outflow in the high latitude magnetosphere, *Space Science Reviews*, *80*(1-2), 27–48.

- André, M., H. Koskinen, L. Matson, and R. Erlandson (1988), Local transverse ion energization in and near the polar cusp, *Geophysical research letters*, *15*(1), 107–110.
- André, M., P. Norqvist, L. Andersson, L. Eliasson, A. Eriksson, L. Blomberg, R. Erlandson, and J. Waldemark (1998), Ion energization mechanisms at 1700 km in the auroral region, *Journal of Geophysical Research: Space Physics (1978–2012)*, *103*(A3), 4199–4222.
- Andrews, D., L. Andersson, G. Delory, R. Ergun, A. Eriksson, C. Fowler, T. McEnulty, M. Morooka, T. Weber, and B. Jakosky (2015), Ionospheric plasma density variations observed at Mars by MAVEN/LPW, *Geophysical Research Letters*, *42*(21), 8862–8869.
- Arge, C., and V. Pizzo (2000), Improvement in the prediction of solar wind conditions using near-real time solar magnetic field updates, *Journal of Geophysical Research: Space Physics*, *105*(A5), 10,465–10,479.
- Baker, V., R. Kochel, J. Laity, and A. Howard (1990), Spring sapping and valley network development, *Groundwater Geomorphology: The role of subsurface water in earth-surface processes and landforms*, *252*, 235–265.
- Bale, S., M. Balikhin, T. Horbury, V. Krasnoselskikh, H. Kucharek, E. Möbius, S. Walker, A. Balogh, D. Burgess, B. Lembège, et al. (2005), Quasi-perpendicular shock structure and processes, *Space science reviews*, *118*(1-4), 161–203.
- Banks, P. M., and T. E. Holzer (1968), The polar wind, *Journal of Geophysical Research*, *73*(21), 6846–6854.
- Barabash, S., R. Lundin, H. Andersson, J. Gimholt, M. Holmström, O. Norberg, M. Yamauchi, K. Asamura, A. Coates, D. Linder, et al. (2004), ASPERA-3: Analyser of space plasmas and energetic ions for Mars Express, in *Mars Express: The Scientific Payload*, vol. 1240, pp. 121–139.
- Basu, S., K. Groves, S. Basu, and P. Sultan (2002), Specification and forecasting of scintillations in communication/navigation links: current status and future plans, *Journal of atmospheric and solar-terrestrial physics*, *64*(16), 1745–1754.
- Benna, M., P. Mahaffy, J. Grebowsky, J. L. Fox, R. V. Yelle, and B. M. Jakosky (2015), First measurements of composition and dynamics of the Martian ionosphere by MAVEN’s Neutral Gas and Ion Mass Spectrometer, *Geophysical Research Letters*, *42*(21), 8958–8965.
- Bernhardt, P. A., M. A. Hei, C. L. Siefring, and M. R. Wilkens (2014), Predictions of HF system performance for propagation through disturbed ionospheres measured using low-Earth-orbit satellite radio beacon tomography, *Radio Science*, *49*(7), 506–517.
- Bertucci, C., C. Mazelle, D. Crider, D. Vignes, M. Acuña, D. Mitchell, R. Lin, J. Connerney, H. Reme, P. Cloutier, et al. (2003), Magnetic field draping enhancement at the Martian magnetic pileup boundary from Mars global surveyor observations, *Geophysical research letters*, *30*(2).
- Bertucci, C., C. Mazelle, D. Crider, D. Mitchell, K. Sauer, M. Acuña, J. Connerney, R. Lin, N. Ness, and D. Winterhalter (2004), MGS MAG/ER observations at the magnetic pileup boundary of Mars: Draping enhancement and low frequency waves, *Advances in Space Research*, *33*(11), 1938–1944.

- Bertucci, C., F. Duru, N. Edberg, M. Fraenz, C. Martinecz, K. Szego, and O. Vaisberg (2011), The induced magnetospheres of Mars, Venus, and Titan, *Space science reviews*, 162(1-4), 113–171.
- Bertucci, C., N. Romanelli, J. Chaufray, D. Gomez, C. Mazelle, M. Delva, R. Modolo, F. González-Galindo, and D. Brain (2013), Temporal variability of waves at the proton cyclotron frequency upstream from Mars: Implications for Mars distant hydrogen exosphere, *Geophysical Research Letters*, 40(15), 3809–3813.
- Borg, L., and M. J. Drake (2005), A review of meteorite evidence for the timing of magmatism and of surface or near-surface liquid water on Mars, *Journal of Geophysical Research: Planets*, 110(E12).
- Bougher, S., D. Pawlowski, J. Bell, S. Nelli, T. McDunn, J. Murphy, M. Chizek, and A. Ridley (2015a), Mars Global Ionosphere-Thermosphere Model: Solar cycle, seasonal, and diurnal variations of the Mars upper atmosphere, *Journal of Geophysical Research: Planets*, 120(2), 311–342.
- Bougher, S., D. Pawlowski, J. Bell, S. Nelli, T. McDunn, J. Murphy, M. Chizek, and A. Ridley (2015b), Mars Global Ionosphere-Thermosphere Model: Solar cycle, seasonal, and diurnal variations of the Mars upper atmosphere, *Journal of Geophysical Research (Planets)*, 120, 311–342, doi:10.1002/2014JE004715.
- Brace, L., R. Theis, and A. Dalgarno (1973), The cylindrical electrostatic probes for Atmosphere Explorer-C,-D, and-E, *Radio Science*, 8(4), 341–348.
- Brace, L. H. (1998), Langmuir probe measurements in the ionosphere, *Measurement Techniques in Space Plasmas: Particles*, pp. 23–35.
- Brain, D., F. Bagenal, M. Acuna, J. Connerney, D. Crider, C. Mazelle, D. Mitchell, and N. Ness (2002), Observations of low-frequency electromagnetic plasma waves upstream from the Martian shock, *Journal of Geophysical Research: Space Physics*, 107(A6).
- Brain, D., J. Halekas, R. Lillis, D. Mitchell, R. Lin, and D. Crider (2005), Variability of the altitude of the Martian sheath, *Geophysical Research Letters*, 32(18).
- Brain, D., J. Halekas, L. Peticolas, R. Lin, J. Luhmann, D. Mitchell, G. Delory, S. Bougher, M. Acuña, and H. Rème (2006), On the origin of aurorae on Mars, *Geophysical research letters*, 33(1).
- Brain, D., R. Lillis, D. Mitchell, J. Halekas, and R. Lin (2007), Electron pitch angle distributions as indicators of magnetic field topology near Mars, *Journal of Geophysical Research: Space Physics*, 112(A9).
- Brain, D., A. Baker, J. Briggs, J. Eastwood, J. Halekas, and T.-D. Phan (2010), Episodic detachment of Martian crustal magnetic fields leading to bulk atmospheric plasma escape, *Geophysical Research Letters*, 37(14).
- Brain, D. A., and B. M. Jakosky (1998), Atmospheric loss since the onset of the Martian geologic record: Combined role of impact erosion and sputtering, *Journal of Geophysical Research: Planets*, 103(E10), 22,689–22,694.

- Brain, D. A., J. McFadden, J. S. Halekas, J. Connerney, S. W. Bougher, S. Curry, C. Dong, Y. Dong, F. Eparvier, X. Fang, et al. (2015), The spatial distribution of planetary ion fluxes near Mars observed by MAVEN, *Geophysical Research Letters*, *42*(21), 9142–9148.
- Brecht, S., S. Ledvina, and J. Luhmann (2003), Mars Ion Loss Rates from a Global Hybrid Model of the Solar Wind Interaction, in *AAS/Division for Planetary Sciences Meeting Abstracts #35, Bulletin of the American Astronomical Society*, vol. 35, p. 934.
- Burgess, D., E. Lucek, M. Scholer, S. Bale, M. Balikhin, A. Balogh, T. Horbury, V. Krasnoselskikh, H. Kucharek, B. Lembège, et al. (2005a), Quasi-parallel shock structure and processes, in *Outer Magnetospheric Boundaries: Cluster Results*, pp. 205–222, Springer.
- Burgess, D., E. Lucek, M. Scholer, S. Bale, M. Balikhin, A. Balogh, T. Horbury, V. Krasnoselskikh, H. Kucharek, B. Lembège, E. Möbius, S. Schwartz, M. Thomsen, and S. Walker (2005b), Quasi-parallel Shock Structure and Processes, *Space science reviews*, *118*, 205–222, doi: 10.1007/s11214-005-3832-3.
- Carr, M. (1996), Water on Mars.
- Carr, M. (2006), The Surface of Mars.
- Carr, M. H., and G. D. Clow (1981), Martian channels and valleys: Their characteristics, distribution, and age, *Icarus*, *48*(1), 91–117.
- Carr, M. H., and J. W. Head (2003), Oceans on Mars: An assessment of the observational evidence and possible fate, *Journal of Geophysical Research: Planets*, *108*(E5).
- Carr, M. H., and J. W. Head (2010), Geologic history of mars, *Earth and Planetary Science Letters*, *294*(3), 185–203.
- Chaffin, M. S., J.-Y. Chaufray, J. Deighan, N. M. Schneider, W. E. McClintock, A. I. F. Stewart, E. Thiemann, J. T. Clarke, G. M. Holsclaw, S. K. Jain, et al. (2015), Three-dimensional structure in the Mars H corona revealed by IUVS on MAVEN, *Geophysical Research Letters*, *42*(21), 9001–9008.
- Chang, T., G. Crew, N. Hershkowitz, J. Jasperse, J. Retterer, and J. Winningham (1986), Transverse acceleration of oxygen ions by electromagnetic ion cyclotron resonance with broad band left-hand polarized waves, *Geophysical Research Letters*, *13*(7), 636–639.
- Chapman, C. R., and K. L. Jones (1977), Cratering and obliteration history of Mars, *Annual Review of Earth and Planetary Sciences*, *5*, 515–540.
- Chapman, S. (1931a), The absorption and dissociative or ionizing effect of monochromatic radiation in an atmosphere on a rotating earth, *Proceedings of the Physical Society*, *43*(1), 26.
- Chapman, S. (1931b), The absorption and dissociative or ionizing effect of monochromatic radiation in an atmosphere on a rotating earth part ii. grazing incidence, *Proceedings of the Physical Society*, *43*(5), 483.
- Chassefière, E., and F. Leblanc (2004), Mars atmospheric escape and evolution; interaction with the solar wind, *Planetary and Space Science*, *52*(11), 1039–1058.

- Chaufray, J.-Y., R. Modolo, F. Leblanc, G. Chanteur, R. Johnson, and J. Luhmann (2007), Mars solar wind interaction: Formation of the Martian corona and atmospheric loss to space, *Journal of Geophysical Research: Planets*, 112(E9).
- Chaufray, J.-Y., J.-L. Bertaux, F. Leblanc, and E. Quémerais (2008), Observation of the hydrogen corona with SPICAM on Mars Express, *Icarus*, 195(2), 598–613.
- Chevrier, V., and P. Mathé (2007), Mineralogy and evolution of the surface of Mars: a review, *Planetary and Space Science*, 55(3), 289–314.
- Chyba, C., T. Owen, and W. Ip (1994), Impact delivery of volatiles and organic molecules to Earth, in *Hazards due to comets and asteroids*, vol. 1, p. 9, University of Arizona Press, Tucson.
- Collinson, G., D. Mitchell, A. Glocer, J. Grebowsky, W. Peterson, J. Connerney, L. Andersson, J. Espley, C. Mazelle, J. Sauvaud, et al. (2015), Electric Mars: The first direct measurement of an upper limit for the Martian polar wind electric potential, *Geophysical Research Letters*, 42(21), 9128–9134.
- Connerney, J., M. Acuna, P. J. Wasilewski, N. F. Ness, H. Reme, C. Mazelle, D. Vignes, R. Lin, D. Mitchell, and P. Cloutier (1999), Magnetic lineations in the ancient crust of Mars, *Science*, 284(5415), 794–798.
- Connerney, J., J. Espley, P. Lawton, S. Murphy, J. Odom, R. Oliverson, and D. Shepard (2015), The MAVEN Magnetic Field Investigation, *Space Science Reviews*, doi:10.1007/s11214-015-0169-4.
- Craddock, R. A., and A. D. Howard (2002), The case for rainfall on a warm, wet early Mars, *Journal of Geophysical Research: Planets*, 107(E11).
- Craddock, R. A., and T. A. Maxwell (1993), Geomorphic evolution of the Martian highlands through ancient fluvial processes, *Journal of Geophysical Research: Planets*, 98(E2), 3453–3468.
- Crider, D. H., J. Espley, D. A. Brain, D. L. Mitchell, J. E. Connerney, and M. H. Acuña (2005), Mars Global Surveyor observations of the Halloween 2003 solar superstorm's encounter with Mars, *Journal of Geophysical Research: Space Physics*, 110(A9).
- Cunnold, D. (1969), Drift-dissipative plasma instability and equatorial spread F, *Journal of Geophysical Research*, 74(24), 5709–5720.
- Curry, S. M., J. G. Luhmann, Y. J. Ma, C. Dong, D. Brain, F. Leblanc, R. Modolo, Y. Dong, J. McFadden, J. Halekas, et al. (2015), Response of Mars O<sup>+</sup> pickup ions to the 8 March 2015 ICME: Inferences from MAVEN data-based models, *Geophysical Research Letters*, 42(21), 9095–9102.
- Dalgarno, A., M. McElroy, and R. Moffett (1963), Electron temperatures in the ionosphere, *Planetary and Space Science*, 11(5), 463–484.
- Deighan, J., M. Chaffin, J.-Y. Chaufray, A. I. F. Stewart, N. Schneider, S. K. Jain, A. Stiepen, M. Crismani, W. E. McClintock, J. T. Clarke, et al. (2015), MAVEN IUVS observation of the hot oxygen corona at Mars, *Geophysical Research Letters*, 42(21), 9009–9014.

- Dong, Y., X. Fang, D. Brain, J. McFadden, J. Halekas, J. Connerney, S. Curry, Y. Harada, J. Luhmann, and B. Jakosky (2015), Strong plume fluxes at Mars observed by MAVEN: An important planetary ion escape channel, *Geophysical Research Letters*, *42*(21), 8942–8950.
- Dubinin, E., M. Fraenz, A. Fedorov, R. Lundin, N. Edberg, F. Duru, and O. Vaisberg (2011), Ion energization and escape on Mars and Venus, *Space science reviews*, *162*(1-4), 173–211.
- Dubinin, E., M. Fraenz, J. Woch, R. Modolo, G. Chanteur, F. Duru, D. Gurnett, S. Barabash, and R. Lundin (2012), Upper ionosphere of Mars is not axially symmetrical, *Earth, planets and space*, *64*(2), 113–120.
- Duru, F., D. Gurnett, R. Frahm, J. Winningham, D. Morgan, and G. Howes (2009), Steep, transient density gradients in the Martian ionosphere similar to the ionopause at Venus, *Journal of Geophysical Research: Space Physics*, *114*(A12).
- Eastwood, J., D. Brain, J. Halekas, J. Drake, T. Phan, M. Øieroset, D. Mitchell, R. Lin, and M. Acuña (2008), Evidence for collisionless magnetic reconnection at Mars, *Geophysical Research Letters*, *35*(2).
- Edberg, N., M. Lester, S. Cowley, D. Brain, R. Modolo, M. Fränz, and S. Barabash (2009a), Plasma boundary variability at Mars as observed by Mars Global Surveyor and Mars Express, *Annales Geophysicae*, *27*, 3537–3550.
- Edberg, N., U. Auster, S. Barabash, A. Bößwetter, D. Brain, J. Burch, C. Carr, S. Cowley, E. Cupido, F. Duru, A. Eriksson, M. Fränz, K. Glassmeier, R. Goldstein, M. Lester, R. Lundin, R. Modolo, H. Nilsson, I. Richter, M. Samara, and J. Trotignon (2009b), Rosetta and Mars Express observations of the influence of high solar wind pressure on the Martian plasma environment, in *Annales Geophysicae*, vol. 27, pp. 4533–4545, Copernicus GmbH.
- Edberg, N., H. Nilsson, A. Williams, M. Lester, S. Milan, S. Cowley, M. Fränz, S. Barabash, and Y. Futaana (2010), Pumping out the atmosphere of Mars through solar wind pressure pulses, *Geophysical Research Letters*, *37*(3).
- Eparvier, F., P. Chamberlin, T. Woods, and E. Thiemann (2015), The solar extreme ultraviolet monitor for MAVEN, *Space Science Reviews*, *195*(1-4), 293–301.
- Ergun, R., L. Andersson, W. Peterson, D. Brain, G. Delory, D. Mitchell, R. Lin, and A. Yau (2006), Role of plasma waves in Mars' atmospheric loss, *Geophysical research letters*, *33*(14).
- Ergun, R., D. Malaspina, I. Cairns, M. Goldman, D. Newman, P. Robinson, S. Eriksson, J. Bougeret, C. Briand, S. Bale, et al. (2008), Eigenmode structure in solar-wind Langmuir waves, *Physical review letters*, *101*(5), 051,101.
- Ergun, R., M. Morooka, L. Andersson, C. Fowler, G. Delory, D. Andrews, A. Eriksson, T. McEnulty, and B. Jakosky (2015a), Dayside electron temperature and density profiles at Mars: First results from the MAVEN Langmuir probe and waves instrument, *Geophysical Research Letters*, *42*(21), 8846–8853.
- Ergun, R., L. Andersson, C. Fowler, A. Woodson, T. Weber, G. Delory, D. Andrews, A. Eriksson, T. McEnulty, M. Morooka, et al. (2016), Enhanced O<sub>2</sub><sup>+</sup> Loss at Mars due to an ambipolar electric field from electron heating, *Journal of Geophysical Research: Space Physics*.

- Ergun, R. E., M. W. Morooka, L. Andersson, C. M. Fowler, G. T. Delory, D. J. Andrews, A. I. Eriksson, T. McEnulty, and B. M. Jakosky (2015b), Dayside electron temperature and density profiles at Mars: First results from the MAVEN LPW instrument, *This Issue*.
- Espley, J., P. Cloutier, D. Brain, D. Crider, and M. Acuña (2004), Observations of low-frequency magnetic oscillations in the Martian magnetosheath, magnetic pileup region, and tail, *Journal of Geophysical Research: Space Physics*, 109(A7).
- Espley, J., P. Cloutier, D. Crider, D. Brain, and M. Acuña (2005), Low-frequency plasma oscillations at Mars during the October 2003 solar storm, *Journal of Geophysical Research: Space Physics*, 110(A9).
- Fairfield, D. (1971), Average and unusual locations of the Earth's magnetopause and bow shock, *Journal of Geophysical Research*, 76(28), 6700–6716.
- Fallows, K., P. Withers, and M. Matta (2015), An observational study of the influence of solar zenith angle on properties of the M1 layer of the Mars ionosphere, *Journal of Geophysical Research: Space Physics*, 120(2), 1299–1310.
- Fassett, C. I., and J. W. Head (2005), Fluvial sedimentary deposits on Mars: Ancient deltas in a crater lake in the Nili Fossae region, *Geophysical Research Letters*, 32(14).
- Fejer, B. G., and M. Kelley (1980), Ionospheric irregularities, *Reviews of Geophysics*, 18(2), 401–454.
- Fjeldbo, G., A. Kliore, and B. Seidel (1970), The Mariner 1969 occultation measurements of the upper atmosphere of Mars, *Radio Science*, 5(2), 381–386.
- Fowler, C., L. Andersson, R. Ergun, M. Morooka, G. Delory, D. J. Andrews, R. J. Lillis, T. McEnulty, T. Weber, T. Chamandy, et al. (2015), The first in situ electron temperature and density measurements of the Martian nightside ionosphere, *Geophysical Research Letters*, 42(21), 8854–8861.
- Fowler, C., L. Andersson, J. Halekas, J. Espley, R. Ergun, J. Connerney, and B. Jakosky (2016), Electric and magnetic variations in the near Mars environment, *Journal of Geophysical Research: Space Physics*, *Under peer review*.
- Fox, J. L. (1993a), Upper limits to the nightside ionosphere of Mars, *Geophysical Research Letters*, 20(13), 1339.
- Fox, J. L. (1993b), On the escape of oxygen and hydrogen from Mars, *Geophysical research letters*, 20(17), 1747–1750.
- Fox, J. L. (1997), Upper limits to the outflow of ions at Mars: Implications for atmospheric evolution, *Geophysical research letters*, 24(22), 2901–2904.
- Fox, J. L., and F. Bakalian (2001), Photochemical escape of atomic carbon from Mars, *J. Geophys. Res.*, 106, 28,785–28,795.
- Fox, J. L., and A. Dalgarno (1979), Ionization, luminosity, and heating of the upper atmosphere of Mars, *Journal of Geophysical Research: Space Physics*, 84(A12), 7315–7333.

- Fox, J. L., and A. Hać (1999), Velocity distributions of C atoms in CO+ dissociative recombination: Implications for photochemical escape of C from Mars, *Journal of Geophysical Research-Space Physics*, *104*(A11), 24,729.
- Fox, J. L., and K. Sung (2001), Solar activity variations of the Venus thermosphere/ionosphere, *Journal of Geophysical Research: Space Physics*, *106*(A10), 21,305–21,335.
- Fox, J. L., P. Zhou, and S. W. Bougher (1996), The Martian thermosphere/ionosphere at high and low solar activities, *Advances in Space Research*, *17*(11), 203–218.
- Frahm, R., J. Winningham, J. Sharber, J. Scherrer, S. Jeffers, A. Coates, D. Linder, D. Kataria, R. Lundin, S. Barabash, et al. (2006), Carbon dioxide photoelectron energy peaks at Mars, *Icarus*, *182*(2), 371–382.
- Futaana, Y., S. Barabash, M. Yamauchi, S. McKenna-Lawlor, R. Lundin, J. Luhmann, D. Brain, E. Carlsson, J.-A. Sauvaud, J. Winningham, et al. (2008), Mars Express and Venus Express multi-point observations of geoeffective solar flare events in December 2006, *Planetary and Space Science*, *56*(6), 873–880.
- Ganguli, S. B. (1996), The polar wind, *Reviews of Geophysics*, *34*(3), 311–348.
- Geisler, J., and S. Bowhill (1965), Ionospheric temperatures at sunspot minimum, *Journal of Atmospheric and Terrestrial Physics*, *27*(4), 457–474.
- Golombek, M., and N. Bridges (2000), Erosion rates on Mars and implications for climate change: Constraints from the Pathfinder landing site, *Journal of Geophysical Research*, *105*, 1841–1854, doi:10.1029/1999JE001043.
- Grard, R., A. Pedersen, S. Klimov, S. Savin, A. Skalsky, J. Trotignon, and C. Kennel (1989), First measurements of plasma waves near Mars, *Nature*, *341*(6243), 607–609.
- Groves, K., S. Basu, E. Weber, M. Smitham, H. Kuenzler, C. Valladares, R. Sheehan, E. MacKenzie, J. Secan, P. Ning, et al. (1997), Equatorial scintillation and systems support, *Radio Science*, *32*(5), 2047–2064.
- Gulick, V. (1998), Magmatic intrusions and a hydrothermal origin for fluvial valleys on Mars, *Journal of Geophysical Research: Planets*, *103*(E8), 19,365–19,387.
- Gurnett, D., D. Kirchner, R. Huff, D. Morgan, A. Persoon, T. Averkamp, F. Duru, E. Nielsen, A. Safaeinili, J. Plaut, et al. (2005), Radar soundings of the ionosphere of Mars, *Science*, *310*(5756), 1929–1933.
- Guyodo, Y., and J.-P. Valet (1999), Global changes in intensity of the Earth's magnetic field during the past 800 kyr, *Nature*, *399*(6733), 249–252.
- Haider, S. (1997), Chemistry of the nightside ionosphere of Mars, *Journal of Geophysical Research: Space Physics (1978–2012)*, *102*(A1), 407–416.
- Haider, S., and K. Mahajan (2014), Lower and Upper Ionosphere of Mars, *Space Science Reviews*, *182*, 19–84, doi:10.1007/s11214-014-0058-2.

- Haider, S., J. Kim, A. Nagy, C. Keller, M. Verigin, K. Gringauz, N. Shutte, K. Szego, and P. Kiraly (1992), Calculated ionization rates, ion densities, and airglow emission rates due to precipitating electrons in the nightside ionosphere of Mars, *Journal of Geophysical Research: Space Physics* (1978–2012), *97*(A7), 10,637–10,641.
- Halekas, J., E. Taylor, G. Dalton, G. Johnson, D. Curtis, J. McFadden, D. Mitchell, R. Lin, and B. Jakosky (2015), The Solar Wind Ion Analyzer for MAVEN, *Space Science Reviews*, doi: 10.1007/s11214-013-0029-z.
- Halekas, J., S. Ruhunusiri, Y. Harada, G. Collinson, D. Mitchell, C. Mazelle, J. McFadden, J. Connerney, J. Espley, F. Eparvier, J. Luhmann, and B. Jakosky (2016), Structure, Dynamics, and Seasonal Variability of the Mars-Solar Wind Interaction: MAVEN Solar Wind Ion Analyzer In-flight Performance and Science Results, *Journal of Geophysical Research: Space Physics, This Issue*.
- Hanson, W., and G. Mantas (1988), Viking electron temperature measurements: Evidence for a magnetic field in the Martian ionosphere, *Journal of Geophysical Research: Space Physics* (1978–2012), *93*(A7), 7538–7544.
- Hanson, W., S. Sanatani, and D. Zuccaro (1977), The Martian ionosphere as observed by the Viking retarding potential analyzers, *Journal of Geophysical Research*, *82*(28), 4351–4363.
- Hantsch, M., and S. Bauer (1990), Solar control of the Mars ionosphere, *Planetary and space science*, *38*(4), 539–542.
- Hartmann, W. K., and G. Neukum (2001), Cratering chronology and the evolution of Mars, in *Chronology and evolution of Mars*, pp. 165–194, Springer.
- Hodges, R. R. (2000), Distributions of hot oxygen for Venus and Mars, *Journal of Geophysical Research: Planets*, *105*(E3), 6971–6981.
- Hoegy, W., S. Curtis, L. Brace, N. Maynard, and R. Heelis (1982), Dynamics Explorer observations of equatorial spread F: Evidence for drift waves, *Geophysical Research Letters*, *9*(9), 993–996.
- Howard, A., J. Moore, R. Irwin, and R. Craddock (2005a), Identification of a Martian Sedimentary Platform in Margaritifer Sinus, Meridiani Terra, and Arabia, in *AGU Fall Meeting Abstracts*.
- Howard, A. D., J. M. Moore, and R. P. Irwin (2005b), An intense terminal epoch of widespread fluvial activity on early Mars: 1. Valley network incision and associated deposits, *Journal of Geophysical Research: Planets*, *110*(E12).
- Howell, E. (2015), A Brief History of Mars Missions, <http://www.space.com/13558-historic-mars-missions.html>.
- Huang, C.-S., C. Miller, and M. Kelley (1994), Basic properties and gravity wave initiation of the midlatitude F region instability, *Radio Science*, *29*(1), 395–405.
- Hutchins, K. S., and B. M. Jakosky (1996), Evolution of Martian atmospheric argon: Implications for sources of volatiles, *Journal of Geophysical Research: Planets*, *101*(E6), 14,933–14,949.
- Hynek, B. M., and R. J. Phillips (2003), New data reveal mature, integrated drainage systems on Mars indicative of past precipitation, *Geology*, *31*(9), 757–760.

- Irwin, R. P., and A. D. Howard (2002), Drainage basin evolution in Noachian Terra Cimmeria, Mars, *Journal of Geophysical Research: Planets*, 107(E7).
- Irwin, R. P., T. A. Maxwell, A. D. Howard, R. A. Craddock, and D. W. Leverington (2002), A large paleolake basin at the head of Ma'adim Vallis, Mars, *Science*, 296(5576), 2209–2212.
- Irwin, R. P., T. R. Watters, A. D. Howard, and J. R. Zimbelman (2004), Sedimentary resurfacing and fretted terrain development along the crustal dichotomy boundary, Aeolis Mensae, Mars, *Journal of Geophysical Research: Planets*, 109(E9).
- Jakosky, B., and R. Phillips (2001), Mars' volatile and climate history, *nature*, 412(6843), 237–244.
- Jakosky, B., R. Lin, J. Grebowsky, J. Luhmann, D. Mitchell, G. Beutelschies, T. Priser, M. Acuna, L. Andersson, D. Baird, et al. (2015a), The Mars Atmosphere and Volatile Evolution (MAVEN) Mission, *Space Science Reviews*, pp. 1–46.
- Jakosky, B. M., R. O. Pepin, R. E. Johnson, and J. L. Fox (1994), Mars atmospheric loss and isotopic fractionation by solar-wind-induced sputtering and photochemical escape, *Icarus*, 111(2), 271–288.
- Jakosky, B. M., J. M. Grebowsky, J. G. Luhmann, J. Connerney, F. Eparvier, R. Ergun, J. Halekas, D. Larson, P. Mahaffy, J. Mcfadden, et al. (2015b), MAVEN observations of the response of Mars to an interplanetary coronal mass ejection, *Science*, 350(6261), aad0210.
- Johnson, R. (1994), Plasma-induced sputtering of an atmosphere, *Space Science Reviews*, 69(3-4), 215–253.
- Johnson, R., D. Schnellenberger, and M. Wong (2000), The sputtering of an oxygen thermosphere by energetic O<sup>+</sup>, *Journal of Geophysical Research: Planets*, 105(E1), 1659–1670.
- Kallio, E., and P. Janhunen (2002), Ion escape from Mars in a quasi-neutral hybrid model, *Journal of Geophysical Research: Space Physics*, 107(A3).
- Kass, D., and Y. Yung (1995), Loss of atmosphere from Mars due to solar wind-induced sputtering, *Science*, 268(5211), 697.
- Kass, D., Y. Yung, et al. (1996), The loss of atmosphere from Mars-response, *Science*, 274(5294), 1932–1933.
- Kelley, M., R. Pfaff, K. Baker, J. Ulwick, R. Livingston, C. Rino, and R. Tsunoda (1982), Simultaneous rocket probe and radar measurements of equatorial spread F/Transitional and short wavelength results, *Journal of Geophysical Research: Space Physics*, 87(A3), 1575–1588.
- Kim, J., A. F. Nagy, J. L. Fox, and T. E. Cravens (1998), Solar cycle variability of hot oxygen atoms at Mars, *Journal of Geophysical Research: Space Physics*, 103(A12), 29,339–29,342.
- Kintner, P., B. Ledvina, E. De Paula, and I. Kantor (2004), Size, shape, orientation, speed, and duration of GPS equatorial anomaly scintillations, *Radio Science*, 39(2).
- Kliore, A., G. Fjeldbo, and B. Seidel (1970), First Results of the Mariner-6 Radio Occultation Measurement of the Lower Atmosphere of Mars, *Radio Science*, 5(2), 373–379.

- Kolesnikova, E., and C. Béghin (2001), Instability problem of the electric field antennas on the Polar spacecraft, *Radio Science*, *36*(2), 203–221.
- Kolesnikova, E., C. Béghin, R. Grard, and C. Escoubet (2001), The electrical stability of the electric field antennas in the plasmasphere, *Journal of Atmospheric and Solar-Terrestrial Physics*, *63*(11), 1217–1224.
- Krasnopolsky, V. A. (2002), Mars' upper atmosphere and ionosphere at low, medium, and high solar activities: Implications for evolution of water, *Journal of Geophysical Research: Planets*, *107*(E12).
- Laframboise, J., and J. Rubinstein (1976), Theory of a cylindrical probe in a collisionless magnetoplasma, *Physics of Fluids (1958-1988)*, *19*(12), 1900–1908.
- Lammer, H., and S. Bauer (1991), Nonthermal atmospheric escape from Mars and Titan, *Journal of Geophysical Research: Space Physics*, *96*(A2), 1819–1825.
- Lammer, H., W. Stumtner, and S. J. Bauer (1996), Loss of H and O from Mars: implications for the planetary water inventory, *Geophysical research letters*, *23*(23), 3353–3356.
- Lammer, H., H. Lichtenegger, C. Kolb, I. Ribas, E. Guinan, R. Abart, and S. Bauer (2003), Loss of water from Mars: Implications for the oxidation of the soil, *Icarus*, *165*(1), 9–25.
- Larson, D. E., R. J. Lillis, C. O. Lee, P. A. Dunn, K. Hatch, M. Robinson, D. Glaser, J. Chen, D. Curtis, C. Tiu, et al. (2015), The MAVEN solar energetic particle investigation, *Space Science Reviews*, *195*(1-4), 153–172.
- Lasue, J., N. Mangold, E. Hauber, S. Clifford, W. Feldman, O. Gasnault, C. Grima, S. Maurice, and O. Mouis (2013), Quantitative assessments of the martian hydrosphere, *Space Science Reviews*, *174*(1-4), 155–212.
- Leblanc, F., and R. Johnson (2001), Sputtering of the Martian atmosphere by solar wind pick-up ions, *Planetary and Space Science*, *49*(6), 645–656.
- Leblanc, F., and R. Johnson (2002), Role of molecular species in pickup ion sputtering of the Martian atmosphere, *Journal of Geophysical Research: Planets*, *107*(E2).
- Leblanc, F., J. Luhmann, R. Johnson, and E. Chassefiere (2002), Some expected impacts of a solar energetic particle event at Mars, *Journal of Geophysical Research: Space Physics*, *107*(A5).
- Lillis, R. J., and X. Fang (2015), Electron impact ionization in the Martian atmosphere: interplay between scattering and crustal magnetic field effects, *Journal of Geophysical Research*.
- Lillis, R. J., M. O. Fillingim, L. M. Peticolas, D. A. Brain, R. P. Lin, and S. W. Bougher (2009), Nightside ionosphere of Mars: Modeling the effects of crustal magnetic fields and electron pitch angle distributions on electron impact ionization, *Journal of Geophysical Research: Planets (1991-2012)*, *114*(E11).
- Lillis, R. J., M. O. Fillingim, and D. A. Brain (2011), Three-dimensional structure of the Martian nightside ionosphere: Predicted rates of impact ionization from Mars Global Surveyor magnetometer and electron reflectometer measurements of precipitating electrons, *Journal of Geophysical Research: Space Physics (1978-2012)*, *116*(A12).

- Lillis, R. J., D. A. Brain, S. W. Bougher, F. Leblanc, J. G. Luhmann, B. M. Jakosky, R. Modolo, J. Fox, J. Deighan, X. Fang, et al. (2015), Characterizing atmospheric escape from Mars today and through time, with MAVEN, *Space Science Reviews*, 195(1-4), 357–422.
- Lindal, G. F., H. B. Hotz, D. N. Sweetnam, Z. Shippony, J. P. Brenkle, G. V. Hartsell, R. T. Spear, and W. H. Michael (1979), Viking radio occultation measurements of the atmosphere and topography of Mars: Data acquired during 1 Martian year of tracking, *Journal of Geophysical Research: Solid Earth*, 84(B14), 8443–8456.
- Liu, Y., A. Nagy, T. Gombosi, D. DeZeeuw, and K. Powell (2001), The solar wind interaction with Mars: Results of three-dimensional three-species MHD studies, *Advances in Space Research*, 27(11), 1837–1846.
- Luhmann, J. (1997), Correction to The ancient oxygen exosphere of Mars: Implications for atmosphere evolution by Zhang et al., *Journal of Geophysical Research: Planets*, 102(E1), 1637–1637.
- Luhmann, J., R. Johnson, and M. Zhang (1992), Evolutionary impact of sputtering of the Martian atmosphere by O<sup>+</sup> pickup ions, *Geophysical research letters*, 19(21), 2151–2154.
- Lundin, R., A. Zakharov, R. Pellinen, H. Borg, B. Hultqvist, N. Pissarenko, E. Dubinin, S. Barabash, I. Liede, and H. Koskinen (1989), First measurements of the ionospheric plasma escape from Mars, *Nature*, 341(6243), 609–612.
- Lundin, R., A. Zakharov, R. Pellinen, S. Barabash, H. Borg, E. Dubinin, B. Hultqvist, H. Koskinen, I. Liede, and N. Pissarenko (1990), ASPERA/Phobos measurements of the ion outflow from the Martian ionosphere, *Geophysical Research Letters*, 17(6), 873–876.
- Lundin, R., S. Barabash, H. Andersson, M. Holmström, A. Grigoriev, M. Yamauchi, J. Sauvaud, A. Fedorov, E. Budnik, J. Thocaven, et al. (2004), Solar wind-induced atmospheric erosion at Mars: First results from ASPERA-3 on Mars Express, *Science*, 305(5692), 1933–1936.
- Lundin, R., D. Winningham, S. Barabash, R. Frahm, M. Holmström, J.-A. Sauvaud, A. Fedorov, K. Asamura, A. Coates, Y. Soobiah, et al. (2006a), Plasma acceleration above Martian magnetic anomalies, *Science*, 311(5763), 980–983.
- Lundin, R., D. Winningham, S. Barabash, R. Frahm, H. Andersson, M. Holmström, A. Grigoriev, M. Yamauchi, H. Borg, J. Sharber, et al. (2006b), Ionospheric plasma acceleration at Mars: ASPERA-3 results, *Icarus*, 182(2), 308–319.
- Lundin, R., S. Barabash, M. Holmström, H. Nilsson, M. Yamauchi, M. Fraenz, and E. Dubinin (2008), A comet-like escape of ionospheric plasma from Mars, *Geophysical Research Letters*, 35(18).
- Lundin, R., S. Barabash, M. Yamauchi, H. Nilsson, and D. Brain (2011), On the relation between plasma escape and the Martian crustal magnetic field, *Geophysical Research Letters*, 38(2).
- Ma, Y., A. F. Nagy, K. C. Hansen, D. L. DeZeeuw, T. I. Gombosi, and K. Powell (2002), Three-dimensional multispecies MHD studies of the solar wind interaction with Mars in the presence of crustal fields, *Journal of Geophysical Research: Space Physics*, 107(A10).

- Mahaffy, P., M. Benna, M. Elrod, R. Yelle, S. Bougher, S. Stone, and B. Jakosky (2015a), Structure and composition of the neutral upper atmosphere of Mars from the MAVEN NGIMS investigation, *Geophysical Research Letters*, *42*(21), 8951–8957.
- Mahaffy, P. R., M. Benna, T. King, D. N. Harpold, R. Arvey, M. Barciniak, M. Bendt, D. Carrigan, T. Errigo, V. Holmes, et al. (2015b), The neutral gas and ion mass spectrometer on the Mars atmosphere and volatile evolution mission, *Space Science Reviews*, *195*(1-4), 49–73.
- Malaspina, D. (2010), *Microphysics of the solar wind*.
- Malin, M. C., and K. S. Edgett (2003), Evidence for persistent flow and aqueous sedimentation on early Mars, *Science*, *302*(5652), 1931–1934.
- Martínez, G., and N. O. Renno (2013), Water and brines on Mars: current evidence and implications for MSL, *Space Science Reviews*, *175*(1-4), 29–51.
- Mathews, J., S. Gonzalez, M. Sulzer, Q.-H. Zhou, J. Urbina, E. Kudeki, and S. Franke (2001), Kilometer-scale layered structures inside spread-F, *Geophysical research letters*, *28*(22), 4167–4170.
- Matta, M., M. Galand, L. Moore, M. Mendillo, and P. Withers (2014), Numerical simulations of ion and electron temperatures in the ionosphere of Mars: Multiple ions and diurnal variations, *Icarus*, *227*, 78–88.
- Mazelle, C., H. Reme, F. Neubauer, and K.-H. Glassmeier (1995), Comparison of the main magnetic and plasma features in the environments of comets Grigg-Skjellerup and Halley, *Advances in Space Research*, *16*(4), 41–45.
- McClintock, W. E., N. M. Schneider, G. M. Holsclaw, J. T. Clarke, A. C. Hoskins, I. Stewart, F. Montmessin, R. V. Yelle, and J. Deighan (2015), The imaging ultraviolet spectrograph (IUVS) for the MAVEN mission, *Space Science Reviews*, *195*(1-4), 75–124.
- McElroy, M. B. (1972), Mars: An evolving atmosphere, *Science*, *175*(4020), 443–445.
- McElroy, M. B., and T. M. Donahue (1972), Stability of the Martian atmosphere, *Science*, *177*, 986–988.
- McElroy, M. B., and Y. L. Yung (1976), Oxygen isotopes in the Martian atmosphere: Implications for the evolution of volatiles, *Planetary and Space Science*, *24*(12), 1107–1113.
- McElroy, M. B., T. Y. Kong, and Y. L. Yung (1977), Photochemistry and evolution of Mars' atmosphere: A Viking perspective, *Journal of Geophysical Research*, *82*(28), 4379–4388.
- McFadden, J., O. Kortmann, D. Curtis, G. Dalton, G. Johnson, R. Abiad, R. Sterling, K. Hatch, P. Berg, C. Tiu, et al. (2015), MAVEN SupraThermal And Thermal Ion Composition (STATIC) instrument, *Space Science Reviews*, *195*(1-4), 199–256.
- McSween, H. Y., T. L. Grove, R. C. Lentz, J. C. Dann, A. H. Holzheid, L. R. Riciputi, and J. G. Ryan (2001), Geochemical evidence for magmatic water within Mars from pyroxenes in the Shergotty meteorite, *Nature*, *409*(6819), 487–490.
- Melosh, H., and A. Vickery (1989), Impact erosion of the primordial atmosphere of Mars., *Nature*, *338*(6215), 487–489.

- Mitchell, D., R. Lin, C. Mazelle, H. Rème, P. Cloutier, J. Connerney, M. Acuña, and N. Ness (2001), Probing Mars' crustal magnetic field and ionosphere with the MGS Electron Reflectometer, *Journal of Geophysical Research: Planets*, 106(E10), 23,419–23,427.
- Mitchell, D., C. Mazelle, J. Sauvaud, J. Thocaven, J. Rouzaud, A. Fedorov, P. Rouger, D. Toubanc, E. Taylor, D. Gordon, et al. (2016), The MAVEN Solar Wind Electron Analyzer, *Space Science Reviews*, 200(1-4), 495–528.
- Mitchell, H., Jr, J. Fedder, M. Keskinen, and S. Zalesak (1985), A simulation of high latitude F-layer instabilities in the presence of magnetosphere-ionosphere coupling, *Geophysical research letters*, 12, 283–286, doi:10.1029/GL012i005p00283.
- Modolo, R., G. Chanteur, E. Dubinin, and A. Matthews (2005), Influence of the solar EUV flux on the Martian plasma environment, in *Annales Geophysicae*, vol. 23, pp. 433–444, Copernicus GmbH.
- Moore, J. M., A. D. Howard, W. E. Dietrich, and P. M. Schenk (2003), Martian layered fluvial deposits: Implications for Noachian climate scenarios, *Geophysical Research Letters*, 30(24).
- Morgan, D., D. Gurnett, D. Kirchner, J. L. Fox, E. Nielsen, and J. Plaut (2008), Variation of the Martian ionospheric electron density from Mars Express radar soundings, *Journal of Geophysical Research: Space Physics*, 113(A9).
- Morschhauser, A., V. Lesur, and M. Grott (2014), A spherical harmonic model of the lithospheric magnetic field of Mars, *Journal of Geophysical Research: Planets*, 119(6), 1162–1188.
- Mott-Smith, H. M., and I. Langmuir (1926), The theory of collectors in gaseous discharges, *Physical review*, 28(4), 727.
- Mutch, T., and J. Head (1975), The geology of Mars: A brief review of some recent results, *Reviews of Geophysics*, 13(3), 411–416.
- Nagy, A., D. Winterhalter, K. Sauer, T. Cravens, S. Brecht, C. Mazelle, D. Crider, E. Kallio, A. Zakharov, E. Dubinin, et al. (2004), The plasma environment of Mars, in *Mars Magnetism and Its Interaction with the Solar Wind*, pp. 33–114, Springer.
- Nagy, A. F., T. I. Gombosi, K. Szego, R. Sagdeev, V. Shapiro, and V. Shevchenko (1990), Venus mantle-Mars planetosphere: What are the similarities and differences?, *Geophysical Research Letters*, 17(6), 865–868.
- Nagy, A. F., M. W. Liemohn, J. L. Fox, and J. Kim (2001), Hot carbon densities in the exosphere of Mars, *Journal of Geophysical Research-Space Physics*, 106(A10), 21,565.
- Nagy, A. F., D. Winterhalter, K. Sauer, T. E. Cravens, S. Brecht, C. Mazelle, D. Crider, E. Kallio, A. Zakharov, E. Dubinin, M. Verigin, G. Kotova, W. I. Axford, C. Bertucci, and J. G. Trotignon (2004), The plasma environment of Mars, *Space Science Reviews*, 111, 33–114.
- Nelder, J., and R. Mead (1965), A simplex method for function minimization, *The computer journal*, 7(4), 308–313.
- Němec, F., D. Morgan, D. Gurnett, and F. Duru (2010), Nightside ionosphere of Mars: Radar soundings by the Mars Express spacecraft, *Journal of Geophysical Research: Planets*, 115(E12).

- Němec, F., D. Morgan, D. Gurnett, F. Duru, and V. Truhlík (2011), Dayside ionosphere of Mars: Empirical model based on data from the MARSIS instrument, *Journal of Geophysical Research: Planets*, 116(E7).
- Nier, A., and M. McElroy (1977), Composition and structure of Mars' upper atmosphere: Results from the neutral mass spectrometers on Viking 1 and 2, *Journal of Geophysical Research*, 82(28), 4341–4349.
- Nilsson, H., N. J. Edberg, G. Stenberg, S. Barabash, M. Holmström, Y. Futaana, R. Lundin, and A. Fedorov (2011), Heavy ion escape from Mars, influence from solar wind conditions and crustal magnetic fields, *Icarus*, 215(2), 475–484.
- Norqvist, P., M. André, and M. Tyrland (1998), A statistical study of ion energization mechanisms in the auroral region, *Journal of Geophysical Research: Space Physics*, 103(A10), 23,459–23,473.
- Ossakow, S. L. (1981), Spread-F theories A review, *Journal of Atmospheric and Terrestrial Physics*, 43(5-6), 437–452.
- Ott, E. (1978), Theory of Rayleigh-Taylor bubbles in the equatorial ionosphere, *Journal of Geophysical Research: Space Physics*, 83(A5), 2066–2070.
- Owen, T., and A. Bar-Nun (1995), Comets, impacts, and atmospheres, *Icarus*, 116(2), 215–226.
- Parker, T., S. Clifford, and W. Banerdt (2000), Argyre Planitia and the Mars Global Hydrologic Cycle, in *Lunar and Planetary Science Conference, Lunar and Planetary Science Conference*, vol. 31.
- Parker, T. J., R. S. Saunders, and D. M. Schneeberger (1989), Transitional morphology in west Deuteronilus Mensae, Mars: Implications for modification of the lowland/upland boundary, *Icarus*, 82(1), 111–145.
- Parker, T. J., D. S. Gorsline, R. S. Saunders, D. C. Pieri, and D. M. Schneeberger (1993), Coastal geomorphology of the Martian northern plains, *Journal of Geophysical Research: Planets*, 98(E6), 11,061–11,078.
- Picardi, G., D. Biccari, R. Seu, J. Plaut, W. Johnson, R. Jordan, A. Safaeinili, D. Gurnett, R. Huff, R. Orosei, et al. (2004), MARSIS: Mars advanced radar for subsurface and ionosphere sounding, in *Mars Express: The Scientific Payload*, vol. 1240, pp. 51–69.
- Pieri, D. C. (1980), Martian valleys- Morphology, distribution, age, and origin, *Science*, 210(4472), 895–897.
- Pollack, J. B. (1979), Climatic change on the terrestrial planets, *Icarus*, 37(3), 479–553.
- Pollack, J. B., and O. B. Toon (1982), Quasi-periodic climate changes on Mars: A review, *Icarus*, 50(2), 259–287.
- Pollack, J. B., J. F. Kasting, S. M. Richardson, and K. Poliakoff (1987), The case for a wet, warm climate on early Mars, *Icarus*, 71(2), 203–224.
- Pollock, C., M. Chandler, T. Moore, J. Waite, C. Chappell, and D. Gurnett (1990), A survey of upwelling ion event characteristics, *Journal of Geophysical Research: Space Physics*, 95(A11), 18,969–18,980.

- Press, W. (2007), *Numerical recipes 3rd edition: The art of scientific computing*, Cambridge university press.
- Raghavarao, R., R. Suhasini, H. Mayr, W. Hoegy, and L. Wharton (1999), Equatorial spread-F (ESF) and vertical winds, *Journal of atmospheric and solar-terrestrial physics*, 61(8), 607–617.
- Reme, H., C. Mazelle, J. Sauvaud, C. d’Uston, F. Froment, R. Lin, K. Anderson, C. Carlson, D. Larson, A. Korth, et al. (1993), Electron plasma environment at comet Grigg-Skjellerup: General observations and comparison with the environment at comet Halley, *Journal of Geophysical Research: Space Physics*, 98(A12), 20,965–20,976.
- Riouisset, J., C. Paty, R. Lillis, M. Fillingim, S. England, P. Withers, and J. Hale (2014), Electrodynamics of the Martian dynamo region near magnetic cusps and loops, *Geophysical Research Letters*, 41, 1119–1125, doi:10.1002/2013GL059130.
- Rubinstein, J., and J. Laframboise (1982), Theory of a spherical probe in a collisionless magnetoplasma, *Physics of Fluids (1958-1988)*, 25(7), 1174–1182.
- Ruhunusiri, S., J. Halekas, J. Connerney, J. Espley, J. McFadden, D. Larson, D. Mitchell, C. Mazelle, and B. Jakosky (2015), Low-frequency waves in the Martian magnetosphere and their response to upstream solar wind driving conditions, *Geophysical Research Letters*, 42, 8917–8924.
- Russell, C., J. Luhmann, K. Schwingenschuh, W. Riedler, and Y. Yeroshenko (1990), Upstream waves at Mars: Phobos observations, *Geophysical Research Letters*, 17(6), 897–900.
- Russell, D. A., and E. Ott (1979), The linear theory of the Raleigh-Taylor instability in the equatorial ionosphere, *Journal of Geophysical Research: Space Physics*, 84(A11), 6573–6579.
- Sagdeev, R., V. Shapiro, V. Shevchenko, A. Zacharov, P. Kiraly, K. Szego, A. Nagy, and R. Grard (1990), Wave activity in the neighborhood of the bowshock of Mars, *Geophysical Research Letters*, 17(6), 893–896.
- Savich, N., and V. Samovol (1976), The night time ionosphere of Mars from Mars 4 and Mars 5 dual-frequency radio occultation measurements, in *Space research XVI*, vol. 1, pp. 1009–1011.
- Savich, N. A., and V. A. Samovol (1976a), The night time ionosphere of Mars from Mars 4 and Mars 5 dual-frequency radio occultation measurements, in *Space research XVI*, edited by M. J. Rycroft, pp. 1009–1011.
- Savich, N. A., and V. A. Samovol (1976b), The night time ionosphere of Mars from Mars 4 and Mars 5 dual-frequency radio occultation measurements, in *Space research XVI*, edited by M. J. Rycroft, pp. 1009–1011.
- Schneider, N., J. Deighan, A. Stewart, W. McClintock, S. Jain, M. Chaffin, A. Stiepen, M. Crismani, J. Plane, J. Carrillo-Sánchez, et al. (2015), MAVEN IUVS observations of the aftermath of the Comet Siding Spring meteor shower on Mars, *Geophysical Research Letters*, 42(12), 4755–4761.
- Schunk, R., and A. Nagy (2009), *Ionospheres: physics, plasma physics, and chemistry*, Cambridge university press.
- Singh, S., F. Johnson, and R. Power (1997), Gravity wave seeding of equatorial plasma bubbles, *Journal of Geophysical Research: Space Physics*, 102(A4), 7399–7410.

- Slavin, J., K. Schwingenschuh, W. Riedler, and Y. Yeroshenko (1991), The solar wind interaction with Mars: Mariner 4, Mars 2, Mars 3, Mars 5, and Phobos 2 observations of bow shock position and shape, *Journal of Geophysical Research: Space Physics*, *96*(A7), 11,235–11,241.
- Squyres, S., and J. Kasting (1994), Early Mars, *Science*, *265*, 744–749.
- Stepinski, T., and W. O'Hara IV (2003), Vertical analysis of martian drainage basins, in *Lunar and Planetary Science Conference*, vol. 34, p. 1659.
- Stone, E., A. Frandsen, R. Mewaldt, E. Christian, D. Margolies, J. Ormes, and F. Snow (1998), The advanced composition explorer, in *The Advanced Composition Explorer Mission*, pp. 1–22, Springer.
- Sultan, P. (1996), Linear theory and modeling of the Rayleigh-Taylor instability leading to the occurrence of equatorial spread F, *Journal of Geophysical Research: Space Physics*, *101*(A12), 26,875–26,891.
- Szuszczewicz, E., R. Tsunoda, R. Narcisi, and J. Holmes (1980), Coincident radar and rocket observations of equatorial spread-F, *Geophysical Research Letters*, *7*(7), 537–540.
- Thiemann, E., F. Eparvier, L. Andersson, C. Fowler, W. Peterson, P. Mahaffy, S. England, D. Larson, D. Lo, N. Schneider, et al. (2015), Neutral density response to solar flares at Mars, *Geophysical Research Letters*, *42*(21), 8986–8992.
- Toon, O. B., T. Segura, and K. Zahnle (2010), The formation of martian river valleys by impacts, *Annual Review of Earth and Planetary Sciences*, *38*, 303–322.
- Ungstrup, E., D. Klumpar, and W. Heikkila (1979), Heating of ions to superthermal energies in the topside ionosphere by electrostatic ion cyclotron waves, *Journal of Geophysical Research: Space Physics*, *84*(A8), 4289–4296.
- Verigin, M., K. Gringauz, N. Shutte, S. Haider, K. Szego, P. Kiraly, A. Nagy, and T. Gombosi (1991), On the possible source of the ionization in the nighttime Martian ionosphere: 1. Phobos 2. HARP electron spectrometer measurements, *Journal of Geophysical Research: Space Physics* (1978–2012), *96*(A11), 19,307–19,313.
- Vignes, D., C. Mazelle, H. Rme, M. Acuna, J. Connerney, R. Lin, D. Mitchell, P. Cloutier, D. Crider, and N. Ness (2000), The solar wind interaction with Mars: Locations and shapes of the bow shock and the magnetic pile-up boundary from the observations of the MAG/ER Experiment onboard Mars Global Surveyor, *Geophysical Research Letters*, *27*(1), 49–52.
- Vogt, M. F., P. Withers, P. R. Mahaffy, M. Benna, M. K. Elrod, J. S. Halekas, J. E. Connerney, J. R. Espley, D. L. Mitchell, C. Mazelle, et al. (2015), Ionopause-like density gradients in the Martian ionosphere: A first look with MAVEN, *Geophysical Research Letters*, *42*(21), 8885–8893.
- Witasse, O., T. Cravens, M. Mendillo, J. Moses, A. Kliore, A. Nagy, and T. Breus (2008a), Solar system ionospheres, in *Comparative Aeronomy*, pp. 235–265, Springer.
- Witasse, O., T. Cravens, M. Mendillo, J. Moses, A. Kliore, A. Nagy, and T. Breus (2008b), Solar System Ionospheres, *Space Science Reviews*, *139*, 235–265.

- Withers, P. (2009), A review of observed variability in the dayside ionosphere of Mars, *Advances in Space Research*, 44(3), 277–307.
- Withers, P., M. Mendillo, D. Hinson, and K. Cahoy (2008), Physical characteristics and occurrence rates of meteoric plasma layers detected in the Martian ionosphere by the Mars Global Surveyor Radio Science Experiment, *Journal of Geophysical Research: Space Physics*, 113(A12).
- Withers, P., M. Fillingim, R. Lillis, B. Häusler, D. Hinson, G. Tyler, M. Pätzold, K. Peter, S. Tellmann, and O. Witasse (2012), Observations of the nightside ionosphere of Mars by the Mars express radio science experiment (MaRS), *Journal of Geophysical Research: Space Physics*, 117(A12).
- Withers, P., M. Vogt, M. Matta, P. Mahaffy, M. Benna, M. Elrod, S. Bougher, C. Dong, J. Y. Chaufray, Y. Ma, and B. M. Jakosky (2015), Comparison of model predictions for the composition of the ionosphere of Mars to MAVEN NGIMS data, *This Issue*.
- Wordsworth, R., F. Forget, E. Millour, J. Head, J.-B. Madeleine, and B. Charnay (2013), Global modelling of the early martian climate under a denser CO<sub>2</sub> atmosphere: Water cycle and ice evolution, *Icarus*, 222(1), 1–19.
- Wordsworth, R. D., L. Kerber, R. T. Pierrehumbert, F. Forget, and J. W. Head (2015), Comparison of warm and wet and cold and icy scenarios for early Mars in a 3-D climate model, *Journal of Geophysical Research: Planets*, 120(6), 1201–1219.
- Yiğit, E., S. L. England, G. Liu, A. S. Medvedev, P. R. Mahaffy, T. Kuroda, and B. M. Jakosky (2015), High-altitude gravity waves in the Martian thermosphere observed by MAVEN/NGIMS and modeled by a gravity wave scheme, *Geophysical Research Letters*, 42(21), 8993–9000.
- Zhang, M., J. Luhmann, and A. Kliore (1990), An observational study of the nightside ionospheres of Mars and Venus with radio occultation methods, *Journal of Geophysical Research: Space Physics (1978–2012)*, 95(A10), 17,095–17,102.
- Zhang, M., J. Luhmann, A. Nagy, J. Spreiter, and S. Stahara (1993a), Oxygen ionization rates at Mars and Venus: Relative contributions of impact ionization and charge exchange, *Journal of Geophysical Research: Planets*, 98(E2), 3311–3318.
- Zhang, M., J. Luhmann, S. Bougher, and A. Nagy (1993b), The ancient oxygen exosphere of Mars: Implications for atmosphere evolution, *Journal of Geophysical Research: Planets*, 98(E6), 10,915–10,923.

## Appendix A

### Overview of the MAVEN spacecraft

The Mars Atmosphere and Volatile EvolutioN (MAVEN) spacecraft is the latest NASA orbiter to visit Mars and it entered orbit about the planet in September 2014. The primary science goal of MAVEN is to understand how the atmosphere has evolved over time and to determine the relative importances of the various atmospheric loss processes active at the planet, both for present day and past Mars (*Jakosky et al., 2015a*). The overarching goal is to be able to determine the total amount of atmosphere lost to space over the course of the planet's history, enabling more accurate estimates of the volume of water once present on the surface. The spacecraft's 4.5 hour orbit is designed such that it precesses about the planet, enabling it to eventually sample the entire near-Mars space environment over the course of its mission. Although originally planned as a single Earth year mission, MAVEN is currently undertaking its second, extended year of science operations and at the time of writing has been approved for a third extended year. Observations made across a wide range of spatial and temporal locations enable a greater understanding of the physical processes active at the planet. The Sun is a key driver of atmospheric escape at Mars; Martian seasons and the Solar cycle for example, are thought to greatly affect atmospheric loss to space. A longer duration mission allows MAVEN to make observations across multiple Martian seasons and solar conditions, furthering our understanding of these drivers and their effects on atmospheric loss to space.

The implications for understanding atmospheric loss processes at Mars, and to ultimately 'count back' in time how much water has been lost from the planet, will greatly improve our

understanding of how our solar system formed and of the key processes required to maintain a warm, wet, aqueous environment. Knowledge gained about our own Solar system may well enable us to discover similar, potentially life-harboring planets, orbiting other stars in our galaxy.

### A.1 Overarching science goals

The Mars Atmosphere and Volatile Evolution mission (MAVEN) is the first spacecraft carrying a complete aeronomy package to Mars. MAVEN entered Mars orbit in September 2014; its 4.5 hour orbit is designed to sample the deep ionosphere of Mars, down to typical altitudes of  $\sim 150$  km. At these altitudes, MAVEN samples the exobase and highly collisional region below it, the regions influencing the bulk of atmospheric loss to space at Mars. The spacecraft also regularly samples the upstream solar wind at apoapsis, and the various plasma boundaries in between. The primary science goals of the MAVEN mission, as listed in *Jakosky et al. (2015a)*, are:

- (1) Measure the composition and structure of the upper atmosphere and ionosphere today, and determine the processes responsible for controlling them.
- (2) Measure the rate of loss of gas from the top of the atmosphere to space, and determine the processes responsible for controlling them.
- (3) Determine properties and characteristics that will allow us to extrapolate backwards in time to determine the integrated loss to space over the four-billion-year history recorded in the geological record.

To achieve these goals MAVEN will undertake several key measurements during its science mission. Solar energy inputs to Mars will be monitored, namely the solar EUV flux and the sporadic occurrence of CMEs and flares. MAVEN is able to monitor these inputs using several instruments carried onboard (as will be discussed in Section YGH) but synthesis with other Solar observatories and modeling tools greatly enhance this ability. Additional Solar monitoring resources include the Advanced Composition Explorer (ACE, *Stone et al. (1998)*) satellite at Earth and the

Wang-Sheeley-Arge-ENLIL (WSA-ENLIL, e.g. *Arge and Pizzo (2000)*) model, for example. The response of the Martian system to these drivers can be measured by MAVEN; magnetospheric responses, such as changing plasma boundaries, and atmospheric responses, including composition, temperature and structure, are all thought to play an important role in determining energy transfer from the solar wind down to the atmosphere. Spatial variations are expected as a result of differing incidence angles between the solar wind and various plasma boundaries at Mars. The precession of MAVEN's orbit about Mars will allow it to ultimately obtain close to complete coverage of these regions. The presence of localized crustal magnetic fields adds an interesting complication in the form of varying interactions with the solar wind which depend on the local orientation and topology of these crustal fields with respect to the upstream solar wind.

## A.2 MAVEN scientific instruments

Here we briefly describe each of the nine scientific instruments onboard MAVEN. Further information can be found in *Jakosky et al. (2015a)* and the respective instrument citations. The Langmuir Probe and Waves instrument will be discussed further in Chapter gfh.

- (1) **Extremer Ultra Violet Monitor (EUVM):** EUVM observes light in three wavelength bands which span the wavelength range most important for energy input into the Martian atmosphere. These are labeled the EUV (0.1 - 3 nm and 17 - 22 nm); soft X-ray (0.1 - 7 nm) and Lyman Alpha (121 - 122 nm) bands. The instrument points at the Sun for the majority of MAVEN's orbit and the 1 s measurement cadence allows the instrument to observe rapid changes in EUV irradiance into the Martian atmosphere as a result of, for example, solar flares (*Eparvier et al., 2015; Thiemann et al., 2015*).
- (2) **Imaging UltraViolet Spectrograph (IUVS):** IUVS observes far and mid UV light to determine atmospheric structure and composition. By measuring the emission of light from atmospheric gases, properties such as vertical density and abundance can be derived for major neutral species (H, C, N, O, CO, N<sub>2</sub>). IUVS can derive these properties between

30 km altitude up to about 4500 km and various observing modes are utilized throughout different altitude regimes. The precession of MAVEN's orbit will allow derivation of these properties to span all longitudes, latitudes and local times (*McClintock et al.*, 2015).

- (3) **Langmuir Probe and Waves (LPW):** LPW consists of two  $\sim 7$  m booms separated by an angular distance of  $\sim 110^\circ$ . The instrument is able to make alternating measurements of current-voltage (IV) characteristics and electric field wave power spectra. Typical instrument cadence at periapsis is between 1 and 4 seconds depending on the exact instrument mode being run at the time. Analysis of measured IV curves allows for the derivation of several plasma parameters, including electron density ( $N_e$ ), electron temperature ( $T_e$ ) and spacecraft potential ( $V_{sc}$ ) (*Andersson et al.*, 2014; *Ergun et al.*, 2015a). More detailed discussion of LPW follows in Section FDG.
- (4) **Magnetometer (MAG):** MAG is a fluxgate magnetometer that measures the vector magnetic field at a rate of 32 Hz (*Connerney et al.*, 2015). The lack of a strong, global magnetic field at Mars means the local magnetic field vector strongly influences the motion of charged particles and is key to understanding the various physical processes acting at Mars. Synthesis of this information with ion and electron data allows for the derivation of pitch angle distributions, for example, which can yield insight as to the sources of various charged particle populations.
- (5) **Neutral Gas and Ion Mass Spectrometer (NGIMS):** NGIMS utilizes a mass quadrupole filter that only allows ions of a specific  $m/z$  (mass to charge) ratio to reach a pulse counting detector. The instrument is able to measure multiple  $m/z$  values in quick succession, and is able to measure both neutral and ion species during the same periapsis pass. The measurement cadence for any one species is typically around 2.6 s, but this can vary depending on the number of species being measured on any given periapsis pass (*Mahaffy et al.*, 2015a,b; *Benna et al.*, 2015).

- (6) **Solar Energetic Particle (SEP):** SEP measures the high energy radiation environment at Mars. Two solid state detectors are able to observe energetic electrons (20 - 1000 keV) and ions (20 - 6000 keV) that are incident on the Martian atmosphere (*Larson et al.*, 2015). The Sun was thought to be much more active in its past and subsequently the effect of high energy particles on the Martian atmosphere may have played a vital role in determining the structure, variability and rate of atmospheric loss then. Understanding current day effects is key to interpolating these effects backwards in time.
- (7) **Suprathermal and Thermal Ion Composition (STATIC):** STATIC is an electrostatic top hat analyzer that uses time of flight to determine ion mass. Electrostatic deflectors give the instrument a  $360^\circ \times 90^\circ$  field of view and it is able to measure energies down to below 1 eV up to several keV. STATIC has a measurement cadence of 4 s; various operation modes enable it to measure cold ionospheric plasma at low altitudes and high energy pickup ions, for example, at higher altitudes (*McFadden et al.*, 2015).
- (8) **Solar Wind Electron Analyzer (SWEA):** SWEA is a hemispherical electrostatic analyzer that measures electron fluxes from a few eV up to 25 keV. It has a  $360^\circ \times 120^\circ$  field of view provided by electrostatic deflectors and a time resolution of 4 s (*Mitchell et al.*, 2016). In the ionosphere it typically measures the superthermal electron population, the high energy tail of the bulk, cold population measured by LPW. At higher altitudes where the ionospheric density falls off and solar wind plasma dominates, the high energy electron population dominates and negligible densities are measured by LPW.
- (9) **Solar Wind Ion Analyzer (SWIA):** SWIA is an electrostatic top hat analyzer that measures ion fluxes from 25 eV up to 25 keV. The instrument also utilizes electrostatic deflectors to achieve a  $360^\circ \times 90^\circ$  field of view and has a time resolution of 4 s. The instrument is designed to observe high energy solar wind ions and as such does not directly determine mass. The mass of observed charged particles can however be inferred from their energy due to the well known and stable composition of the solar wind (*Halekas*

*et al.*, 2015).

### **A.3 MAVEN ‘deep dip’ campaigns**

Occasionally the MAVEN periapsis will be lowered in altitude for what is known as a deep dip campaign. The lowered periapsis altitude is based on a density corridor which typically lies at around 125 km. These deep dip campaigns occur at a cadence of every few months and last for approximately a week. At the time of writing, 5 out of 9 planned deep dip campaigns have been successfully implemented; the limited number of deep dip campaigns arises due to increased fuel usage required to maintain the lower periapsis altitudes. The ability to sample deeper into the collisional region of Mars’ atmosphere sheds further light on the physical processes acting there and their ability to supply particles up to the exobase where the probability of loss to space greatly increases.

## Appendix B

### The LPW instrument

#### B.1 General overview

The LPW instrument consists of two cylindrical sensors 40 cm long by 0.003175 cm in radius, mounted on two 7.1 m booms. The booms are mounted to the MAVEN spacecraft body and are separated by an angular distance of  $\sim 110^\circ$ . Several processing boards and preamplifiers accompany these booms and deal with signal processing. Detailed engineering information and description of operational modes of the LPW instrument can be found in *Andersson et al. (2014)*.

#### B.2 LPW science goals

The primary science goal of the LPW instrument is to measure electron density ( $N_e$ ) and electron temperature ( $T_e$ ) in the Martian ionosphere. These parameters play significant roles in determining various photochemical reaction rates when  $N_e$  is greater than  $\sim 100 \text{ cm}^{-3}$  and are necessary for understanding current and past atmospheric composition and escape rates. Prior to MAVEN only two electron temperature profiles existed at Mars and these were measured by the Viking landers in 1976. Only one of those has been deemed accurate enough for scientific use (*Hanson et al., 1977; Hanson and Mantas, 1988*). Electron density profiles have been measured by spacecraft at Mars using remote sounding techniques, such as the Mars Advanced Radar for Subsurface and Ionosphere Sounding (MARSIS, *Picardi et al. (2004)*) experiment onboard MEX. Various radio occultation measurements of the ionosphere have also been made by the Mars, Mariner and Viking spacecraft (e.g. *Fjeldbo et al. (1970); Savich and Samovol (1976b); Lindal et al. (1979)*).

These density profiles have provided important constraints on the Martian ionosphere but were limited by their various measurement techniques. MARSIS was able to measure electron density along line a vertical line of sight by analyzing the frequencies of radar pulses reflected from different density layers of the ionosphere. Density cavities cannot be measured with this technique and this has limited the number of complete nightside density profiles obtained by MARSIS due to the patchy nature of the nightside ionosphere at Mars. Radio occultations are limited in spatial coverage by the geometrical requirement for the spacecraft to have a direct line of sight through the entire ionosphere to Earth; subsequently no data exist for the nightside and at the sub solar point for these measurements.

The in-situ nature of the LPW  $N_e$  measurements combined with the precession of MAVEN's orbit mean that all longitudes, latitudes and local times can be sampled, greatly enhancing the existing dataset of ionospheric density profiles. The accompanying  $T_e$  measurements made by LPW will provide an entirely new dataset; these temperature (and density) profiles have already been shown to vary spatially across Mars (e.g. *Ergun et al. (2015a)*; *Fowler et al. (2015)*; *Andrews et al. (2015)*) and will provide significantly enhanced accuracy in relation to future modeling studies of the Martian atmosphere.

Wave sounding in the electric field measurement mode fulfills two main goals: the first is to act as an absolute calibration source for the LP derived electron densities; the second is to provide electric field wave power spectra of the Martian plasma environment. Prior observations of plasma waves have been made at Mars (e.g. *Lundin et al. (2004)*; *Espley et al. (2004)*; *Brain et al. (2006)*; *Ergun et al. (2006)*) and waves may result in ion heating or acceleration by electric fields which may significantly impact atmospheric loss. Low frequency waves (0.05 Hz - 10 Hz) typically lie close to the ion gyro frequencies; higher frequency waves indicate electron driven wave phenomena. Further discussion and analysis of LPW wave spectra data is presented in Section YUJ of this thesis.

## Appendix C

### Derivation of $\beta$

Investigation of the LPW probe sheath behavior showed that the parameter  $\beta$  provided a suitable empirical adaptation for the transitional sheath behavior observed. A derivation of  $\beta$  is presented in this appendix; the electron current collected by the probe is first required, given by Equation C.1:

$$I_e = A_p \cdot n_e \cdot e \cdot v_{\text{the}} \quad (\text{C.1})$$

Where  $A_p$  is the probe surface area,  $n_e$  is the ambient electron density,  $e$  is the electron charge and  $v_{\text{the}}$  is the electron thermal velocity, an expression for which is derived in Equation C.3 below.

Let us assume a planar probe surface sitting within the ambient plasma; when the thermal velocity of the collected species is much greater than the Langmuir probe velocity through the plasma (as is the case for electrons in the Martian ionosphere) the Langmuir probe can be assumed stationary with respect to the electron population. In this case, half of the electron population travels towards the probe surface and half travels away from it. The only unknown in Equation C.1 is an expression for  $v_{\text{the}}$  and this is derived next, assuming that electrons with positive velocity travel towards the probe surface, and velocities in the  $v_y$  and  $v_z$  directions have been integrated across all values:

$$v_{\text{the}} = \int_0^{+\infty} v_x \cdot n_e \cdot \left( \frac{m_e}{2\pi T_e} \right)^{\frac{1}{2}} \exp\left( \frac{-m_e v_x^2}{2T_e} \right) dv_x \quad (\text{C.2})$$

Integration of Equation C.2 yields Equation C.3:

$$v_{\text{the}} = \left( \frac{T_e}{2\pi m_e} \right)^{\frac{1}{2}} \quad (\text{C.3})$$

Substitution into Equation C.1 leads to Equation C.4:

$$I_e = A.n_e.e. \left( \frac{T_e}{2\pi m_e} \right)^{\frac{1}{2}} \quad (\text{C.4})$$

This defines the electron current collected by the probe surface for an ambient electron temperature  $T_e$  and no potential applied to the probe. The asymptotic solution to Equation C.4 can be used to define the electron current collected when a potential  $\Phi$  is applied to the probe. Theoretical analytical solutions (see Section 3.3 in Chapter 3) show that for cylindrical probes at large positive potentials,  $I_e \propto (1 + \frac{\Phi}{T_e})^{\frac{1}{2}}$  (for example, Equation 3.1 in Chapter 3); and for spherical probes,  $I_e \propto (1 + \frac{\Phi}{T_e})^1$ . Thus, it is assumed that this asymptotic behavior can be approximated by  $I_e \propto (1 + \frac{\Phi}{T_e})^\beta$ :

$$I_e \approx A.n_e.e. \left( \frac{T_e}{2\pi m_e} \right)^{\frac{1}{2}} \left( 1 + \frac{\Phi}{T_e} \right)^\beta \quad (\text{C.5})$$

The parameter  $\beta$  is now included that characterizes the sheath behavior. The derivative of  $I_e$  with respect to  $\Phi$  is then:

$$\frac{dI_e}{d\Phi} \approx \frac{\beta}{T_e} A.n_e.e. \left( \frac{T_e}{2\pi m_e} \right)^{\frac{1}{2}} \left( 1 + \frac{\Phi}{T_e} \right)^{\beta-1} \quad (\text{C.6})$$

An expression for  $\beta$  can then be obtained by dividing the collected electron current by this derivative, Equation C.5 divided by Equation C.6:

$$\frac{I_e}{\frac{dI_e}{d\Phi}} \approx \frac{T_e}{\beta} \left( 1 + \frac{\Phi}{T_e} \right) \quad (\text{C.7})$$

At low altitudes  $\frac{\Phi}{T_e} \gg 1$  and Equation C.7 reduces to:

$$\frac{I_e}{\frac{dI_e}{d\Phi}} \approx \frac{\Phi}{\beta} \quad (\text{C.8})$$

Thus,  $\beta$  can be defined as:

$$\beta \approx \frac{dI_e}{d\Phi} \frac{\Phi}{I_e} \quad (\text{C.9})$$

## Appendix D

### Summary of variables used in Chapter 3

A summary of the parameters found in Chapter 3 are presented in Table D; the first column shows each parameter; the second is a brief description of each parameter; the third column shows the value of each parameter if it is constant throughout the entire fitting routine; the fourth column shows the corresponding equation number or section that the parameter is derived or described in within the main text (if applicable).

Variable	Description	Value if constant	Reference in text
Subscript $i$	Cylindrical or spherical sheath case	1 (cylinder), 2 (sphere)	S 3.5.1, 3.5.2
$r_{p,i=1}$	Cylindrical probe radius	0.003175 m	E 3.6
$r_{p,i=2}$	Spherical probe radius	0.02546 m	E 3.6
$L_p$	Probe length	0.408 m	S 3.5.1
$A_p$	Probe surface area	0.0081 m <sup>2</sup>	E 3.6
$N_e$	Electron density (m <sup>-3</sup> )	-	S 3.4.1
$T_e$	Electron temperature (K)	-	S 3.4.1
$\lambda_D$	Debye length (m)	-	E 3.7
$v_{th}$	Electron thermal speed (ms <sup>-1</sup> )	-	E 3.20
$V, V_p, \Phi$	Probe potential wrt spacecraft ground (V)	-	S 3.1, 3.5.1, 3.5.2
$a_j$	Sheath impact parameter (m)	-	E 3.9, 3.31
$\sin(\theta_j)$	Sheath solid angle parameter (°)	-	E 3.24
$V_{scp}$	Spacecraft potential (V)	-	S 3.4.3.1
$\beta$	Sheath behavior	0.5 (cylinder), 1 (sphere)	E 3.39
$M_i$	Average ion mass (kg)	-	S 3.5.2, 3.5.5.3(5)
$V_{ramp}$	Start of $T_e$ fit region	-	S 3.5.5.3(1)
$V_{sc,abs}$	Absolute spacecraft velocity (ms <sup>-1</sup> )	-	S 3.4, 3.5.2
$f(v)_{2D}$	2D Maxwellian distribution of electrons	-	E 3.14
$f(v)_{3D}$	3D Maxwellian distribution of electrons	-	E 3.17
$V_{sc}$	Ion-probe relative velocity (ms <sup>-1</sup> )	-	E 3.28
$J_{cyl}$	Ion current density (Am <sup>-2</sup> , cylinder)	-	E 3.32
$J_{sph}$	Ion current density (Am <sup>-2</sup> , sphere)	-	E 3.33
$I_{e,cyl}$	Numerically int. electron current (A, cyl)	-	E 3.22
$I_{e,sph}$	Numerically int. electron current (A, sph)	-	E 3.23
$I_e$	Cold, bulk electron current (A)	-	S 3.4.1
$I_{spe}$	Spacecraft+boom photoelectron current (A)	-	S 3.4.1
$I_{pe}$	Probe photoelectron current (A)	-	S 3.4.1
$I_{hot}$	Hot electron current (A)	-	S 3.4.1
$I_{ion}$	Ion current (A)	-	S 3.4.1

Table D.1: Summary of the parameters used throughout Chapter 3. The first column is the variable, the second column is a brief description, the third column is the value if constant throughout the fitting algorithm, the fourth column references the section (S) or equation (E) within the main text where the variable is discussed.